**The Dissertation Committee for Zoya Heidari Certifies that this is the approved version of the following dissertation:**

# Estimation of Static and Dynamic Petrophysical Properties from Well Logs in Multi-Layer Formations

**Committee:**

Carlos Torres-Verdín, Supervisor

Ekwere J. Peters

William E. Preeg

Erich A. Schneider

Kamy Sepehrnoori

# Estimation of Static and Dynamic Petrophysical Properties from Well Logs in Multi-Layer Formations

**by**

**Zoya Heidari, B.Sc.; M.Sc.**

**Dissertation**

Presented to the Faculty of the Graduate School of

The University of Texas at Austin

in Partial Fulfillment

of the Requirements

for the Degree of

**Doctor of Philosophy**

**The University of Texas at Austin**

**August 2011**

# Dedication

To Peyman, for his love, patience, and support.

To my parents, Soheila and Iraj, for inspiring me to strive to achieve my dreams.

To my brother, Siamak, for cheering me up in the toughest situations.

To my grandparents, for teaching me the importance of hard work and education.

# Acknowledgements

Although this dissertation is a document presenting my research and its conclusions, its creation would not have been possible without the support of a great many people. I owe my gratitude to every individual who helped and inspired me in performing my research and preparing my dissertation.

I would like to express my sincerest gratitude to my supervising professor, Dr. Carlos Torres-Verdín, for his outstanding support and for being an abundant source of motivation. Through his outstanding leadership and insight, I was able to gain a state-of-the-art knowledge of petroleum engineering and formation evaluation, and to aim my research toward the challenging areas of petroleum engineering. His invaluable input into my research has been the key to the successful development of this project. I also want to take this opportunity to thank the other members of my graduate committee, Dr. Ekwere J. Peters, Dr. William E. Preeg, Dr. Erich A. Schneider, and Dr. Kamy Sepehrnoori for their time reviewing my work and for contributing insightful technical comments. Additionally, my special thanks go to the graduate advisor of the Department of Petroleum and Geosystems Engineering, Dr. Sepehrnoori, for his wonderful support during my studies at The University of Texas at Austin.

I was fortunate to work with many members of the formation evaluation group at The University of Texas at Austin. I am pleased to thank all of my current and former team-mates who aided me during my research project. My deepest gratitude goes to Dr. Alberto Mendoza, Jorge Sanchez, Dr. Jesús Mauricio Salazar, Dr. Renzo Angeles, Dr. Robert Mallan, Dr. Gong Li Wang, Ben Voss, Olabode Ijasan, Dr. David Wolf, Chicheng Xu, Andrew Popielski, Philippe Marouby, Haryanto Adiguna, Ali Moinfar, and Rohollah

Abdollah Pour. Special thanks go to Dr. Jesús Mauricio Salazar, Silvia Solano, Jordan Mimoun, Ankur Gandhi, Kanay Jerath, Elton Ferreira, Abhishek Bansal, and Antoine Montaut, for being wonderful office-mates during my four years of studies at The University of Texas at Austin. My great team-mates helped me by taking part in discussions, making great suggestions, and asking constructive questions.

I am grateful to co-authors of my papers, Dr. Alberto Mendoza, Dr. Gong Li Wang, Dr. William Preeg, Olabode Ijasan, and Ben Voss for their technical contributions and for reviewing my work. Special gratitude goes to Dr. Alberto Mendoza and Olabode Ijason for their technical assistance in numerical simulation of nuclear logs. My work would be stressful without the administrative support of Rey Casanova, Frankie Hart, Cheryl Kruzie, special thanks to all of them. Many thanks to Dr. Roger Terzian who kept my computer updated during these four years.

A special note of gratitude goes to Bruce Bilodeau, Keith Boyle, and the anonymous reviewers of one of my papers for their constructive technical and editorial comments which improved the first version of the manuscript. I would like to thank Dr. John Quirein for technical discussions concerning linear conventional multi-mineral solvers. I am grateful of Dr. Ursula Hammes (Bureau of Economic Geology of The University of Texas at Austin), for technical discussions concerning the mineralogy of the Haynesville formation. I am pleased to thank Paul Connolly, Dr. Renzo Angeles, Hani Elshahawi, and Dr. Jesús Salazar for technical discussions concerning the interpretation of field data presented in this dissertation. Special thanks go to Echezona A. Uzoh, German Merletti, Tobi Odumosu, and David Spain for their technical comments about the Haynesville shale-gas play. I thank BP, the Andrew Field Partner Group, and Kerr-McGee (now Anadarko) for providing the data sets used in the field studies.

The knowledge and experience that I gained during my summer internships at Anadarko Petroleum Corporation, and at Marathon Oil Corporation were very helpful for the progress of my research. Thanks go to my mentor and my supervisor at Anadarko Petroleum Corporation, Andrew Perry and Thuy Roque, respectively and also to my mentor and my supervisor at Marathon Oil Corporation, Jeffry Hamman and Dr. Peter Day, respectively who provided opportunities for me to test some parts of my research on challenging field examples. My deepest gratitude goes to all of them.

The work reported in this dissertation was possible with funding from The University of Texas at Austin's Research Consortium on Formation Evaluation, jointly sponsored by Anadarko, Apache Corporation, Aramco, Baker Hughes, BG, BHP Billiton, BP, Chevron, ConocoPhillips, ENI, ExxonMobil, Halliburton, Hess, Maersk, Marathon Oil Corporation, Mexican Institute for Petroleum, Nexen, Pathfinder, Petrobras, Repsol, RWE, Schlumberger, Statoil, TOTAL, and Weatherford. My thanks go to all of them.

I was fortunate to receive fellowships from the Petroleum Engineering Department and Dr. Russ Allen. Their generous endowment was very helpful for me in paying part of my expenses for studying and living at The University of Texas at Austin. I also received travel grants from The University of Texas at Austin, which helped me attend conferences where I could present my research and gain technical experience.

I want to thank my friends, Pooneh Sabouri, Parvaneh Karimi, Saeedeh Mohebbinia, Tatyana Torskaya, Cigdem Omurlu Metin, Amir Frooqnia, Javad Behseresht, Sahar Ayazian, Sahar Asadi, Atefeh Khoshnood, and Maryam Mahnama. Their friendship and cheerful spirit has always been a great source of encouragement to overcome everyday technical and non-technical challenges during my graduate life at The University of Texas at Austin.

Finally yet importantly, I would like to thank my parents and my husband for their abundant encouragement, patience, and love. My achievements would not be possible without their ample help and inspiration. I owe every step of this journey to them.

# Estimation of Static and Dynamic Petrophysical Properties from Well Logs in Multi-Layer Formations

Publication No._____

Zoya Heidari, Ph.D.

The University of Texas at Austin, 2011

Supervisor: Carlos Torres-Verdín

Reliable assessment of static and dynamic petrophysical properties of hydrocarbon-bearing reservoirs is critical for estimating hydrocarbon reserves, identifying good production zones, and planning hydro-fracturing jobs. Conventional well-log interpretation methods are adequate to estimate static petrophysical properties (i.e., porosity and water saturation) in formations consisting of thick beds. However, they are not as reliable when estimating dynamic petrophysical properties such as absolute permeability, movable hydrocarbon saturation, and saturation-dependent capillary pressure and relative permeability. Additionally, conventional well-log interpretation methods do not take into account shoulder-bed effects, radial distribution of fluid saturations due to mud-filtrate invasion, and differences in the volume of investigation of the various measurements involved in the calculations.

This dissertation introduces new quantitative methods for petrophysical and compositional evaluation of water- and hydrocarbon-bearing formations based on the combined numerical simulation and nonlinear joint inversion of conventional well logs.

Specific interpretation problems considered are those associated with (a) complex mineral compositions, (b) mud-filtrate invasion, and (c) shoulder-bed effects. Conventional well logs considered in the study include density, photoelectric factor (PEF), neutron porosity, gamma-ray (GR), and electrical resistivity. Depending on the application, estimations yield static petrophysical properties, dynamic petrophysical properties, and volumetric/weight concentrations of mineral constituents. Assessment of total organic carbon (TOC) is also possible in the case of hydrocarbon-bearing shale.

Interpretation methods introduced in this dissertation start with the detection of bed boundaries and population of multi-layer petrophysical properties with conventional petrophysical interpretation results or core/X-Ray Diffraction (XRD) data. Differences between well logs and their numerical simulations are minimized to estimate final layer-by-layer formation properties. In doing so, the interpretation explicitly takes into account (a) differences in the volume of investigation of the various well logs involved, (b) the process of mud-filtrate invasion, and (c) the assumed rock-physics model.

Synthetic examples verify the accuracy and reliability of the introduced interpretation methods and quantify the uncertainty of estimated properties due to noisy data and incorrect bed boundaries. Several field examples describe the successful application of the methods on (a) the assessment of residual hydrocarbon saturation in a tight-gas sand formation invaded with water-base mud (WBM) and a hydrocarbon-bearing siliciclastic formation invaded with oil-base mud (OBM), (b) estimation of dynamic petrophysical properties of water-bearing sands invaded with OBM, (c) estimation of porosity and volumetric concentrations of mineral and fluid constituents in carbonate formations, and (d) estimation of TOC, total porosity, total water saturation, and volumetric concentrations of mineral constituents in the Haynesville shale-gas formation. Comparison of results against those obtained with conventional petrophysical

interpretation methods, commercial multi-mineral solvers, and core/XRD data confirm the advantages and flexibility of the new interpretation techniques introduced in this dissertation for the quantification of petrophysical and compositional properties in a variety of rock formations.

# Table of Contents

# List of Tables

# List of Figures

**Figure 4.7:** Synthetic Case No. 3, consisting of multi-layer, successive thin beds in two hydraulically separated gas-bearing and water-bearing zones. Comparison of final simulated well logs (dash-dotted black line) and input well logs (solid line). The left-hand panel shows the spatial distribution (radial and vertical directions) of water saturation after 3 days of WBM-filtrate invasion. Results are shown for array-induction resistivity (second left-hand panel), PEF (third left-hand panel), GR (fourth left-hand panel), density and neutron porosity (water-filled limestone porosity units, fifth left-hand panel) logs. The three right-hand panels compare volumetric concentrations of shale and mineral constituents, porosity, and water saturation obtained from conventional linear and nonlinear joint inversion (Method No. 1) of resistivity, density, neutron porosity, GR, and PEF logs against actual values.168

# Chapter 1: Introduction

This dissertation introduces new methods for petrophysical/compositional evaluation of conventional and unconventional reservoirs based on nonlinear joint inversion of nuclear and electrical resistivity well logs. First, this dissertation investigates the possibility of quantifying dynamic petrophysical properties such as residual hydrocarbon saturation and saturation-dependent capillary pressure in siliciclastic sedimentary sequences based on the combined numerical simulation of nuclear and electrical resistivity logs. Second, algorithms are introduced for nonlinear joint inversion of nuclear and electrical resistivity well logs to automatically assess porosity and volumetric/weight concentrations of mineral/fluid constituents. Finally, the new interpretation methods are applied to petrophysical/compositional evaluation of measurements acquired in carbonate and organic-shale formations.

## 1.1 BACKGROUND

Reliable assessment of static and dynamic petrophysical properties is necessary to evaluate and quantify hydrocarbon reserves and production. Static petrophysical properties include porosity, water saturation, and volumetric concentration of shale, whereas dynamic petrophysical properties consist of absolute permeability, movable hydrocarbon saturation, and saturation-dependent relative permeability and capillary pressure. Petrophysical evaluation based on well logs has been successful mostly in the assessment of static petrophysical properties. Dynamic petrophysical properties are usually estimated based on empirical correlations (Land, 1968; Land, 1971), pore-scale models (Suicmez et al., 2007; Mohanty et al., 1987), or core laboratory measurements. Mineralogy assessment is equally important in petrophysical evaluation because of the direct influence of mineral concentrations on estimates of grain density, porosity, and,

consequently, on fluid saturation. Additionally, in rocks with complex lithology, such as organic-shale formations, accurate knowledge of mineralogy is necessary to detect optimal zones for fracturing jobs. Estimating petrophysical/ compositional properties from well logs has been challenging in the presence of light hydrocarbon, thinly-bedded formations, mud-filtrate invasion, and complex lithology because of borehole environmental effects, non-uniqueness, and differences in vertical resolution and radial length of investigation of measurements involved in the interpretation.

Mud-filtrate invasion is a common concern in the petrophysical evaluation of well logs. Mud-filtrate invasion originates from overbalance pressure in boreholes, which causes drilling mud to invade permeable formations. The spatial distribution of mud-filtrate invasion depends on static/dynamic rock properties, properties of formation fluids and mud, and invasion parameters such as time of invasion, overbalance pressure, and mud-cake properties. Mud-filtrate invasion significantly affects the spatial distribution of fluid saturations in the near-wellbore region and, consequently, well logs. Numerical simulation of water-base mud- (WBM) and oil-base mud- (OBM) filtrate invasion as well as numerical simulation of well logs is often used to quantify environmental effects and formation parameters on borehole measurements.

Recent publications take advantage of the relationship between well logs, mud-filtrate invasion, and formation properties to estimate absolute permeability from well logs by honoring the physics of mud-filtrate invasion and by numerically simulating array-induction resistivity logs (Salazar et al., 2006). A combined numerical simulation of other petrophysical borehole measurements, such as nuclear logs, can also be used to assess dynamic formation properties such as residual hydrocarbon saturation and saturation-dependent capillary pressure and relative permeability. Combined simulation of resistivity with other measurements takes into account the different radial lengths of

investigation of measurement instruments and also decreases non-uniqueness of results. Angeles (2009) and Alpak et al. (2008) used formation-tester measurements to assess dynamic formation properties such as saturation-dependent capillary pressure and relative permeability, but emphasized the non-uniqueness of results. They found that the simultaneous inversion of formation-tester measurements is ill-posed and heavily dependent on the initial guess.

Non-uniqueness of results is a significant challenge in all petrophysical/ compositional evaluations. It arises if (a) more than one parameter affects the measurement, (b) the number of unknown formation properties is greater than the number of laboratory measurements and logs used in the interpretation, or (c) the sensitivity of borehole measurements to formation properties is marginal. An example of significant non-uniqueness of results occurs in the presence of rocks with complex lithology such as carbonate and organic-shale formations.

Lithology quantification methods from well logs were first introduced with the use of density-sonic, density-photoelectric factor, neutron-sonic, neutron-density, and Matrix Identification (MID) cross-plots (Clavier and Rust, 1976; Schlumberger, 2005). Although these methods are reliable for the case of two minerals, they are unreliable in formations with multi-mineral composition. Neutron-capture spectroscopy measurements were recently introduced to quantify complex mineralogy (Herron and Herron, 1996; Herron et al., 2002). However, these measurements can also be significantly affected by shoulder beds.

Artificial neural networks, fuzzy logic, and neuro-fuzzy models have been used to diagnose and quantify lithofacies (Cuddy, 2000; Gonçalves et al., 1995). Such methods require substantial training with core measurements to warrant reliable and accurate estimations and can easily fail in the presence of complex lithology and thinly-bedded

rock sequences. A common approach in the petroleum industry to quantify lithology is linear/quasi-linear joint inversion of well logs. This method has been implemented in commercial multi-mineral and petrophysical interpretation software (Mayer and Sibbit, 1980).

Quirein et al. (1986) suggested a probabilistic approach that lumps similar minerals and estimates mineral and fluid concentrations in order to decrease the non-uniqueness of results associated with linear/quasi-linear joint inversion of well logs. However, there are two major problems with conventional joint inversion techniques: First, conventional software (a) assumes linear/quasi-linear correlations between log responses and volumetric concentrations of formation constituents (Doveton, 1994; Mayer and Sibbit, 1980; Quirein et al., 1986), and (b) uses empirical or approximate formulae to simulate log responses. Experience shows that such an assumption and formulae are not reliable, for instance, in the case of neutron porosity when light hydrocarbon, saline connate water, and complex lithology are present. Second, conventional methods usually deliver depth-by-depth petrophysical interpretation, which fails to take into account shoulder-bed effects. Correcting for shoulder-bed effects requires accurate numerical simulation of instrument responses. Although numerical simulation of electrical resistivity logs is commonly used by the petroleum industry, there are no methods that can numerically simulate nuclear measurements in an efficient manner.

Traditional numerical simulation of nuclear logs is based on the Monte Carlo method, which is not time-efficient for inversion purposes. Recently, Mendoza et al. (2010) introduced a fast iterative refinement method for numerical simulation of nuclear logs based on pre-calculated Flux Sensitivity Functions (FSFs). This new fast simulator

for nuclear logs opens the possibility of joint inversion with resistivity logs to improve petrophysical/compositional evaluation and reduce non-uniqueness of results.

## 1.2 STATEMENT OF THE PROBLEM

In conventional interpretation techniques, quantitative assessment of dynamic petrophysical properties has been traditionally linked to static petrophysical properties (Timur, 1968; Land, 1968). However, the assessment of static petrophysical properties is itself affected by phenomena and properties such as mud-filtrate invasion, presence of light hydrocarbon in the formation, shoulder-bed effects, and complex lithology.

Coping with mud-filtrate invasion and shoulder-bed effects in conventional petrophysical interpretation is a major technical challenge. Mud-filtrate invasion is usually considered to be a piston-like front. The piston-like assumption can cause inaccuracy in the assessment of petrophysical properties. In addition to the effects of mud-filtrate invasion on well logs, correcting for shoulder-bed effects on nuclear logs has also been impractical in the petroleum industry due to lack of a fast numerical method for the simulation of nuclear measurements. In this dissertation, I take into account the effects of mud-filtrate invasion and shoulder beds on well logs by simulating the process of invasion and by applying a recently introduced fast iterative refinement method to simulate nuclear logs (Mendoza et al., 2010).

Additionally, I use the effect of mud-filtrate invasion on well logs to quantitatively estimate dynamic petrophysical properties. Subsequently, I estimate residual hydrocarbon saturation, absolute permeability, and saturation-dependent capillary pressure and relative permeability from the combined numerical simulation of nuclear and resistivity logs, and by honoring the physics of mud-filtrate invasion, thereby

explicitly taking into account the different radial lengths of investigation of measurements involved in the interpretation.

Another aspect of this dissertation focuses on the compositional evaluation of formations where conventional multi-mineral solvers are not accurate. I introduce methods based on the nonlinear joint inversion of nuclear and resistivity logs to improve the assessment of porosity and volumetric concentrations of mineral/fluid constituents (a) in formations with complex lithology, (b) in thinly-bedded formations, and (c) in formations affected by mud-filtrate invasion. In addition to formation properties, bed properties such as density, neutron migration length, photoelectric factor (PEF), electrical conductivity, and uranium (Ur), thorium (Th), and potassium (K) concentrations are outcomes of the new interpretation methods.

Next, I test the reliability of the new nonlinear joint inversion methods on carbonate formations with complex lithology and thin beds to assess volumetric/weight concentrations of minerals, porosity, and fluid saturations.

The final goal is to develop a quantitative petrophysical/compositional interpretation method based on well logs for organic-shale formations to assess total organic carbon (TOC), total porosity, total water saturation, and volumetric/weight concentrations of mineral constituents. Conventional petrophysical/compositional interpretation methods are often unreliable in organic-shale formations in the presence of kerogen, where complex lithology and thin beds are commonplace. The interpretation technique developed in this dissertation for organic-shale evaluation is not dependent on either an empirical formula or a calibration for TOC.

## 1.3 RESEARCH OBJECTIVES

This dissertation focuses on (1) quantifying the effects of mud-filtrate invasion, dynamic/static petrophysical properties, and shoulder beds on nuclear and electrical resistivity measurements, and (2) quantitatively combining nuclear and electrical resistivity logs to improve the assessment of petrophysical/compositional properties by reducing the associated non-uniqueness. The objectives of the research are as follows:

i. To develop methods to quantify residual hydrocarbon saturation based on a dynamic petrophysical model that explicitly honors the well logs. To that end, I consider both the vertical character of well logs across fluid-saturated units and the influence of radial invasion on well logs acquired in permeable formations.

ii. To introduce methods to estimate dynamic petrophysical properties such as saturation-dependent capillary pressure and relative permeability by taking into account the radial distribution of water saturation after mud-filtrate invasion.

iii. To implement inversion techniques separately on density, neutron porosity, gamma-ray spectroscopy, PEF, and electrical resistivity logs to estimate accurate bed properties in thinly-bedded formations. In doing so, inversion of nuclear logs is implemented with a newly introduced fast iterative refinement method for numerical simulation.

iv. To develop joint inversion methods for density, neutron porosity, gamma-ray (GR)/GR-spectroscopy, PEF, and electrical resistivity logs to estimate porosity and volumetric/weight concentrations of mineral/fluid constituents in thinly-bedded and/or invaded formations.

v. To appraise the reliability of the newly introduced interpretation methods on a variety of challenging field examples, including tight-gas sands, carbonates, and organic-shale formations.

## 1.4 METHOD OVERVIEW

In the first part of this dissertation, I quantify the effects of static and dynamic petrophysical properties on electrical resistivity and nuclear measurements in the presence of WBM- and OBM-filtrate invasion. I introduce interpretation methods based on the combined iterative simulation of density, neutron porosity, GR, PEF, and electrical resistivity well logs to assess dynamic petrophysical properties such as residual hydrocarbon saturation and saturation-dependent capillary pressure. The iterative combined simulation of well logs begins with an initial guess of the multi-layer initial petrophysical model. Simulation of the process of mud-filtrate invasion is then implemented to describe the spatial distribution of fluid saturation, water salinity, and fluid density in the near-borehole region. The next step is the numerical simulation of nuclear and electrical resistivity logs based on the estimated spatial distribution of fluid saturation. I then reduce the difference between well logs and their numerical simulations iteratively by updating the initial guess of unknown properties. Numerical synthetic examples are followed by several field examples, including a tight-gas sand reservoir and an oil-bearing siliciclastic sedimentary sequence, to assess residual hydrocarbon saturation. Three hydrocarbon-bearing siliciclastic sedimentary sequences underlain by active aquifers confirm the successful application of the new method for assessment of saturation-dependent capillary pressure in agreement with calculated vertical variations of water saturation.

The next part of the dissertation introduces three nonlinear joint inversion techniques for estimating porosity and volumetric/weight concentrations of mineral/fluid constituents based on density, neutron porosity, GR/GR-spectroscopy, PEF, and electrical resistivity logs.

The first method considers the effect of mud-filtrate invasion in the process of non-linear joint inversion of well logs. An initial multi-layer petrophysical model is updated with linear iterations until reaching a good agreement between measured logs and their numerical simulations. In each linear iteration, simulated logs are updated based on the new layer-by-layer model properties and the updated spatial distribution of formation fluids, water salinity, and fluid density, which are calculated based on the simulation of mud-filtrate invasion. Although this method consumes the most CPU time, it is recommended for interpretation of thinly-bedded invaded formations that include complex lithology.

The second method corrects the estimated physical bed properties for shoulder-bed effects on well logs, in addition to assimilating the general nonlinear relationship between volumetric concentrations of formation constituents and well logs. This method consists of two steps: the first step is separate inversion of well logs (i.e., density, neutron porosity, GR-spectroscopy, PEF, and electrical resistivity) to estimate bed physical properties (i.e., layer-by-layer density, migration length, Ur, Th, and K concentrations, PEF, and electrical conductivity) corrected for shoulder-bed effects. I implement a fast linear inversion algorithm to density, PEF, and GR-spectroscopy measurements, which is based on pre-calculated FSF functions. A nonlinear gradient-based inversion algorithm is applied to neutron porosity and electrical resistivity/conductivity measurements to assess layer-by-layer neutron migration length and electrical resistivity/conductivity, respectively. The second step is a nonlinear joint inversion of bed properties to estimate

porosity and volumetric/weight concentrations of mineral constituents. This second method of interpretation is reliable in the presence of thinly-bedded formations with complex lithology, where the effect of mud-filtrate invasion is negligible.

The third method is a fast depth-by-depth joint inversion of well logs, which takes into account the nonlinear relationship between volumetric concentrations of formation constituents and well logs. This method is recommended for formations with thick beds and complex lithology.

Synthetic examples confirm the reliability of the new inversion methods in the interpretation of well logs acquired in formations with complex lithology, thin beds, and those affected by mud-filtrate invasion. I also document successful applications of the proposed methods on three complex carbonate formations.

Finally, I introduce a method for petrophysical/compositional evaluation of organic shale. This method is based on nonlinear joint inversion of bed properties, which is modified by adopting a petrophysically consistent model for organic-shale formations. The method is applied to a well in the Haynesville shale-gas formation and results are successfully compared against (a) core/X-Ray Diffraction (XRD) data and (b) conventional mineralogy analysis and petrophysical interpretation.

## 1.5 OUTLINE OF THE DISSERTATION

This dissertation consists of seven chapters. Following the introductory chapter, Chapter 2 examines the possibility of quantifying residual hydrocarbon saturation from well logs. It introduces an interpretation method based on the combined numerical simulation of nuclear and electrical resistivity logs to estimate residual hydrocarbon saturation in hydrocarbon-bearing formations including WBM and OBM. Applications of

the new interpretation method are documented in both tight-gas sands and siliciclastic oil-bearing formations.

Chapter 3 examines the influence of the dynamic petrophysical properties of water-bearing sands on electrical resistivity and nuclear logs. It also suggests the combined numerical simulation and inversion of nuclear and electrical resistivity logs to estimate both static (porosity and water saturation) and dynamic (absolute permeability, saturation-dependent capillary pressure, and relative permeability) petrophysical properties of water-bearing sands. The suggested method is verified on water-bearing zones of three siliciclastic hydrocarbon-bearing reservoirs underlain by active aquifers.

Chapter 4 develops three new nonlinear joint inversion methods to assess petrophysical/compositional properties (porosity and the volumetric/weight concentrations of mineral/fluid constituents) of thinly-bedded invaded formations with complex mineralogy.

Chapter 5 documents the successful application of the new nonlinear joint inversion strategies on three challenging carbonate formations.

Chapter 6 modifies one of the previously introduced nonlinear joint inversion methods for petrophysical/compositional evaluation of organic-shale formations. A field example from the Haynesville shale-gas formation verify the accuracy of the modified method for assessment of TOC, total porosity, total water saturation, and volumetric/weight concentrations of mineral constituents.

Finally, Chapter 7 summarizes the contributions of the research stemming from this dissertation and draws conclusions and pertinent recommendations for future research.

## 1.6 LIST OF PUBLICATIONS

Several journal and conference papers based on the research described in this dissertation have been published or submitted for peer review; they are listed below.

### 1.6.1 Refereed Journal Publications

Heidari, Z., Torres-Verdín, C., Mendoza, A., and Wang, G. L., 2011, Assessment of residual hydrocarbon saturation with the combined quantitative interpretation of resistivity and nuclear logs: *Petrophysics*, vol. 52, no. 3, pp. 217–237.

Heidari, Z. and Torres-Verdín, C., 2011, Estimation of dynamic petrophysical properties of water-bearing sands invaded with oil-base mud from multi-physics borehole geophysical measurements, *Geophysics* (to be submitted for review).

Heidari, Z., Torres-Verdín, C., and Preeg, W. E., 2011, Improved estimation of mineral and fluid volumetric concentrations in thinly-bedded and invaded formations, Part I: Numerical Examples, *Geophysics* (submitted for review).

Heidari, Z., Torres-Verdín, C., and Preeg, W. E., 2011, Improved estimation of mineral and fluid volumetric concentrations in thinly-bedded and invaded formations, Part II: Field Applications, *Geophysics* (to be submitted for review).

Heidari, Z., Torres-Verdín, C., and Preeg, W. E., 2011, Quantitative method for estimating total organic carbon and porosity, and for diagnosing mineral constituents in shale gas formations from well logs, *Petrophysics* (to be submitted for review).

### 1.6.2 Refereed Conference Proceedings

Heidari, Z., Hamman, J. G., Day, P. I., Gorney, D. L., and Alfred D., 2011, Assessment of movable gas saturation and rock typing based on the combined simulation of petrophysical borehole measurements: *52nd Annual Logging Symposium Transactions*: Society of Professional Well Log Analysts, Colorado Springs, Colorado, May 14-18.

Heidari, Z., Torres-Verdín, C., and Preeg, W. E., 2011, Quantitative method for estimating total organic carbon and porosity, and for diagnosing mineral constituents in shale gas formations from well logs: *52nd Annual Logging*

*Symposium Transactions*: Society of Professional Well Log Analysts, Colorado Springs, Colorado, May 14-18.

Marouby, P., Heidari, Z., and Torres-Verdín, C., 2011, Assessment of in-situ elastic properties of shale-gas formations with the joint quantitative interpretation of sonic, nuclear, and resistivity logs: *52nd Annual Logging Symposium Transactions*: Society of Professional Well Log Analysts, Colorado Springs, Colorado, May 14-18.

Heidari, Z. and Torres-Verdín, C., 2010, Estimation of dynamic petrophysical properties of water-bearing sands invaded with oil-base mud from multi-physics borehole geophysical measurements: *80th SEG international exposition and annual meeting*: Society of Exploration Geophysicists, Denver, Colorado, October 17-22.

Heidari, Z., Torres-Verdín, C., and Preeg, W. E., 2010, Improved estimation of mineral and fluid volumetric concentrations in thinly-bedded and invaded formations: *51st Annual Logging Symposium Transactions*: Society of Professional Well Log Analysts, Perth, Australia, June 19-23.

Heidari, Z., Torres-Verdín, C., Mendoza, A., Ijasan, O., Voss, B., and Preeg, W. E., 2009, Rapid, interactive assessment of petrophysical and geometrical effects on density and neutron logs acquired in vertical and deviated wells: *Society of Petroleum Engineers (SPE) 2009 Annual International Meeting*, New Orleans, Louisiana, October 4-7.

Heidari, Z., Torres-Verdín, C., Mendoza, A., and Wang, G.L., 2009, Improving the assessment of residual hydrocarbon saturation with the combined quantitative interpretation of resistivity and nuclear logs: *50th Annual Logging Symposium Transactions*: Society of Professional Well Log Analysts, The Woodlands, Texas, June 21-24.

# Chapter 2: Assessment of Residual Hydrocarbon Saturation

Estimation of residual hydrocarbon saturation remains an outstanding challenge in formation evaluation and core analysis. Standard interpretation methods for nuclear-resistivity logs cannot distinguish between mobile and residual hydrocarbon saturation. In extreme cases, fluid pumpout or production testing are the only options to ascertain whether the reservoir's in-situ hydrocarbon is mobile.

This chapter sets forth a new method to distinguish mobile from residual hydrocarbon and to quantify residual hydrocarbon saturation. The method combines modeling of resistivity and nuclear logs with the physics of mud-filtrate invasion to quantify the effect of residual hydrocarbon saturation on both nuclear and resistivity logs. This strategy explicitly takes into account the different volumes of investigation of resistivity and nuclear measurements and does not assume that the near-borehole region is flushed to the level of residual hydrocarbon saturation. The method begins with an initial multi-layer petrophysical model which is constructed via standard procedures of well-log interpretation and core measurements. Thereafter, we simulate the physics of mud-filtrate invasion and the corresponding resistivity, density, and neutron porosity logs. Initial estimates of residual hydrocarbon saturation and parametric relative permeability are refined until achieving a good agreement between simulated and measured neutron porosity and density logs. Next, we refine initial estimates of water saturation, porosity, and permeability until we secure a good match between numerically simulated and measured resistivity logs.

The method of interpretation considers two specific options for implementation: (1) quantification of the influence of residual hydrocarbon saturation on the radial

distribution of fluid saturation due to invasion, and (2) appraisal of invasion effects on the vertical distribution of fluid saturation within a flow unit that exhibits both hydrocarbon and water saturation in capillary equilibrium.

Application examples are described for the cases of tight-gas sand reservoirs invaded with water-base mud (WBM) and oil-bearing reservoirs invaded with oil-base mud (OBM). In the case of tight-gas sands, the method explains the marginal productivity of deeply invaded beds that exhibit cross-over between density and neutron porosity logs. For a 0.15-porosity formation, when the residual gas saturation increases by 0.10, the cross-over between neutron porosity and density logs increases by 2.4 sandstone porosity units. Interpretation results indicate measurable sensitivity of nuclear logs to residual hydrocarbon saturation in cases of deep WBM invasion due to immiscibility between invaded and in-situ fluids. However, the accuracy of the method decreases with increasing values of both hydrocarbon pore volume and hydrocarbon density. In the case of OBM invasion, reliable estimations of residual hydrocarbon saturation are possible with relative density differences above 15% between mud filtrate and in-situ hydrocarbon.

## 2.1 INTRODUCTION

Conditions of residual hydrocarbon saturation in porous and permeable rocks commonly arise because of repeated cycles of hydrocarbon-water imbibition and drainage promoted by trap breaching and aquifer encroachment. Depending on the porosity, permeability, and wettability of the rock, a significant portion of the original oil in place could remain in residual form within reservoir rocks after imbibition. In some situations, residual hydrocarbon saturation is large enough to cause false indications of mobile hydrocarbon saturation with standard well-log interpretation methods. This latter

condition is difficult to ascertain from well logs alone, especially in the presence of deep radial invasion. Incorrect estimates of mobile hydrocarbon saturation routinely cause financial losses to exploration and development companies.

Residual hydrocarbon saturation is a dynamic petrophysical property that plays an important role in production behavior. Without the use of a dynamic petrophysical model, standard well-log interpretation methods cannot distinguish between residual and mobile hydrocarbon saturation. The main objective of this chapter is to explore methods to ascertain and quantify residual hydrocarbon saturation based on a dynamic petrophysical model that explicitly honors the well logs. To that end, we consider both the vertical character of well logs across fluid-saturated units and the influence of radial invasion on well logs acquired in permeable formations. The novelty of this work resides in the quantitative, concomitant use of both nuclear and resistivity logs to assess sensitivity to invasion and fluid displacement.

Previous related publications studied different trapping mechanisms, including hydrodynamic, solution, mineral, and capillary trapping (Pentland et al., 2008). The focus of this chapter is on estimating trapped hydrocarbon in the rock's pore space due to capillary forces. In many publications, capillary trapped hydrocarbon is referred to as trapped hydrocarbon. To avoid confusion about different trapping mechanisms, in this chapter we refer to the capillary trapped hydrocarbon in porous rocks as residual hydrocarbon saturation. All the synthetic cases and field examples studied comprise siliciclastic sedimentary sequences, where non-connected porosity is negligible and estimates of trapped or immobile hydrocarbon saturation are equivalent to residual hydrocarbon saturation. The main difference between the method introduced in this chapter and conventional interpretation methods is the way in which we take into account flushed-zone saturation. In conventional methods, residual hydrocarbon saturation in

imbibition cases is often assumed to be equal to flushed-zone saturation. This assumption is invalid in cases of shallow mud-filtrate invasion, where well-log measurements are affected by the non-invaded zone. Moreover, invasion with WBM does not necessarily imply that the flushed zone saturation is equal to trapped or residual hydrocarbon saturation. Flushed-zone saturation can be equal or lower than residual hydrocarbon saturation, depending on static/dynamic petrophysical and invasion properties. With the method introduced here, we numerically simulate the radial invasion profile and quantify the effect of mud-filtrate invasion on measured well logs. Another advantage of the introduced method over conventional methods is the explicit consideration of the different volumes of investigation inherent to the borehole measurements involved in the interpretation. Variations of dynamic petrophysical properties, including residual hydrocarbon saturation, affect the shape and radial length of mud-filtrate saturation and, consequently, influence well log measurements.

Standard well-log analysis usually provides acceptable estimates of initial hydrocarbon saturation. Estimation of residual hydrocarbon saturation, however, is vastly more challenging. Prior studies invoked correlations between initial and residual hydrocarbon saturation to estimate residual hydrocarbon saturation for a given value of initial hydrocarbon saturation. Most of these correlations were developed based on rock-core laboratory measurements. Land's equation (Land, 1968, 1971) represents one of the first methods used to estimate imbibition residual hydrocarbon saturation based on initial hydrocarbon saturation. The relationship between residual and initial gas saturation proposed by Land is given by

$$S_{gr}^{*} = \frac{S_{gi}^{*}}{1 + CS_{gi}^{*}}, \tag{2.1}$$

where $C$ is a constant expressed by

$$C = \frac{1}{\left(S_{gr}^{*}\right)_{\max}} - 1, \tag{2.2}$$

where $S_{gi}$ is initial gas saturation, $S_{gr}$ is residual gas saturation, and the symbol $S^*$ identifies effective saturation, defined as

$$S^{*} = \frac{S_h}{1 - S_{wr}}, \tag{2.3}$$

where $S_{wr}$ is connate or irreducible water saturation and $S_h$ is hydrocarbon saturation. **Figure 2.1** shows the general behavior of residual versus initial hydrocarbon saturation predicted by Land's (1971) equation, which describes a monotonically increasing trend that becomes constant at high values of initial hydrocarbon saturation.

Ma and Youngren (1994) extended Land's equation to explain their oil-wet experimental data. Jerauld (1997) modified Land's equation to match mix-wet core-sample measurements. Aissaoui (1983) developed an alternative form of Land's equation based on extensive experimental data. The corresponding equations were subsequently compared to experimental studies performed on various core samples (Suzanne et al., 2003; Pentland et al., 2008; Kleppe et al., 1997). However, measurements did not match predictions performed with Land's equation. Suzanne et al. (2003) and Pentland et al. (2008) confirmed that Aissaoui's (1983) is a reliable empirical model. In general, the empirical nature of all the proposed equations leads to non-universal correlations between residual and initial hydrocarbon saturation.

There are studies that investigate qualitative relationships between residual hydrocarbon saturation and reservoir properties, such as lithology type, porosity, permeability, pore-size distribution, microporosity, initial hydrocarbon saturation, and irreducible water saturation, among others (Chierici et al., 1963; Suzanne et al., 2001; Kralik et al., 2000). However, these studies did not converge to similar trends in their attempts to correlate residual hydrocarbon saturation with reservoir properties. For instance, Kralik et al. (2000) found a decrease of trapped gas saturation with increasing porosity. Suzanne et al. (2001) reported a probable increase of maximum residual gas saturation with increasing porosity, while Chierici et al. (1963) found no correlation between residual gas saturation and porosity.

Pore-scale network modeling is another approach to study correlations between residual hydrocarbon saturation and other petrophysical properties (Suicmez et al., 2007; Mohanty et al., 1987). Suicmez et al. (2007) investigated the effect of wettability on residual hydrocarbon saturation. Their results contradicted Land's (1971) predictions in the presence of variable wettability conditions, such as those arising in strongly oil-wet rocks.

Another approach to evaluate residual hydrocarbon saturation is with specialized core laboratory measurements. Steady-state displacement, co-current imbibition, counter-current imbibition, and centrifuge drainage are some methods normally used to measure residual hydrocarbon saturation and saturation-dependent relative permeability in the laboratory (Mulyadi et al., 2000).

Hydrocarbon trapping at the microscopic scale affects well-log responses at the macroscopic scale. A solid understanding of trapping mechanisms is necessary to interpret well logs. Hydrocarbon trapping can be affected by capillary forces, viscous

forces, inertial forces, and mineral binding forces. Well-log analysis together with rock-fluid modeling techniques can enable the quantification of residual hydrocarbon.

Trewin et al. (1990) applied resistivity log analysis to calculate residual oil saturation ($S_{or}$) and compared the corresponding results to core data. They concluded that their method was not successful due to poor quality of core measurements and inaccurate selection of the saturation exponent used in resistivity calculations. Spears et al. (2008) documented a field case wherein classical well-log petrophysical interpretation led to a non-commercial outcome concerning gas production. Standard well-log interpretation indicated high gas saturation but subsequent production tests yielded mostly water. Despite a prominent neutron-density cross-over, gas production was poor because the reservoir was already at residual gas saturation.

Uncertainties in the estimation of residual hydrocarbon saturation, as explained above, encouraged us to develop general diagnostic methods not based on experimental formulations or core measurements. We chose to study the sensitivity of well logs to the process of mud-filtrate invasion given that invasion is to a large extent governed by dynamic petrophysical properties, including residual hydrocarbon saturation. Indeed, we believe that reliable discrimination between mobile and residual hydrocarbon is not possible with conventional petrophysical log interpretation methods that invoke a static petrophysical model. It is necessary that well logs be interpreted in combination with a dynamic petrophysical model that involves the physics of mud-filtrate invasion and the corresponding role played by residual hydrocarbon saturation in porous and permeable formations.

Several published works have invoked well-log simulation based on the physics of mud-filtrate invasion to estimate dynamic petrophysical properties (Salazar et al., 2006; Torres-Verdín et al., 2006). In all these works, the authors assumed constant

saturation-dependent relative permeability and capillary pressure properties based on core data. To our knowledge, there have been no attempts to estimate residual hydrocarbon saturation using the physics of mud-filtrate invasion. The use of nuclear and resistivity logs in combination with mud-filtrate invasion opens the possibility of a new method to diagnose and quantify residual hydrocarbon saturation. Moreover, neutron porosity and density logs are shallow-sensing measurements that remain influenced by non-displaced hydrocarbon saturation within the fully invaded radial zone.

The simulation method proposed in this chapter requires well logs, fluid properties, rock-fluid properties, petrophysical properties, core data, mud properties, and invasion time. Rock-fluid properties consist of saturation-dependent relative permeability and capillary pressure. The latter properties may vary with petrophysical properties. Several researchers developed interpretation models to describe saturation-dependent two-phase or multi-phase relative permeability (Jacobsen et al., 2006; Honarpour et al., 1986; Honarpour et al., 1982). These models can be categorized as capillary-driven representations (such as Kozeny-Carman) statistical correlations, empirical correlations (Honarpour et al., 1982), and correlations based on network representations (Honarpour et al., 1986). Brooks and Corey (1964) developed one of the most popular capillary pressure-saturation relationships. In this dissertation we adopt their parametric model to define rock-fluid curves. The corresponding equations are given in terms of relative permeability end points, as well as residual and irreducible fluid saturations.

The first step in the simulation process is standard well-log interpretation to calculate initial petrophysical properties. Average layer-by-layer petrophysical properties obtained from this analysis become the entry point for the simulation method. The second step consists of constructing rock-fluid properties and simulation of the process of mud-filtrate invasion. We assume that rocks are water-wet and that formation fluids are first-

contact miscible. The third step consists of numerically simulating well logs using as input the spatial distribution of fluid saturation resulting from the simulation of invasion. This latter step yields numerically simulated resistivity, density, and neutron porosity well logs which are immediately compared to measured logs to appraise their agreement; hence the reliability of the input static and dynamic petrophysical properties.

Depending on the specific values of residual hydrocarbon saturation and hydrocarbon end-point of relative permeability, reconstructing the process of mud-filtrate invasion and subsequently matching nuclear and resistivity logs could indicate the sensitivity of well logs to these two properties. Likewise, vertical variations of water-hydrocarbon saturation prior to and after the process of invasion typical of residual hydrocarbon saturation can have a measurable influence on both nuclear and resistivity logs.

We investigate the possibility of diagnosing and quantifying the condition of residual hydrocarbon saturation of porous and permeable rocks based on two approaches. In the first case, we apply the physics of mud-filtrate invasion to assess the influence of residual hydrocarbon saturation on the spatial distribution of fluid saturation resulting from radial displacement of the original hydrocarbons by mud filtrate. Depending on the petrophysical and fluid properties involved, such radial variations of fluid saturation can have a measurable influence both on nuclear and on resistivity logs, thereby lending themselves to the assessment of residual hydrocarbon saturation. In the second case, we explore the possibility of detecting vertical variations of water saturation in the virgin, non-invaded zone typical of permeable units that are in capillary equilibrium but partially depleted because of a nearby breached pressure seal. These vertical variations of water saturation are usually characterized by an upper fluid section that exhibits moveable oil almost immediately followed by a lower zone that includes free water saturation and

residual hydrocarbon saturation. Based on the physics of mud-filtrate invasion and on the numerical simulation of nuclear and resistivity logs, we study the conditions whereby detection of such zones could be possible.

In the ensuing sections, we describe the interpretation method developed to diagnose and quantify residual hydrocarbon saturation invoking the physics of mud-filtrate invasion as the underlying dynamic petrophysical model. Two options for interpretation are introduced: radial and vertical variations of fluid saturation. Examples of this application include actual field measurements as well as synthetic models based on field measurements. We consider cases that include partially-depleted hydrocarbon-bearing sands and tight-gas sands.

## 2.2 SIMULATION METHOD

### 2.2.1 Petrophysical Analysis

We use well-log interpretation and petrophysical analysis to estimate petrophysical properties such as porosity, permeability, volumetric concentration of shale, and water saturation. These values become the initial entries for numerical simulation and iterative refinement. We use gamma-ray, neutron porosity, and density measurements to derive volumetric concentration of shale. Porosity is calculated using neutron porosity and density logs. Water saturation is calculated based on the dual-water model (Clavier et al., 1977) and we use Timur's equation (Timur, 1968) to calculate permeability. Subsequently, we average the calculated petrophysical properties within the depth interval chosen for analysis and use them as the departure point for the simulation process.

### 2.2.2 Mud-Filtrate Invasion

Fluid flow simulation is performed with CMG (Computer Modeling Group Ltd., 2008), a commercial reservoir simulator capable of solving three-dimensional (3D), three-phase fluid-flow equations for porous media. Among the various CMG simulators available, we use STARS® for WBM simulations and GEM®, a compositional simulator, for OBM simulations. Two-dimensional (2D) simulations are implemented in cylindrical coordinates to model invasion in vertical wells under the assumptions of cylindrical flow and permeability isotropy. The petrophysical model is the input for fluid-flow simulation and is defined using parameters obtained from petrophysical analysis and core measurements; it consists of non-shale porosity, initial water saturation, absolute permeability, rock-fluid properties, formation fluid properties, invasion parameters, and formation fluid and mud properties.

We use Brooks-Corey's equations to describe saturation-dependent relative permeability and capillary pressure (Corey, 1994). Capillary pressure is given by

$$P_c = P_c^0 \sqrt{\frac{\phi_t}{k}} \left(1 - S_N\right)^{e_p}, \tag{2.4}$$

where $P_c$ is capillary pressure [psi], $P_c{}^0$ is a constant coefficient [psi.darcy$^{1/2}$], $\phi_t$ is total porosity, $k$ is absolute permeability [darcy], $e_p$ is pore-size distribution exponent, and $S_N$ is normalized water-phase saturation. In the presence of water-wet rocks, $S_N$ is given by

$$S_N = \frac{S_w - S_{wr}}{1 - S_{wr} - S_{hr}}, \tag{2.5}$$

where $S_w$ is total water saturation, $S_{wr}$ is irreducible water saturation, and $S_{hr}$ is residual hydrocarbon saturation. Water-phase, and hydrocarbon-phase saturation-dependent relative permeabilities, $k_{rw}$ and $k_{rh}$, are given by

$$k_{rw} = k_{rw}^{0} S_N^{e_w}, \tag{2.6}$$

and

$$k_{rh} = k_{rh}^{0} \left(1 - S_N\right)^{e_h}, \tag{2.7}$$

respectively, where $k^0_{rw}$ and $k^0_{rh}$ are relative permeability end points, and $e_w$ and $e_h$ are experimental exponents for water and hydrocarbon phase, respectively.

Although the above equations assume drainage, we use them to estimate rock-fluid properties for WBM and OBM invasion cases. One can define end points of relative permeability and capillary pressure curves using core measurements; otherwise they are calculated using an iterative process that simultaneously honors resistivity and nuclear logs.

Rates of mud-filtrate invasion are calculated using the one-dimensional (1D) radial method described by Salazar and Torres-Verdín (2009), which considers the interplay between mudcake buildup and rock petrophysical properties.

### 2.2.3 Simulation of Well Logs

From the simulation of mud-filtrate invasion we obtain new values for petrophysical properties such as water saturation and salt concentration. Density, neutron migration length, and resistivity for each simulation grid are updated with the new petrophysical properties. Density values are calculated based on volumetric concentration

of shale, matrix type, and different fluid saturations. We calculate bulk density ($\rho_b$) via the equation

$$\rho_b = \rho_{sh} C_{sh} + \rho_m \left(1 - C_{sh} - \phi_s\right) + \rho_f \phi_s \,, \tag{2.8}$$

where $\rho_{sh}$ is shale density, $C_{sh}$ is volumetric concentration of shale, $\rho_m$ is matrix density, $\phi_s$ is non-shale porosity, and $\rho_f$ is fluid density.

To calculate migration length for each simulation grid (which is used for the simulation of neutron porosity measurements), we use Schlumberger's commercial software, SNUPAR (McKeon and Scott, 1989). Chemical compositions for each grid and their corresponding volumetric concentrations are input to SNUPAR in order to calculate the corresponding migration lengths.

For resistivity calculations, we use the dual-water model, which works adequately at high values of volumetric concentration of shale (Clavier et al., 1977). This model is given by

$$\frac{1}{R_t} = \frac{\phi_t^m S_w^n}{a} \cdot \left( \frac{1}{R_w} + \frac{S_{wb}}{S_w} \left( \frac{1}{R_{wb}} - \frac{1}{R_w} \right) \right), \tag{2.9}$$

where $R_t$ is true formation resistivity, $m$ is Archie's cementation exponent, $n$ is Archie's saturation exponent, $a$ is Archie's tortuosity factor, $S_{wb}$ is bounded water saturation, $R_{wb}$ is bounded water resistivity, and $R_w$ is connate water saturation. We calculate $R_w$ from salinity and temperature, whereas $S_w$ is the output of fluid-flow simulation within each grid. Total porosity, $\phi_t$, and $S_{wb}$ are calculated via the formulae

$$\phi_t = \phi_s + C_{sh} \phi_{sh} \,, \tag{2.10}$$

and

$$S_{wb} = C_{sh} \frac{\phi_{sh}}{\phi_t}, \tag{2.11}$$

respectively, where $\phi_{sh}$ is shale porosity. There are two options for estimating $R_{wb}$ and $\phi_{sh}$: (a) by nonlinear inversion wherein these properties are iteratively adjusted until securing an acceptable match between numerically-simulated and measured nuclear and resistivity logs in a pure-shale zone close to the depth zone of interest, and (b) using data obtained from laboratory analysis.

We calculate the spatial distribution of electrical resistivity to numerically simulate array-induction resistivity measurement (AIT[1]). Likewise, we use a recently-developed, fast linear iterative refinement method to simulate density and neutron porosity logs (Mendoza et al., 2007)

### 3.2.3 Iterative Algorithm to Estimate Petrophysical Properties

The interpretation method begins with an initial guess of multi-layer petrophysical properties. We then simulate the process of mud-filtrate invasion to generate spatial distributions of fluid saturation from which we numerically simulate the corresponding resistivity and nuclear logs. By comparing simulated to measured well logs, we update the petrophysical properties of the multi-layer model to further decrease the difference between measured and numerically simulated well logs. Numerical simulations assume that measured logs have been corrected for borehole environmental effects.

**Figure 2.2** is a flowchart that describes the simulation method and the iterative algorithm used to adjust multi-layer petrophysical properties until securing an acceptable

[1] Mark of Schlumberger

match with measured logs. Available core data can be used to adjust some of the unknown input properties and to decrease non-uniqueness of inverted results.

## 2.3 METHOD FOR DIAGNOSING RESIDUAL HYDROCARBON SATURATION

We propose two different methods to diagnose residual hydrocarbons. The first method examines the formation in the radial direction to detect fluid saturation changes due to mud-filtrate invasion; it quantifies the effect of residual hydrocarbon saturation in the invaded radial zone on resistivity, neutron porosity, and density logs. The second method is a vertical approach intended to examine vertical variations of water saturation within a flow unit, from irreducible water saturation in the upper section of the unit to residual hydrocarbon saturation in the lower section.

Two synthetic cases exemplify the simulation and diagnostic processes. These synthetic cases are designed based on field data. In the analysis of synthetic cases, we use forward numerical simulation assuming a known model and generate well logs to describe the interpretation method and to perform sensitivity analyses. Verification of the two interpretation methods proposed for diagnosing residual hydrocarbons is followed by two field examples. The first example considers a tight-gas sand invaded with WBM; the second considers an oil-bearing zone invaded with OBM. We estimate multi-layer petrophysical properties by matching the measured well logs via iterative refinements of residual hydrocarbon saturation.

### 2.3.1 Radial Invasion Approach

When mud filtrate invades porous and permeable formations, it radially displaces mobile water and hydrocarbon, with the remaining fluids in the invaded zone being primarily irreducible water and residual hydrocarbon, mixed with mud filtrate. Because neutron porosity and density logs represent shallow-sensing measurements, they respond

primarily to the near wellbore radial segment of displaced fluid-saturation and exhibit negligible sensitivity to the vertical variation of fluid saturation. In the case of WBM invasion, residual hydrocarbon saturation, porosity, and volumetric concentration of shale control the separation between neutron porosity and density logs. However, the effect of residual hydrocarbon saturation on the separation of neutron porosity and density logs is more significant in the presence of gas. We may observe cross-over between these two logs in some cases of high residual saturation even after deep radial invasion. As an example, we implement the interpretation method to analyze a synthetic case of tight-gas sand invaded with WBM.

#### *2.3.1.1 Synthetic Case No. 1: Tight-Gas Sand*

Residual gas saturation in tight-gas sands can significantly affect the radial distribution of fluid saturation, and consequently well logs. The objective of this synthetic case is to quantify residual hydrocarbon saturation from the signature of invasion on both resistivity and nuclear logs. In addition, the controlled nature of the synthetic example enables us to quantify the limits of detectability and applicability of the proposed interpretation method.

This synthetic case includes one petrophysical layer. The sand is assumed clay-free and to be at irreducible water saturation. **Table 2.1** summarizes the assumed Archie's parameters and matrix, mud, fluid, and formation properties. These properties are used in both petrophysical analysis and simulation of mud-filtrate invasion.

**Table 2.2** summarizes the petrophysical properties assumed for the synthetic single-layer tight-gas sand, which are chosen based on the North Louisiana's tight-gas sand described in a subsequent section of this chapter. **Table 2.3** describes the rock-fluid

properties assumed to describe saturation-dependent relative permeability and capillary pressure using Brooks-Corey's formulation.

**Figure 2.3** shows the invasion flow rate and the average flow rate calculated after five days of invasion. As mudcake builds up, the flow rate converges to a constant value after two days of invasion. Salazar and Torres-Verdín (2009) showed that the volumetrically-averaged, time-constant flow rate is a suitable approximation to describe the effect of the time-variable flow rate of invasion. Thus, in the simulations that follow, we simulate invasion of mud-filtrate using that approximation. Based on the results shown in Figure 2.3, the rate of mud-filtrate invasion is 0.93 $ft^3$/day/ft for residual gas saturation in the range from zero to 0.50.

**Figure 2.4** shows the simulated spatial distributions (vertical and radial directions) of water saturation, salt concentration, electrical resistivity, fluid density, and neutron migration length after five days of mud-filtrate invasion. Results shown in Figure 2.4 correspond to a formation with 0.30 residual gas saturation. Radial length of invasion is approximately 8 ft. We observe an annulus in the spatial distributions of both resistivity and neutron migration length due to the difference in salt concentration between formation fluid and invading mud filtrate.

**Figure 2.5** shows the simulated resistivity and nuclear logs for the case of 0.30 residual gas saturation. The cross-over between neutron porosity and density logs is an indication of residual gas saturation. To quantify the sensitivity of these logs to residual gas saturation, we simulate the process of mud-filtrate invasion in the same formation with zero residual gas saturation; **Figure 2.6** shows the corresponding simulated resistivity and nuclear logs. Results indicate that residual gas saturation affects both nuclear and resistivity logs. The cross-over between neutron porosity and density logs disappears whereas shallow apparent resistivity values decrease.

Sensitivity analysis was performed to quantify the effect of residual hydrocarbon saturation on neutron porosity and density logs. Specifically, we quantify the cross-over between neutron porosity and density logs for several values of residual gas saturation, both before invasion (BI) and after invasion (AI). **Figure 2.7** shows the results of this analysis in the case of a permeable 0.15-porosity sand. Archie's parameters and matrix, mud, fluid and formation properties, and rock-fluid properties used in this model are identical to those used to construct the first synthetic tight-gas sand model.

**Figure 2.7** indicates a linear trend for the simulated values of neutron porosity and density porosity with respect to residual gas saturation. The variable A in the figure describes the difference between neutron porosity and density porosity after invasion; it increases with increasing residual gas saturation. On the other hand, variable B in the same figure, which identifies the difference between neutron porosity and density porosity before invasion, remains constant because residual gas saturation does not affect the logs before invasion. We found that decreasing porosity (i.e., decreasing hydrocarbon pore volume) decreases the slope of the linear trends shown in Figure 2.7, indicating that the sensitivity of density and neutron porosity logs to residual hydrocarbon saturation decreases linearly with decreasing hydrocarbon pore volume (**Figure 2.8**).

Residual hydrocarbon saturation also affects the resistivity logs. **Figure 2.9** shows the calculated sensitivity of apparent resistivity logs to residual hydrocarbon saturation. The figure indicates a 300% increase in shallow resistivity due to a 50% increase of residual hydrocarbon saturation. Deep resistivity remains approximately constant.

Another important property of interest in this research is the relative permeability of the wetting phase at residual hydrocarbon saturation. This property affects the saturation-dependent relative permeability and, consequently, radial invasion. We expect the corresponding effect on logs to be negligible. The sensitivity analysis quantifies the

influence of end points of relative permeability curves on both resistivity and nuclear logs. We adjust residual gas saturation to 0.30, vary the end point of $k_{rw}$ in the range from 0.2 to 0.92 and simulate neutron porosity and density logs under a 78% change of the end point of relative permeability. Results indicate negligible sensitivity of neutron porosity and density logs to a 78% change in $k_{rw}$ and approximately 0.4% sensitivity of resistivity logs to the same parameter. The effect of $k_{rw}$ on invasion rate is about 1%, which is negligible. Results from the sensitivity analysis confirm that the end point of relative permeability has no appreciable effect on neutron porosity, density, or resistivity measurements.

#### *2.3.1.2 Field Example No. 1: Tight-Gas Sand*

We analyze a North Louisiana tight-gas sand as an example of the proposed radial invasion approach to diagnose and quantify residual hydrocarbon saturation. The formation was drilled with WBM. Large separation between resistivity logs with different radial lengths of investigation is an indication of deeply invaded beds (**Figure 2.10**). Despite the fact that invasion is deep, neutron porosity and density logs exhibit a prominent cross-over due to residual gas saturation. Quantifying this separation with the proposed simulation method enables the estimation of residual gas saturation.

The sedimentary rock contains very fine- to fine-grained sandstone and some fossiliferous oolitic limestone. Texturally, it is a mature quartz arenite and subarkose sand (Salazar et al., 2006) originated from fluvial deposition during early Cretaceous times. Archie's parameters and matrix, mud, fluid and formation properties, and rock-fluid properties are identical to those reported for the tight-gas sand synthetic case in Tables 2.1 and 2.3. We perform the petrophysical analysis and associated numerical simulations in a 22-ft thick sand interval. **Table 2.4** describes the average values for porosity, initial

water saturation, and permeability for the sand under consideration. These values are calculated by averaging the properties obtained from standard well-log interpretation. We assume that there is no free water in the formation, and hence initial water saturation is equal to irreducible water saturation.

After detecting petrophysical bed boundaries using gamma-ray (GR) and density logs, the iterative simulation procedure begins with an initial guess obtained from the layer-by-layer averages of porosity, permeability, and volumetric concentration of shale. **Table 2.5** describes the petrophysical properties of the initial multi-layer model.

There are no core data available to initialize residual gas saturation. It is important to begin the process with a realistic value of residual hydrocarbon saturation; the main reason is because residual hydrocarbon saturation affects shallow-sensing resistivity curves in addition to nuclear logs. With the initial values listed in Table 2.5, we iteratively adjust residual gas saturation to match the cross-over between simulated and measured neutron porosity and resistivity logs. This process yields 0.30 residual gas saturation for the tight-gas sand formation. The sensitivity analysis shown in Figure 2.7 for the first synthetic case provides us with a good initial guess. In the next step, we iteratively adjust the remaining parameters based on the procedure described in Figure 2.2. Figure 2.10 shows the final simulation results. **Table 2.6** summarizes the final petrophysical properties obtained at the end of the iterative process. The average difference between simulated and measured logs in the cleanest sands is 2% for neutron porosity, 3% for density, and 10% for resistivity.

It is necessary to verify that the separation of apparent resistivity curves is not due to post-processing artifacts. Accordingly, we numerically simulate the logs before invasion to ensure that there is no separation between apparent resistivity curves. **Figure 2.11** shows the numerically simulated resistivity and nuclear logs before invasion.

Apparent resistivity curves do not exhibit separation before invasion. On the other hand, simulated density and neutron porosity logs exhibit a larger cross-over compared to that measured after invasion, which is expected because of higher gas saturation in the pre-invaded formation.

Salazar et al. (2006) used the same field data to estimate permeability by matching simulated and measured resistivity logs in the presence of mud-filtrate invasion. They assumed 0.10 residual gas in their numerical simulations. **Figure 2.12** shows the corresponding simulation results with the same properties listed in Table 2.6 and with a residual gas saturation of 0.10. In our analysis, we observe that neutron porosity and density logs no longer match the measured logs, with their cross-over decreased from 8 to 0.5 sandstone porosity units. Moreover, the shallow measured and simulated resistivity logs are no longer in good agreement due to lower gas saturation in the radially shallow part of the reservoir.

As established by the sensitivity analysis described earlier, residual hydrocarbon saturation affects resistivity logs. Performing simulations with accurate estimation of residual gas saturation will cause variations of the numerically simulated resistivity logs. Consequently, by improving the estimation of residual gas saturation we expect to improve the estimation of permeability. The maximum permeability obtained with our interpretation method is 12% higher than the maximum permeability reported by Salazar et al. (2006) (based solely on the inversion of resistivity logs).

### 2.3.2 Analysis of Vertical Well-Log Variations within a Flow Unit

Inspection of the vertical variations of fluid saturation within a flow unit can help to diagnose capillary equilibrium in the presence of residual hydrocarbon saturation,

especially in cases where there are significant, sudden variations of water saturation with depth that are unrelated to porosity variations. We consider a synthetic case to exemplify how the vertical behavior of well logs could enable the diagnosis and quantification of residual hydrocarbon saturation. The synthetic case is designed after a reported field case of sandstone saturated with medium-grade oil and invaded with OBM.

#### *2.3.2.1 Synthetic Case No. 2: Oil-Bearing Zone*

The sand unit under consideration contains light oil and is invaded with OBM filtrate. Compared to cases of WBM invasion, miscibility of in-situ and invading oil decreases the sensitivity of nuclear logs to residual oil saturation. The objectives of this synthetic case are (a) to study the effect of sudden vertical variations in fluid saturation due to residual oil saturation on resistivity and nuclear logs, and (b) to investigate the sensitivity of nuclear logs to in-situ oil density in the presence of residual oil saturation.

We assume that free water saturation increases with depth but is subject to capillary equilibrium. Residual hydrocarbon saturation is zero in the rock type located in the upper depth zone and increases with depth to a maximum of 0.20 in the rock type located in the lower portion of the sand unit. **Table 2.7** summarizes the assumed Archie's parameters and matrix, and formation properties for this synthetic model. **Table 2.8** lists the assumed mud-filtrate and fluid properties. **Table 2.9** describes the corresponding rock-fluid properties assumed to describe saturation-dependent relative permeability and capillary pressure using Brooks-Corey's formulation. **Figure 2.13** shows the rock-fluid properties assumed for this synthetic case under a constant irreducible water saturation of 0.20. The model consists of five petrophysical layers. **Table 2.10** lists the petrophysical properties of each layer. The first layer includes zero residual hydrocarbon saturation and zero free water saturation.

Neutron porosity and density logs are not sensitive to residual hydrocarbon saturation in this OBM synthetic case because the assumption of first-contact miscibility causes the invaded oil to mix with formation oil as it enters the formation. Consequently, one cannot estimate residual oil saturation using the radial invasion approach discussed earlier. This situation does not indicate that the measured logs are unaffected by residual oil saturation and end points of relative permeability. The two properties do influence the radial distribution of mud filtrate and, consequently, the well logs. Even in the cases of deep radial invasion, where nuclear logs are scarcely affected by invasion, resistivity logs could be affected by residual oil saturation and end points of relative permeability.

**Figure 2.14** shows the numerically simulated resistivity and nuclear logs for the oil-bearing synthetic sand case. The left-hand panel in this figure describes the vertical variations of residual oil saturation against initial oil saturation. This behavior is similar to that predicted by Land's (1971) equation and is illustrated in Figure 2.1— residual oil saturation becomes constant at high values of initial oil saturation.

Numerically simulated resistivity logs for this multi-layer synthetic case exhibit both a rapid decrease of deep apparent resistivity and an increase in the separation between apparent resistivity curves, which is caused by the corresponding increase of free water saturation displaced by OBM-filtrate invasion. Despite the fact that residual hydrocarbon saturation in some layers is 0.20 and practically most of the in-situ oil is not producible, we observe cross-over between neutron porosity and density logs. Low in-situ oil density and low volumetric concentration of shale are the main reasons for the cross-over of neutron porosity and density logs.

We perform numerical simulations of density and neutron porosity logs to quantify their sensitivity to oil density assuming a single-layer synthetic model. Table 2.7

summarizes the Archie's parameters and matrix, and formation properties assumed for this study.

The synthetic case assumes non-shale porosity equal to 0.25, total permeability equal to 10 md, irreducible water saturation equal to 0.25, residual oil saturation equal to 0.30, mud-filtrate density equal to 0.804 g/cm$^3$, and zero free water saturation. We vary in-situ oil density in the range from 0.7 to 1 g/cm$^3$ and simulate neutron porosity and density porosity logs after and before mud-filtrate invasion. **Figure 2.15** shows the numerically simulated neutron porosity and density porosity logs in water-filled sandstone porosity units for a range of in-situ oil density. Results indicate that invasion decreases the limit of in-situ oil density for which we observe cross-over between neutron porosity and density logs. However, even after mud-filtrate invasion, we observe cross-over between neutron porosity and density logs for in-situ oil densities lower than 0.75 g/cm$^3$.

#### *2.3.2.2 Field Example No. 2: Oil-Bearing Zone*

The second field example considers an oil-bearing sand saturated with high viscosity oil. Based on well-log interpretation, it follows that volumetric concentration of shale is very high in this formation due to high gamma-ray values and large separation between density and neutron porosity logs.

The formation of interest was drilled with OBM. Negligible separation between resistivity curves indicates zero free water saturation in the top zone (**Figure 2.16**, third panel from the left), increasing to 0.30 ten feet below. Even though resistivity logs suggest high water saturation in the bottom zone (depth interval of 5-12 ft), production tests conclusively indicate zero water production. Based on pressure measurements in the depth interval of 0-15 ft, it is known that all the layers in this sand are in hydraulic

communication. A hypothesis to explain this behavior is presence of high residual oil saturation in the bottom zone. In addition, it is likely that overbalance and production pressures are lower than water capillary trapping forces. Yet another equally plausible explanation is the presence of high irreducible water saturation due to variable particle-size distribution and associated mixed wettability conditions. The lack of neutron-density cross-over, which is due to high volumetric concentration of shale, renders the analysis even more complicated. Clearly, the separation between neutron porosity and density logs cannot be treated exclusively as a function of in-situ fluid saturation because of the effect of shale. Numerical simulation of mud-filtrate invasion and well-log responses is one way of providing a viable interpretation alternative in this case to quantify residual oil saturation in the bottom depth zone.

The well was drilled with a deviation angle of 27° but is here approximated with a vertical well. Reported hydrocarbon components from PVT analysis are lumped into five pseudo-components for the in-situ oil and three for OBM (Angeles et al., 2011). **Table 2.11** summarizes the corresponding mud-filtrate and fluid properties.

Archie's parameters and matrix, and formation properties for this field example are similar to those reported in Table 2.7 for the second synthetic case. The time-constant average rate of mud-filtrate invasion is 1.35 $ft^3$/day/ft for one day of invasion. This value was obtained from the simulation of mud-filtrate invasion and mudcake buildup using the method introduced by Salazar and Torres-Verdín (2009).

Initial values for petrophysical properties within each layer were calculated by averaging log interpretation results. **Table 2.12** describes the average petrophysical properties assumed for the oil-bearing sand in this field example. **Table 2.13** lists the initial values of multi-layer petrophysical properties. Parameters $e_p$, $k_{rnw}^{\,0}$, $e_{nw}$, $k_{rw}^{\,0}$, and $e_w$ are the same as those shown in Table 2.9 for the second synthetic case. Core data indicate

values of absolute permeability and irreducible water saturation of 50 md and 0.25, respectively.

We iteratively match numerically simulated and measured well logs by adjusting residual oil saturation, relative permeability end point, non-shale porosity, and water saturation. Figure 2.16 shows the final match between numerically simulated and measured array-induction resistivity and nuclear logs. The average matching error is 6% for neutron porosity logs, 1% for density logs, and 5% for resistivity logs. **Table 2.14** describes the final values of porosity, volumetric concentration of shale, water saturation, residual oil saturation, and water-phase relative permeability obtained after reaching an acceptable match between simulated and measured well logs.

Final results indicate an increase of water saturation with increasing depth, that is, a decrease of initial oil saturation with increasing depth. However, residual oil saturation remains approximately constant. This behavior can be explained with Land's (1971) predictions (Figure 2.1), that is, residual hydrocarbon saturation decreases with decreasing values of initial hydrocarbon saturation. At high values of initial hydrocarbon saturation, residual hydrocarbon saturation remains constant. Studies have shown that initial oil saturation decreases as depth increases but residual oil saturation remains high and constant. Consequently, the amount of producible oil decreases with increasing depth in the sand unit. This interpretation method enables us to infer a high value of residual oil saturation, which is difficult to quantify with conventional well-log interpretation.

The lack of neutron-density cross-over is due to high density of in-situ oil, high volumetric concentration of shale, and deep radial invasion. By neglecting the presence of clay, simulated density and neutron porosity measurements decrease by 2% and 40%, respectively, and a density-neutron cross-over arises in the sand unit.

**Figure 2.17** shows the numerically simulated logs before mud-filtrate invasion. It can be seen that, in the absence of mud-filtrate invasion, a slight cross-over occurs between neutron porosity and density logs. The effect of invasion is about 1% on density logs and 13% on neutron porosity logs in the oil-bearing sand. Comparison of these results against those obtained for the gas-bearing zone of Field Example No. 1 indicates that the density log is less sensitive to mud-filtrate invasion in oil-bearing than in gas-bearing sands. This behavior can be explained by the small density difference of approximately 0.25 g/cm$^3$ between oil and water. However, neutron porosity logs remain sensitive to oil saturation because the neutron migration length of in-situ hydrocarbon is approximately 5 cm longer than that of water.

## 2.4 CONCLUSIONS

To diagnose and quantify residual hydrocarbon saturation in porous and permeable rocks, we combined the process of mud-filtrate invasion with the quantitative response of nuclear and resistivity logs to radial invasion. This method enables two separate implementation approaches when analyzing field data. One approach considers the radial variations of fluid saturation resulting from invasion and the corresponding effect on well logs. We emphasized that this approach is suitable when the invaded zone exhibits fluid saturation close to that of residual hydrocarbon. The second approach considers vertical variations of fluid saturation within a hydraulically connected flow unit in order to detect high residual hydrocarbon saturation in the lower portion of the same unit.

Although neutron porosity and density logs are often sensitive to residual hydrocarbon saturation, discriminating between mobile and residual saturation with the two logs is challenging without explicit consideration of the process of mud-filtrate

invasion. The cross-over between density and neutron porosity logs in invaded formations is, to some extent, governed by the residual hydrocarbon pore volume. In WBM cases, residual hydrocarbon saturation can be efficiently diagnosed because invading fluid and in-situ hydrocarbon are immiscible. Sensitivity analysis of residual hydrocarbon saturation in a synthetic model invaded with WBM indicated that, for a 0.15-porosity formation, when residual gas saturation increases by 0.10, (a) the cross-over between neutron porosity and density logs increases by 2.4 sandstone porosity units, (b) the simulated neutron porosity decreases by 0.014, and (c) the simulated density porosity increases by 0.010, thereby confirming the measurable sensitivity of these logs to residual gas saturation.

Even though nuclear logs can be used to diagnose residual hydrocarbon in WBM cases, the interpretation method introduced in this chapter cannot diagnose residual hydrocarbon in beds with shallow invasion. The proposed method is effective when the radial length of mud-filtrate invasion is larger than the radial length of nuclear log investigation. On the other hand, the sensitivity of nuclear logs to residual hydrocarbon saturation decreases as either in-situ hydrocarbon density increases or porosity decreases. Based on the sensitivity analysis shown in Figure 2.15, we observed cross-over between neutron porosity and density logs for relative density differences above 15% between mud filtrate and in-situ hydrocarbon. In such cases the cross-over could be used to reliably diagnose residual hydrocarbon saturation.

In OBM cases, differences between the migration length of invaded oil and in-situ hydrocarbon are negligible. In addition, invading oil is partially miscible with formation oil, whereby detecting residual hydrocarbon saturation with nuclear logs is unreliable for the case of OBM. However, even in these extreme cases, nuclear logs remain sensitive to residual hydrocarbon saturation because they are affected by radial invasion.

Furthermore, formation fluid properties change due to mixing with invading oil. In some of these cases, one can still observe cross-over between neutron porosity and density logs due to residual hydrocarbon saturation.

In complex detection cases, such as those of OBM invasion, resistivity logs can be used in combination with neutron porosity and density logs, especially when the separation of apparent resistivity curves is affected by the radial distribution of fluid saturation due to invasion. In addition, including resistivity logs in the interpretation method reduces ambiguity and non-uniqueness.

Estimation of residual hydrocarbon is also affected by petrophysical properties, mud properties, invasion rate, and time of invasion assumed in the simulation of mud-filtrate invasion. Uncertain and/or inaccurate input properties will lead to unreliable simulation results and hence to biased residual hydrocarbon estimation.

We selected two challenging field examples to verify the proposed detection and interpretation methods. The radial invasion method was applied to a field example of tight-gas sand, whereas the vertical analysis method was implemented with a field example of oil-bearing formation invaded with OBM. In both cases, conventional well-log interpretation did not provide indication of the high residual hydrocarbon saturation and the very low relative permeability of the water phase.

We estimated 0.30 residual gas saturation in the tight-gas sand. This high residual gas saturation affected the estimation of permeability for the various petrophysical layers. Comparison of the results documented in this chapter to the results of Salazar et al. (2006) indicated a 12% increase in permeability with the matching of nuclear logs. The second field example was more challenging due to the high viscosity and density of in-situ oil, thereby rendering nuclear logs less sensitive both to residual oil saturation and to end-point of relative permeability. However, resistivity measurements helped to diagnose

0.30 residual oil saturation in the bottom depth zone, whereas the top depth zone was diagnosed with negligible (0.05) residual oil saturation. The rapid vertical variation of water saturation was interpreted as due to hydrocarbon trapping. Quantifying this effect enabled us to detect zones with low residual hydrocarbon saturation for perforation.

The proposed method can be improved with automatic inversion to estimate multi-layer petrophysical properties. Furthermore, it could be readily combined with Nuclear Magnetic Resonance (NMR) measurements to ascertain whether fluid signatures interpreted from transverse magnetic relaxation are due to residual or to mobile hydrocarbon saturation.

**Table 2.1:** Archie's parameters and matrix, mud, fluid and formation properties assumed in both the first synthetic case and North Louisiana's tight-gas sand.

| Variable | Value | Units |
|---|---|---|
| Archie's tortuosity factor, *a* | 1.00 | - |
| Archie's cementation exponent, *m* | 1.95 | - |
| Archie's saturation exponent, *n* | 1.75 | - |
| Connate water salt concentration | 160 | kppm NaCl |
| Mud-filtrate salt concentration | 3.60 | kppm NaCl |
| Shale density | 2.68 | $g/cm^3$ |
| Matrix density | 2.65 | $g/cm^3$ |
| Water density | 1.00 | $g/cm^3$ |
| Water viscosity | 1.00 | cp |
| Gas density | 0.0016 | $g/cm^3$ |
| Gas viscosity | 0.02 | cp |
| Mud-filtrate density | 1.00 | $g/cm^3$ |
| Mud-filtrate viscosity | 1.00 | cp |
| Formation temperature | 210 | °F |
| Initial formation pressure | 5000 | psi |
| Mud hydrostatic pressure | 5825 | psi |
| Mudcake reference permeability | 0.03 | md |
| Mudcake reference porosity | 0.30 | [ ] |
| Mud solid fraction | 0.06 | [ ] |
| Mudcake maximum thickness | 1.02 | cm |
| Mudcake compressibility exponent | 0.40 | [ ] |
| Mudcake exponent multiplier | 0.10 | [ ] |
| Wellbore radius | 10.26 | cm |
| Formation maximum invasion time | 5.00 | days |
| Irreducible water saturation | 0.40 | [ ] |

**Table 2.2:** Petrophysical properties assumed in the first synthetic case.

| Variable | Value | Units |
|---|---|---|
| Thickness | 19 | ft |
| Absolute permeability, $k$ | 25 | md |
| Non-shale porosity, $\phi_s$ | 0.15 | [ ] |
| Total water saturation, $S_w$ | 0.40 | [ ] |
| Volumetric concentration of shale, $C_{sh}$ | 0.00 | [ ] |

**Table 2.3:** Rock-fluid properties assumed in the first synthetic case and North Louisiana's tight-gas sand.

| $P_c^0$ [psi.darcy$^{1/2}$] | $e_p$ | $k^0_{rh}$ | $e_h$ | $k^0_{rw}$ | $e_w$ | $S_{wr}$ | $S_{hr}$ |
|---|---|---|---|---|---|---|---|
| 1.4 | 4.5 | 0.92 | 2.5 | 0.85 | 2.0 | 0.4 | 0.01-0.5 |

**Table 2.4:** Averaged petrophysical properties assumed in North Louisiana's tight-gas sand.

| Variable | Value | Units |
|---|---|---|
| Thickness | 22 | ft |
| Absolute permeability, $k$ | 210 | md |
| Non-shale porosity, $\phi_s$ | 0.121 | [ ] |
| Total water saturation, $S_w$ | 0.631 | [ ] |
| Volumetric concentration of shale, $C_{sh}$ | 0.176 | [ ] |
| Shale porosity, $\phi_{sh}$ | 0.06 | [ ] |

**Table 2.5:** Initial values of model properties assumed in North Louisiana's tight-gas sand in different petrophysical layers.

| Layer thickness [ft] | $k$ [$md$] | $\phi_s$ | $C_{sh}$ | $S_w$ |
|---|---|---|---|---|
| 3 | 58 | 0.043 | 0.358 | 0.926 |
| 2 | 312 | 0.170 | 0.117 | 0.481 |
| 5 | 257 | 0.153 | 0.069 | 0.448 |
| 5 | 334 | 0.176 | 0.100 | 0.452 |
| 3 | 259 | 0.154 | 0.126 | 0.574 |
| 3 | 30 | 0.033 | 0.278 | 0.976 |
| 1 | 0.0004 | 0.0001 | 0.515 | 1.000 |

**Table 2.6:** Final multi-layer petrophysical properties obtained after matching the measured logs with numerical simulations for North Louisiana's tight-gas sand.

| Layer thickness [ft] | $k$ [$md$] | $\phi_s$ | $C_{sh}$ | $S_w$ | $S_{gr}$ |
|---|---|---|---|---|---|
| 3 | 1.50 | 0.15 | 0.40 | 0.45 | 0.30 |
| 2 | 7.50 | 0.18 | 0.09 | 0.45 | 0.30 |
| 5 | 45.80 | 0.14 | 0.06 | 0.45 | 0.30 |
| 5 | 25.05 | 0.159 | 0.09 | 0.48 | 0.30 |
| 3 | 0.30 | 0.16 | 0.04 | 0.60 | 0.20 |
| 3 | 0.10 | 0.07 | 0.10 | 0.90 | 0.10 |
| 1 | 0.015 | 0.145 | 0.08 | 0.80 | 0.10 |

**Table 2.7:** Archie's parameters and matrix, and formation properties assumed in both the second synthetic case and the oil-bearing field example.

| Variable | Value | Units |
|---|---|---|
| Archie's tortuosity factor, *a* | 1.00 | - |
| Archie's cementation exponent, *m* | 1.9 | - |
| Archie's saturation exponent, *n* | 2.1 | - |
| Connate water salt concentration | 105 | kppm NaCl |
| Bound water resistivity | 0.038 | Ohm.m |
| Shale density | 2.76 | $g/cm^3$ |
| Matrix density | 2.65 | $g/cm^3$ |
| Formation temperature | 254 | °F |
| Initial formation pressure | 18949 | psi |
| Mud hydrostatic pressure | 19500 | psi |
| Mudcake reference permeability | 0.03 | md |
| Mudcake reference porosity | 0.30 | [ ] |
| Mud solid fraction | 0.06 | [ ] |
| Mudcake maximum thickness | 1.02 | cm |
| Mudcake compressibility exponent | 0.40 | [ ] |
| Mudcake exponent multiplier | 0.10 | [ ] |
| Wellbore radius | 10.79 | cm |
| Formation maximum invasion time | 1.00 | Day |

**Table 2.8:** Mud and fluid properties assumed in the second synthetic case.

| Variable | Value | Units |
|---|---|---|
| Water density | 1.00 | $g/cm^3$ |
| Water viscosity | 1.00 | cp |
| In-situ oil density | 0.644 | $g/cm^3$ |
| In-situ oil viscosity | 1.00 | cp |
| Mud-filtrate density | 0.732 | $g/cm^3$ |
| Mud-filtrate viscosity | 1.50 | cp |

**Table 2.9:** Rock-fluid properties assumed in both the second synthetic case and the oil-bearing field example.

| $P_c^0$ [psi.darcy$^{1/2}$] | $e_p$ | $k^0_{rh}$ | $e_h$ | $k^0_{rw}$ | $e_w$ |
|---|---|---|---|---|---|
| 20 | 4.5 | 0.9 | 2.48 | 0.13-0.8 | 2 |

**Table 2.10:** Multi-layer petrophysical properties assumed in the second synthetic case.

| Layer thickness [ft] | $k$ [$md$] | $\phi_s$ | $C_{sh}$ | $S_{or}$ | $S_w$ |
|---|---|---|---|---|---|
| 10 | 10 | 20 | 0.10 | 0.00 | 0.20 |
| 2 | 10 | 20 | 0.00 | 0.20 | 0.40 |
| 2 | 10 | 20 | 0.00 | 0.20 | 0.50 |
| 2 | 10 | 20 | 0.00 | 0.20 | 0.60 |
| 4 | 10 | 20 | 0.00 | 0.10 | 0.80 |
| 4 | 10 | 20 | 0.00 | 0.00 | 1.00 |

**Table 2.11:** Mud and fluid properties assumed in the oil-bearing field example.

| Variable | Value | Units |
|---|---|---|
| Water density | 1.00 | $g/cm^3$ |
| Water viscosity | 1.00 | cp |
| In-situ oil density | 0.87 | $g/cm^3$ |
| In-situ oil viscosity | 5.50 | cp |
| Mud-filtrate density | 0.8 | $g/cm^3$ |
| Mud-filtrate viscosity | 2.00 | cp |

**Table 2.12:** Averaged petrophysical properties calculated in the oil-bearing field example.

| Variable | Value | Units |
|---|---|---|
| Thickness | 15 | ft |
| Absolute permeability, $k$ | 35 | md |
| Non-shale porosity, $\phi_s$ | 0.21 | [ ] |
| Total water saturation, $S_w$ | 0.29 | [ ] |
| Volumetric concentration of shale, $C_{sh}$ | 0.25 | [ ] |
| Shale porosity, $\phi_{sh}$ | 0.12 | [ ] |

**Table 2.13:** Initial multi-layer petrophysical properties for the oil-bearing field example.

| **Layer thickness [ft]** | $k$ [$md$] | $\phi_s$ | $C_{sh}$ | $S_w$ |
|---|---|---|---|---|
| 2 | 31 | 0.22 | 0.24 | 0.23 |
| 3 | 53 | 0.22 | 0.18 | 0.19 |
| 2 | 30 | 0.20 | 0.21 | 0.25 |
| 3 | 71 | 0.22 | 0.24 | 0.26 |
| 2 | 14 | 0.18 | 0.26 | 0.30 |
| 1 | 2 | 0.17 | 0.19 | 0.46 |
| 1 | 1 | 0.14 | 0.49 | 0.56 |
| 1 | 0.001 | 0.20 | 0.33 | 0.38 |

**Table 2.14:** Final multi-layer petrophysical properties obtained from the matching of measured logs with numerical simulations in the oil-bearing field example.

| **Layer thickness [ft]** | $\phi_s$ | $C_{sh}$ | $S_w$ | $S_{or}$ | $k_{rw}$ |
|---|---|---|---|---|---|
| 2 | 0.230 | 0.15 | 0.28 | 0.05 | 0.6 |
| 3 | 0.220 | 0.05 | 0.25 | 0.05 | 0.6 |
| 2 | 0.220 | 0.10 | 0.35 | 0.05 | 0.6 |
| 3 | 0.220 | 0.08 | 0.33 | 0.30 | 0.3 |
| 2 | 0.190 | 0.26 | 0.42 | 0.35 | 0.2 |
| 1 | 0.150 | 0.45 | 0.50 | 0.30 | 0.3 |
| 1 | 0.145 | 0.53 | 0.75 | 0.30 | 0.3 |
| 1 | 0.230 | 0.29 | 0.33 | 0.30 | 0.3 |

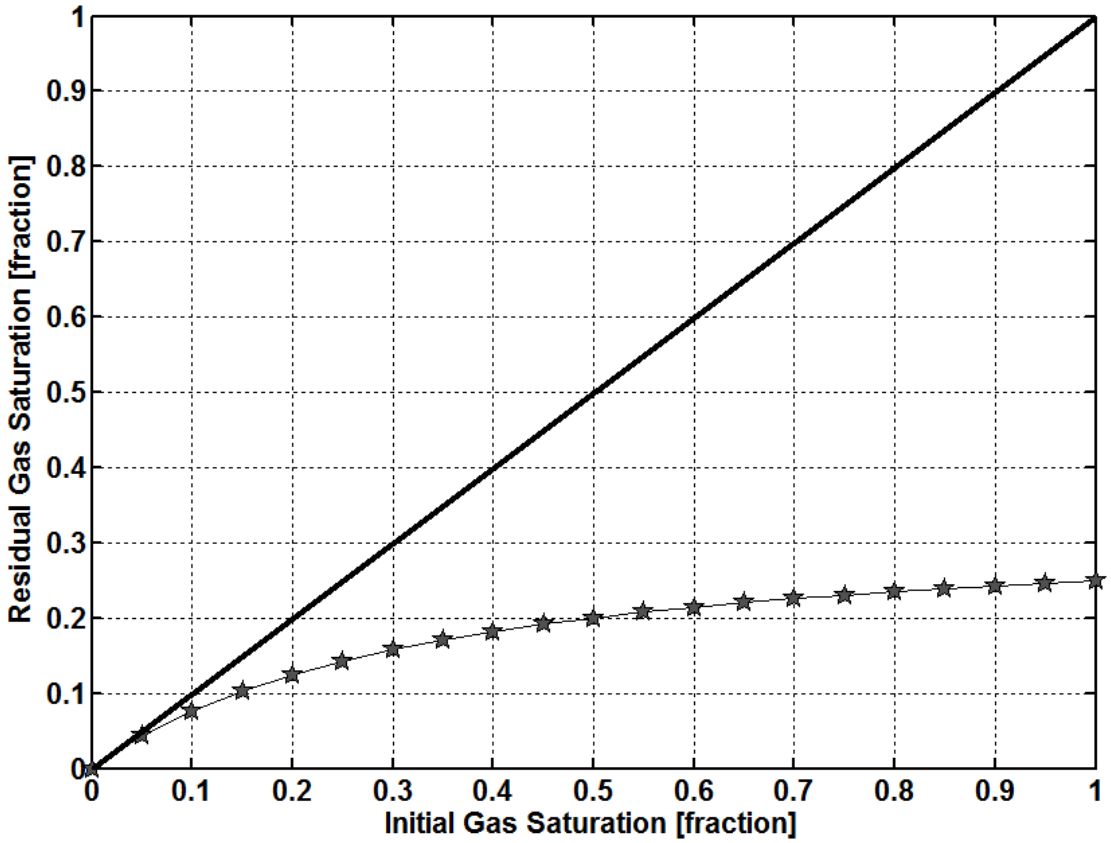


**Figure 2.1:** Typical relationship between initial and residual gas saturation based on Land's (1971) equation: residual gas saturation (shown with stars) becomes approximately constant at high values of initial gas saturation, and significantly deviates from that of a straight line (solid black curve).

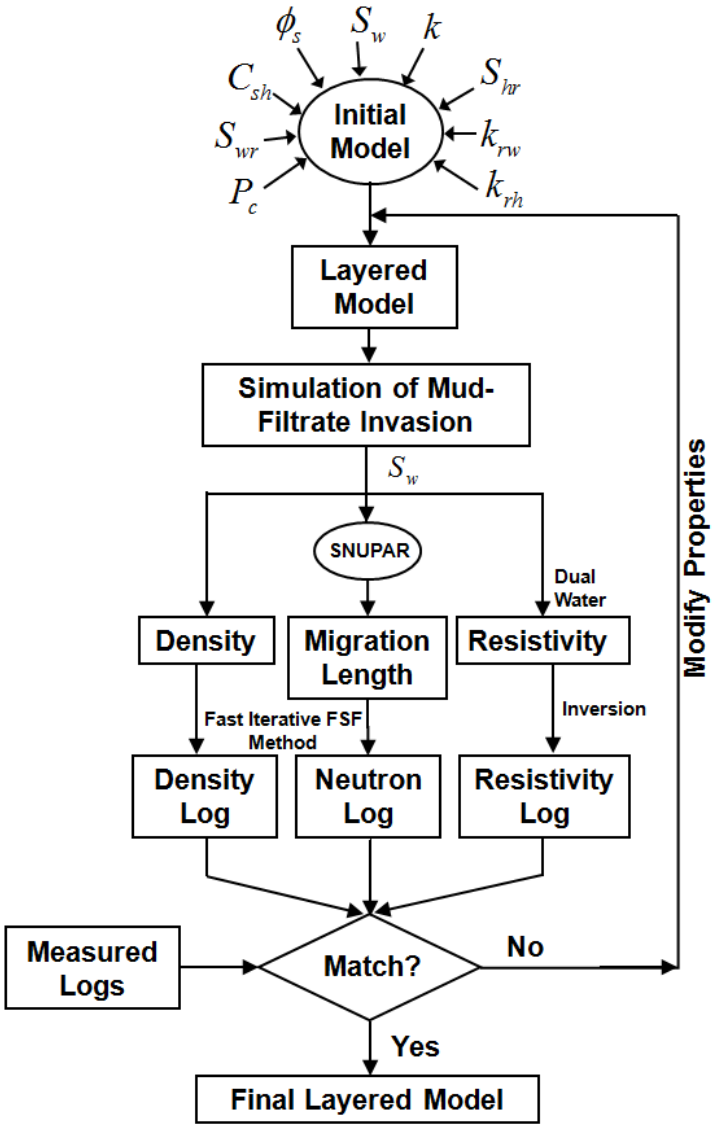


**Figure 2.2:** Iterative workflow adopted in this chapter to estimate unknown petrophysical properties. Iterations are intended to progressively improve the agreement between measured and numerically simulated resistivity and nuclear well logs by making adjustments to layer-by-layer petrophysical properties.

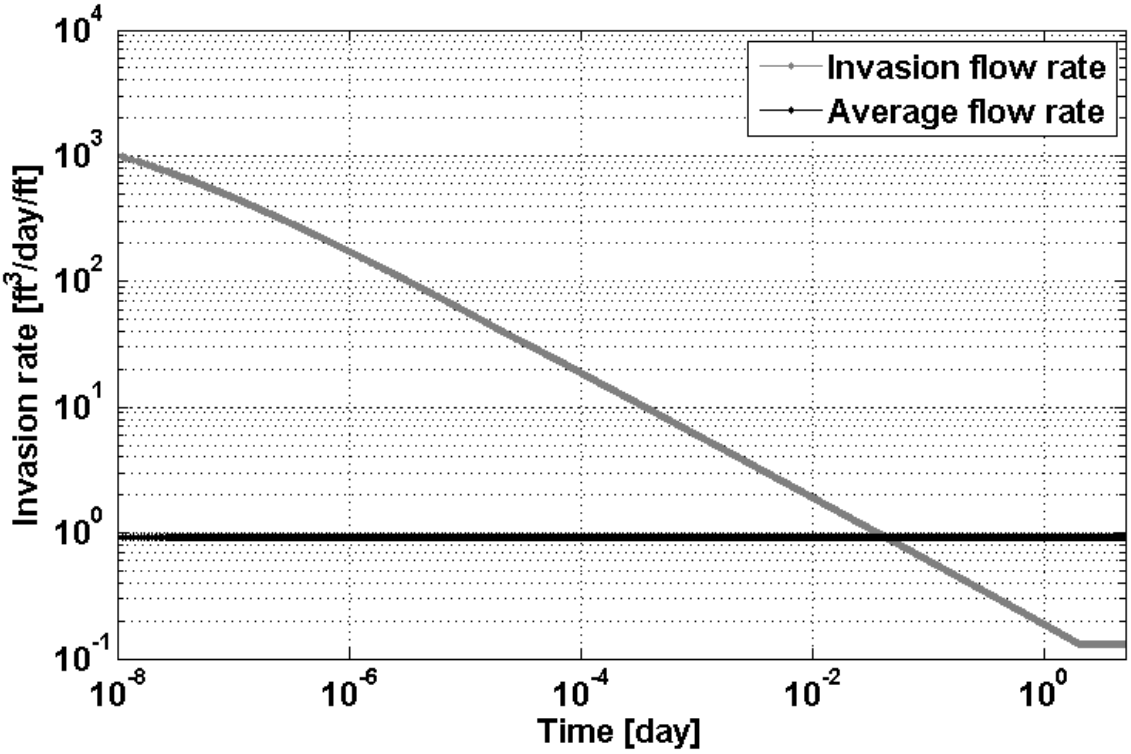


**Figure 2.3:** Time-variable flow rate of invasion and the corresponding time-constant average after five days of mud-filtrate invasion calculated with mudcake buildup in the tight-gas sand synthetic case.

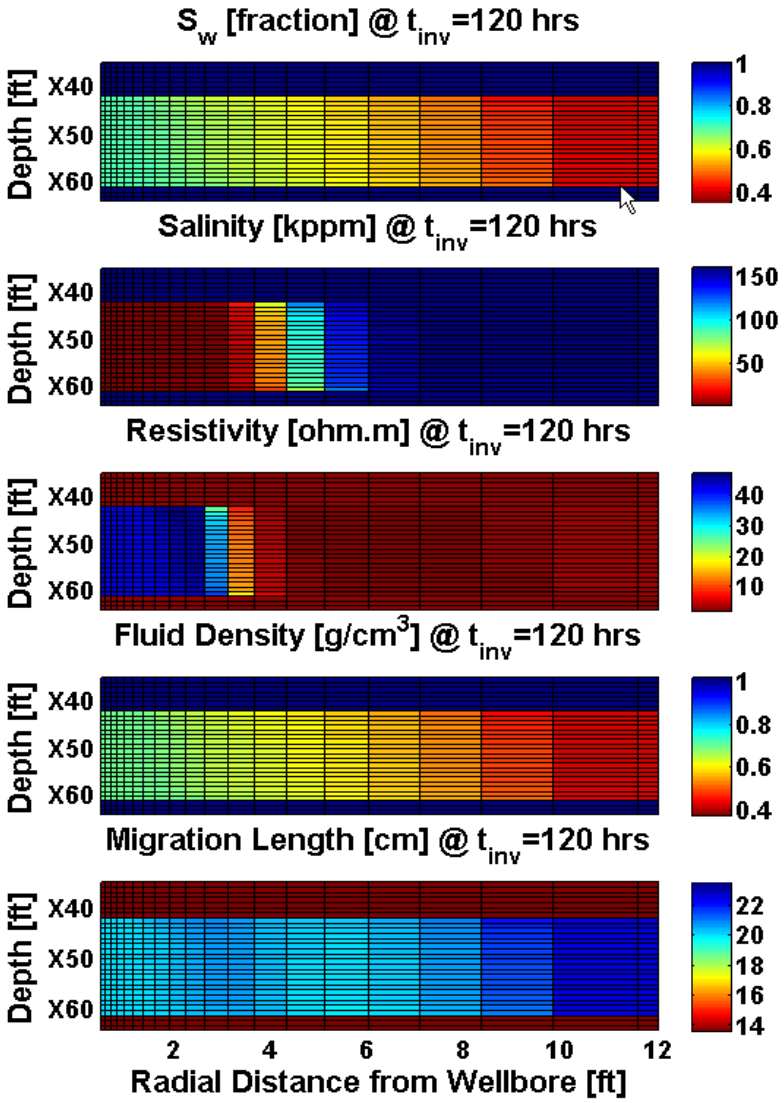


**Figure 2.4:** Spatial distributions (radial and vertical directions) of water saturation, salt concentration, electrical resistivity, fluid density, and migration length numerically simulated for the tight-gas sand synthetic case. Time of mud-filtrate invasion ($t_{inv}$) is five days.

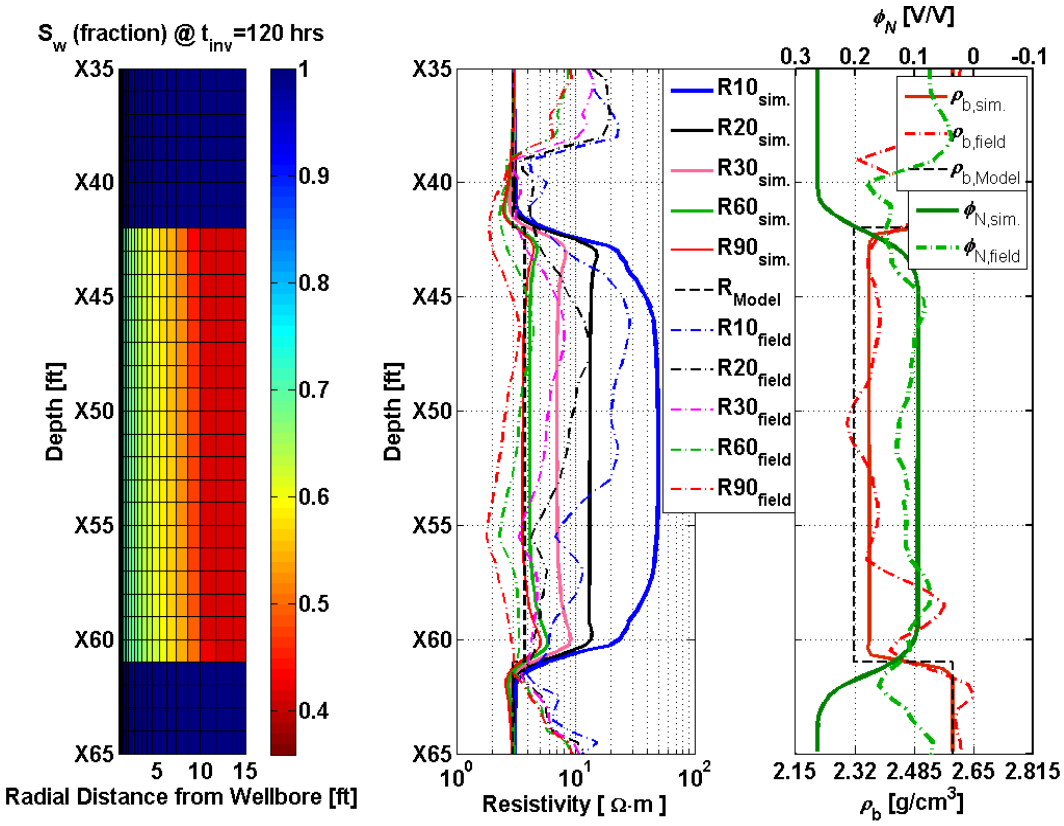


**Figure 2.5:** Comparison of numerically simulated (solid lines) and measured (dashed lines) array-induction apparent resistivity logs (center panel), and neutron porosity and density logs (right-hand panel) for the tight-gas sand synthetic case with residual gas saturation of 0.30. The left-hand panel shows the spatial distribution (radial and vertical directions) of water saturation. Time of mud-filtrate invasion ($t_{inv}$) is five days.

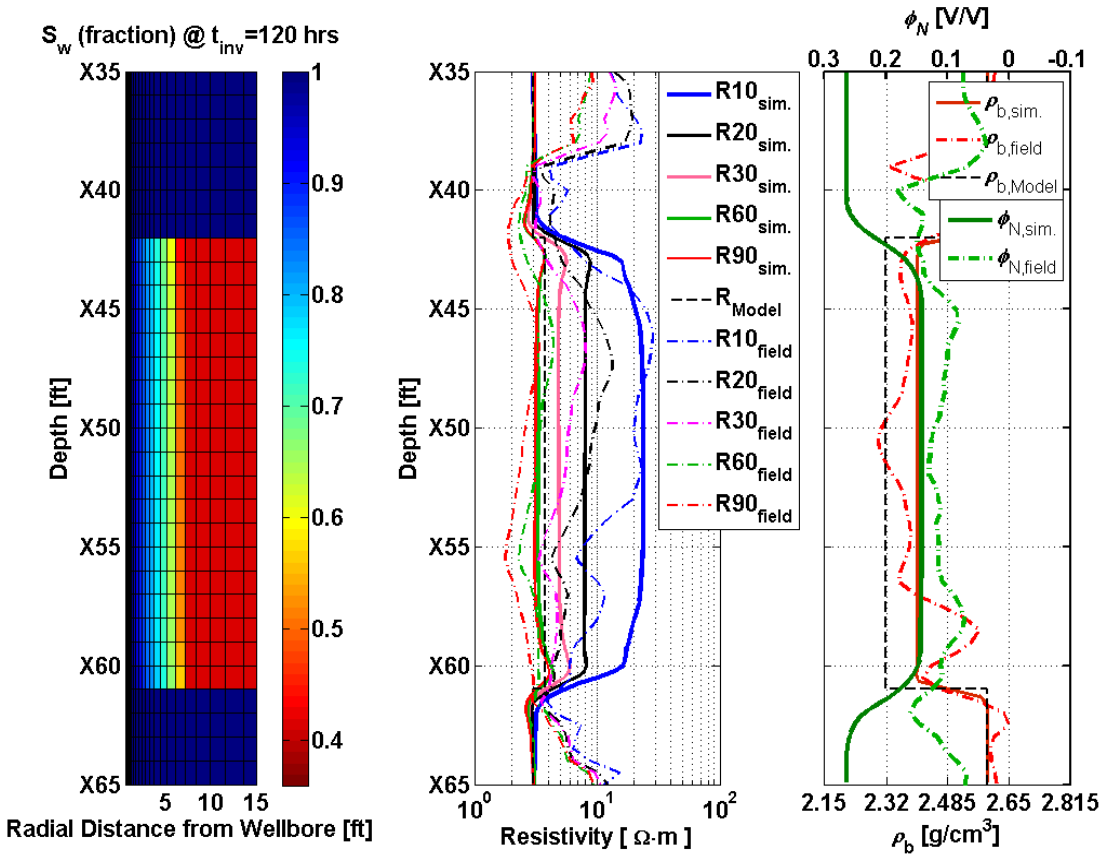


**Figure 2.6:** Comparison of numerically simulated (solid lines) and measured (dashed lines) array-induction apparent resistivity logs (center panel) and neutron porosity and density logs (right-hand panel) for the tight-gas sand synthetic case with zero residual gas saturation. The left-hand panel shows the spatial distribution (radial and vertical directions) of water saturation. Time of mud-filtrate invasion ($t_{inv}$) is five days.

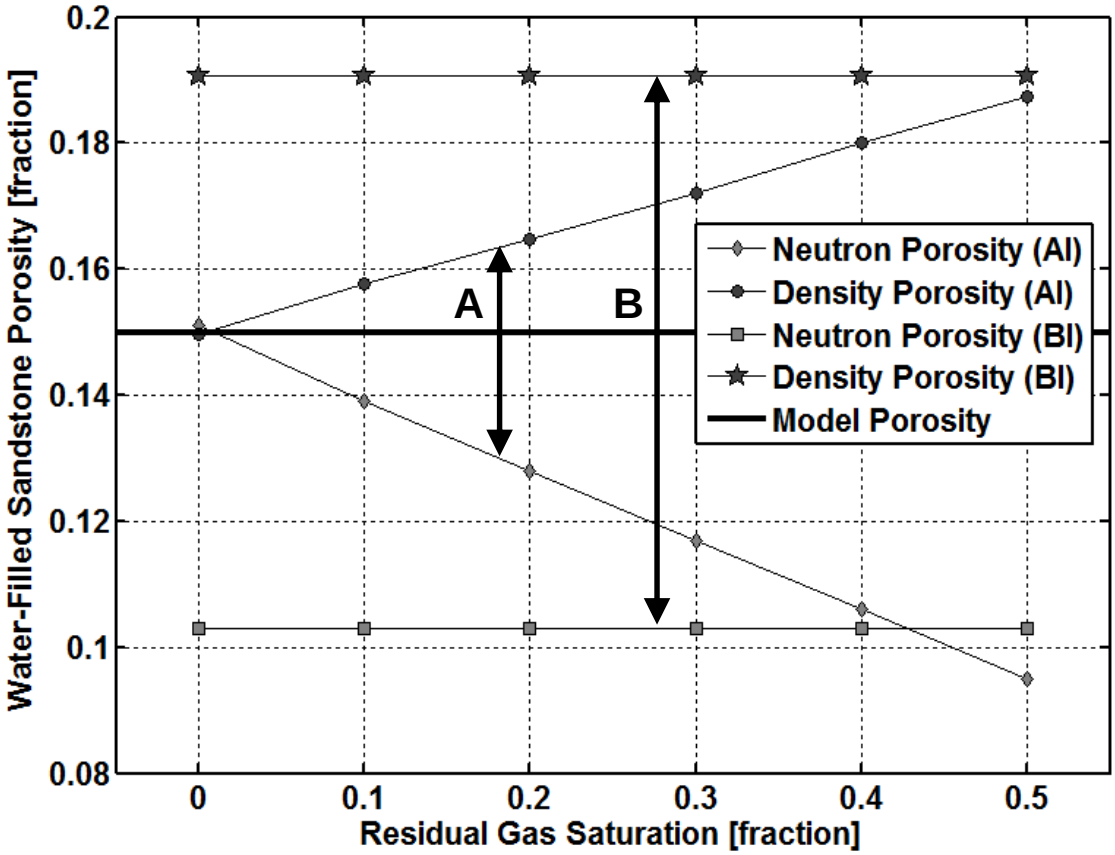


**Figure 2.7:** Sensitivity analysis of residual gas saturation for density porosity and neutron porosity measurements in a permeable sand with porosity of 0.15. Density porosity and neutron porosity measurements were numerically simulated before (BI) and after (AI) mud-filtrate invasion. Variables A and B describe the difference between neutron porosity and density porosity after and before mud-filtrate invasion, respectively. Time of mud-filtrate invasion is five days.

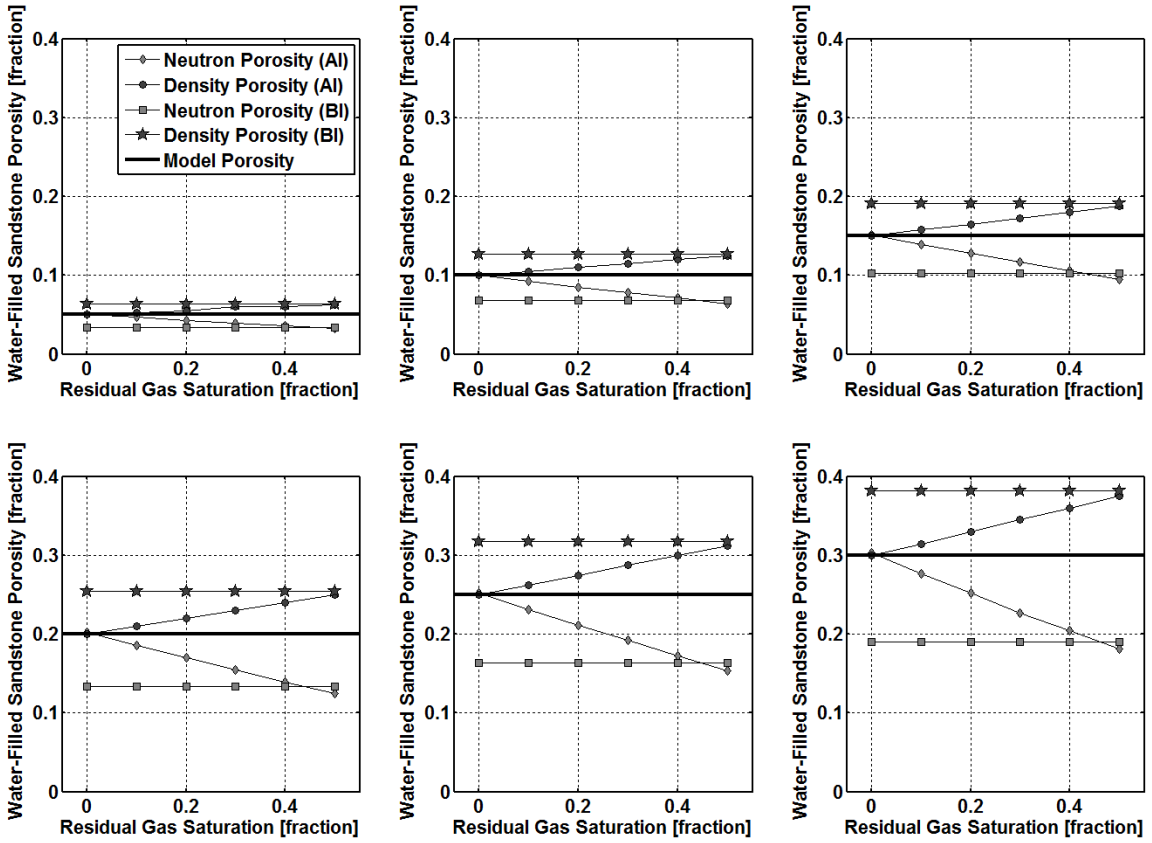


**Figure 2.8:** Sensitivity analysis of residual gas saturation for density porosity and neutron porosity measurements in a permeable sand where porosity varies between 0.05 and 0.30. Density porosity and neutron porosity measurements were numerically simulated before (BI) and after (AI) mud-filtrate invasion. Increasing porosity from 0.05 (top left) to 0.30 (bottom right) increases the slope of the linear trends of neutron porosity and density porosity vs. residual gas saturation.

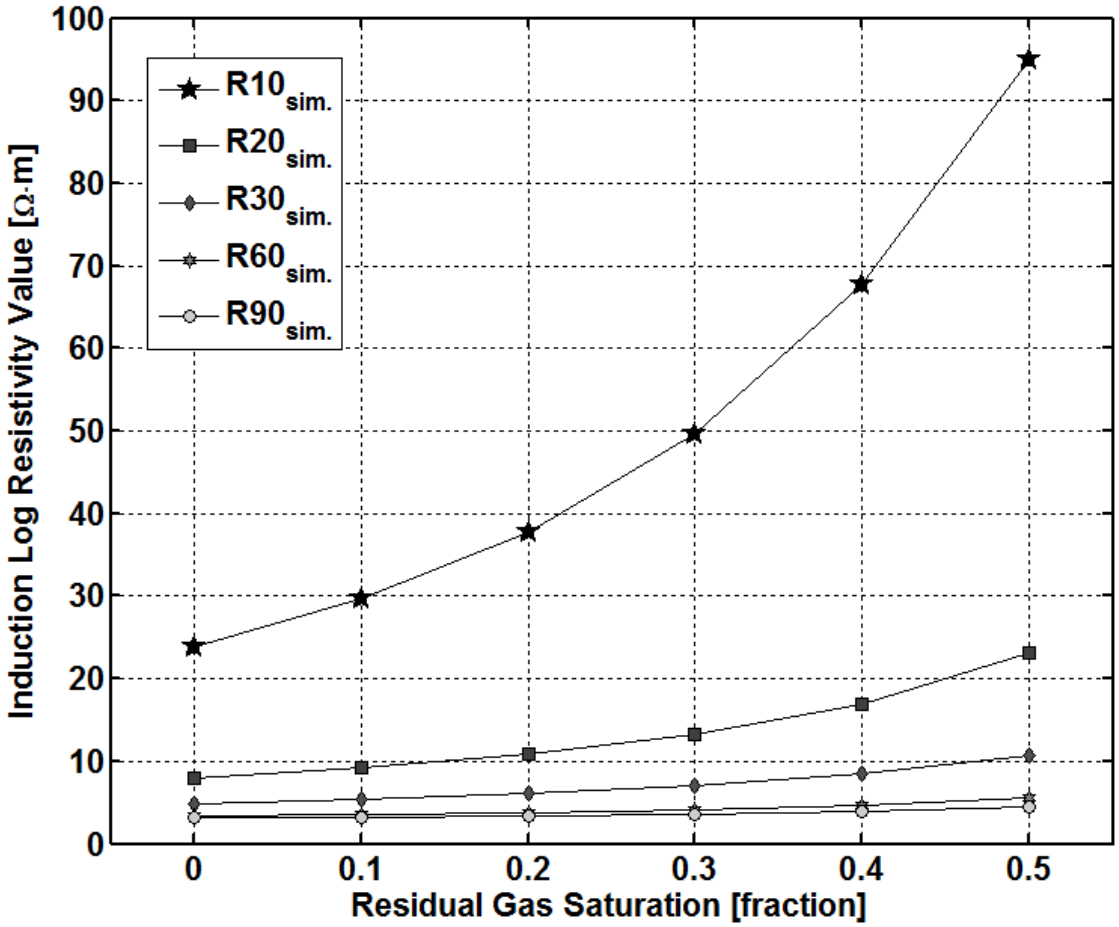


**Figure 2.9:** Sensitivity analysis of induction apparent resistivity measurements to residual gas saturation in the single-layer synthetic tight-gas sand. Curves describe numerically simulated AIT apparent resistivity curves for different radial lengths of investigation. Residual gas saturation varies between 0 and 0.50. Time of mud-filtrate invasion is five days in all cases.

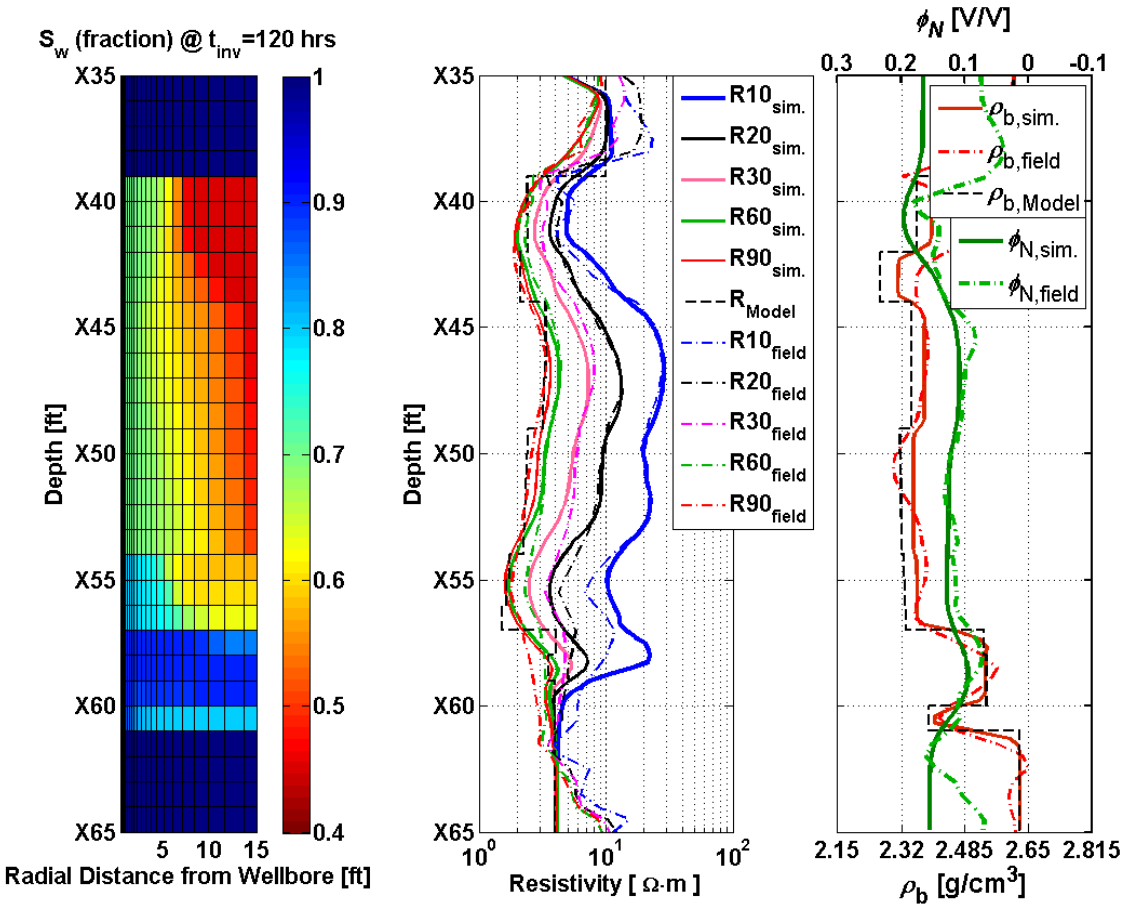


**Figure 2.10:** Comparison of numerically simulated (solid lines) and measured (dashed lines) array-induction apparent resistivity logs (center panel) and neutron porosity and density logs (right-hand panel) for the multi-layer model of North Louisiana's tight-gas sand. The left-hand panel shows the spatial distribution (radial and vertical directions) of water saturation. Time of mud-filtrate invasion ($t_{inv}$) is five days. Petrophysical properties were obtained from the matching of field logs with numerical simulations (Table 2.6).

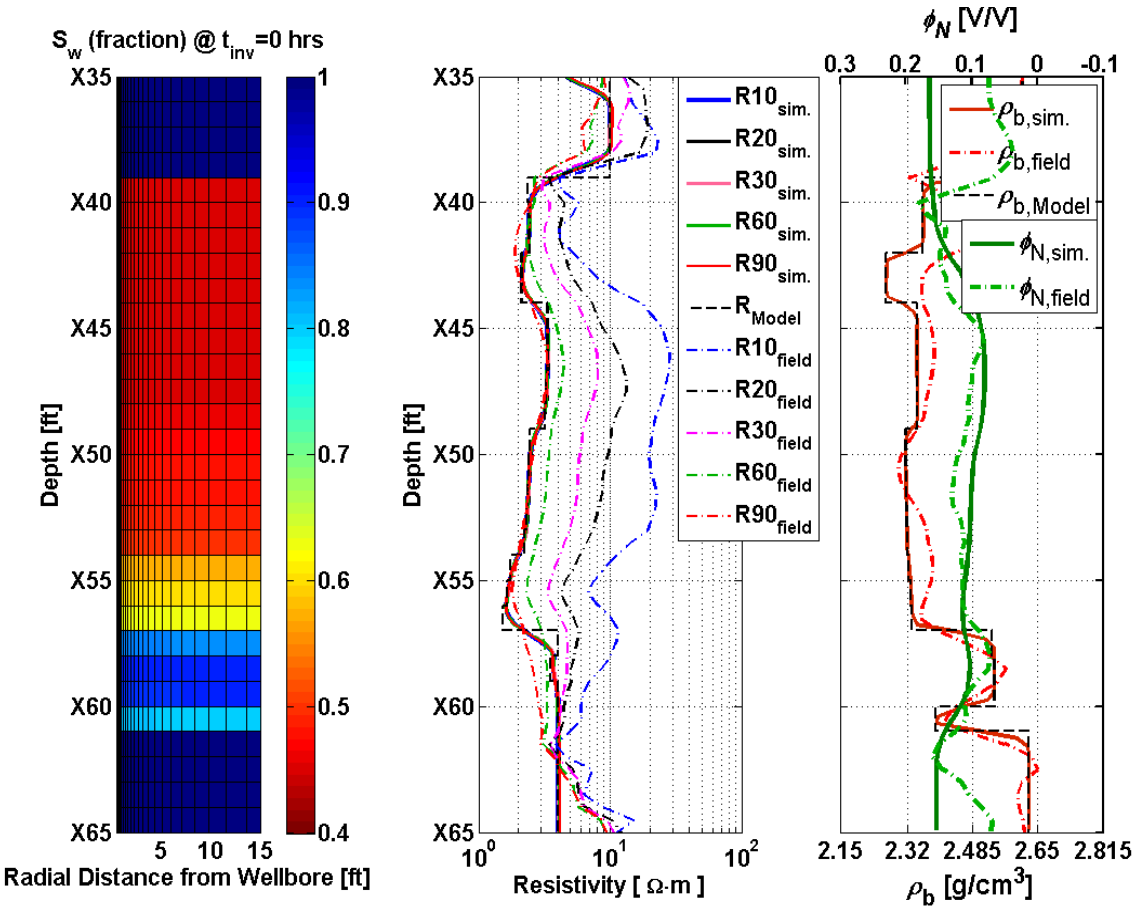


**Figure 2.11:** Comparison of numerically simulated (solid lines) and measured (dashed lines) array-induction apparent resistivity logs (center panel) and neutron porosity and density logs (right-hand panel) for the multi-layer model of North Louisiana's tight-gas sand before invasion. The left-hand panel shows the spatial distribution (radial and vertical directions) of water saturation.

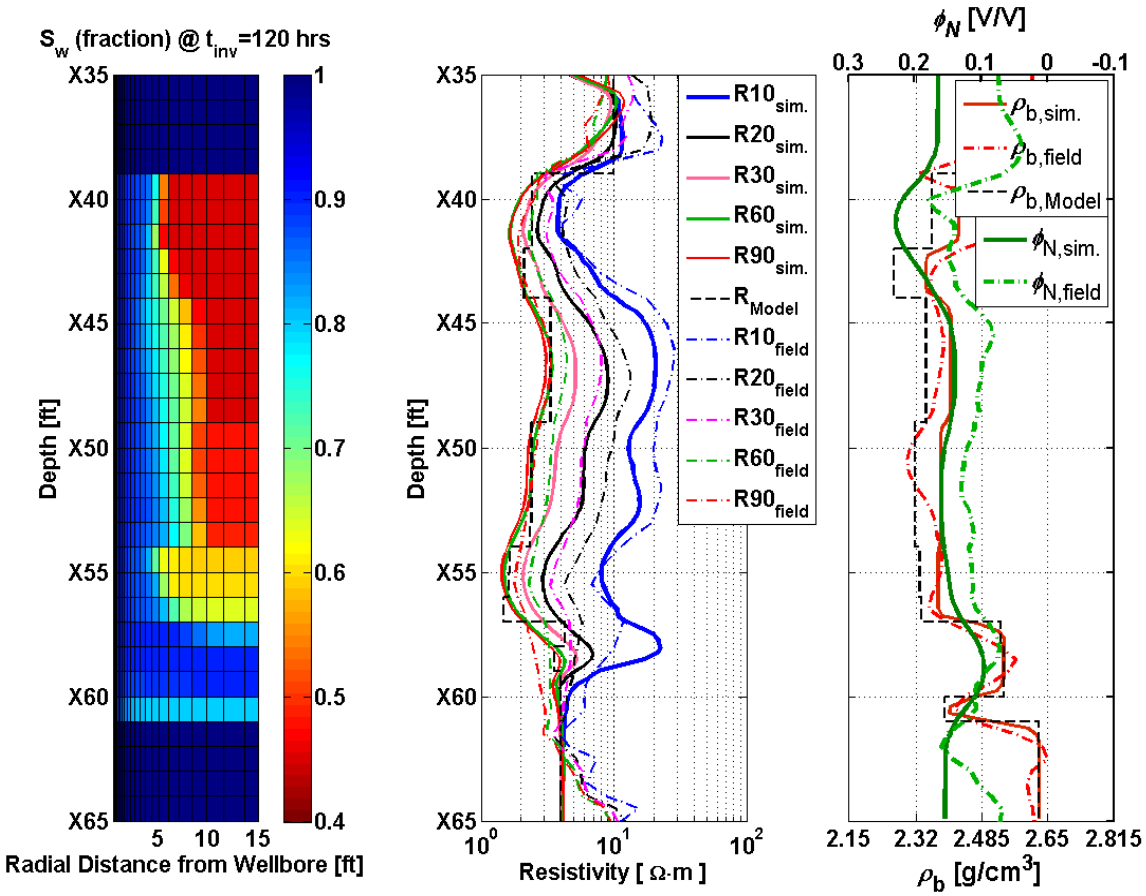


**Figure 2.12:** Comparison of the numerically simulated (solid lines) and measured (dashed lines) array-induction apparent resistivity logs (center panel) and neutron porosity and density logs (right-hand panel) for the multi-layer model of North Louisiana's tight-gas sand. Residual gas saturation is assumed equal to 0.10. Remaining layer petrophysical properties are equal to those of estimated values. The left-hand panel shows the spatial distribution (radial and vertical directions) of water saturation. Time of mud-filtrate invasion ($t_{inv}$) is five days.

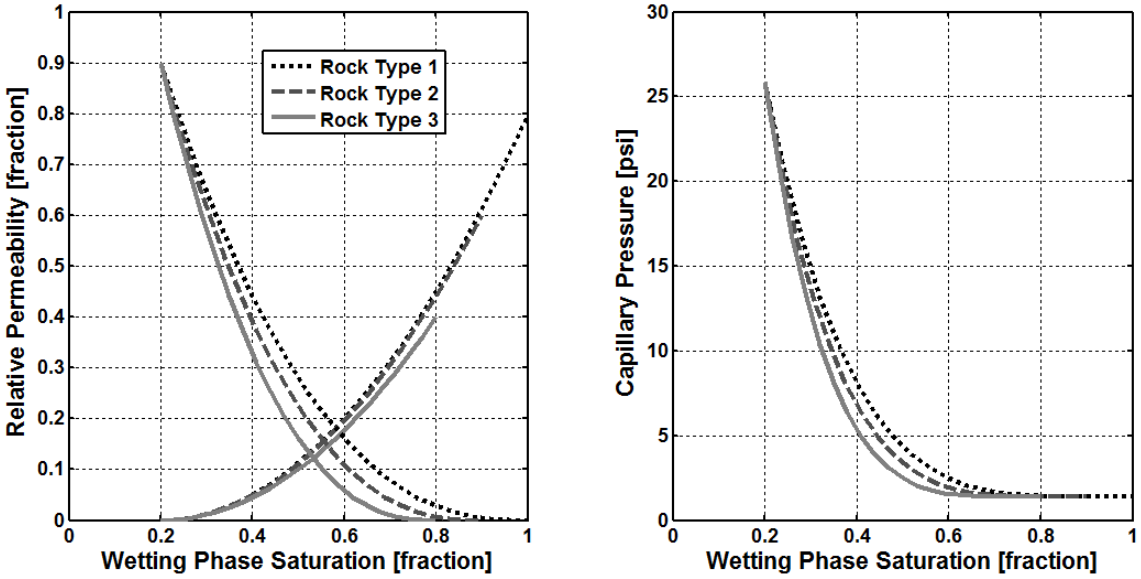


**Figure 2.13:** Graphical description of the Brooks-Corey water-oil relative permeability (left-hand panel) and capillary pressure (right-hand panel) curves assumed in the simulation of the process of mud-filtrate invasion in the oil-bearing synthetic zone. Irreducible water saturation is assumed constant and equal to 0.20, whereas residual oil saturation varies in the range of 0-0.20 for the three rock types assumed in the second synthetic case.

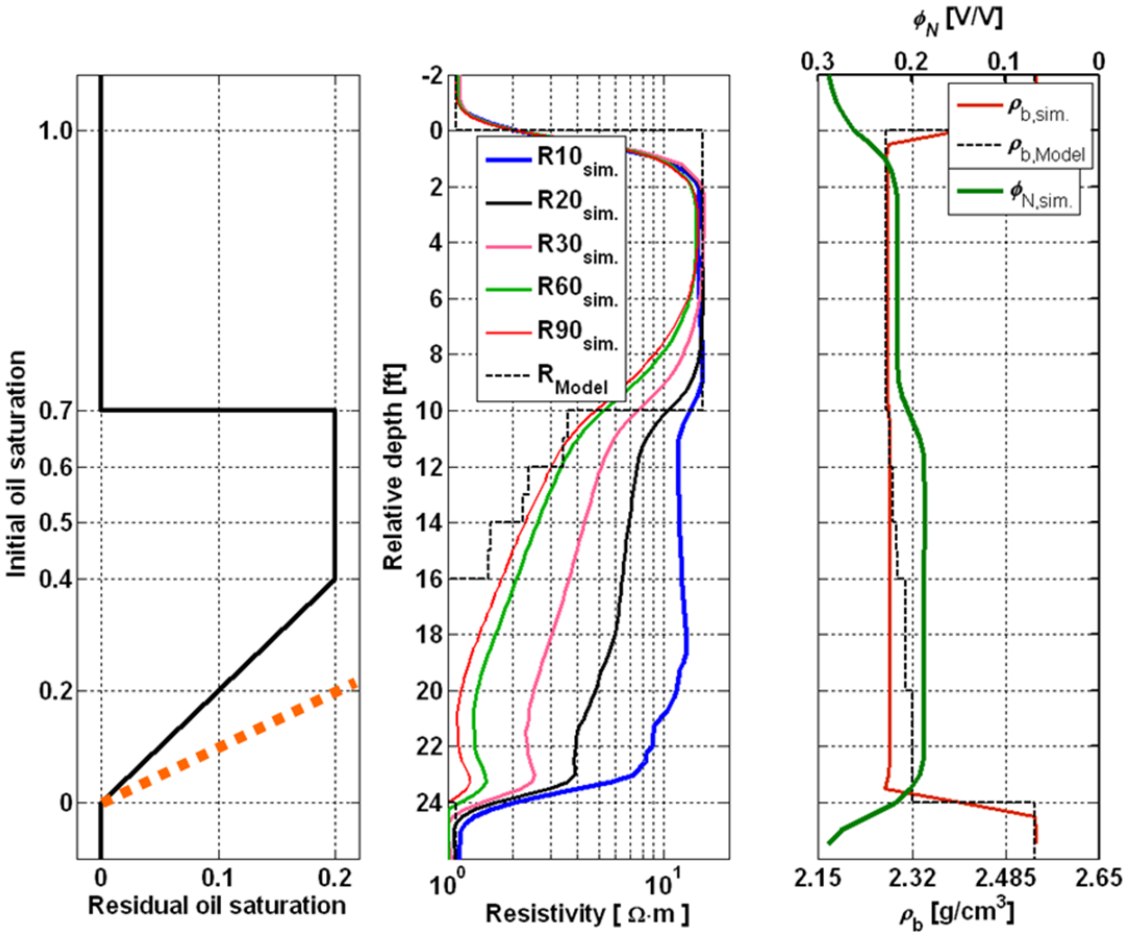


**Figure 2.14:** Numerically simulated array-induction apparent resistivity logs (center panel) and neutron porosity and density logs (right-hand panel) for the multi-layer oil-bearing synthetic case. Time of mud-filtrate invasion is one day. The left-hand panel shows the assumed initial oil saturation with depth vs. residual oil saturation. Similar to Land's (1971) behavior, the solid black line deviates with respect to the dashed orange line, where the latter indicates linear correlation between initial and residual oil saturation.

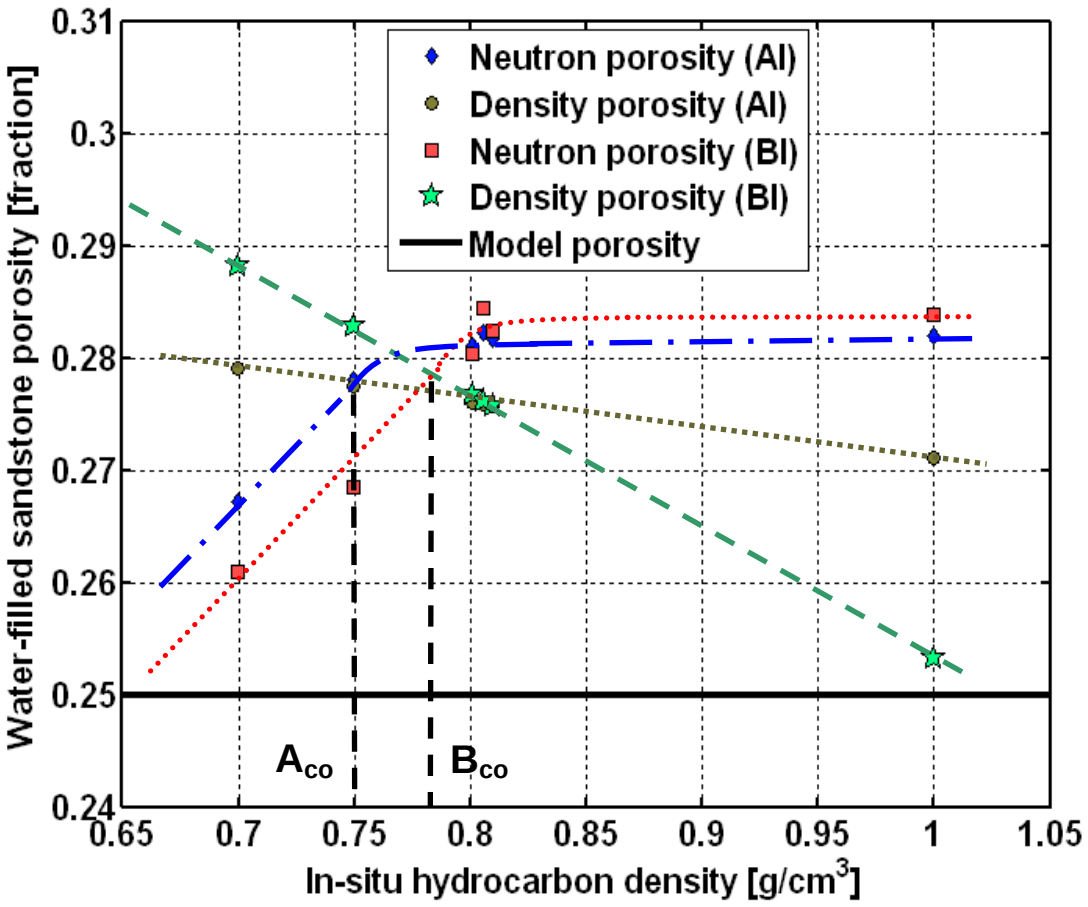


**Figure 2.15:** Sensitivity analysis of neutron porosity and density porosity measurements to in-situ oil density. Numerical simulations assume a single-layer, oil-bearing sandstone model. Density of in-situ oil varies between 0.7 and 1 g/cm$^3$. Parameters $A_{co}$ and $B_{co}$ designate limits of hydrocarbon density necessary to observe density-neutron cross-over after and before mud-filtrate invasion, respectively.

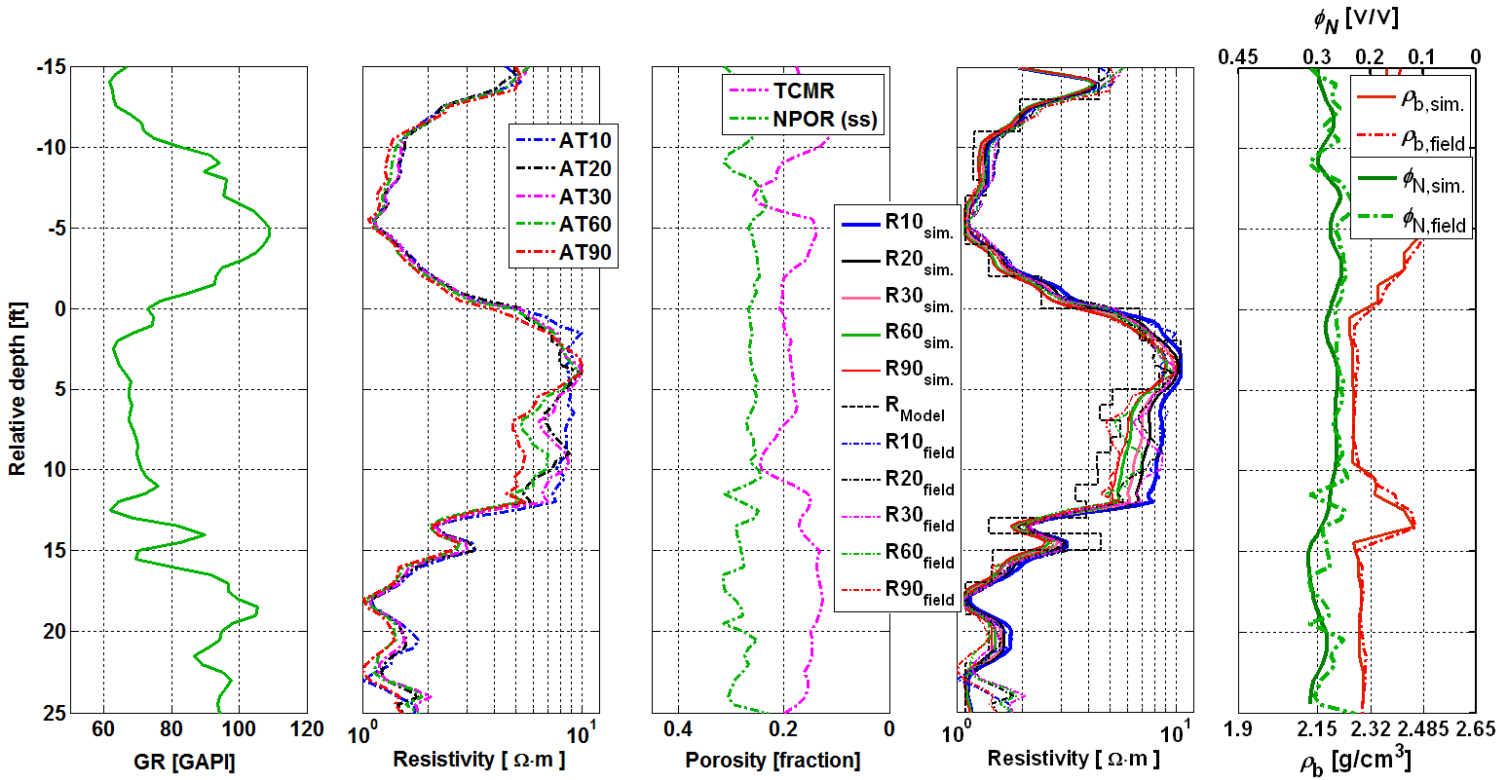


**Figure 2.16:** Comparison of numerically simulated (solid lines) and measured (dashed lines) array-induction apparent resistivity logs (fourth panel from the left) and neutron porosity and density logs (fifth panel from the left) for the multi-layer, oil-bearing field example model. Final petrophysical properties were obtained from the matching of field logs with numerical simulations (Table 2.14). The left-hand panel and the second panel from the left show the measured gamma-ray log and array-induction resistivity logs, respectively. The middle panel shows neutron porosity in sandstone units and total CMR porosity. Time of mud-filtrate invasion ($t_{inv}$) is one day.

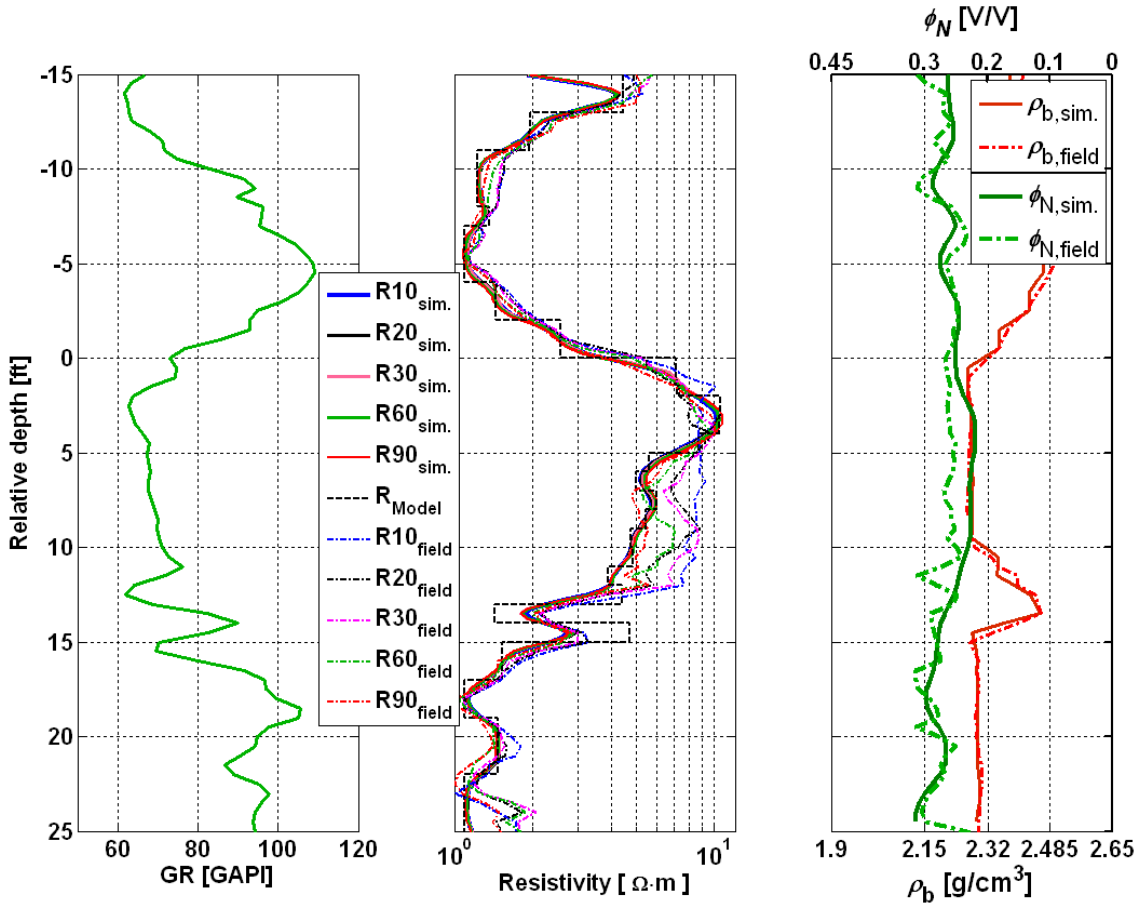


**Figure 2.17:** Comparison of numerically simulated (solid lines) and measured (dashed lines) array-induction apparent resistivity logs (center panel) and neutron porosity and density logs (right-hand panel) for the multi-layer model of the oil-bearing field example before invasion. No separation is observed between apparent resistivity curves while neutron porosity and density porosity logs overlap in the sand zone.

# Chapter 3: Estimation of Dynamic Petrophysical Properties of Water-Bearing Sands Invaded with Oil-Base Mud from Multi-Physics Borehole Geophysical Measurements

Borehole geophysical measurements acquired in water-bearing sands are commonly used to benchmark and calibrate resistivity-porosity-saturation models. This calibration procedure is not always accurate in the presence of oil-base mud (OBM) filtrate invasion or high residual hydrocarbon saturation. In the case of invasion with water-base mud (WBM), the corresponding electrical resistivity response is governed not only by water saturation, but also by salt mixing between connate water and mud filtrate, thereby slightly complicating the interpretation. Conversely, when OBM invades connate water, non-miscible fluid displacement takes place, which does not involve salt mixing. This is a favorable condition for the estimation of dynamic petrophysical properties, including saturation-dependent capillary pressure.

In this chapter, we develop and successfully test a new method to estimate porosity, fluid saturation, permeability, capillary pressure, and relative permeability of water-bearing sands invaded with OBM from multi-physics borehole geophysical measurements. The estimation method simulates the process of mud-filtrate invasion to calculate the corresponding radial distribution of water saturation. Porosity, permeability (mobility), capillary pressure, and relative permeability are iteratively adjusted in the simulation of invasion until density, photoelectric factor (PEF), neutron porosity, and apparent resistivity logs are accurately reproduced with numerical simulations that honor the post-invasion radial distribution of water saturation.

Examples of application include oil- and gas-bearing reservoirs that exhibit a complete capillary fluid transition between water at the bottom and hydrocarbon at irreducible water saturation at the top. We show that the estimated dynamic petrophysical

properties in the water-bearing portion of the reservoir are in agreement with vertical variations of water saturation above the free water-hydrocarbon contact, thereby validating our estimation method. Additionally, it is shown that the radial distribution of water saturation inferred from apparent resistivity and nuclear logs can be used for fluid-substitution analysis of sonic compressional and shear logs.

## 3.1 INTRODUCTION

Conventional well-log interpretation commonly resorts to water-bearing reservoir units to estimate connate-water electrical resistivity based on the relationship between formation porosity and electrical resistivity (Pickett, 1966). However, in the case of non-negligible invasion with WBM-filtrate, it is necessary to account for the effect of salt mixing between connate water and mud filtrate when estimating connate water resistivity. Such interpretation methods can be unreliable in the presence of residual hydrocarbon saturation because the fraction of water saturation sensed by apparent resistivity logs remains unknown. Conversely, in the case of invasion with OBM, the invasion process involves immiscible fluid displacement between OBM-filtrate and water, and therefore no salt exchange. This relatively favorable condition opens the possibility of reliable estimation of dynamic petrophysical properties of the invaded rock formation from the estimation of the radial distribution of water saturation. To date, no petrophysical interpretation method has been advanced to take advantage of the immiscibility between OBM-filtrate and connate water to estimate fundamental dynamic properties of rock formations such as permeability, capillary pressure, and relative permeability.

Recent publications emphasize the importance of numerical simulation of well logs to estimate static and dynamic petrophysical properties of rock formations (Malik et al., 2008; Salazar et al., 2006; Salazar et al., 2007; Heidari et al., 2011). One of the

technical challenges inherent to these studies is the non-uniqueness of the estimation due to the large number of unknown petrophysical properties. A way to approach the solution is to use core data as external information. To overcome the problem of non-uniqueness in the estimation, the interpretation method advanced in this chapter invokes multi-physics measurements and is based on the numerical simulation of gamma-ray (GR), PEF, electrical resistivity, neutron porosity, and density logs from the post-invasion radial distribution of fluid saturation resulting from invasion.

Depending on the dynamic petrophysical properties of the formation—notably permeability (mobility), capillary pressure, and relative permeability—the displacement of water with OBM-filtrate will result in shallow, deep, sharp and/or spatially smooth radial fronts of water saturation away from the borehole wall. The corresponding effect on electrical resistivity measurements with variable radial lengths of investigation will be either "stacked" or "separated" apparent resistivity logs. Because of the relatively low values of formation electrical conductivity in this specific case of analysis (water-bearing sands and salty connate water), induction electrical resistivity logs will exhibit measurable sensitivity to radial variations of water saturation away from the borehole wall.

The interpretation method postulated in this chapter assumes a vertical well, horizontal layers, and axial symmetric invasion. It is initialized with the construction of a multi-layer petrophysical model. Layer-by-layer properties are populated with results obtained with conventional petrophysical interpretation of well logs. The process of mud-filtrate invasion is numerically simulated in permeable layers assuming no hydraulic communication between adjacent beds. Subsequently, apparent resistivity and nuclear logs are numerically simulated from the spatial distribution of water saturation obtained from the simulation of mud-filtrate invasion (nuclear logs are simulated using a recently-

developed fast linear iterative refinement method). We iteratively adjust the initial guess of layer-by-layer petrophysical properties to minimize the difference between well logs and their numerical simulations, thereby rendering final estimates of static and dynamic petrophysical properties.

The procedure is first implemented in pure-shale zones (which are not normally affected by mud-filtrate invasion) to estimate shale porosity, volumetric concentration of clay, and bound-water resistivity. Estimated properties from this first step are assumed equal to those of water-saturated zones to estimate non-shale porosity, absolute permeability, and saturation-dependent capillary pressure and relative permeability. Estimated properties are thereafter used in hydrocarbon-bearing zones to quantify hydrocarbon pore volume. The overall interpretation procedure is verified by correlating the saturation-dependent capillary pressure estimated in water-bearing sands with that of vertical variations of water saturation due to capillary equilibrium in a hydrocarbon reservoir underlain by an active aquifer.

The following sections detail the implementation, application, and limitations of the new interpretation method introduced in this chapter. To verify the reliability and accuracy of results in capillary transition zones, we consider three challenging examples of application that include hydrocarbon-bearing formations above active aquifers. Field examples cover a wide range of porosity and permeability values in various siliciclastic sedimentary sequences.

## 3.2 METHOD

### 3.2.1 Combined Iterative Numerical Simulation of Well Logs to Estimate Petrophysical Properties

Estimation of petrophysical properties is performed with a combined simulation algorithm which iteratively updates unknown properties by reducing the difference between well logs and their numerical simulations. The first step is to construct a layered model and generate an initial guess for static and dynamic petrophysical properties in the identified petrophysical layers of the multi-layer formation. Secondly, we numerically simulate the process of mud-filtrate invasion to determine the radial distributions of water saturations in the near-wellbore region. The next step numerically simulates nuclear and apparent resistivity logs and compares them to available well logs. We then iteratively update the initial guess of layer-by-layer properties to reduce the difference between measurements and simulations. **Figure 3.1** is a flowchart of the implemented procedure for combined iterative numerical simulation and automatic inversion of well logs to estimate porosity, water saturation, permeability, volumetric concentration of shale, and saturation-dependent capillary pressure and relative permeability.

To expedite the estimation process, we begin with the assessment of porosity and volumetric concentration of shale. Next, we approximate irreducible water saturation and initial water saturation by matching deep and shallow apparent resistivity logs with their numerical simulations. The last step is to estimate permeability and Brooks-Corey's parameters of saturation-dependent capillary pressure and relative permeability by matching the separation of apparent resistivity logs. After the first pass, we return to the assessment of porosity and update all the parameters in the second pass to secure a good agreement between well logs and their numerical simulations (**Figure 3.2**). There could be more than one solution for each petrophysical property depending on the availability

of core measurements, sensitivity of well logs to every unknown parameter, and the number of unknown properties. Sensitivity analysis is recommended to quantify (a) the range of sensitivity of available well logs to unknown petrophysical properties, and (b) the expected uncertainty range for estimated properties in different formations. The following sections briefly explain the assumed rock model and every step of the estimation procedure.

#### *3.2.1.1 Petrophysical Analysis and Construction of an Initial Guess*

Conventional well-log interpretation is used to generate an initial guess for layer-by-layer values of porosity, fluid saturation, volumetric concentration of shale, and permeability. We use neutron porosity and density logs to calculate porosity. Shaly-sand resistivity models (e.g., dual water model (Clavier et al., 1977)) are invoked to estimate water saturation. Volumetric concentration of shale is estimated based on GR, density, and neutron porosity logs. Initial guess for permeability values are assessed using Timur's formula (Timur, 1968). Bed boundaries are detected based on inflection points of GR, PEF, and density logs. The initial guess for layer-by-layer petrophysical properties is the average of log-calculated properties between detected bed boundaries.

#### *3.2.1.2 Rock Model*

The rock model assumed in this chapter consists of matrix, shale, and non-shale porosity that includes water and hydrocarbon. Water and hydrocarbon can be movable or trapped. Shale is assumed to be of the dispersed type (Poupon et al., 1970). Even though the specific application considered in this chapter assumes dispersed shale, the formation can be easily modified for the case of laminated shale.

Wet shale consists of clay and silt, which includes clay-bound water. The relationship among the volumetric concentrations of all rock components is expressed as (Mezzatesta et al., 2006)

$$\sum_{i=1}^{n_c} C_i + C_{sh} + \phi_s = 1, \tag{3.1}$$

$C_i$ is volumetric concentration of the assumed mineral constituents in the matrix, $C_{sh}$ is volumetric concentration of shale, $\phi_s$ is non-shale porosity, and $n_c$ is the number of mineral constituents. Volumetric concentration of shale is defined as

$$C_{sh} = \frac{V_{sh}}{V_r}, \tag{3.2}$$

where $V_r$ is rock volume including fluids and $V_{sh}$ is volume of wet shale. We calculate bulk density ($\rho_b$) via the equation

$$\rho_b = \sum_{i=1}^{n_c} \left( C_i \rho_i \right) + \rho_f \phi_s + \rho_{sh} C_{sh}, \tag{3.3}$$

where $\rho_i$ is density of the corresponding mineral, $\rho_f$ is fluid density, and $\rho_{sh}$ is shale density. Fluid density and shale density are given by

$$\rho_f = S_w \rho_w + \left(1 - S_w\right) \rho_h, \tag{3.4}$$

and

$$\rho_{sh} = \rho_{silt}\left(1 - C_{cl} - \phi_{sh}\right) + \rho_{cl}C_{cl} + \rho_w\phi_{sh}, \tag{3.5}$$

respectively, where $S_w$ is water saturation and the output of fluid-flow simulation at each numerical grid (the same numerical grid used for simulation of mud-filtrate invasion), $\phi_{sh}$ is shale porosity, $\rho_w$ is water density, $\rho_h$ is hydrocarbon density, $\rho_{cl}$ is clay density, $\rho_{silt}$ is silt density, and $C_{cl}$ is volumetric concentration of clay, defined as

$$C_{cl} = \frac{V_{cl}}{V_{sh}}, \tag{3.6}$$

where $V_{cl}$ is clay volume.

#### *3.2.1.3 Petrophysical Properties of Shale*

Shale porosity, volumetric concentration of shale, and bound water resistivity are necessary to estimate petrophysical properties of shaly formations. We implement the combined iterative numerical simulation of nuclear and electrical resistivity well logs specifically in pure-shale intervals to estimate shale properties. The assumptions of negligible mud-filtrate invasion, 100% volumetric concentration of shale, and 100% water saturation in shale zones reduce the non-uniqueness of the estimation. Calculated shale properties are assumed equal to those encountered in shaly-sand intervals.

#### *3.2.1.4 Simulation of Mud-Filtrate Invasion*

Simulation of OBM-filtrate invasion is performed with CMG[2] (Computer Modeling Group Ltd., 2008), a commercial reservoir simulator. We use GEM®, a compositional simulator of CMG, which numerically solves the equations of three-phase fluid flow in porous media. Developments considered in this chapter assume a vertical

[2] Mark of Computer Modeling Group

well, horizontal layers, and axial-symmetric invasion. Inputs necessary for the numerical simulation of mud-filtrate invasion are porosity, initial fluid saturation, permeability, in-situ fluid and mud properties, rock-fluid properties, and invasion parameters (including time of invasion, mud and mudcake properties, and overbalance pressure/average invasion flow rate). Numerical simulation of mud-filtrate invasion yields the post-invasion radial distribution of water saturation. Rocks are assumed water wet, whereas rock-fluid properties such as saturation-dependent capillary pressure and relative permeability are described in parametric form via Brooks-Corey's equation (Corey, 1994). Accordingly, capillary pressure is given by

$$P_c = P_c^0 \sqrt{\frac{\phi_t}{k}} \left(1 - S_N\right)^{e_p}, \tag{3.7}$$

where $P_c$ is capillary pressure [psi], $P_c^{\,0}$ is a constant coefficient [psi.darcy$^{1/2}$], $\phi_t$ is total porosity, $k$ is absolute permeability [darcy], $e_p$ is pore-size distribution exponent, and $S_N$ is normalized water-phase saturation, given by

$$S_N = \frac{S_w - S_{wr}}{1 - S_{wr} - S_{hr}}, \tag{3.8}$$

where $S_{wr}$ is irreducible water saturation and $S_{hr}$ is residual hydrocarbon saturation. Water and hydrocarbon saturation-dependent relative permeabilities, $k_{rw}$ and $k_{rh}$, respectively, are given by

$$k_{rw} = k_{rw}^0 S_N^{e_w}, \tag{3.9}$$

and

$$k_{rh} = k_{rh}^{0}\left(1 - S_N\right)^{e_h}, \tag{3.10}$$

where $k^0_{rw}$ and $k^0_{rh}$ are relative permeability end points, and $e_w$ and $e_h$ are experimental exponents for water and hydrocarbon relative permeability, respectively. Capillary-pressure and relative-permeability parameters included in Brooks-Corey's equations are iteratively adjusted when minimizing the difference between well logs and their numerical simulations as part of the nonlinear estimation method.

We emphasize that Brooks-Corey's equation formally describe saturation-dependant properties for immiscible imbibition displacement (the wetting fluid phase displacing the non-wetting fluid phase). In the present study, OBM displaces water (wetting fluid phase), hence the immiscible fluid displacement condition is that of drainage. We assume that Brooks-Corey's equation remain valid. Previous work on mud-filtrate invasion modeling indicates that this is remaining a good approximation (Malik et al., 2008; Salazar et al., 2007).

The Initial guess for Brooks-Corey's parameters can be based on core measurements for saturation-dependent relative permeability and capillary pressure. In the absence of core measurements, water saturation estimated in the flushed zone and hydrocarbon saturation estimated in the virgin zone can be used as the initial guess for irreducible water saturation and for residual hydrocarbon saturation, respectively. The latter method for choosing an initial guess is only valid in the case of OBM invaded water-saturated zones. The rest of Brooks-Corey's parameters can be chosen arbitrarily when constructing an initial guess of layer-by-layer properties.

#### *3.2.1.5 Saturation-Dependent Capillary Pressure*

The proposed interpretation method estimates water-oil capillary pressure based on the physics of OBM-filtrate invasion within water-saturated zones. We modify the calculated radial water-OBM capillary pressure to that of water-hydrocarbon given by

$$P_{c,wg} = P_{c,wo} \frac{\gamma_{wg} \cos\theta_{wg}}{\gamma_{wo} \cos\theta_{wo}}, \tag{3.11}$$

where $\gamma$ is interfacial tension [dynes/cm] and $\theta$ is contact angle between water and hydrocarbon phases (Zinszner and Pellerin, 2007).

Saturation-dependent capillary pressure is converted to a saturation-height distribution using densities of hydrocarbon and water and the assumption of linear hydrostatic variations of pressure with depth (Zinszner and Pellerin, 2007) given by

$$P_c = \left(\rho_w - \rho_h\right) gh, \tag{3.12}$$

where $\rho_w$ is water density, $\rho_h$ is hydrocarbon density, $h$ is depth, and $g$ is gravity constant. This latter step is used for cross-validation of the saturation-dependent capillary pressure estimated from the physics of OBM-filtrate invading a water-saturated rock.

#### *3.2.1.6 Numerical Simulation of Well Logs*

The first step in the numerical simulation of well logs is to assess the radial distributions of density, migration length, photoelectric factor, electrical resistivity, and volumetric concentrations of uranium, potassium, and thorium from post-invasion radial distribution of water saturation. Density (Equation (3.3)), neutron porosity, PEF, array-induction electrical resistivity, and GR logs are numerically simulated based on those radial distributions.

We use Schlumberger's SNUPAR commercial software (McKeon and Scott, 1989) to assess migration length and photoelectric factor from chemical compositions and their corresponding volumetric concentrations in each of the layers. Nuclear logs are thereafter simulated via fast linear iterative refinement (Mendoza et al., 2010).

The radial distribution of electrical resistivity is calculated with the dual-water, shaly-sand resistivity model (Clavier et al., 1977) from the previously calculated radial distribution of water saturation. Such radial distribution is the input for numerical simulation of array-induction apparent resistivity logs (AIT[3]).

### 3.2.2 Nonlinear Inverse Problem

In the field examples investigated in this chapter, beds are usually thick (thicker than 2 ft) and shoulder-bed effects are not significant concerns. Thus, we can safely apply a layer-by-layer inversion on the center-bed values of well logs. Nonlinear inversion of well logs for a single layer is performed by minimizing the quadratic cost function

$$\mathbf{C}(\mathbf{x}) = \left\| \mathbf{W_d} \bullet \left[ \mathbf{d}(\mathbf{x}) - \mathbf{d}_{\boldsymbol{m}} \right] \right\|_2^2 + \alpha^2 \left\| \mathbf{x} \right\|_2^2, \tag{3.13}$$

subject to

$$x_i \geq 0, \tag{3.14}$$

and

$$C_m + C_{sh} + \phi_s = 1, \tag{3.15}$$

[3] Mark of Schlumberger

where $\mathbf{W_d}$ is a data weighting matrix, $\mathbf{d}$ is the vector of numerically simulated logs, $\mathbf{d_m}$ is the vector of well logs, $\alpha$ is a regularization (stabilization) parameter, and $\mathbf{x}$ is the vector of unknown static/dynamic petrophysical properties. Equation (3.15) is only reliable in the presence of dispersed shale. However, depending on the assumed rock model, it can be extended to cases of laminated shale. Vector $\mathbf{x}$ can be expressed as

$$\mathbf{x} = \left[ C_m, C_{sh}, \phi_s, S_w, S_{wr}, k, P_c^0, e_p, k_{rh}^0, e_h \right]^T, \tag{3.16}$$

where the superscript "$T$" indicates transpose and $C_m$ is volumetric concentrations of minerals in each bed. The vector of well logs or their numerical simulation is given by

$$\mathbf{d} = \left[ \phi_N, \rho_b, PEF, GR, \boldsymbol{\sigma} \right]^T, \tag{3.17}$$

where $\phi_N$ is neutron porosity and $\boldsymbol{\sigma}$ identifies all the available apparent conductivity center-bed values from each log. Apparent conductivity logs are inverse of array-induction apparent resistivity measurements that include five curves with different radial lengths of investigation ($\sigma$10, $\sigma$20, $\sigma$30, $\sigma$60, and $\sigma$90).

The data weighting matrix in Equation (3.13) controls the importance of each well log included in the inversion. $\mathbf{W_d}$ is given by

$$\mathbf{W_d} = \begin{bmatrix} \frac{1}{d_{m,1}} & . & . & . & 0 \\ . & . & & & . \\ . & & . & & . \\ . & & & . & . \\ 0 & . & . & . & \frac{1}{d_{m,n_l}} \end{bmatrix}, \tag{3.18}$$

where $n_l$ is the number of well logs. Well logs can be eliminated from inversion process by inputting a negligible value to the corresponding entry of the data weighting matrix.

To effectively enforce the constraints expressed in Equations (3.14) and (3.15), we can change the variable vector $\mathbf{x}$ to $\mathbf{x}'$ given by

$$\mathbf{x}' = \left[ \log V_m, \log V_{sh}, \log V_{ps}, \log S_w, \log S_{wr}, \log k, \log P_c^0, \log e_p, \log k_{rh}^0, \log e_h \right]^T, \qquad (3.19)$$

where $V_m$ is matrix volume and $V_{ps}$ is pore-space volume.

The quadratic cost function defined in Equation (3.13) is minimized using Levenberg-Marquardt's method (Marquardt, 1963), which is a nonlinear gradient-based technique. We calculate the entries of the Jacobian matrix numerically (finite differences) by perturbing each unknown parameter and quantifying the corresponding perturbation of every well log involved in the estimation. Based on experience, the stabilization parameter is needed for this non-unique minimization problem. This parameter reduces non-uniqueness in the presence of noisy, inadequate, and/or incomplete data. We select the stabilization parameter with Hansen's (1994) L-curve strategy. The stabilization parameter takes a large value at the initial iterations to expedite the convergence. It then becomes smaller to secure a stable convergence to the answer, when the results get close to the actual solution.

In the described problem, the number of well logs and equality constraints is usually less than the number of unknown properties/parameters. Consequently, the inversion is under-determined. Experience shows that the simultaneous inversion to estimate all the unknown petrophysical properties and Brooks-Corey's parameters can easily trap into local minima in this non-unique inverse problem. Angeles (2009), Alpak et al. (2008), and Zeybek et al. (2004) also indicated the same challenge in their work.

They claimed that results obtained using joint inversion were significantly influenced by the initial guess. Angeles (2009) introduced a method based on iterative serial inversion loops for joint inversion of formation-tester and electrical resistivity measurements to estimate Brooks-Corey's parameters. In the present chapter, we adopt the same approach using only apparent resistivity logs. Eliminating formation-tester measurements increases non-uniqueness of results. However, the special case of OBM-invaded water-saturated sands reduces the non-uniqueness of results by enhancing the sensitivity of apparent resistivity measurements to radial variations of fluid saturations.

In the first step, we estimate porosity and volumetric concentrations of mineral constituents and shale. As long as the formations under study do not exhibit complex lithology, the uncertainty in the assessment of volumetric concentration of shale and porosity is negligible. Next, array-induction resistivity measurements (five measurements) are used to estimate Brooks-Corey's parameters and absolute permeability in a serial inversion approach. We start the serial inversion to estimate the parameter that has the highest impact on well logs. Then we fix that parameter and estimate the next sensitive parameter, until we estimate all the unknowns. Finally, we return to the first parameter and restart the process with the updated values for unknown properties. **Figure 3.2** shows the different steps of the iterative serial inversion approach. More details about the algorithm are provided in Synthetic Case No. 1.

Brooks-Corey's parameters that can be reliably estimated with this method include $P_c^0$, $e_p$, $S_{wr}$, $S_{hr}$, $k^0_{rh}$, and $e_h$. Assessment of $k^0_{rw}$ and $e_w$ is not reliable due to marginal sensitivity of well logs to these parameters for the case of OBM invading water-saturated sands. However, in the case of WBM invading hydrocarbon-bearing zones, the method yields reliable estimates of $k^0_{rw}$ and $e_w$.

In the following sections we describe the application of the proposed interpretation method to one synthetic case and three field examples. The three field examples are selected to cover a wide range of porosity and permeability values in siliciclastic sedimentary sequences.

## 3.3 SYNTHETIC CASE NO. 1: SINGLE-LAYER HYDROCARBON-BEARING FORMATION

Synthetic Case No. 1 is constructed based on petrophysical properties of a shaly-sand hydrocarbon-bearing formation (i.e., Field Example No. 3). This synthetic example is intended to examine the sensitivity of well logs to dynamic petrophysical properties and to illustrate how the estimation process is implemented with fully automatic inversion. We also quantify the uncertainty of estimated properties.

The synthetic case is a water-saturated zone, invaded with OBM. Archie's parameters and matrix, mud, fluid, and formation properties assumed in Synthetic Case No. 1 are equal to those assumed for Field Example No. 3 (**Table 3.9**). Non-shale porosity, volumetric concentration of shale, and initial water saturation in the single-layer formation are assumed to be 0.14, 0.28, and 0.90, respectively (average formation properties in Field Example No. 3). **Table 3.1** lists the assumed Brooks-Corey's parameters and absolute permeability.

Well logs input to the interpretation process are GR, density, neutron porosity, PEF, and array-induction apparent resistivity. Because PEF and GR are primarily affected by volumetric concentration of shale in the formation, we first estimate volumetric concentration of shale based on PEF and GR. Experience shows that in this case the effect of dynamic petrophysical properties is lower than 0.2 limestone porosity units and 0.005 g/cm$^3$ on neutron porosity and density measurements, respectively.

Consequently, we use density and neutron porosity logs to estimate porosity and do not include them in the inversion of Brooks-Corey's parameters and absolute permeability.

In Synthetic Case No. 1, we first investigate the sensitivity of electrical resistivity measurements to absolute permeability and Brooks-Corey's parameters separately. In the separate inversion of each parameter (assuming that the rest of the parameters are known), the final estimate converges to model values for all the parameters. **Table 3.1** lists model parameters, initial guess, and final estimates of permeability and Brooks-Corey's parameters. The same table describes the corresponding error ranges of final estimates obtained by perturbing array-induction apparent resistivity with 2% random Gaussian additive noise.

Next, we apply iterative serial inversion loops on this case. Based on the error ranges reported in **Table 3.1**, apparent resistivity logs exhibit the maximum sensitivity to $e_p$ and the minimum sensitivity to absolute permeability. Consequently, the first loop starts with an inversion to estimate $e_p$, while the remaining parameters are set to their initial values. Afterward, the second inversion loop estimates $P_c^{\,0}$ with the updated $e_p$ value and the remaining parameters are set to their initial values. We continue in the same way with the third loop to simultaneously estimate $k^0_{rh}$ and $e_h$, and thereafter with the fourth loop to estimate permeability. Next, we return to the first loop and repeat the process with updated parameters until satisfying the convergence criteria (**Figure 3.2**). A convergence criterion is either (a) relative error of less than 1% between well logs and their numerical simulations or (b) constant error in two subsequent iterations. **Table 3.2** describes the results obtained for Brooks-Corey's parameters and permeability after two iterations using the iterative serial inversion approach. Although the final estimates are close to the model values, the uncertainty range is significant. Furthermore, the final results in this case are sensitive to initial guess, due to the non-uniqueness of the results.

For instance, a 10% increase in the initial guess for permeability increases the error in final estimates of permeability by 40%.

## 3.4. SYNTHETIC CASE NO. 2: SENSITIVITY OF WELL LOGS TO DYNAMIC AND STATIC FORMATION PROPERTIES

Synthetic Case No. 2 is a single-layer formation constructed based on Field Example No. 1, with the same formation/fluid properties. This synthetic case is intended to examine the sensitivity of well logs to porosity and permeability (mobility). Drilling mud is OBM and the formation is saturated with both water and residual hydrocarbon. **Table 3.3** and **Table 3.4** describe the assumed Archie's parameters and matrix, mud, fluid, and formation properties as well as rock-fluid properties, respectively, assumed for Synthetic Case No. 2.

### 3.4.1 Sensitivity of Well logs to Formation Properties in the Presence of Mud-Filtrate Invasion

#### *3.4.1.1 Sensitivity of the Radial Profile of Water Saturation to Porosity and Permeability*

The radial profile of water saturation due to invasion is controlled by formation/fluid properties and influences well logs. **Figure 3.3** shows the effect of porosity and permeability on the radial profile of water saturation. Although the permeability-porosity ratio remains constant, the radial length of invasion decreases and the invasion front becomes piston-like with an increase of both porosity and permeability. Furthermore, this example shows that the common assumption of piston-like invasion in the presence of OBM is not valid in formations with low porosity and permeability. Radially smooth variations of water saturation affect well logs and, consequently, conventional well-log interpretation. Next, we investigate the effect of this "ramp-up" radial profile of water saturation on array-induction apparent resistivity logs.

#### *3.4.1.2 Sensitivity of Electrical Resistivity Measurements to Porosity and Permeability*

**Figure 3.4** compares array-induction apparent resistivities for a range of permeability-porosity ratios. The maximum separation between apparent resistivity logs takes place with low permeability and porosity values, where the invasion profile is radially smooth, thereby enabling the estimation of dynamic petrophysical properties.

However, separation between apparent resistivity logs is not the only requirement for accurate permeability assessment. To investigate the possibility of permeability assessment based on separation between apparent resistivity logs, we fix porosity to 0.25, vary permeability in the range from 0.1 to 1000 md, and numerically simulate mud-filtrate invasion and the corresponding apparent resistivity logs. **Figure 3.5** shows the sensitivity of separation between array-induction apparent resistivity logs to permeability. Although separation of apparent resistivity logs increases with an increase of permeability, for permeability values greater than 50 md, array-induction apparent resistivities are not sensitive to permeability values any longer. The limit of sensitivity is different for different rock types.

## 3.5 FIELD EXAMPLE NO. 1: DEEPWATER GULF OF MEXICO

This field example considers turbidite depositional sequence in the deepwater Gulf of Mexico. The reservoir mainly consists of channel levees with unconsolidated shaly sand, which can be observed in the form of massive sand and shale-laminated intervals. Rock formations contain more than 85% quartz and less than 15% clay minerals including illite/smectite, kaolinite, and chlorite (Malik et al., 2008). Porosity and permeability vary in the range from 0.20-0.34 and 10-2500 md, respectively.

**Figure 3.6** shows well logs across the hydrocarbon-bearing zone, underlain by an active aquifer. We observe separation of apparent resistivity logs in the water-bearing zone due to presence of OBM. A sudden separation exists between sonic compressional-

($V_p$) and shear- ($V_s$) wave velocities in the water-saturated zone. To explain this sudden separation of sonic velocities, we construct a synthetic case based on fluid/formation properties and investigate the sensitivity of compressional- and shear-wave velocities to water saturation. Compressional- and shear-wave velocities are calculated using Biot-Gassmann's equations (Biot, 1956; Gassmann, 1951; Mavko et al., 2009) in a formation varying from fully hydrocarbon-saturated to fully water-saturated conditions. **Figure 3.7** shows compressional- and shear-wave velocities as a function of water saturation. For values of water saturation higher than 0.9, a sharp increase in compressional-wave velocity causes an increase in the difference between compressional- and shear-wave velocities. This sensitivity analysis confirms that the presence of light hydrocarbon in that depth zone is responsible for the sharp increase in compressional-wave velocity.

We focus our analysis to the water zone depicted in **Figure 3.8**. Numerically simulated logs compare well to measurements in the top and bottom shale intervals as well as across the water-saturated sand, with a relative error below 5%. **Table 3.3** and **Table 3.4** describe the Archie's parameters and matrix, mud, fluid, and formation properties as well as rock-fluid properties, respectively, assumed for this zone. **Table 3.5** lists the average petrophysical properties of the water zone of interest, which are used to initialize the estimation. Based on results obtained from the estimation in the upper shale zone, shale porosity is 0.15 and clay type is assumed to be illite. Numerical simulations performed in the shale zone also estimate bound water resistivity equal to 0.026 ohm.m at reservoir temperature. The radial length of mud-filtrate invasion is less than 0.7 ft, whereby the sensitivity of array-induction apparent resistivity logs to dynamic petrophysical properties is low. Concomitantly, the shallow radial invasion profile makes the interpretation of neutron porosity and density logs complicated with conventional interpretation methods because one can no longer assume that the volumes of

investigation of density and neutron porosity logs are limited to the invaded zones. Thus, predicting the effect of mud-filtrate invasion on well logs would be difficult without numerical simulation of the process of invasion.

Well logs used in the combined iterative simulation consist of array-induction electrical resistivity, neutron porosity, density, and GR. **Table 3.6** describes the petrophysical properties estimated in the water-saturated zone, including non-shale porosity, absolute permeability, volumetric concentration of shale, and initial water saturation. Due to a sharp radial invasion front and the corresponding stacked array-induction apparent resistivity logs, electrical resistivity measurements exhibit marginal sensitivity to dynamic petrophysical properties. Consequently, the estimated saturation-dependent capillary pressure and relative permeability are not accurate in this case.

## 3.6 FIELD EXAMPLE NO. 2: CENTRAL NORTH SEA SANDSTONE

This example concerns a Paleocene sandstone dome located in the Central North Sea (Martin et al., 2005). The examined depth zone contains an oil-saturated column with a gravity of 40°API underlain by an active aquifer (BP, 2003). Rock formations chiefly consist of non-calcareous, blocky grey mudstone interbedded with sandy, high-density gravity-flow deposits and minor volcaniclastic units. Porosity varies in the range from 0.20-0.28 while permeability ranges from 50 to 1000 md. **Figure 3.9** compares well logs and their numerical simulations in the water-saturated zone. The water-saturated zone is located between two shale layers. Numerically simulated well logs also compare well to available well logs within the two shale intervals. The combined iterative simulation of well logs yields a value of shale porosity equal to 0.09, with clay type assumed to be illite. Bound water resistivity at reservoir temperature is 0.01 ohm.m based on simulation results. **Table 3.7** lists the Archie's parameters and matrix, mud, fluid, and formation

properties assumed for this zone. **Table 3.8** describes average petrophysical properties in the water-saturated zone of interest, which are used as initial guess for combined iterative simulation of well logs. Core measurements for porosity and permeability in the water-saturated zone vary between 0.21-0.25 and between 200-300 md, respectively.

Array-induction apparent resistivity, neutron porosity, density, and GR logs are input to the estimation method. Values estimated for permeability, water saturation, and volumetric concentration of shale at the examined depth interval remain approximately constant and equal to 200 md, 0.85, and 0.05, respectively. The order of magnitude of permeability estimates is in agreement with core measurements (in the range of 200-300 md). **Table 3.9** lists the estimated rock-fluid properties. **Table 3.10** compares layer-by-layer porosity values to core measurements.

To cross-validate interpretation results, **Figure 3.10** compares the estimated capillary pressure curve against the vertical water saturation profile calculated with conventional petrophysical interpretation of well logs. This exercise indicates an agreement in both trend and value between the water-hydrocarbon capillary pressure and the radial water saturation profile within the water-saturated sand invaded with OBM. The left-most track in Figure 3.10 shows an increase in shear-wave slowness and a decrease in compressional-wave slowness between hydrocarbon- and water-bearing zones. Results from Biot-Gassmann's fluid substitution, shown in **Figure 3.11**, are in agreement with measured compressional- and shear- wave slowness in both water- and hydrocarbon-bearing zones.

## 3.7 FIELD EXAMPLE NO. 3: TRINIDAD SHALY SAND

This field example considers a Trinidad shaly-sand sequence located within a delta sedimentary system (Liu, 2007). The formation consists of thinly-bedded sands with

an average bed thickness of 1 ft. Our analysis is focused to a gas-bearing zone located above an aquifer invaded with OBM. Average porosity and permeability in the zone of interest are 0.14 and 500 md, respectively.

**Figure 3.12** shows well logs and their numerical simulations across the water-bearing zone. **Table 3.11** summarizes Archie's parameters and matrix, mud, fluid, and formation properties assumed for this zone. Shale porosity was estimated at 0.10 based on the combined iterative simulation of well logs with the assumption of illite as the dominant clay type. Bound water resistivity was also estimated to be 0.03 ohm.m at reservoir temperature. **Table 3.12** lists the average petrophysical properties for the simulation interval; the same values are used as initial guess for the iterative combined simulation of well logs.

We use array-induction apparent resistivity, neutron porosity, density, PEF and GR logs for the combined iterative simulation of well logs. **Table 3.13** and **Table 3.14** document the estimated values of Brooks-Corey's parameters and non-shale porosity, water saturation, volumetric concentration of shale, and permeability within the water-saturated zone, respectively.

**Figure 3.13** compares the estimated saturation-dependent water-gas capillary pressure against the vertical water saturation profile calculated with conventional well-log interpretation. A good agreement is observed between water-gas capillary pressure and the vertical distribution of water saturation, which verifies the results obtained from the proposed interpretation method. To assess saturation-dependent water-gas capillary pressure, we first estimate water-oil capillary pressure via combined iterative numerical simulation of well logs. Subsequently, saturation-dependent water-gas capillary pressure is estimated based on water-oil capillary pressure (Equation (3.11)).

## 3.8 DISCUSSION

This chapter proposed a method to estimate dynamic (e.g., absolute permeability and saturation-dependent capillary pressure and relative permeability) and static (e.g., porosity and water saturation) petrophysical properties based on combined numerical simulation and inversion of nuclear and resistivity logs. We focused our study on water saturated sands and shaly sands invaded with OBM. In such cases, (a) the separation between array-induction apparent resistivity logs is large and, consequently, the sensitivity of resistivity logs to dynamic properties is maximal, (b) the mud-filtrate and connate water are immiscible, and (c) salt mixing effects between mud-filtrate and connate water are negligible. The latter partially eliminates the effects of uncertainty associated with invasion parameters on the inversion results. We also applied the proposed method on pure shale zones to estimate shale properties such as shale porosity and bound water resistivity. We then used these properties in shaly sand zones to reduce non-uniqueness of the results.

Input data and parameters into the inversion are the following: (a) well logs including array-induction apparent resistivity/conductivity logs with different radial lengths of investigation (five radial lengths of investigation), neutron porosity, density, GR, and PEF, (b) invasion properties such as time of invasion, overbalance pressure, and mud/mud-cake properties, (c) formation and fluid properties such as mineralogy of the formation and density, viscosity, and chemical formula of in-situ fluids, (d) bed boundary locations, (e) a saturation-porosity-resistivity model and associated parameters (e.g., the dual water model and its associate parameters such as connate water and bound water resistivity, tortuosity factor, cementation exponent, and saturation exponent), and (f) a saturation-dependent capillary pressure and relative permeability model (e.g., Brooks-Corey's model). Uncertainty in any of the input data/parameters affects the final

estimates for static and dynamic petrophysical properties. However, inaccuracies in the location of bed boundaries and matrix composition were not significant concerns in this study, because all the field examples were siliciclastic sequences with beds thicker than 2 ft and no complex lithology.

To define the range of reliability of the proposed method in assessment of porosity, absolute permeability, and Brooks-Corey's parameters, we quantified the sensitivity of well logs to those properties, by imposing random perturbations on the well logs. The estimated properties from the highest to lowest reliability were porosity, volumetric concentration of shale, initial water saturation, irreducible water saturation ($S_{wr}$), pore-size distribution exponent ($e_p$), coefficient for capillary pressure equation ($P_c^0$), hydrocarbon-phase exponent for Brooks-Corey's equation ($e_h$), end point of hydrocarbon-phase relative permeability ($k^0_{rh}$), and permeability. The sensitivity of well logs to the end point of water-phase relative permeability ($k^0_{rw}$) and water-phase exponent for Brooks-Corey's equation ($e_w$) is marginal in the presence of OBM invading water-saturated sand zones. Consequently, the introduced method is not reliable in the assessment of $k^0_{rw}$ and $e_w$.

The assessment of dynamic petrophysical properties based on the proposed method is reliable when separation between resistivity measurements is large and smooth. The method's sensitivity to dynamic petrophysical properties is marginal in the presence of (a) "stacked" electrical resistivity logs, (b) shallow radial length of invasion (shallower than 0.5 ft), and (c) very deep radial length of invasion (deeper than 8 ft). Among the three field examples investigated in this chapter, Field Example No. 1 experienced the lowest radial length on invasion, where apparent array-induction resistivity logs were "stacked" and their separation was negligible. Consequently, the proposed method was not reliable in the assessment of dynamic petrophysical properties in this field example.

For the other two field examples, comparison of the estimated saturation-dependent capillary pressure against the vertical distribution of water saturation in the reservoir confirmed the reliability of the proposed method in assessing capillary pressure, which can even be used for upscaling purposes.

In all the synthetic cases and field examples studied in this chapter, the number of well logs was less than the number of unknown petrophysical properties, leading to an under-determined inversion. In such cases, non-uniqueness of the results is a major concern. Furthermore, including more well logs does not always reduce the non-uniqueness of the results, if the well logs do not provide sensitivity to dynamic petrophysical properties (e.g., PEF and GR). We found that the simultaneous inversion of well logs usually traps into local minima, due to non-uniqueness of the results. Thus, we proposed an iterative serial inversion approach to estimate permeability and Brooks-Corey's parameters. Although this method provided accurate results for Synthetic Case No. 1, the final results were still sensitive to initial guess. For achieving the most accurate results in such cases, the initial guess should be chosen close to actual values. Core data can be the best choice for initial guess. However, in the absence of core data, initial guess for porosity, volumetric concentration of shale, permeability, irreducible water saturation, and initial water saturation can be obtained from conventional petrophysical interpretation. Parsimonious initial guesses cam be used for the rest of Brooks-Corey's parameters.

## 3.9 CONCLUSIONS

We introduced a new method to estimate dynamic petrophysical properties of water-bearing rocks invaded by OBM. The method honors the physics of fluid flow in porous and permeable media and takes advantage of the immiscibility between mud

filtrate and connate water. Furthermore, it quantitatively combines electrical resistivity, density, neutron porosity, PEF, and GR logs, explicitly takes into account the differences in volumes of investigation of the various measurement instruments involved, and consistently reduces non-uniqueness in the estimation.

The estimation method was successfully tested on three field examples and two synthetic cases based on actual field examples. All the field examples consider siliciclastic hydrocarbon-bearing reservoirs underlain by active aquifers and cover a wide range of porosity and permeability value to investigate the reliability and accuracy of the estimations. Comparison of saturation-dependent capillary pressure in the water-bearing zones with the estimated radial profile of water saturation confirmed the accuracy and reliability of the method. We also showed that the inferred radial profile of water saturation enables the numerical simulation of borehole sonic logs (compressional- and shear-wave velocity logs) via fluid-substitution equations to match the corresponding measured logs.

The introduced method to estimate dynamic petrophysical properties is best suited for those cases where the radial profile of water saturation resistivity from invasion is smooth, and the separation between apparent resistivity logs is significant. It was found that the accuracy of the estimations decreased in the presence of shallow invasion and/or sharp radial profiles of water saturation. Likewise, the method is not sensitive to dynamic petrophysical properties in cases of radially deep mud-filtrate invasion. In general, any parameter that reduces the separation of array-induction resistivity logs (e.g., presence of fresh connate water in the OBM-invaded formation) reduces the sensitivity of the measurements to dynamic petrophysical properties.

Even though the introduced interpretation method could be applied to cases of WBM or OBM invading water- or hydrocarbon-bearing zones, the specific situation

where OBM invades water-saturated zones gives rise to the maximum sensitivity of apparent resistivity logs to formation properties. However, in the cases of OBM invading water-saturated zones, the estimates of end point and exponent for Brooks-Corey's equation for water-phase relative permeability are not reliable. Although all the cases shown in this chapter have simple lithology and thick beds, the method is capable in interpretation of thinly bedded formations with complex lithology.

The method introduced can provide estimates of static and dynamic petrophysical properties for any depth interval for which conventional well logs are available and reliable. However, core measurements are obtained from small core samples at limited depth intervals, which might not be reliable for upscaling. Finally, we recommend this method for assessment of static and dynamic petrophysical properties in field examples where (a) electrical resistivity measurements with different radial lengths of investigation are available and (b) the separation between electrical resistivity logs are significant and smooth.

**Table 3.1:** Synthetic Case No. 1, inversion of single parameters assuming that remaining parameters are fixed: Assumed model properties, initial guess, final and the corresponding uncertainty range for properties estimated after perturbing well logs with 2% random Gaussian additive noise.

| Parameter | Model | Initial | Final Estimate | Uncertainty Range |
|---|---|---|---|---|
| $P_c^0$ [psi.darcy$^{1/2}$] | 27 | 24 | 27 | 26 – 36.1 |
| $e_p$ [ ] | 5 | 4 | 5 | 4.5 – 5.5 |
| $k^0_{rh}$ [ ] | 0.7 | 0.8 | 0.7 | 0.4 – 0.9 |
| $e_h$ [ ] | 2.5 | 4 | 2.5 | 2 – 3.1 |
| $k$ [md] | 400 | 450 | 400 | 130 – 530 |

**Table 3.2:** Synthetic Case No. 1, iterative serial loop inversion of all unknown properties: Assumed model properties, initial guess, final estimates (after the second iteration of inversion), and the corresponding uncertainty range for properties estimated after perturbing well logs with 2% random Gaussian additive noise.

| Parameter | Model | Initial | Final Estimate | Uncertainty Range |
|---|---|---|---|---|
| $P_c^0$ [psi.darcy$^{1/2}$] | 27 | 24 | 29.8 | 28.7 – 38.6 |
| $e_p$ [ ] | 5 | 4 | 4.6 | 4.1 – 5.1 |
| $k^0_{rh}$ [ ] | 0.7 | 0.8 | 0.75 | 0.50 – 0.98 |
| $e_h$ [ ] | 2.5 | 4 | 2.7 | 2.2 – 3.2 |
| $k$ [md] | 400 | 450 | 446 | 166 – 546 |

**Table 3.3:** Deepwater Gulf of Mexico, Field Example No. 1: Summary of assumed Archie's parameters and matrix, mud, fluid, and formation properties.

| Variable | Value | Units |
|---|---|---|
| Archie's tortuosity factor, *a* | 1.00 | - |
| Archie's cementation exponent, *m* | 1.92 | - |
| Archie's saturation exponent, *n* | 2.00 | - |
| Connate water resistivity at 148 °F | 0.03 | ohm.m |
| Bound water resistivity at 148 °F | 0.026 | ohm.m |
| Water density | 1.00 | $g/cm^3$ |
| Water viscosity | 1.00 | cp |
| In-situ hydrocarbon density | 0.10 | $g/cm^3$ |
| Hydrocarbon viscosity | 0.84 | cp |
| Mud-filtrate density | 0.77 | $g/cm^3$ |
| Mud-filtrate viscosity | 1.50 | cp |
| Formation temperature | 148 | °F |
| Initial formation pressure | 7750 | psi |
| Mudcake reference permeability | 0.03 | md |
| Mudcake reference porosity | 0.30 | [ ] |
| Mud solid fraction | 0.06 | [ ] |
| Mudcake maximum thickness | 1.02 | cm |
| Mudcake compressibility exponent | 0.40 | [ ] |
| Mudcake exponent multiplier | 0.10 | [ ] |
| Wellbore radius | 14.94 | cm |
| Shale porosity | 0.15 | [ ] |
| Over-balance pressure | 250 | psi |
| Formation maximum invasion time | 3 | days |

**Table 3.4:** Deepwater Gulf of Mexico, Field Example No. 1: Summary of assumed rock-fluid properties for the connate water-OBM filtrate fluid system.

| $P_c^0$ [psi.darcy$^{1/2}$] | $e_p$ | $k^0_{rh}$ | $e_h$ | $k^0_{rw}$ | $e_w$ | $S_{wr}$ | $S_{hr}$ |
|---|---|---|---|---|---|---|---|
| 8.0 | 7.0 | 0.99 | 4.0 | 0.37 | 4.2 | 0.15 | 0.02 |

**Table 3.5:** Deepwater Gulf of Mexico, Field Example No. 1: Averaged petrophysical properties obtained from conventional well-log interpretation.

| Variable | Value | Units |
|---|---|---|
| Thickness | 60 | ft |
| Absolute permeability, $k$ | 100 | md |
| Non-shale porosity, $\phi_s$ | 0.22 | [ ] |
| Total water saturation, $S_w$ | 1.00 | [ ] |
| Volumetric concentration of shale, $C_{sh}$ | 0.45 | [ ] |

**Table 3.6:** Deepwater Gulf of Mexico, Field Example No. 1: Multi-layer petrophysical properties obtained after matching well logs with their numerical simulations and the corresponding uncertainty range for properties estimated after perturbing well logs with 5% random Gaussian additive noise.

| Layer thickness [ft] | $k$ [$md$] | $\phi_s$ | $C_{sh}$ | $S_w$ |
|---|---|---|---|---|
| 10.0 (Shale) | < 0.001 | 0.00 | 1.00 | 1.00 |
| 18.0 | 50+[-32,150] | 0.265±0.004 | 0.32±0.012 | 0.96±0.013 |
| 4.0 | 100+[-48,210] | 0.225±0.004 | 0.42±0.014 | 0.97±0.013 |
| 4.0 | 120+[-101,280] | 0.255±0.004 | 0.42±0.014 | 0.98±0.013 |
| 6.0 | 110+[-92,230] | 0.225±0.004 | 0.42±0.014 | 0.98±0.013 |
| 8.0 | < 0.001 | 0.25±0.004 | 0.40±0.014 | 1.00+[-0.016,0] |
| 3.0 | < 0.001 | 0.11±0.003 | 0.65±0.014 | 1.00+[-0.024,0] |
| 7.0 | < 0.001 | 0.245±0.004 | 0.40±0.014 | 1.00+[-0.016,0] |

**Table 3.7:** Central North Sea Sandstone, Field Example No. 2: Summary of assumed Archie's parameters and matrix, mud, fluid, and formation properties.

| Variable | Value | Units |
|---|---|---|
| Archie's tortuosity factor, *a* | 1.00 | - |
| Archie's cementation exponent, *m* | 1.89 | - |
| Archie's saturation exponent, *n* | 1.92 | - |
| Connate water resistivity at 254 °F | 0.025 | ohm.m |
| Bound water resistivity at 254 °F | 0.01 | ohm.m |
| Water density | 1.00 | $g/cm^3$ |
| Water viscosity | 1.00 | cp |
| In-situ oil density | 0.75 | $g/cm^3$ |
| Oil viscosity | 1.00 | cp |
| Mud-filtrate density | 0.73 | $g/cm^3$ |
| Mud-filtrate viscosity | 1.50 | cp |
| Formation temperature | 254 | °F |
| Initial formation pressure | 3650 | psi |
| Mudcake reference permeability | 0.03 | md |
| Mudcake reference porosity | 0.30 | [ ] |
| Mud solid fraction | 0.06 | [ ] |
| Mudcake maximum thickness | 1.02 | cm |
| Mudcake compressibility exponent | 0.40 | [ ] |
| Mudcake exponent multiplier | 0.10 | [ ] |
| Wellbore radius | 15.24 | cm |
| Shale porosity | 0.09 | [ ] |
| Over-balance pressure | 100 | psi |
| Formation maximum invasion time | 1.00 | days |

**Table 3.8:** Central North Sea Sandstone, Field Example No. 2: Summary of calculated average petrophysical properties from conventional well-log interpretation.

| Variable | Value | Units |
|---|---|---|
| Thickness | 60 | ft |
| Absolute permeability, $k$ | 200 | md |
| Non-shale porosity, $\phi_s$ | 0.24 | [ ] |
| Total water saturation, $S_w$ | 1.00 | [ ] |
| Volumetric concentration of shale, $C_{sh}$ | 0.05 | [ ] |

**Table 3.9:** Central North Sea Sandstone, Field Example No. 2: Summary of estimated rock-fluid properties for the connate water-OBM filtrate fluid system and the corresponding uncertainty range for properties estimated after perturbing well logs with 5% random Gaussian additive noise.

| Parameter | Final Estimate | Uncertainty Range |
|---|---|---|
| $P_c^{\,0}$ [psi.darcy$^{1/2}$] | 9.0 | 9.00+ [-4.68,8.13] |
| $e_p$ [ ] | 4.0 | 4.00+ [-2.27,2.74] |
| $k^0_{rh}$ [ ] | 1.0 | 1.00+ [-0.15,0.00] |
| $e_h$ [ ] | 7.0 | 7.00+ [-1.24,1.92] |
| $k^0_{rw}$ [ ] | 0.8 | 0.80+ [-0.56,0.20] |
| $e_w$ [ ] | 3.0 | 3.00+ [-3.00,4.96] |
| $S_{wr}$ [ ] | 0.08 | 0.080+ [0.055,0.046] |
| $S_{hr}$ [ ] | 0.15 | 0.15±0.01 |
| $k$ [md] | 200 | 200+ [-140,640] |

**Table 3.10:** Central North Sea Sandstone, Field Example No. 2: Multi-layer total porosities obtained after matching well logs with their numerical simulations and the corresponding uncertainty range estimated after perturbing well logs with 5% random Gaussian additive noise.

| **Layer thickness [ft]** | $\phi_{t,\ estimated}$ | $\phi_{t,\ core}$ |
|---|---|---|
| 6.0 (shale) | 0.09 | - |
| 5.0 | 0.27±0.003 | 0.27 |
| 2.0 | 0.21±0.003 | 0.20 |
| 5.0 | 0.25±0.003 | 0.23 |
| 2.0 | 0.21±0.003 | 0.21 |
| 16.0 | 0.25±0.003 | 0.23 |
| 3.0 | 0.23±0.003 | 0.22 |
| 8.0 | 0.25±0.003 | 0.24 |
| 2.0 | 0.23±0.003 | 0.22 |
| 8.0 | 0.27±0.003 | 0.26 |
| 3.0 (shale) | 0.09 | - |

**Table 3.11:** Trinidad Shaly Sand, Field Example No. 3: Summary of assumed Archie's parameters and matrix, mud, fluid, and formation properties.

| Variable | Value | Units |
|---|---|---|
| Archie's tortuosity factor, *a* | 1.00 | - |
| Archie's cementation exponent, *m* | 1.72 | - |
| Archie's saturation exponent, *n* | 1.89 | - |
| Connate water resistivity at 133 °F | 0.07 | ohm.m |
| Bound water resistivity at 133 °F | 0.03 | ohm.m |
| Water density | 1.00 | $g/cm^3$ |
| Water viscosity | 1.00 | cp |
| In-situ hydrocarbon density | 0.65 | $g/cm^3$ |
| Hydrocarbon viscosity | 1.0 | cp |
| Mud-filtrate density | 0.8 | $g/cm^3$ |
| Mud-filtrate viscosity | 1.5 | cp |
| Formation temperature | 133 | °F |
| Initial formation pressure | 9800 | psi |
| Mudcake reference permeability | 0.03 | md |
| Mudcake reference porosity | 0.30 | [ ] |
| Mud solid fraction | 0.06 | [ ] |
| Mudcake maximum thickness | 1.02 | cm |
| Mudcake compressibility exponent | 0.40 | [ ] |
| Mudcake exponent multiplier | 0.10 | [ ] |
| Wellbore radius | 18.42 | cm |
| Shale porosity | 0.05 | [ ] |
| Over-balance pressure | 100 | psi |
| Formation maximum invasion time | 4.0 | days |

**Table 3.12:** Trinidad Shaly Sand, Field Example No. 3: Summary of calculated average petrophysical properties from conventional well-log interpretation.

| Variable | Value | Units |
|---|---|---|
| Thickness | 36 | ft |
| Absolute permeability, $k$ | 500 | md |
| Non-shale porosity, $\phi_s$ | 0.14 | [ ] |
| Total water saturation, $S_w$ | 1.00 | [ ] |
| Volumetric concentration of shale, $C_{sh}$ | 0.45 | [ ] |

**Table 3.13:** Trinidad Shaly Sand, Field Example No. 3: Summary of estimated rock-fluid properties for the connate water-OBM filtrate system.

| Parameter | Final Estimate | Uncertainty Range |
|---|---|---|
| $P_c^0$ [psi.darcy$^{1/2}$] | 27 | 27.0+[-4.3,17.4] |
| $e_p$ [ ] | 5.0 | 5.0+[-0.7,0.8] |
| $k^0_{rh}$ [ ] | 0.7 | 0.7+[-0.4,0.3] |
| $e_h$ [ ] | 2.5 | 2.5+[-0.8,1.1] |
| $k^0_{rw}$ [ ] | 0.6 | 0.6+[-0.5,0.4] |
| $e_w$ [ ] | 4.5 | 4.5+[-1.5,10.6] |
| $S_{wr}$ [ ] | 0.15 | 0.15±0.07 |
| $S_{hr}$ [ ] | 0.10 | 0.10±0.02 |

**Table 3.14:** Trinidad Shaly Sand, Field Example No. 3: Multi-layer petrophysical properties obtained after matching well logs with their numerical simulations and the corresponding uncertainty range for properties estimated after perturbing well logs with 5% random Gaussian additive noise.

| **Layer thickness [ft]** | ***k [md]*** | $\phi_s$ | $C_{sh}$ | $S_w$ |
|---|---|---|---|---|
| 3.0 (shale) | <0.001 | 0.00 | 1.00 | 1.00 |
| 5.0 | 700+[-590,130] | 0.10±0.002 | 0.38±0.009 | 0.75±0.015 |
| 6.0 | 700+[-580,140] | 0.11±0.002 | 0.32±0.008 | 0.78±0.015 |
| 2.0 | 700+[-590,170] | 0.125±0.003 | 0.28±0.008 | 0.65±0.012 |
| 3.0 | 400+[-330,410] | 0.115±0.002 | 0.28±0.008 | 0.85±0.014 |
| 3.0 | 400+[-340,500] | 0.155±0.003 | 0.28±0.008 | 0.85±0.012 |
| 1.0 | 3350+[-2220,6940] | 0.13±0.003 | 0.28±0.008 | 0.90±0.014 |
| 6.0 | 3350+[-2240,6500] | 0.14±0.003 | 0.28±0.008 | 0.90±0.014 |
| 3.0 | 400+[-350,490] | 0.155±0.003 | 0.28±0.008 | 0.90±0.014 |
| 3.0 | 0.001 | 0.05±0.002 | 0.52±0.010 | 0.90±0.030 |
| 2.0 (shale) | <0.001 | 0.00 | 1.00 | 1.00 |

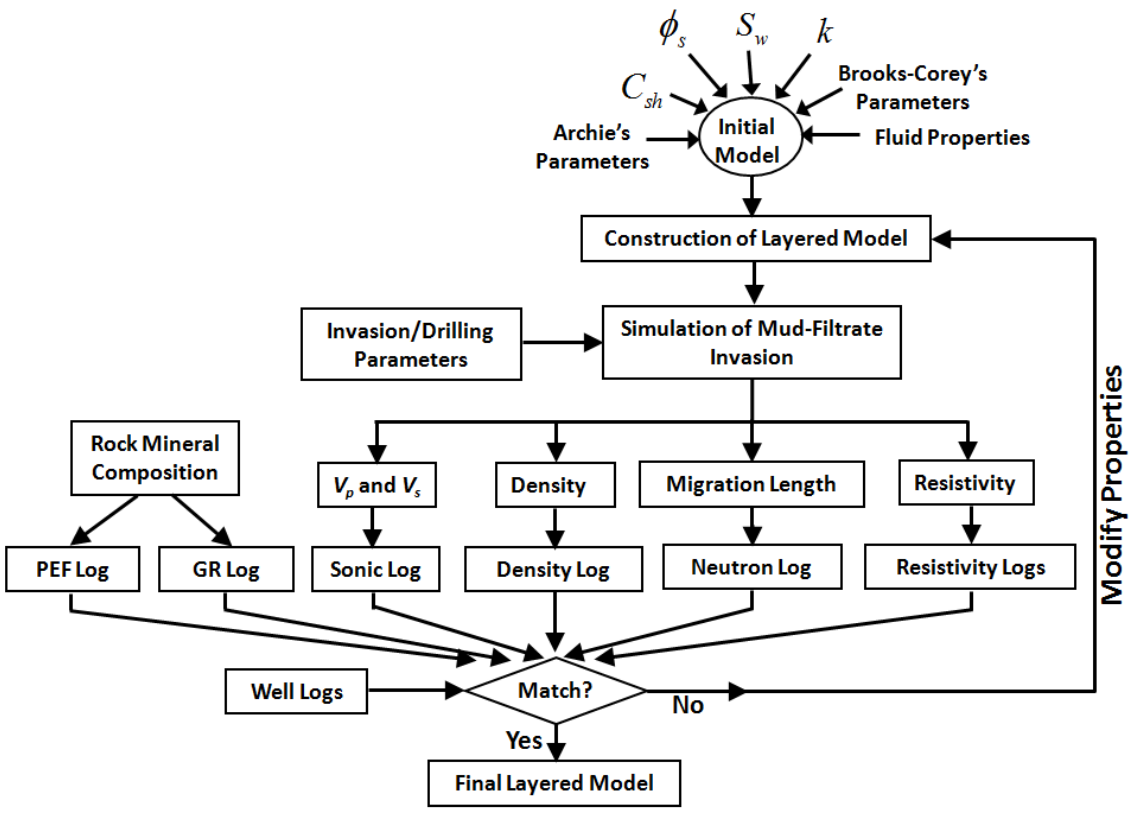


**Figure 3.1:** Iterative workflow adopted in this chapter to estimate unknown petrophysical properties. Nonlinear iterations are intended to progressively improve the agreement between measured and numerically simulated electrical resistivity and nuclear well logs from the adjustment of petrophysical properties.

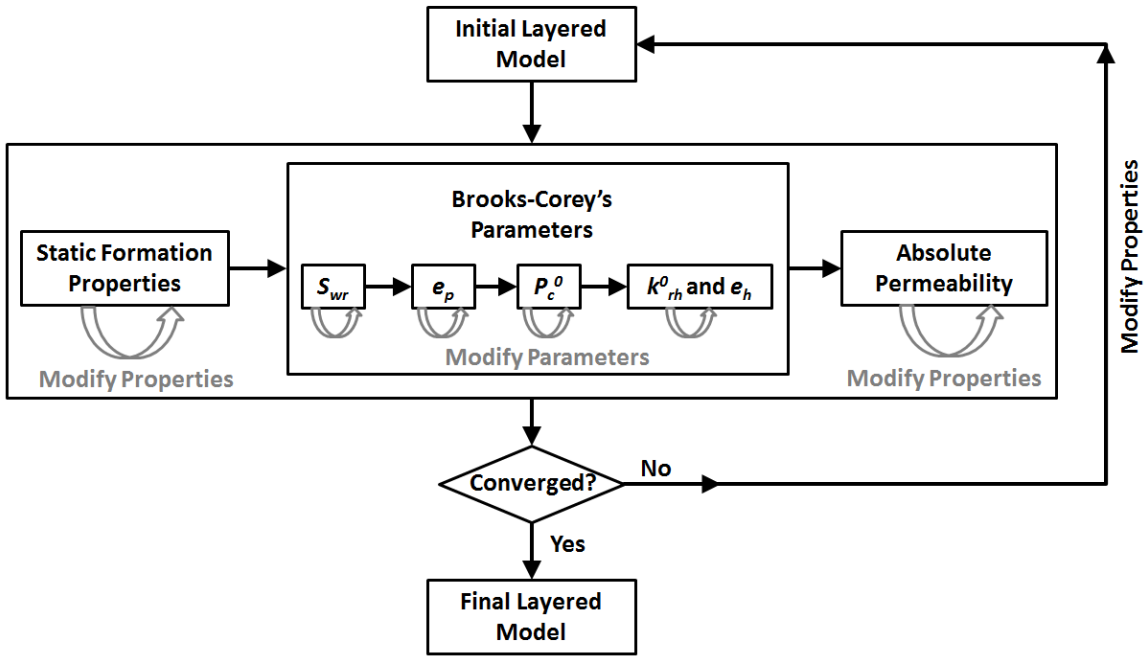


**Figure 3.2:** Iterative serial inversion loops adopted in this paper to estimate layer-by-layer static petrophysical properties (porosity, volumetric concentration of shale, and initial water saturation), Brooks-Corey's parameters, and absolute permeability. Each group of properties is updated in serial inversion loops, assuming that other groups are fixed. This process continues iteratively until convergence is achieved.

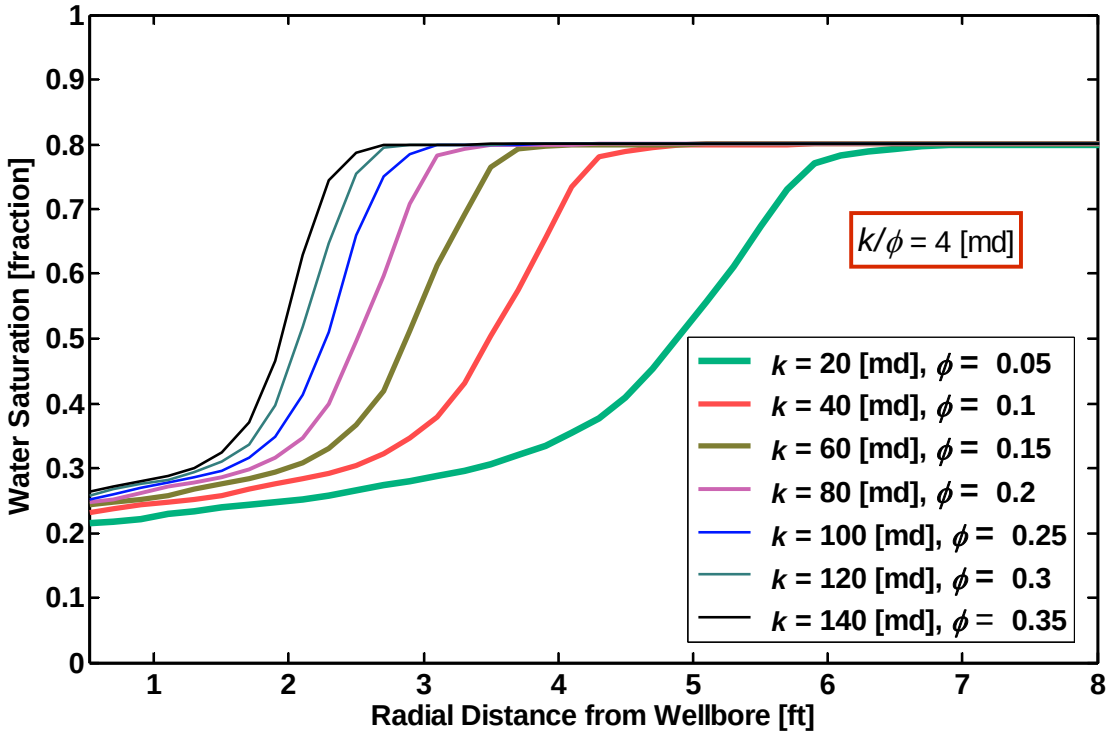


**Figure 3.3:** Synthetic Case No. 2: Sensitivity of the radial profile of water saturation to permeability and porosity. Curves describe radial distributions of water saturation resulting from OBM-filtrate invasion into different water-saturated rock types (defined with different values of porosity and permeability). The permeability-to-porosity ratio is kept constant at 4 md. Saturation-dependant capillary pressure and relative permeability are also kept constant. Porosity ranges from 0.05 to 0.35, while permeability varies between 20 and 140 md. Time of mud-filtrate invasion is three days in all cases. Table 3.3 lists the assumed drilling, invasion, and fluid properties.

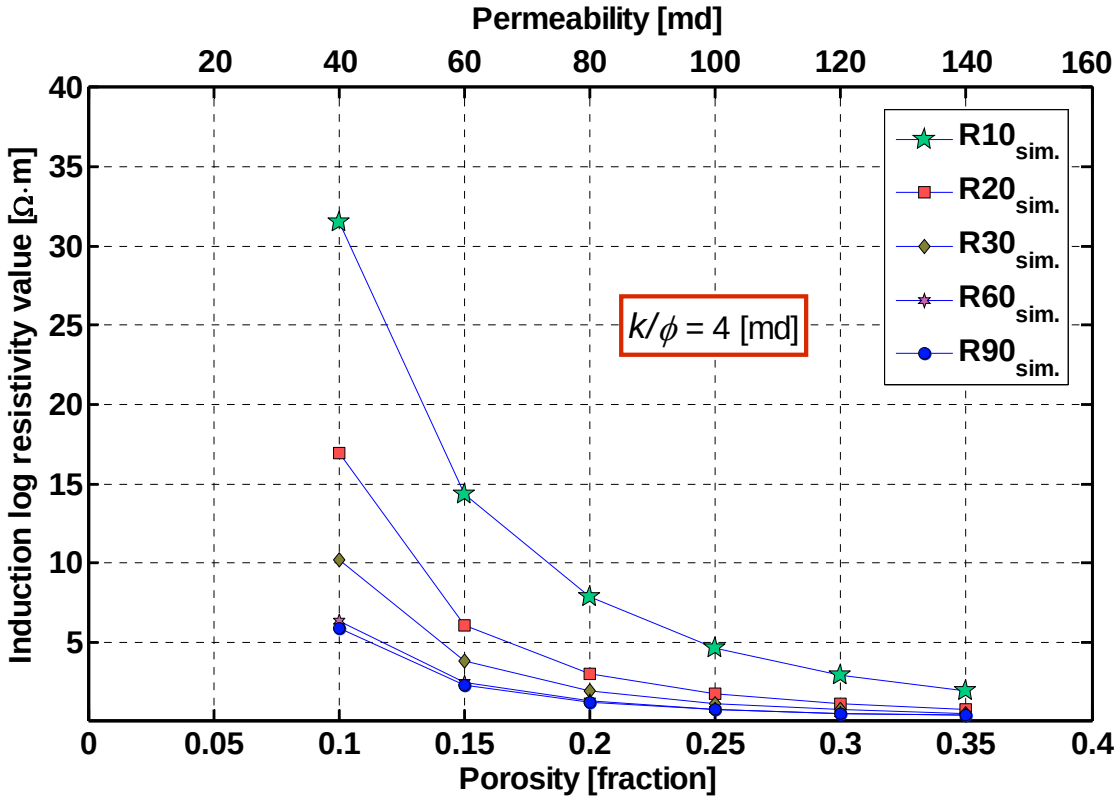


**Figure 3.4:** Synthetic Case No. 2: Sensitivity of induction apparent resistivity to permeability and porosity for the case of OBM-filtrate invasion into a water-saturated sand. Curves describe numerically simulated AIT apparent resistivities (five radial lengths of investigation: R10 (shallowest), R20, R30, R60, and R90 (deepest)). The permeability-to-porosity ratio is kept constant at 4 md. Porosity ranges from 0.10 to 0.35 while permeability varies between 40 and 140 md. Time of mud-filtrate invasion is 3 days in all cases. Table 3.3 lists the assumed drilling, invasion, and fluid properties.

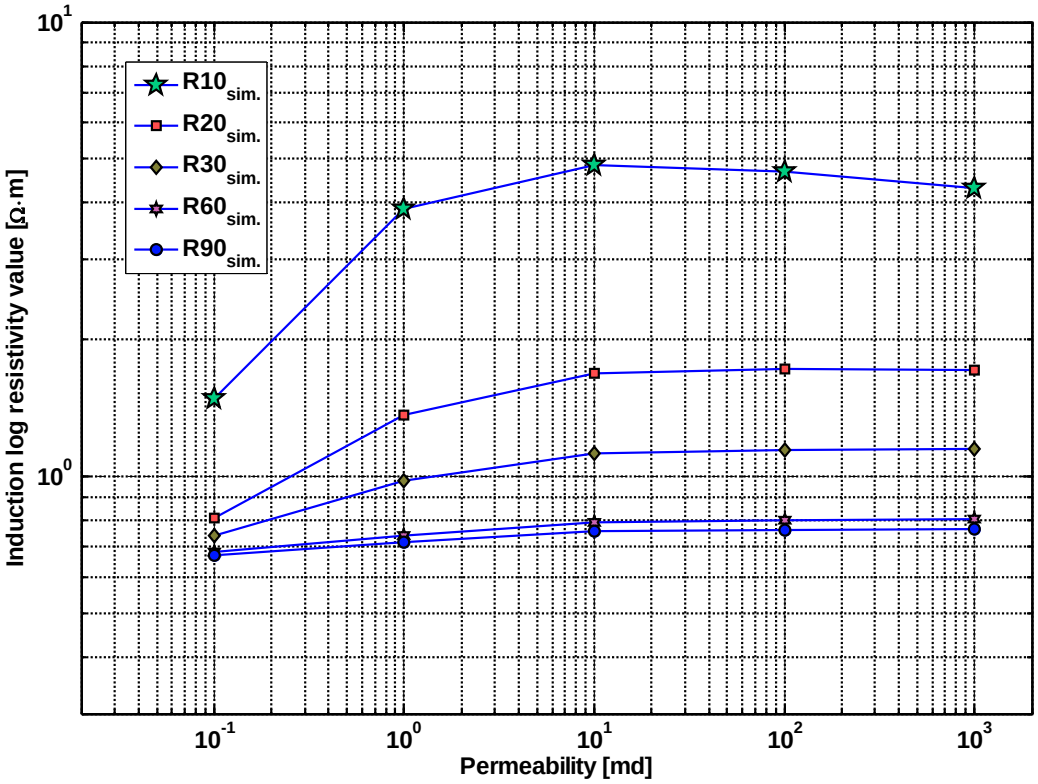


**Figure 3.5:** Synthetic Case No. 2: Sensitivity of induction apparent resistivities to permeability for the case of OBM-filtrate invasion into a water-saturated sand. Curves describe numerically simulated AIT apparent resistivities (five radial lengths of investigation: R10 (shallowest), R20, R30, R60, and R90 (deepest)). Permeability ranges from 0.1 to 1000 md while porosity is kept constant at 0.25. Time of mud-filtrate invasion is 3 days in all cases. Table 3.3 lists the assumed drilling, invasion, and fluid properties.

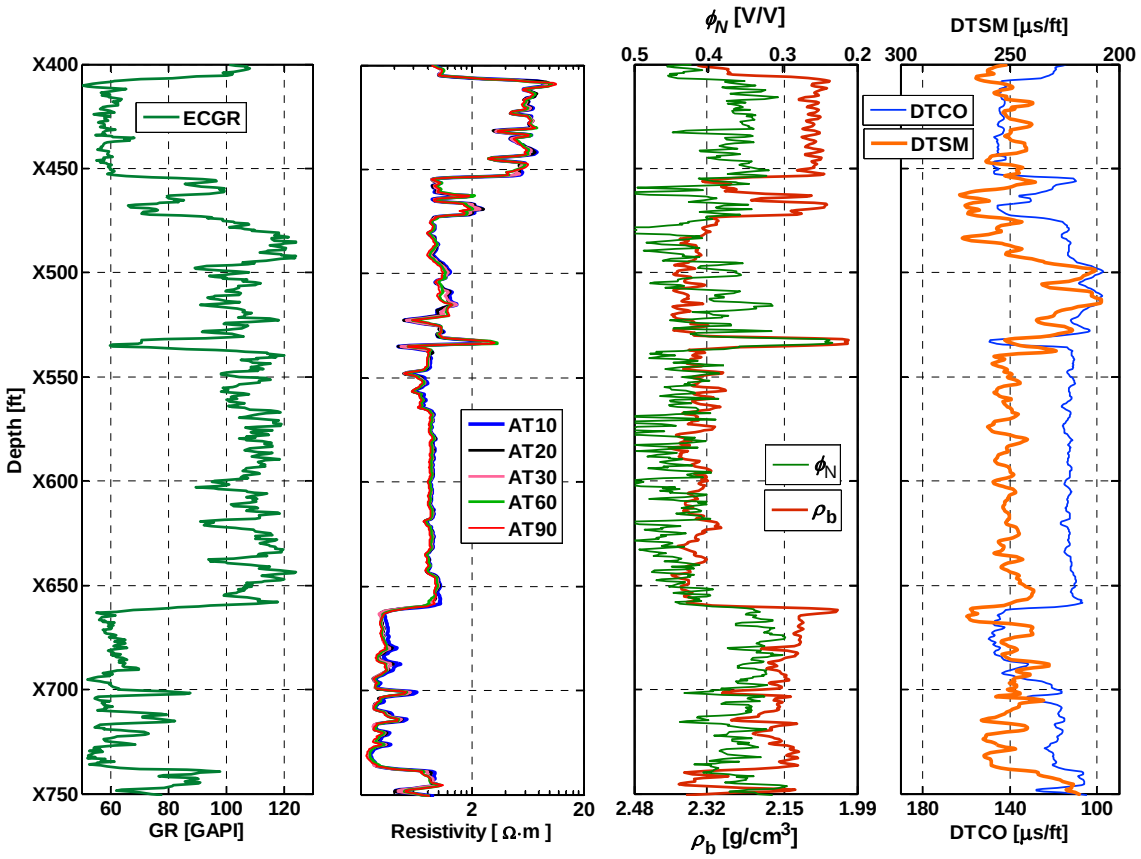


**Figure 3.6:** Gulf of Mexico, Field Example No. 1: Well logs in the hydrocarbon-bearing zone underlain by a water-bearing zone located in the depth interval of X660-X740 ft. Panels from left to right show gamma-ray, array-induction apparent electrical resistivity, neutron porosity and density, and shear- and compressional-wave slowness logs, respectively.

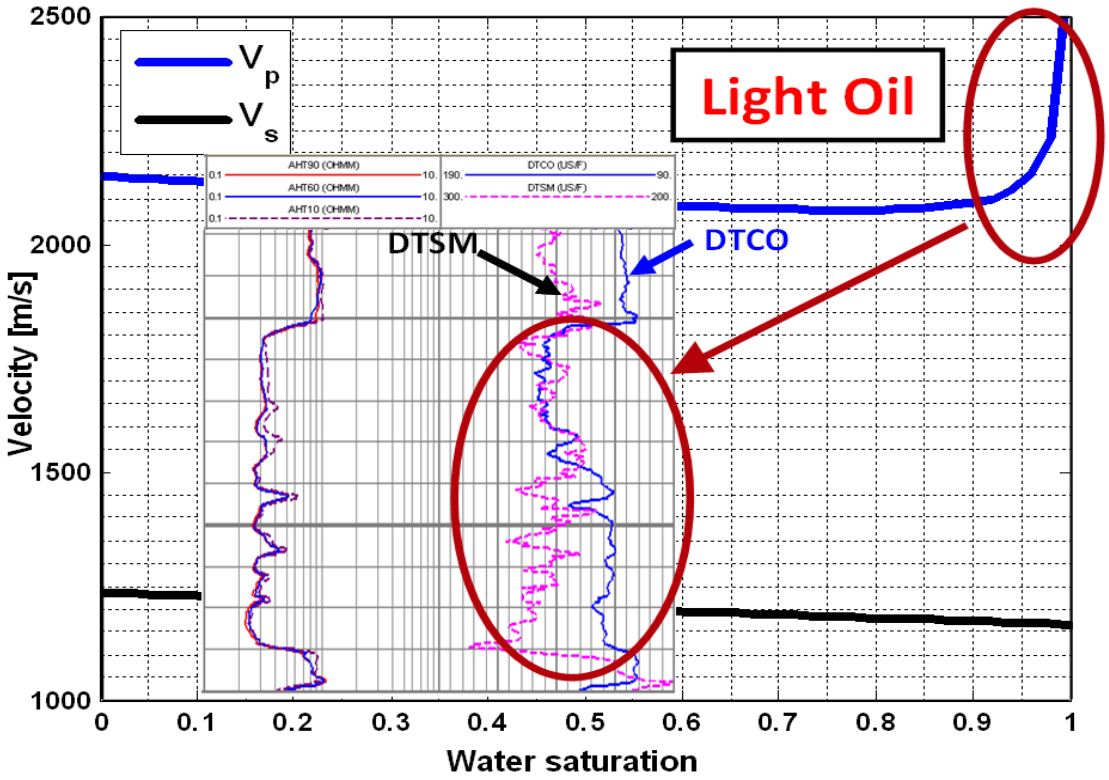


**Figure 3.7:** Synthetic Case No.1: Variations of compressional- and shear-wave velocity due to variations of water saturation in a rock formation containing light oil. Compressional-wave velocity exhibits a sudden increase when water saturation is higher than 0.90. This effect gives rise to a relatively large difference between compressional- and shear-wave sonic velocities in the water-saturated interval.

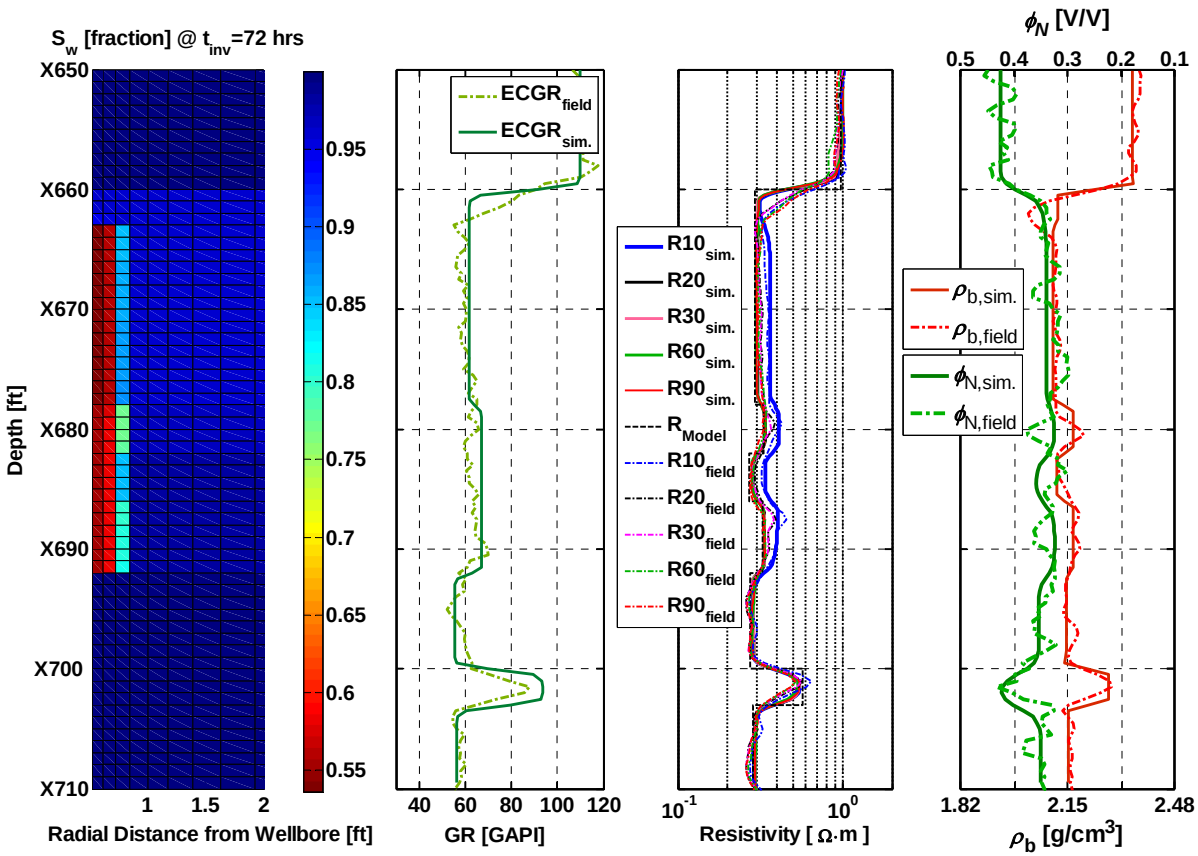


**Figure 3.8:** Deepwater Gulf of Mexico, Field Example No. 1: Comparison of numerically simulated (solid lines) and available (dashed lines) gamma-ray logs (second left-hand panel), array-induction apparent resistivity logs (third left-hand panel), and neutron porosity (sandstone porosity) and density logs (right-hand panel) for the multi-layer model in the water zone. The left-hand panel shows the spatial distribution (radial and vertical directions) of water saturation. Time of mud-filtrate invasion ($t_{inv}$) is three days. Layer-by-layer petrophysical properties were estimated by matching field logs with their numerical simulations (Table 3.6).

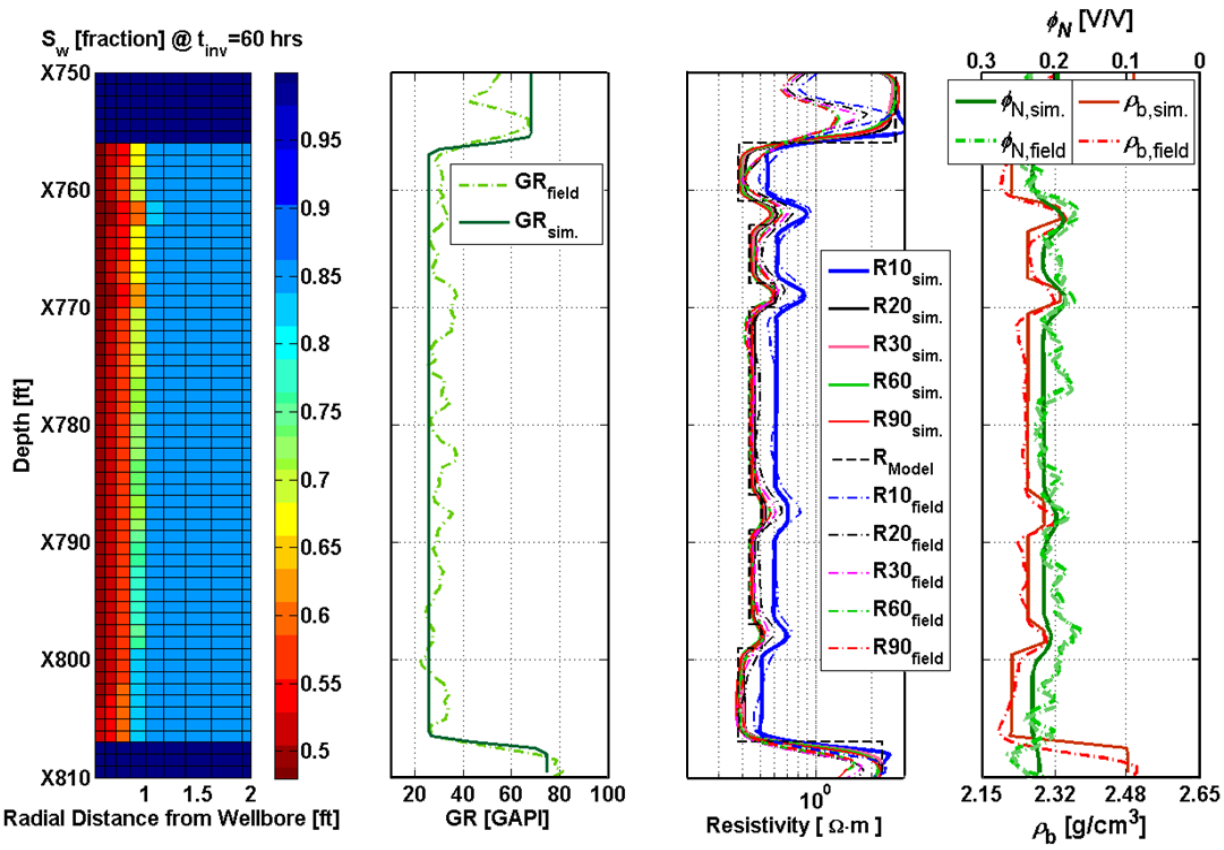


**Figure 3.9:** Central North Sea Sandstone, Field Example No. 2: Comparison of numerically simulated (solid lines) and available (dashed lines) gamma-ray logs (second panel from left), array-induction apparent resistivity logs (third panel from left), and neutron porosity (sandstone porosity) and density logs (right-hand panel) for the multi-layer model in the water zone. The left-hand panel shows the spatial distribution (radial and vertical directions) of water saturation. Time of mud-filtrate invasion ($t_{inv}$) is one day. Layer-by-layer petrophysical properties were estimated by matching field logs with their numerical simulations (Table 3.10).

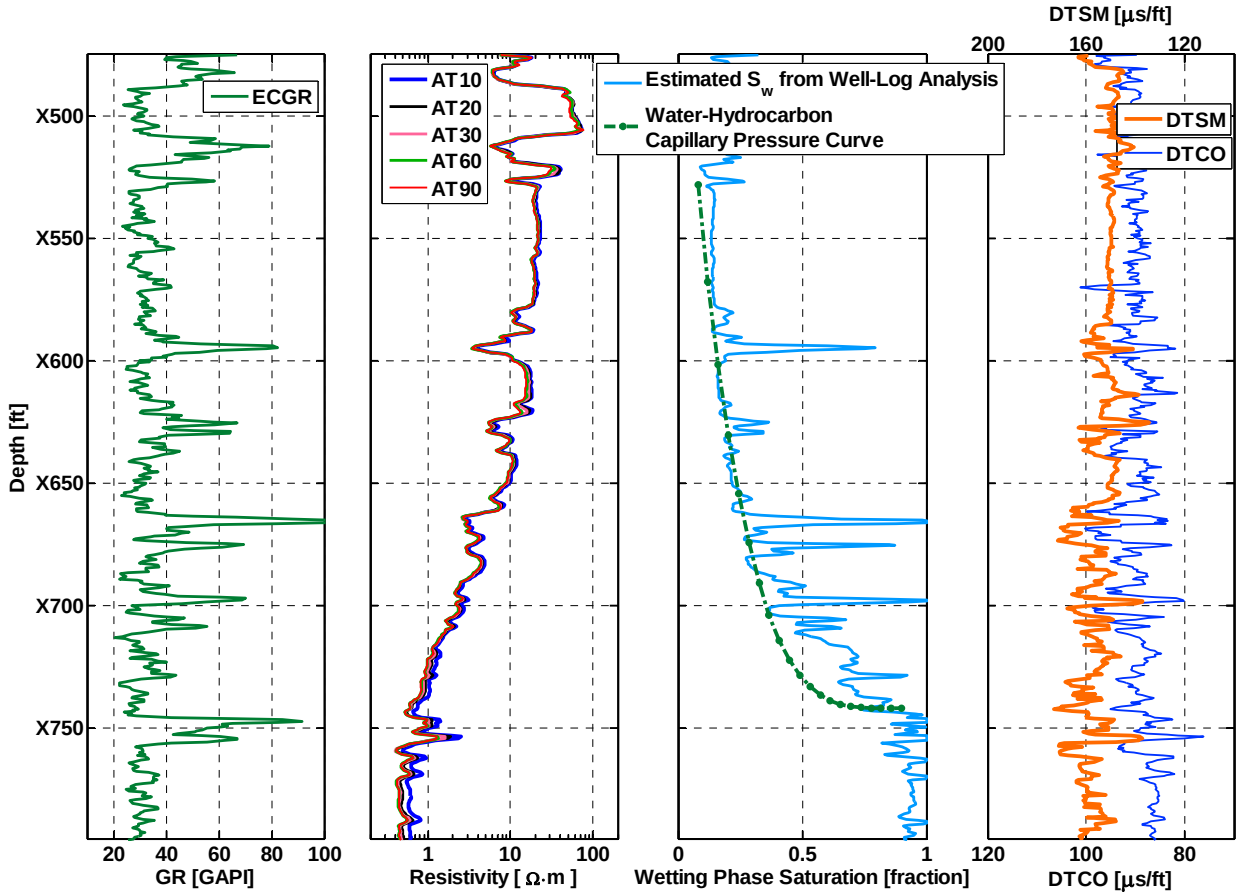


**Figure 3.10:** Central North Sea Sandstone, Field Example No. 2: Comparison of the calculated water-oil capillary pressure curve against the vertical variation of water saturation obtained from petrophysical interpretation of well logs. The capillary pressure curve was obtained by matching field logs with numerical simulations. First and second left-hand panels show gamma-ray and array-induction apparent electrical resistivity logs, respectively. The right-hand panel shows shear- and compressional-wave slowness logs.

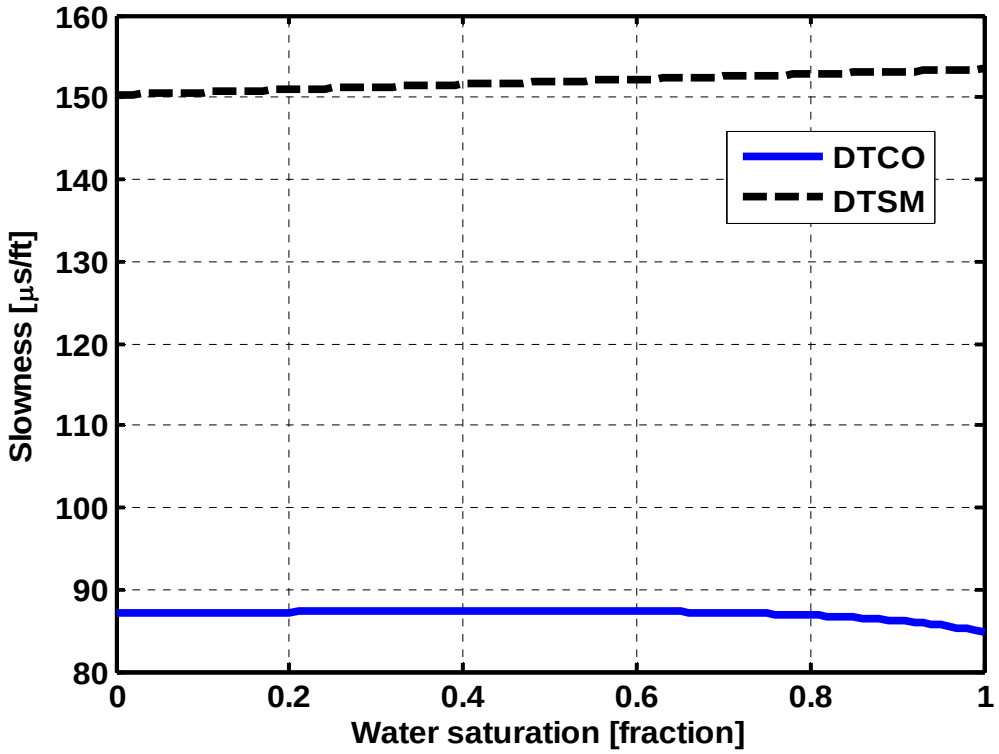


**Figure 3.11:** Central North Sea Sandstone, Field Example No. 2: Variations of compressional- and shear-wave slowness due to variations of water saturation in a rock formation containing oil. The slight decrease of compressional-wave slowness and the slight increase of shear-wave slowness in both water- and hydrocarbon-bearing zones shown above are in agreement with measured logs (Figure 3.9).

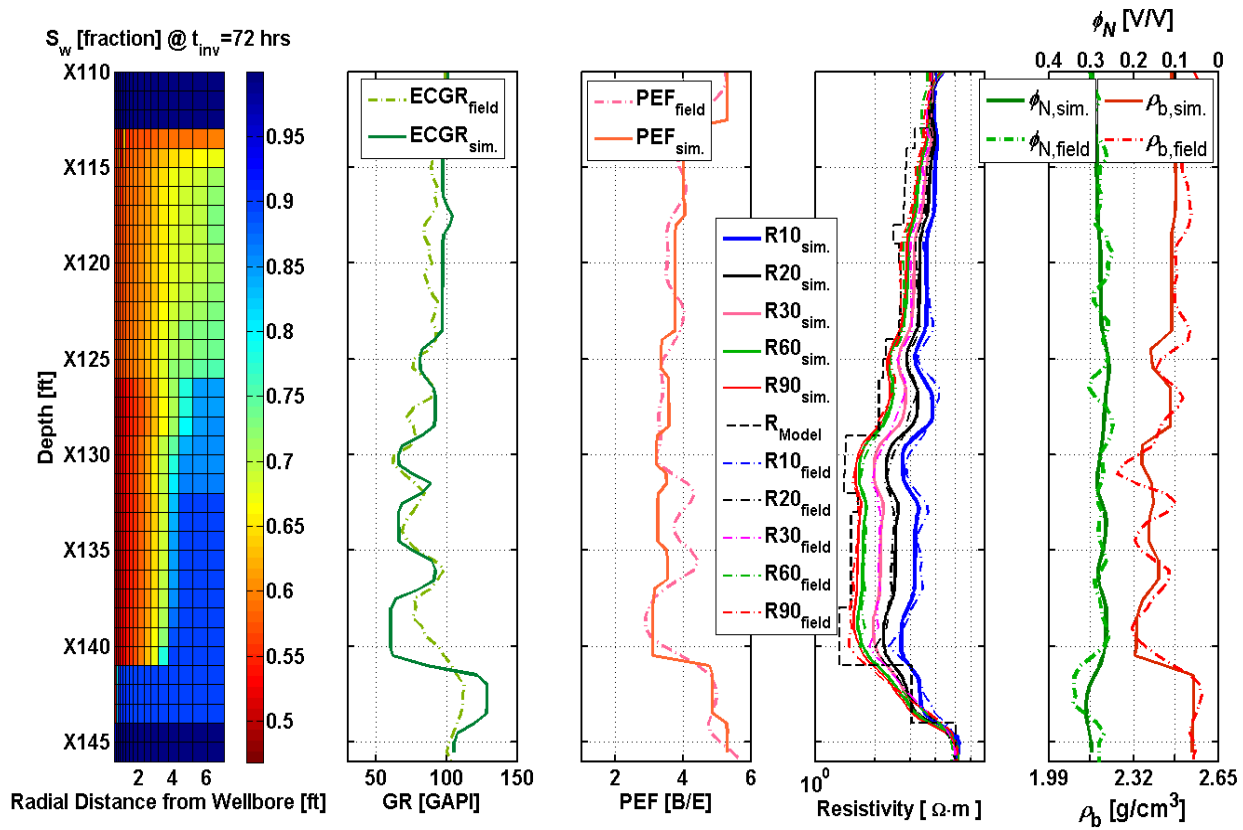


**Figure 3.12:** Trinidad Shaly Sand, Field Example No. 3: Comparison of numerically simulated (solid lines) and available (dashed lines) gamma-ray logs (second panel from left), array-induction apparent resistivity logs (third panel from left), and neutron porosity (sandstone porosity) and density logs (right-hand panel) for the multi-layer model in the water zone. The left-hand panel shows the spatial distribution (radial and vertical directions) of water saturation. Time of mud-filtrate invasion ($t_{inv}$) is three days. Petrophysical properties were obtained by matching field logs with their numerical simulations (Table 3.14).

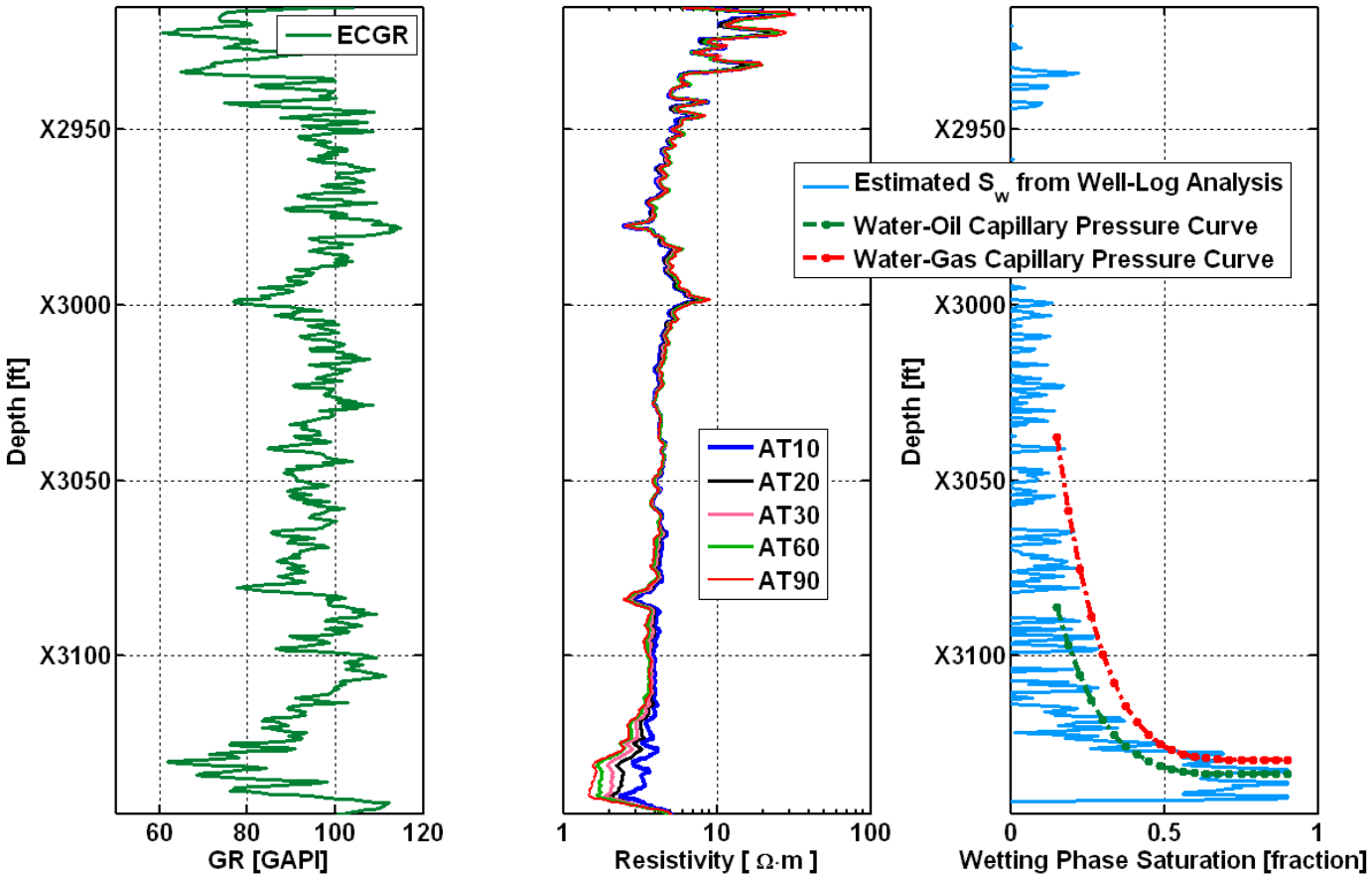


**Figure 3.13:** Trinidad Shaly Sand, Field Example No. 3: Comparison of calculated water-oil capillary pressure curve and corresponding water-gas capillary pressure curve against the vertical variation of water saturation obtained from petrophysical interpretation of well logs (right-hand panel). Capillary pressure curves were obtained by matching field logs with their numerical simulations. Left-hand and center panels show gamma-ray and array-induction apparent resistivity logs, respectively.

# Chapter 4: Improved Estimation of Mineral and Fluid Volumetric Concentrations in Thinly-Bedded and Invaded Formations

Calculation of mineral and fluid volumetric concentrations from well logs is one of the most important outcomes of formation evaluation. Conventional estimation methods assume linear or quasi-linear relationships between volumetric concentrations of solid/fluid constituents and well logs. Experience shows, however, that the relationship between neutron porosity logs and mineral concentrations is generally nonlinear. More importantly, linear estimation methods do not explicitly account for shoulder-bed and/or invasion effects on well logs nor do they account for differences in the volume of investigation of the measurements involved in the estimation. The latter deficiencies of linear estimation methods can cause appreciable errors in the calculation of porosity and hydrocarbon pore volume.

This chapter introduces three nonlinear inversion methods for assessment of porosity, hydrocarbon saturation, volumetric concentration of shale, and volumetric concentrations of mineral constituents. All three of these methods account for the nonlinear relationship between well logs, mineral concentrations, and fluid saturations. The first method accounts for the combined effects of invasion and shoulder beds on well logs. The second method also accounts for shoulder-bed effects, but is developed for cases where mud-filtrate invasion is negligible or very deep. Finally, the third method is designed specifically for analysis of thick beds where mud-filtrate invasion is negligible or very deep.

Numerical synthetic examples of application indicate that nonlinear inversion is a reliable method to quantify complex mineral and fluid compositions in the presence of thin beds and invasion. Comparison of results against those obtained with conventional

multi-mineral estimation methods confirms the advantage of nonlinear inversion in quantifying thinly-bedded invaded formations with variable and complex lithology such as carbonates.

## 4.1 INTRODUCTION

Lithology identification and quantification have been of great interest to formation-evaluation specialists for decades. Core analysis aided by geological logs is a common approach to diagnose lithology. Earlier detection and quantification methods based on well logs included the use of density-sonic, density-photoelectric factor, neutron-sonic, neutron-density, and Matrix Identification (MID) cross-plots (Clavier and Rust, 1976; Schlumberger, 2005).

Estimation of porosity and fluid saturations is the cornerstone in formation evaluation as it affects the calculation of hydrocarbon pore volume. In complex lithologies, reliable assessments of volumetric mineral concentrations from well logs, core data, and geological logs are necessary for the accurate estimation of porosity and hydrocarbon saturation. Practically all commercial software available for detection and estimation of mineral volumetric concentrations assume linear or quasi-linear relationships between formation properties and well logs and do not account for shoulder-bed and/or invasion effects on the estimation. Such conditions often contribute to erroneous estimations of porosity and hydrocarbon pore volume, especially in thinly-bedded and mixed carbonate sequences. This chapter introduces new nonlinear inversion methods to quantify rock mineral and fluid composition based on the systematic and combined use of nuclear and electrical resistivity logs.

Neutron-capture spectroscopy measurements are the basis of yet another approach to quantify complex mineralogy. Volumetric concentrations of minerals and clays are

estimated from elemental spectroscopy measurements (Herron and Herron, 1996; Herron et al., 2002). This method can be applied to both open- and cased-hole environments. Herron et al. (2002) integrated neutron-capture spectroscopy measurements with electrical resistivity, neutron porosity, and density logs to quantify porosity, water saturation, and irreducible water saturation, and to diagnose presence of gas.

Numerical methods have also been developed to diagnose and quantify lithofacies based on artificial neural networks, fuzzy logic, and neuro-fuzzy models (Cuddy, 2000; Gonçalves et al., 1995). These methods require substantial training with core measurements to warrant reliable and accurate estimations and can easily fail in the presence of complex mineralogy and thinly-bedded rock sequences.

Linear inversion of well logs is the most common numerical method used to quantify lithology in the presence of multi-mineral lithologies (Doveton, 1994; Mayer and Sibbit, 1980; Quirein et al., 1986). The implicit assumption of linear estimation methods is that measurements such as density, photoelectric factor (PEF), neutron porosity, and sonic transient time are linear functions of the volumetric concentrations of the assumed rock mineral and fluid constituents. Volumetric concentrations of mineral and fluid constituents are then obtained depth-by-depth by minimizing the difference between well logs and their linear prediction, formally expressed as

$$\min \left\| \mathbf{A} \bullet \mathbf{x} - \mathbf{b} \right\|_2^2, \tag{4.1}$$

subject to

$$0 \le x_i \le 1, \tag{4.2}$$

and

$$\sum_{i=1}^{n_c+2} x_i = 1, \tag{4.3}$$

where **x** is the *n*-size vector of volumetric mineral and fluid concentrations, given by

$$\mathbf{x} = \left[ C_1, C_2, ..., C_{n_c}, C_{sh}, \phi_s \right]^T, \tag{4.4}$$

Where "*T*" indicates transposition, $C_i$ is volumetric concentration of the assumed mineral constituents, $C_{sh}$ is volumetric concentration of shale, $\phi_s$ is non-shale porosity, and $n_c$ is the pre-defined number of mineral constituents. In Equation (4.1), matrix **A** is expressed as

$$\mathbf{A} = \begin{bmatrix} \rho_{b,1} & \rho_{b,2} & .... & \rho_{b,n_c} & \rho_{b,sh} & \rho_{fluid} \\ \phi_{N,1} & \phi_{N,2} & .... & \phi_{N,n_c} & \phi_{N,sh} & \phi_{N,fluid} \\ \Delta t_1 & \Delta t_2 & .... & \Delta t_{n_c} & \Delta t_{sh} & \Delta t_{fluid} \\ U_1 & U_2 & .... & U_{n_c} & U_{sh} & U_{fluid} \end{bmatrix}, \tag{4.5}$$

and vector **b** as

$$\mathbf{b} = \left[ \rho_b \quad \phi_N \quad \Delta t \quad U \right]^T, \tag{4.6}$$

where **b** is the vector of available well-log measurements, $\phi_N$ is neutron porosity, $\rho_b$ is bulk density, $U$ is volumetric photoelectric factor, and $\Delta t$ is sonic interval transient time. The entries of matrix **A** above are defined as well-log measurements acquired in rocks or fluids with "pure" elemental compositions.

It is emphasized that the above constrained linear estimation method presupposes knowledge of the number and type of mineral and fluid components prior to performing the estimation. Moreover, fluid saturations affect the assessment of porosity and volumetric concentrations of mineral constituents. Resistivity measurements are used in combination with the described linear estimation method to assess fluid saturations based on the estimated porosity and a pre-defined saturation-porosity-resistivity model. Saturation estimates obtained this way are updated iteratively using resistivity measurements and entered into matrix **A** (Equation (4.5)) to define fluid properties.

Doveton (1994) introduced a robust linear inversion algorithm to estimate unknown properties based on Equations (4.1) through (4.6). In most practical cases of lithology quantification, the number of unknowns (i.e., minerals and petrophysical properties such as porosity and water saturation) included in Equation (4.1) is greater than the number of data (i.e., the number of well logs). The latter condition gives rise to under-determined estimation whose solution requires outside (a-priori) constraints and/or subjective selections of relationships among unknown properties. Another complication of linear inversion methods is the lack of reliable well-log responses across "pure" lithologies and fluids, which are necessary to define the entries of matrix **A** in Equation (4.5). Well-log responses across "pure" lithologies and fluids cannot be drawn from tabulated values, as some of them may vary according to local conditions of sedimentation and diagenesis. Users of linear inversion methods commonly define these entries by trial and error, albeit usually guided by geological logs and core measurements. However, it is commonly the case that small perturbations in the entries of matrix **A** lead to sizable perturbations in the calculated mineral volumetric concentrations and porosity. Experience is necessary to parse petrophysical acceptable solutions from those that are not.

Several commercial software packages use the above method to evaluate volumetric concentrations of mineral constituents, porosity, and water saturation. Mayer and Sibbit (1980) introduced perhaps the first commercial software for linearized inversion. They also incorporated water saturation into the inversion to estimate fluid saturations together with volumetric concentrations of mineral constituents. Other commercial methods (and software) iteratively estimate mineral concentrations using the linear inversion method given by Equation (4.1) in sequence with the calculation of fluid saturations until reaching convergence between the two calculations. Quirein et al. (1986) suggested a probabilistic approach to estimate mineral and fluid concentrations based on Equation (4.1) that combined various saturation-porosity-resistivity models. Alternative approaches make use of statistical estimation methods to calculate volumetric mineral and fluid concentrations together with their uncertainty (Busch et al., 1987).

Even though constrained linear inversion is a fast and efficient method that yields accurate estimations in many simple situations, it can fail in the presence of complex mineral compositions. A significant drawback of linear inversion methods is that the assumption of a linear relationship between properties and mineral volumetric concentrations is usually invalid, especially in the presence of light hydrocarbon and clay. For instance, neutron porosity measurements are usually corrected for presence of dispersed shale via the formula (Thomas and Stieber, 1975)

$$\phi_N^{sh} = \phi_N - C_{sh}\phi_{N,sh}\,, \tag{4.7}$$

where $\phi_{N,sh}$ is neutron porosity in a "pure" shale zone and $\phi_N^{sh}$ is neutron porosity corrected for shale. Equation (4.7) is valid with errors lower than 20% in water-saturated zones. The error increases, however, for decreasing values of shale porosity and non-

shale porosity. Furthermore, Equation (4.7) is no longer valid in saline formations or in the presence of halite. In such situations, it is necessary to correct neutron porosity for formation salinity before applying the linear shale-correction equation. Although errors associated with Equation (4.7) might be acceptable in water-bearing formations, the linear correction usually fails in the presence of gas, where the equation needs to consider both neutron porosity and density measurements in the nonlinear form given by Gaymard and Poupon, (1968):

$$\phi_s = \sqrt{\frac{\left(\phi_N^{sh}\right)^2 + \left(\phi_D^{sh}\right)^2}{2}}, \tag{4.8}$$

where $\phi_D{}^{sh}$ is density porosity corrected for shale, expressed as

$$\phi_D^{sh} = \phi_D - C_{sh}\phi_{D,sh}. \tag{4.9}$$

$\phi_{D,sh}$ is density porosity in a "pure" shale zone and $\phi_D$ is density porosity. Equation (4.8) quantifies non-shale porosity with errors lower than 3% within the shale-porosity range of 0.00 to 0.20. The assumption of linear relationship between non-shale porosity and volumetric concentration of shale is therefore no longer valid.

Another important remark concerning the linear estimation method is that the sonic model commonly assumed in Equations (4.1) through (4.6) is Wyllie's slowness mixing formula (Wyllie et al., 1956). This formula is not accurate in soft and unconsolidated sediments, organic shale, and fractured formations, to name a few but important cases. Specialized effective medium theories need to be invoked to reliably relate sonic transient times with fluids and mineral compositions (Mavko et al., 2009).

It is also known that linear inversion methods can break down under conditions such as presence of iron in the rock matrix or in gas-bearing formations. More

importantly, linear inversion methods are implemented depth-by-depth and hence do not explicitly account for shoulder-bed effects on the logs included in the estimation. Finally, the calculation tacitly neglects mud-filtrate invasion effects on well logs.

Joint inversion of electrical resistivity, gamma-ray (GR), and density logs was previously implemented to improve the petrophysical assessment of thinly-bedded siliciclastic formations (Liu et. al, 2007; Sanchez-Ramirez et. al, 2009). The task remaining is to implement similar methods and to include additional well logs in the estimation of volumetric mineral/fluid concentrations in carbonate and complex mixed sedimentary sequences that include thin beds and are subject to invasion.

The objective in this chapter is to introduce, cross-validate, and benchmark new, automatic nonlinear methods to estimate volumetric mineral/fluid concentrations from well logs in the presence of complex matrix composition, mud-filtrate invasion, and bed-boundary effects. These new methods are possible because of the availability of newly developed algorithms for the rapid numerical simulation of nuclear logs (Mendoza et al., 2010). Such well-log simulation methods explicitly quantify the generally nonlinear relationship between rock/fluid properties and nuclear logs, thereby accounting for the volume of investigation of the measurements involved in the estimation as well as presence of shoulder beds and invasion.

We introduce three methods for the assessment of petrophysical and compositional properties of hydrocarbon-bearing formations exhibiting complex lithology. The first method takes into account the effects of radial variations of fluid saturation and salt concentration on well logs due to mud-filtrate invasion. It also accounts for shoulder-bed effects on well logs and nonlinear deterministic relationships between volumetric concentrations of mineral/fluid constituents. This method assumes a multi-layer reservoir model constructed with the detection of bed boundaries from

density, PEF, and GR logs. Subsequently, nonlinear inversion is initialized with a multi-layer petrophysical model that consists of volumetric mineral/fluid concentrations combined with resistivity-saturation equations. Nonlinear inversion combined with numerical simulation of mud-filtrate invasion minimizes the difference between well logs and their numerical simulations across the depth zone of interest by making progressive adjustments to fluid and mineral concentrations in each layer.

The second method quantifies petrophysical/compositional properties in thinly-bedded formations exhibiting complex lithology, where the effect of mud-filtrate invasion is negligible. This method estimates bed physical properties (layer-by-layer density, neutron migration length, PEF, conductivity/resistivity, and uranium (Ur), thorium (Th), and potassium (K) concentrations) based on the separate inversion of well logs. Separate linear inversion of density, PEF, and GR-spectroscopy logs is implemented with a recently introduced method for fast modeling of nuclear logs, which uses pre-calculated Flux Sensitivity Functions (FSFs). The final step of the second method implements joint inversion of estimated properties to assess mineral and fluid concentrations.

The third method estimates petrophysical/compositional properties in formations with complex lithology and thick beds, where the effect of mud-filtrate invasion is negligible. We quantify the nonlinear deterministic relationship between volumetric concentrations of mineral/fluid constituents and well logs via Schlumberger's commercial software, SNUPAR (McKeon and Scott, 1989) to assess neutron migration length and PEF. Chemical formulae and volumetric/weight concentrations of mineral/fluid constituents are input to SNUPAR. Similar to conventional petrophysical/compositional interpretation, however, this method does not account for either shoulder-bed or mud-filtrate invasion effects on well logs.

The introduction of three nonlinear inversion methods is necessary to perform estimation in an efficient and stable way; the choice of method depends on the assumed degree of complexity in the formations under consideration. In the following sections, we describe and successfully implement the three nonlinear inversion methods. Examples of application are described for three challenging synthetic formations constructed to replicate actual field examples. Chapter 5 describes the application of the inversion methods to carbonate field examples.

## 4.2 METHOD

Inputs to the three estimation methods introduced in this chapter are conventional well logs such as density, neutron porosity, PEF, GR/GR-spectroscopy, and electrical resistivity/conductivity logs. The possibility also exists of considering subsets of these logs. For instance, one could ignore PEF in cases where it is not reliable due to presence of barite in the mud. The methods in this chapter are described for estimating volumetric concentrations of mineral constituents. However, they are reliable in assessing weight concentrations of mineral constituents as well.

Depending on the number of minerals in the formation, the number of equality constraints, and the number of reliable well logs, the problem could be even-, over-, or under-determined. Most well logging problems involve under-determined estimations wherein the number of unknowns is greater than the number of logs and equality constraints, whereby, there are more than one set of solutions which satisfy both well logs and petrophysical constraints. In under-determined estimations, the choice of initial guess is important. The following sections detail the assumed rock model, the three nonlinear interpretation methods, and the strategies adopted for initial guess construction. **Figure 4.1** is a flowchart describing the processes of numerical simulation of well logs

and nonlinear inversion to estimate multi-layer petrophysical properties and volumetric/weight concentrations of mineral constituents.

### 4.2.1 Rock Model

The rock model consists of different mineral components in the matrix, shale, and non-shale porosity that includes water and hydrocarbon. Water in non-shale porosity can be movable or irreducible. Hydrocarbon may also be movable or residual. Shale is assumed to be of the dispersed type (Poupon et al., 1970). Even though the specific application considered in this chapter assumes dispersed shale, the formation can be easily modified for the case of laminated shale.

Wet shale consists of clay and silt, which includes clay-bound water. The relationship among the volumetric concentrations of all matrix components is expressed as (Mezzatesta et al., 2006)

$$\sum_{i=1}^{n_c} C_i + C_{sh} + \phi_s = 1, \tag{4.10}$$

with volumetric concentration of shale is defined as

$$C_{sh} = \frac{V_{sh}}{V_r}, \tag{4.11}$$

where $V_r$ is rock volume including fluids and $V_{sh}$ is volume of wet shale. We calculate bulk density ($\rho_b$) based on volumetric concentrations of mineral components via the equation

$$\rho_b = \sum_{i=1}^{n_c} \left( C_i \, \rho_i \right) + \rho_f \phi_s + \rho_{sh} C_{sh}, \tag{4.12}$$

where $\rho_i$ is density of the corresponding mineral, $\rho_f$ is fluid density, and $\rho_{sh}$ is shale density. Fluid density and shale density are given by

$$\rho_f = S_w \rho_w + \left(1 - S_w\right) \rho_h, \tag{4.13}$$

and

$$\rho_{sh} = \rho_{silt} \left(1 - C_{cl} - \phi_{sh}\right) + \rho_{cl} C_{cl} + \rho_w \phi_{sh}, \tag{4.14}$$

respectively, where $S_w$ is water saturation and the output of fluid-flow simulation at each numerical grid (the same numerical grid used for simulation of mud-filtrate invasion), $\phi_{sh}$ is shale porosity, $\rho_w$ is water density, $\rho_h$ is hydrocarbon density, $\rho_{cl}$ is clay density, $\rho_{silt}$ is silt density, and $C_{cl}$ is volumetric concentration of clay, defined as

$$C_{cl} = \frac{V_{cl}}{V_{sh}}, \tag{4.15}$$

where $V_{cl}$ is clay volume.

A reliable mixing law can define the physical relationship between compressional- and shear-wave sonic logs and mineral concentrations and their dry bulk moduli (compressional and shear), as well as the corresponding effect of fluid components and their saturations (Mavko et al., 2009). Sonic measurements can then be included in the inversion.

### 4.2.2 Method No. 1: Nonlinear Multi-Layer Joint Inversion of Well Logs in the Presence of Mud-Filtrate Invasion

This method accounts for the effects of mud-filtrate invasion and shoulder beds on well logs. After data quality control, applying necessary corrections for depth shift, defining bed boundaries, and constructing the multi-layer reservoir model, the first step of nonlinear inversion is the construction of an initial guess of layer-by-layer petrophysical properties. Such initial guess can be selected from: (a) results obtained from conventional/linear multi-mineral solvers, (b) core/XRD (X-Ray Diffraction) data, or (c) results obtained from depth-by-depth nonlinear inversion of well logs (Method No. 3).

Nonlinear inversion is performed by minimizing the quadratic cost function

$$\mathbf{C}(\mathbf{x}) = \left\| \mathbf{W_d} \bullet \left[ \mathbf{d}(\mathbf{x}) - \mathbf{d_m} \right] \right\|_2^2 + \alpha^2 \left\| \mathbf{x} \right\|_2^2, \tag{4.16}$$

subject to

$$0 \le x_j \le 1, \tag{4.17}$$

and

$$\sum_{i=1}^{n_c} C_i + C_{sh} + \phi_s = 1, \tag{4.18}$$

where $\mathbf{W_d}$ is a data weighting matrix, $\mathbf{d}$ is the vector of numerically simulated logs, $\mathbf{d}_m$ is the vector of available well logs, $\alpha$ is a regularization (stabilization) parameter, and $\mathbf{x}$ is the vector of petrophysical properties and volumetric concentrations of mineral constituents of all beds, given by

$$\mathbf{x} = \left[ \mathbf{x_1}, \mathbf{x_2}, ..., \mathbf{x}_{n_b} \right]^T, \tag{4.19}$$

where the superscript "*T*" indicates transposition and $\mathbf{x_i}$ is given by

$$\mathbf{x_i} = \left[ C_{1,i}, C_{2,i}, ..., C_{n_c,i}, C_{sh,i}, \phi_{s,i}, S_{w,i} \right]^T, \tag{4.20}$$

where $n_b$ is the number of beds. The vector of numerically simulated logs is given by

$$\mathbf{d} = \left[ \boldsymbol{\phi_N}, \boldsymbol{\rho_b}, \boldsymbol{PEF}, \boldsymbol{GR}, \boldsymbol{\sigma}, \boldsymbol{Ur}, \boldsymbol{Th}, \boldsymbol{K} \right]^T, \tag{4.21}$$

where vectors $\boldsymbol{\phi_N}$, $\boldsymbol{\rho_b}$, ***PEF***, ***GR***, $\boldsymbol{\sigma}$, ***Ur***, ***Th***, and ***K*** include $n_{sp}$ measured points of neutron porosity, density, PEF, GR, apparent conductivity, Ur, Th, and K logs. $\boldsymbol{\sigma}$ is a vector that includes all the available apparent electrical conductivity logs (i.e., inverse of apparent resistivity logs with variable radial lengths of investigation). Size of vector **d** depends on sampling interval and number of well logs included in the inversion.

To effectively enforce the constraints expressed in Equations (4.17) and (4.18), we can change the variable vector $\mathbf{x_i}$ to $\mathbf{x}'_{\mathbf{i}}$ given by

$$\mathbf{x}'_{\mathbf{i}} = \left[ \log V_{1,i}, \log V_{2,i}, ..., \log V_{n_c,i}, \log V_{sh,i}, \log V_{ps,i}, \log S_{w,i} \right]^T, \tag{4.22}$$

where $V_{j,i}$ is the volume of the *j*th mineral in the *i*th bed, $V_{sh,i}$ is the volume of shale in the *i*th bed, and $V_{ps,i}$ is the volume of non-shale pore space in the *i*th bed. The relationship between $V_{j,i}$ and $C_{j,i}$, $V_{sh,i}$ and $C_{sh,i}$, and $V_{ps,i}$ and $\phi_{s,i}$ are respectively given by

$$C_{j,i} = \frac{V_{j,i}}{\sum_{j=1}^{n_c} V_{j,i} + V_{sh,i} + V_{ps,i}}, \tag{4.23}$$

$$C_{sh,i} = \frac{V_{sh,i}}{\sum_{j=1}^{n_c} V_{j,i} + V_{sh,i} + V_{ps,i}}, \tag{4.24}$$

and

$$\phi_{s,i} = \frac{V_{ps,i}}{\sum_{j=1}^{n_c} V_{j,i} + V_{sh,i} + V_{ps,i}}. \tag{4.25}$$

Volumetric concentration of shale consists of shale porosity, volumetric concentration of clay, and volumetric concentration of silt, which are obtained from inversion results applied to "pure" shale zones and thereafter set fixed or assumed to be known in synthetic cases. We assume that both shale porosity and volumetric concentration of clay in permeable zones are equal to those of shale zones. Although in the above description the initial guess and estimation results are described as volumetric concentrations, the method can be readily adapted to estimate both volumetric and weight concentrations of mineral/fluid constituents.

Experience shows that for this application the cost function defined by Equation (4.16) is quite often flat around the minimum, thereby giving rise to non-unique results. Moreover, there might be several minima due to more unknown properties than well logs and equality constraints (under-determined estimation problem). Accordingly, the stabilization parameter, $\alpha$, included in the quadratic cost function is intended to reduce non-uniqueness in the presence of noisy, inadequate, and/or incomplete data. The

stabilization parameter controls the relative importance between fitting the data and finding a stable and smooth solution. During the first iterations, a large value of $\alpha$ expedites the convergence by giving more importance to the agreement between well logs (data) and their numerical simulations. The value of $\alpha$ decreases gradually to guarantee a stable solution at the end of the estimation.

The data weighting matrix, $\mathbf{W_d}$, is included in Equation (4.16) to control the importance of each well log in the joint inversion. If all well logs are assigned the same importance, then the data weighting matrix scales the well logs to the same order of magnitude. The data weighting matrix, $\mathbf{W_d}$, is given by

$$\mathbf{W_d} = \begin{bmatrix} \left[\frac{1}{\left\|\mathbf{d}_{m,1}\right\|_2}\mathbf{I}_{n_{sp}\times n_{sp}}\right] & \cdots & 0 \\ \vdots & & \vdots \\ 0 & \cdots & \left[\frac{1}{\left\|\mathbf{d}_{m,n_l}\right\|_2}\mathbf{I}_{n_{sp}\times n_{sp}}\right] \end{bmatrix}, \tag{4.26}$$

where $\mathbf{I}$ is the unity matrix, $n_l$ is the number of well logs, and $n_{sp}$ is the number of sampling points in each well log. In the presence of noisy well logs, the influence of a given log on inversion results can be reduced by assuming a relatively small value to the corresponding entry of the data weighting matrix.

We minimize the cost function defined in Equation (4.16) with Levenberg-Marquardt's method (Marquardt, 1963). Accordingly, entries of the Jacobian matrix are calculated numerically (finite differences) at every linear iteration and the stabilization parameter is selected with Hansen's (1994) L-curve strategy. At every iteration, unknown

properties are updated based on the calculated Jacobian matrix and the difference between well logs and their numerical simulations. The minimization comes to a halt when (a) the relative difference between the norms of data residuals yielded by two subsequent iterations is less than 0.01% or (b) after reaching a prescribed maximum number of iterations.

The entries of the Jacobian matrix for this problem is given by

$$J_{ij} = \frac{\partial d_i}{\partial x_j}, \qquad 1 \le i \le n_l \bullet n_{sp}, \quad 1 \le j \le n_u \bullet n_b, \tag{4.27}$$

where $n_u$ is the number of unknowns in the assumed multi-layer formation. If the input well logs include density, neutron porosity, deep electrical conductivity, PEF, and GR (five well logs), the logging sampling rate is 0.25 feet, and there are six unknown petrophysical properties in each bed, then in a 100 ft reservoir with approximately 50 beds, the dimensions of Jacobian matrix will be 2000×300. This large matrix is usually ill-conditioned. Furthermore, accurate numerical calculation of the entries of the Jacobian matrix requires $1+n_u \times n_b$ forward numerical simulations for each well log. For instance, in the example of a 100-ft multi-layer formation, 300 forward numerical simulations will be required for each log. In reality, however, many of the entries of the Jacobian matrix are negligible or extremely small because well logs originate from local measurements. Thus, the Jacobian matrix can be calculated locally to avoid unnecessary calculations. On a related subject, Wang et al. (2009) introduced a domain decomposition method for fast two-dimensional (2D) resistivity inversion. They divided the entire depth interval into overlapping depth sub-domains, assuming that variations of formation resistivity in each sub-domain do not affect resistivity measurements acquired in other depth sub-domains.

The inverse problem was then solved in each sub-domain separately, with a smaller Jacobian matrix.

In addition to electrical resistivity measurements, we include nuclear logs and numerical simulation of mud-filtrate invasion as part of the inverse problem. CPU time in such a problem increases compared to the case that Wang et al. (2009) described. Thus, to approach the described inverse problem in a time-efficient manner, we approximate the Jacobian matrix by assuming that small perturbations on formation physical properties in each bed do not affect well logs acquired in other beds. This assumption is valid because the calculation of the Jacobian matrix invokes the minimum possible perturbation on formation petrophysical properties that affects well logs. Jacobian simplification reduces the required number of forward numerical simulations for each well log to $1+n_u$. The remaining entries of the Jacobian matrix are set to zero. Consequently, we decompose the original inverse problem to depth-by-depth inverse problems in each iteration. Then we average the estimated depth-by-depth updated formation petrophysical properties as the entry for the next iteration of nonlinear inversion.

The following sections describe the specific strategies adopted for simulation of mud-filtrate invasion and numerical simulation of nuclear and electrical resistivity logs. Further details about the forward numerical simulation of well logs can be found in Chapter 2.

#### *4.2.2.1 Mud-Filtrate Invasion*

Mud-filtrate invasion is simulated with a one-dimensional (1D) radial compositional fluid flow algorithm included in UTAPWeLS[4] software (Abdollah Pour,

[4] Developed by The University of Texas at Austin's Joint Industry Consortium on Formation Evaluation

2008). This algorithm simulates both water-base mud (WBM) and oil-base mud (OBM) invasion and calculates rates of mud-filtrate invasion resulting from mudcake buildup. We assume that vertical variations of fluid saturation due to capillary equilibrium are negligible across short depth intervals and simulate invasion separately within each petrophysical layer. Petrophysical layers include radial numerical grids used for finite-difference simulation of fluid-flow equations. Inputs to the simulation of mud-filtrate invasion are in-situ fluid and mud properties, rock-fluid properties, non-shale porosity, absolute permeability, initial fluid saturation, mud-cake properties, and invasion properties such as time of mud-filtrate invasion and overbalance pressure (or rate of mud-filtrate invasion). Rocks are assumed to be water-wet. Saturation-dependent capillary pressure and relative permeability, referred to as rock-fluid properties, are described with Brooks-Corey's parametric equations (Corey, 1994). Outputs from the fluid-flow simulator are layer-by-layer radial distribution of fluid saturation.

We emphasize that simulating the process of mud-filtrate invasion is optional in the nonlinear inversion method. Experience shows that this option is necessary in cases where the radial profile of invasion is smooth and apparent resistivity logs with different radial lengths of investigation do not "stack."

#### *4.2.2.2 Numerical Simulation of Well Logs*

Numerical simulation of well logs requires the construction of numerical grids used for assimilation of radially varying properties (such as water saturation and salt concentration resulting from the process of mud-filtrate invasion) in the estimation. We then calculate grid-by-grid electrical conductivity values for simulation of electrical resistivity logs, density values for density logs (Equation (4.12)), migration length for

neutron porosity logs, photoelectric factor for PEF logs, and volumetric concentrations of Ur, Th, and K for the numerical simulation of GR/GR-spectroscopy logs.

Neutron porosity and PEF logs are simulated from neutron migration length and photoelectric factor, respectively, defined at each grid. We use Schlumberger's SNUPAR commercial software (McKeon and Scott, 1989) to calculate migration length and photoelectric factor from chemical compositions and their corresponding volumetric concentrations. Volumetric concentrations of Ur, Th, and K are also calculated based on volumetric concentrations of mineral components in the formation.

Nuclear logs are simulated with the fast linear iterative refinement method developed by Mendoza et al. (2010), which explicitly incorporates borehole and environmental conditions. The CPU time required by the linear iterative refinement method to simulate nuclear logs is hundreds of times shorter than the CPU time required by alternative Monte-Carlo simulation methods. This unique advantage of Mendoza et al.'s (2010) method over Monte-Carlo simulation methods makes it feasible to implement nonlinear inversion within practical CPU times.

For calculation of the spatial distribution of electrical resistivity from the spatial distributions of water saturation and salt concentration, we adopt pertinent shaly-sand descriptions such as the dual-water model (Clavier et al., 1977). The calculated distributions of electrical resistivity (radial and vertical directions) are then used as input for the numerical simulation of array-induction and/or dual laterolog resistivity logs (AIT[5] and DLT[5]).

[5] Mark of Schlumberger

### 4.2.3 Method No. 2: Fast Nonlinear Joint Inversion of Bed Physical Properties

Even though Method No. 1 is accurate in the presence of mud-filtrate invasion and thin beds, it is not always computationally efficient. To quantify the effects of mud-filtrate invasion and shoulder beds on the Jacobian matrix, one needs to simulate mud-filtrate invasion and its effect on well logs for every unknown formation property. Repeating this process at every iteration renders the inversion extremely slow. If the effect of mud-filtrate invasion on well logs is negligible, then the correction for shoulder-bed effects can be implemented in a more efficient manner.

The second inversion method was designed to exclusively take into account the effect of shoulder beds on logs when performing the estimation of layer-by-layer mineral and fluid constituents, thereby improving the interpretation of thinly-bedded formations. This method consists of five sequential steps: (1) pre-analysis of available well logs and correction of depth shifts, (2) detection of bed boundaries based on all the available well logs or borehole images, (3) separate inversion of density, neutron porosity, electrical resistivity, PEF, and GR-spectroscopy logs to estimate layer-by-layer physical properties such as density, migration length, PEF, electrical conductivity, and Ur, Th, and K concentrations, respectively, (4) construction of a multi-layer petrophysical model based on an initial guess of petrophysical properties and volumetric concentrations of minerals and fluids, and (5) implementation of a nonlinear joint inversion algorithm on the estimated bed petrophysical properties to estimate layer-by-layer petrophysical and compositional properties. This latter step is approached with Schlumberger's SNUPAR commercial software (McKeon and Scott, 1989).

Method No. 2 only requires specific chemical mineral/fluid constituents in addition to well logs to estimate volumetric/weight concentrations of mineral and fluids. Mineral properties are calculated using SNUPAR based on input chemical formulae for

minerals/fluids. However, most of conventional lithology evaluators require calibration with XRD data for pure mineral properties. The following sections describe the techniques implemented for separate inversion of well logs and nonlinear joint inversion of bed physical properties via Method No. 2.

#### *4.2.3.1 Separate Inversion of Well Logs to Estimate Bed Physical Properties*

The first step in log inversion algorithms is the detection of bed boundaries. Inflection points in well logs are assumed to be indicative of bed boundaries. Conventional methods usually assume center-bed value or average log values within each petrophysical bed as the actual bed physical property. These approaches are not reliable in the presence of thin beds wherein shoulder-bed effects are not negligible. For the case of density and PEF measurements acquired in beds thicker than 1 ft, shoulder-bed effects are usually negligible at the center of the bed whereby one can safely use the center-bed value as the actual bed property.

For separate inversion of density, PEF, and GR-spectroscopy logs, we make use of a linear inversion algorithm based on pre-calculated Monte-Carlo derived FSFs for density, PEF, and GR measurements. Mendoza et al. (2010) successfully applied the same approach to logging-while-drilling (LWD) density measurements acquired in high-angle wells to estimate bed densities. **Appendix A** provides additional details about the linear inversion of density, PEF, and GR-spectroscopy logs. The main assumption in the FSF-based linear inversion algorithm is that the pre-calculated FSFs remain constant across different formation properties. Although this assumption is usually valid for density, PEF, and GR logs, sensitivity functions for neutron porosity and resistivity measurements vary with formation properties. Consequently, the linear inversion algorithm is applicable to neither neutron porosity nor electrical resistivity measurements.

Inversion of GR-spectroscopy, density, and PEF is done in one-step linear inversion and does not require iterations. For separate inversion of neutron porosity and electrical resistivity measurements, we introduce a nonlinear numerical inversion method detailed in **Appendix B**. The method iteratively updates estimates of layer-by-layer migration length and electrical conductivity. Inputs to the inversion algorithm are migration length and apparent conductivity logs instead of neutron porosity and apparent resistivity logs in order to improve the sensitivity of measurements to bed physical properties, hence to improve the rate of convergence of nonlinear inversion. Nonlinear inversion is initialized with readings of well logs taken at the center of the corresponding bed.

#### *4.2.3.2 Joint Inversion of Bed Physical Properties to Estimate Porosity and Volumetric/Weight Concentrations of Mineral/Fluid Constituents*

After separate inversion of well logs, estimating bed physical properties, and constructing an initial multi-layer petrophysical model, Schlumberger's commercial software, SNUPAR is used for the layer-by-layer joint inversion of bed physical properties to assess total porosity, fluid saturations, and volumetric concentrations of mineral constituents. The inversion is initiated with guess values for porosity and volumetric concentrations of minerals/fluids at each depth. SNUPAR then calculates corresponding values of migration length and PEF. Electrical conductivity is calculated separately using a saturation-porosity-resistivity model, which is assumed valid in the formation of interest (e.g., Archie, dual water, Waxman-Smits, etc.). Density (Equation (4.12)) and Ur, Th, and K concentrations are also calculated based on the linear correlations between volumetric concentrations of minerals with density and Ur, Th, and K concentrations of pure minerals. Inversion iteratively reduces the difference between numerically calculated and previously estimated values of migration length, density, PEF,

electrical conductivity, and concentrations of Th, Ur, and K by updating the volumetric/weight concentrations of minerals/fluids. **Appendix C** provides additional details about the nonlinear joint inversion algorithm.

### 4.2.4 Method No. 3: Nonlinear Joint Inversion of Individual Layer Properties

Method No. 3 does not take into account shoulder-bed effects and assumes that physical properties are equal to center-bed readings of well logs. This assumption is reliable in formations with thick beds and significantly decreases CPU time. The third method begins with pre-analysis of available well logs and correction for depth shifts. Next, bed boundaries are detected based on inflection points of well logs or borehole images. This method assumes that bed physical properties (density, migration length, PEF, electrical conductivity, and Ur, Th, and K concentrations) are equal to center-bed values obtained from well logs. Next, similar to Method No. 2, SNUPAR is used for the layer-by-layer joint inversion of bed physical properties to assess total porosity, fluid saturations, and volumetric concentrations of mineral constituents in every bed, where each bed is treated separately and independently. The main difference between the layer-by-layer nonlinear joint inversion approaches in Methods No. 2 and No. 3 are the values input to the inversion. In Method No. 2, inputs to the inversion are the results from separate inversion of well logs, whereas in Method No. 3, inputs are center-bed property values calculated from well logs. Method No. 3 can also be applied at every log-sampling point instead of at every layer. **Appendix C** provides additional details about the nonlinear joint inversion algorithm used to estimate bed petrophysical and compositional properties.

### 4.2.5 Initial Guess of Layer-by-Layer Unknown Properties

The joint inversion algorithms described above are implemented with three possible choices for initial guess: (a) parsimonious initial guess, (b) initial guess based on results obtained from conventional petrophysical interpretation of well logs and conventional/linear multi-mineral solvers, and (c) initial guess based on XRD/core data. Results obtained from depth-by-depth nonlinear inversion of well logs can also be used as initial guess for Method No. 2, whereas results obtained from Method No. 2 become suitable to initialize Method No. 3. The latter choices of initial guess expedite the convergence rate and decrease CPU time for Methods No. 2 and No. 3. We suggest choosing XRD/core data as initial guess in formations where mineral compositions are complex and/or non-uniqueness of results is prevalent. Results obtained from depth-by-depth nonlinear inversion of well logs or from conventional/linear multi-mineral solvers are good choices for initial guess when XRD/core data are not available.

## 4.3 SYNTHETIC CASE NO. 1: COMPARISON OF POROSITY ESTIMATES OBTAINED WITH NONLINEAR AND CONVENTIONAL LINEAR INVERSION METHODS

The first synthetic case is intended to quantify the reliability and accuracy of nonlinear inversion to estimate petrophysical properties in gas-and water-saturated beds in the absence of mud-filtrate invasion. We assume that formations are clay-free, comprised of thick layers of pure limestone, pure dolomite, and pure quartz. First, we assume that the formation is fully saturated with saline water. Input well logs for both nonlinear and linear inversion methods are array-induction apparent resistivity, neutron porosity, density, PEF, and GR sampled at 0.25 ft. **Table 4.1** summarizes the assumed matrix and petrophysical properties.

This estimation problem is even-determined because the number of unknown properties (porosity, saturation, volumetric concentrations of shale, quartz, limestone, and

dolomite) is equal to the number of well logs (density, neutron porosity, GR, PEF, and apparent electrical resistivity) plus the number of equality constraints (Equation (4.18)). We use Method No. 3 (individual layer-by-layer estimation) for estimation in this case due to the presence of thick beds and negligible shoulder-bed effects in the center of beds. The initial guess for inversion is chosen close to shale properties to test the stability of the method. We use dual-water saturation-resistivity model (Clavier et al., 1977) in both nonlinear and linear inversion methods applied on this example. **Figure 4.2** compares input electrical resistivity and nuclear logs to those used to initialize the inversion (calculated from the initial guess of properties) and simulated from final inversion products. The separation between neutron porosity and density logs in the water saturated limestone zone is due to connate water salinity. Panels in the same figure describe estimates of volumetric concentrations of mineral constituents, non-shale porosity, and fluid saturations obtained with both nonlinear and conventional linear estimation methods. In the case of fully water-saturated beds, both linear and nonlinear inversion methods yield accurate estimates for porosity and volumetric concentrations of mineral constituents. However, we observe small discrepancies between results obtained with conventional linear and nonlinear inversion methods near bed boundaries. The reason for this behavior is that commercial software does not explicitly account for shoulder-bed effects in the estimation when performing depth-by-depth inversion.

Next, we replace water with gas in the same formations to investigate the effect of gas on nonlinear inversion and conventional linear results. **Figure 4.3** compares input electrical resistivity and nuclear logs to those used to initialize the inversion and simulated from final inversion products. Panels in the same figure describe the final estimates of volumetric concentrations of mineral constituents, non-shale porosity, and fluid saturations obtained with both nonlinear and linear methods. For conventional linear

mineralogy evaluation, we adopt the same matrix for pure element responses calibrated for the water-saturated example. However, to obtain the most accurate estimates from commercial software in the presence of gas, we had to set the volumetric concentration of shale to its actual value. Furthermore, we did not include apparent resistivity measurements in the linear joint inversion of well logs; however, they are used to estimate water saturation in parallel to the joint inversion process. In the nonlinear joint inversion method, however, volumetric concentration of shale remains unknown, and apparent resistivity logs are explicitly included in the joint inversion. In this case, both nonlinear inversion and conventional linear methods remain stable in the presence of gas and yield porosity and volumetric concentrations of mineral constituents with errors smaller than 1% and 4%, respectively.

When setting volumetric concentration of shale as unknown in both methods, linear inversion does not properly resolve mineral concentrations in the dolomite layer. Estimates for volumetric concentration of quartz, calcite, and shale in the pure dolomite layer obtained with commercial software are 0.28, 0.58, and 0.06, respectively. We also observe errors of 43% and 55% in the assessment of porosity and water saturation, respectively. The main reason for such relatively high errors is the non-uniqueness of results. Indeed, by eliminating volumetric concentration of shale in the set of unknown variables, we decrease non-uniqueness of results and, consequently, decrease the corresponding errors.

### 4.4 SYNTHETIC CASE NO.2: EFFECT OF LAYER THICKNESS ON INVERSION RESULTS IN A GAS-BEARING, SINGLE-LAYER FORMATION

The second synthetic case is intended to appraise the reliability and accuracy of nonlinear inversion when estimating formation properties in the presence of thin beds. Target layers include in-situ gas and irreducible water, which have been subject to WBM-

filtrate invasion for three days. Solid constituents of permeable beds include quartz, limestone, dolomite, and shale and are separated by intermediate pure shale layers. Inversion results are obtained for bed thicknesses of ten, two, one, and 0.5 ft. Well logs are sampled at a rate of 0.25 ft. The resistivity-saturation-porosity model used in this synthetic case is dual water model. **Table 4.2** summarizes the matrix and petrophysical properties assumed for this synthetic case, whereas **Table 4.3** describes the corresponding assumed rock-fluid properties. Clay composition is exclusively chlorite.

Synthetic Case No. 2 involves an even-determined estimation problem. Method No. 1 is used in this case due the presence of thin beds and mud-filtrate invasion. Nonlinear inversion is initialized with shale properties assigned to all beds in order to evaluate the stability and reliability of the results. In this synthetic case, we assumed that formation properties are known in pure shale beds. Final inversion products are compared to equivalent results obtained with linear inversion implemented with commercial software.

**Figure 4.4** describes estimates of total porosity, total fluid saturation, and volumetric concentrations of quartz, limestone, dolomite, and shale for all permeable layers obtained with nonlinear inversion. Error (uncertainty) bars for inverted properties in each layer were calculated by adding 5% zero-mean Gaussian random noise to all well logs input to the inversion. We observe that the uncertainty of inversion products due to the noisy data increases with decreasing layer thickness. **Figure 4.5** compares input apparent resistivity and nuclear logs to those used to initialize the inversion and simulated from final inversion products. The same figure compares porosity, water saturation, volumetric concentration of shale, and volumetric concentrations of mineral constituents estimated with both conventional linear and nonlinear inversion methods. **Table 4.4**

summarizes the results obtained from conventional linear and nonlinear inversion methods for formations with different thicknesses but similar petrophysical properties.

**Table 4.5** describes the relative errors of inversion products obtained with both conventional linear and nonlinear inversion methods with respect to actual values. Differences between nonlinear inversion results and actual values are negligible. On the other hand, the discrepancy between inversion products obtained with conventional linear inversion and actual values increases with decreasing bed thickness. Additionally, conventional linear inversion underestimates hydrocarbon pore volume in all the beds due to mud-filtrate invasion effects. Conversely, inverted products obtained with nonlinear inversion differ by less than 3% with respect to actual values when bed thickness is larger than 0.5 ft. Prior to mud-filtrate invasion, permeable beds are saturated with gas and irreducible water. Even though in this case nonlinear inversion still provides accurate estimates, uncertainty bars calculated with 5% Gaussian noise increase by more than 100%, when compared to the case of no invasion. Indeed, presence of mud-filtrate invasion decreases the uncertainty of estimated formation petrophysical properties as long as the estimation explicitly includes the simulation of the process of invasion. Neglecting the effect of mud-filtrate invasion in the inversion, however, seriously increases estimation errors (which is also the case with linear inversion results obtained with commercial software).

Next, we compare estimations obtained with both nonlinear and conventional linear inversion methods assuming the same bed sequence but with permeable beds fully saturated with saline water. **Figure 4.6** compares inversion products obtained with linear and nonlinear inversion to actual properties. Nonlinear inversion yields results with errors smaller than 1%. On the other hand, conventional linear inversion software correctly identifies mineral constituents for the case of water-saturated beds. However, due to the

presence of salty connate water, volumetric mineral concentrations obtained with linear inversion exhibit errors above 20% for the thickest bed. Even though gas is no longer present in target beds, shoulder-bed effects on well logs increase the error in the volumetric mineral concentrations estimated with conventional linear inversion.

To investigate the effect of bed-boundary locations in the estimation of unknown properties, we perturbed bed boundaries by ± a log-sampling interval (i.e., 0.25 ft in Synthetic Case No. 2). In the thickest bed, estimation errors due to bed-boundary perturbation are below 5%. However, in beds thinner than 2 ft, errors increase to 30% or higher. These exercises emphasize the importance of proper selection of bed boundaries and depth-matching of well logs to secure reliable inversion results in thin beds.

## 4.5 SYNTHETIC CASE NO. 3: THINLY-BEDDED GAS-BEARING FORMATION

The third synthetic case was constructed based on actual field measurements and is intended to appraise nonlinear inversion results for the case of successive thin beds. It comprises a thinly-bedded and shaly carbonate formation and two hydraulically separated depth intervals. The top zone is a gas-bearing formation, while the bottom zone is water saturated with the same volumetric concentrations of mineral constituents and petrophysical properties as the top zone. Drilling mud is WBM and well logs are sampled at a rate of 0.25 ft. The resistivity-saturation-porosity model used in this synthetic case is dual water model. **Table 4.6** describes the assumed matrix and petrophysical properties. Rock-fluid properties and clay type are similar to those of Synthetic Case No. 2 (**Table 4.3**). **Table 4.7** summarizes the assumed values of porosity, water saturation, volumetric concentration of shale, and volumetric concentrations of mineral constituents. We assume that shale properties are reliable and obtained from inversion performed across pure shale depth intervals.

Synthetic Case No. 3 also involves an even-determined estimation problem. We initialize the nonlinear inversion with a parsimonious guess close to shale properties, and compare the results of nonlinear inversion to those of conventional linear inversion implemented with commercial software. **Figures 4.7** and **4.8** describe the spatial distribution of water saturation, actual model properties, and final estimates obtained with nonlinear inversion after and before mud-filtrate invasion, respectively. We use Method No. 2 and Method No. 1 in the cases of estimation before and after mud-filtrate invasion, respectively. The same figures compare final layer-by-layer porosity, water saturation, volumetric concentration of shale, and volumetric concentrations of mineral constituents obtained with nonlinear and conventional linear inversion methods to those of the actual model.

Prior to mud-filtrate invasion, array-induction apparent resistivity logs overlap ("stack") and there is crossover between neutron porosity and density logs in the gas-bearing zone. However, shoulder-bed effects in thin beds occasionally mask the crossover, and may lead to underestimation of gas reserves. After three days of mud-filtrate invasion, a smooth radial variation of water saturation causes separation between array-induction resistivity logs with different radial lengths of investigation. Because radial length of invasion is deeper than 2 ft and larger than the volume of investigation of nuclear logs, the crossover between neutron porosity and density logs disappears. The first advantage of nonlinear over conventional linear inversion is its ability to correct for magnified shoulder-bed effects due to successive thin beds. Another advantage of nonlinear inversion is the explicit assimilation of invasion effects on well logs in the estimation of properties. The effect of invasion on apparent resistivity logs becomes important when the radial invasion front is either smooth or shallow.

Nonlinear inversion yields errors lower than 5% for porosity and lower than 3% for water saturation in the gas-saturated zone prior to mud-filtrate invasion. After mud-filtrate invasion, errors decrease to 2% for porosity, and 3% for water saturation. Overall, the corresponding errors in the water-saturated zone decrease compared to those in gas-saturated zones.

Conventional linear inversion yields acceptable estimates of porosity, water saturation, and volumetric concentrations of mineral constituents in the water-saturated zone (errors lower than 30% for water saturation). In the presence of thin beds, however, we observe significant errors due to shoulder-bed effects. Furthermore, errors as high as 40% arises when quantifying mineral composition across the gas-bearing zone, which deleteriously influences estimates of porosity and water saturation. Both shoulder-bed and gas effects give rise to errors as high as 70% in estimates of water saturation prior to mud-filtrate invasion. After mud-filtrate invasion, conventional linear inversion yields results with increased errors, as high as 90% and 25% in the estimates of water saturation in the gas- and the water-bearing zones, respectively. Increased errors in estimates of water saturation after mud-filtrate invasion are due to limitations of commercial software to take into account invasion effects in a quantitative manner. We also observe error increase in the assessment of volumetric concentrations of mineral constituents after mud-filtrate invasion.

## 4.6 DISCUSSION

This chapter introduced three methods to estimate porosity, fluid saturation, and volumetric concentrations of mineral constituents from conventional well logs. The first method is the most general one, applicable to the evaluation of invaded and thinly-bedded formations. The second method explicitly accounts for shoulder-bed effects on well logs,

but does not account for mud-filtrate invasion. The third method is only recommended for evaluation of formations where shoulder-bed and mud-filtrate invasion effects on well logs are negligible. Associated CPU times for a 50-ft formation with 25 beds are 5 hours, 1 hour, and 10 minutes for Methods No. 1, No. 2, and No. 3, respectively, when implemented on a PC with a 3 GHz processor and 4 GB RAM. Compared to conventional petrophysical interpretation methods, the advantages of the inversion methods introduced in this chapter are the explicit assimilation of shoulder-bed and invasion effects on well logs, and the accurate numerical simulation of well log cases for arbitrary perturbations of petrophysical and mineral/fluid compositional properties of rock formations.

Input data and parameters for the evaluation of invaded formations include: (a) conventional well logs such as density, neutron porosity, PEF, GR/GR-spectroscopy, and electrical resistivity, (b) number, type, and chemical formula for mineral and fluid constituents, (c) saturation-porosity-resistivity model and associated parameters (e.g., Archie's model and Archie's parameters, such as electrical resistivity of connate water, tortuosity factor, cementation exponent, and saturation exponent), (d) formation and fluid properties such as density, permeability, and saturation-dependent relative permeability and capillary pressure, (f) invasion parameters such as overbalance pressure, time of invasion, and mud/mud-cake properties, and (g) bed boundary locations. Invasion parameters and dynamic petrophysical properties are not needed when invasion is negligible or radially deep. Inversion results consist of porosity, hydrocarbon saturation, and volumetric/weight concentrations of mineral constituents.

Uncertainty in any of the input parameters affects inversion results. For instance, an uncertainty of four degrees of magnitude in permeability in Synthetic Case No. 2 (i.e., permeability of 0.005 md instead of 50 md) causes 37% uncertainty in estimates of water

saturation for the thickest bed (10 ft). This uncertainty increased to 55% in the thinnest bed (0.5 ft). Estimates of porosity and volumetric concentrations of mineral constituents, however, exhibited less sensitivity to uncertainty in permeability (uncertainty of less than 20% in assessment of volumetric concentrations of mineral constituents and less than 5% in assessment of porosity).

Another cause of uncertainty of inversion results is noisy well logs. We showed that this uncertainty increases across thin beds. The stabilization parameter included in the three inversion algorithms is intended to stabilize the estimations in the presence of noisy and/or inadequate data. Large values of stabilization parameter provide a smooth solution, whereas small values cause oscillatory solutions. Hansen's L-curve method estimates the stabilization parameter in each iteration based on the difference between actual measurements and their numerical simulations. Consequently, the stabilization parameter takes large values at the initial iterations to guarantee the convergence to the actual properties. Gradually, its value decreases in order to secure a stable convergence to the solution, when we get close to the answer.

When the total number of unknown properties and equality constraints are equal or less than the number of available well logs, the inversion is rendered even- or over-determined. Accurate and reliable estimates of petrophysical/compositional properties are possible in over- or even-determined inversions when input parameters are reliable. We showed that in those cases inversion results are stable and independent of the initial guess. In the case of over- or even-determined inversions, results remain accurate even when assuming mineral components, which are not present in the examined rock formations.

When the total number of unknown properties and equality constraints are greater than the number of available well logs, the inversion is rendered under-determined. In

those cases, non-uniqueness of results is a significant concern and, consequently, the choice of initial guess becomes critical to secure accurate and reliable results. Two approaches to overcome this problem are: (a) choosing an initial guess close to actual values and (b) starting the inversion from different initial guesses. We suggested different choices for initial guess close to actual formation properties to avoid trapping into local minima as well as to expedite convergence. In the case of under-determined inversion, a wrong choice of assumed mineral components caused significant errors in inversion results. Experience shows that the corresponding error is smaller for porosity, water saturation, and volumetric concentration of shale, than for volumetric concentrations of mineral constituents. The uncertainty of estimated properties depends on the type and properties of assumed minerals, petrophysical properties, and on the initial guess.

To secure reliable petrophysical and compositional results, we suggest inputting the maximum number of available well logs to the inversion. However, it is possible that some well logs are not reliable due to noise (e.g., PEF in the presence of barite in mud). The effect of unreliable well logs on inversion results can be controlled by the data weighting matrix. Absence of PEF, GR, or density in under-determined problems can change estimated properties by more than 50%, but does not affect estimates of porosity and water saturation significantly (Synthetic Case No. 1). Absence of electrical resistivity measurements, however, has a significant influence on estimates of porosity and water saturation (changes of 25% for porosity and 200% for water saturation). Among all mineral constituents, shale concentration is the most stable outcome of inversion, whenever GR is available.

We quantified the accuracy of the introduced inversion methods when interpreting petrophysical and compositional properties of thinly-bedded formations. It was shown that inversion methods yield accurate results only when beds are thicker than twice the

log-sampling interval. Furthermore, uncertainty in bed boundary locations significantly affects inversion results for thin beds. For instance, it was found that bed-boundary uncertainty equal to one log-sampling interval in beds as thick as four times a log-sampling interval affects inversion results by more than 30%.

Even though the estimation methods introduced in this chapter do not explicitly include the use of compressional- and shear-wave sonic logs, they could be readily included in the inversion with a reliable mixing law that takes into account mineral concentrations and their dry bulk moduli (compressional and shear), as well as the corresponding effects of fluid components and their saturations. Including sonic measurements in the inversion significantly reduces non-uniqueness of the results.

## 4.7 CONCLUSIONS

We introduced and successfully tested new nonlinear inversion methods to estimate porosity, fluid saturation, and volumetric mineral concentrations from combinations of well logs. The estimation was made possible by a recently-developed algorithm to rapidly simulate nuclear logs. Synthetic examples indicate that the new nonlinear inversion methods are effective to reduce shoulder-bed and invasion effects on logs in the estimation compared to commercial software based on linearized well-log responses. Moreover, we showed that nonlinear inversion is reliable when permeable beds include gas saturation and complex mineralogy because the simulation of well logs accurately reproduces the generally nonlinear relationship between formation and fluid properties and measurements. It was also shown that the integration of the process of mud-filtrate invasion in the estimation of petrophysical properties is important when electrical resistivity logs indicate a relatively smooth radial invasion profile. Even though commercial software based on linearized inversion is fast and accurate in siliciclastic

sequences with clean and thick beds, it does not perform well in invaded and/or thinly-bedded formations which include complex mineral compositions and light hydrocarbons.

The number and type of available well logs, location of bed boundaries, and the number of unknown properties influence the results obtained with nonlinear inversion. Results are stable and accurate when non-noisy density, neutron porosity, PEF, GR, and electrical resistivity logs are available for the estimation. Sensitivity analysis indicated that perturbations of bed-boundary locations equal to a log-sampling interval could cause errors higher than 30% when estimating unknown properties of beds thinner than 2 ft. This error becomes negligible in thick beds. These results indicate that proper estimation of bed boundaries and correction of depth-matching errors on well logs are important to secure reliable inversion results in thin beds.

Nonlinear inversion is reliable to estimate hydrocarbon pore volume in gas-bearing formations that are not deeply invaded. However, in the presence of high-density hydrocarbons, the sensitivity of neutron porosity and density logs to hydrocarbon pore volume decreases, thereby leading to significant estimation errors in some cases. We also emphasize that presence of noisy measurements affects the final estimates of petrophysical properties more severely in the presence of light than of heavy hydrocarbon; it was shown that presence of 5% noise in nuclear and electrical resistivity logs could affect final inversion products by as much as 50% in gas-bearing formations and 30% in a heavy oil-bearing formations.

Combining the nonlinear inversion methods with neutron-capture spectroscopy measurements is a good alternative that improves the detection and estimation of mineral volumetric concentrations. We anticipate that nonlinear inversion could be effective in the petrophysical interpretation of carbonate formations and unconventional plays such as

tight-gas sands and gas/oil shales, where rapid depth variations of mineral/fluid constituents and bed thickness are commonplace.

**Table 4.1:** Synthetic Case No. 1: Summary of assumed Archie's parameters and matrix, fluid, and formation properties.

| Variable | Value | Units |
|---|---|---|
| Archie's tortuosity factor, *a* | 1.00 | [ ] |
| Archie's cementation exponent, *m* | 2.00 | [ ] |
| Archie's saturation exponent, *n* | 2.00 | [ ] |
| Salt concentration of connate water | 160 | kppm NaCl |
| Water density | 1.00 | $g/cm^3$ |
| Water viscosity | 1.00 | cp |
| Gas density | 0.0016 | $g/cm^3$ |
| Gas viscosity | 0.02 | cp |
| Formation temperature | 230 | °F |
| Volumetric concentration of shale | 0.00 | [ ] |
| Wellbore radius | 14.54 | cm |
| Formation maximum invasion time | 0.00 | day |

**Table 4.2:** Synthetic Case No. 2: Summary of assumed Archie's parameters and matrix, mud, fluid, and formation properties.

| Variable | Value | Units |
|---|---|---|
| Archie's tortuosity factor, *a* | 1.00 | [ ] |
| Archie's cementation exponent, *m* | 2.00 | [ ] |
| Archie's saturation exponent, *n* | 2.00 | [ ] |
| Connate water salt concentration | 160 | kppm NaCl |
| Mud-filtrate salt concentration | 7.5 | kppm NaCl |
| Bound water resistivity at 230°F | 0.018 | ohm.m |
| Water density | 1.00 | $g/cm^3$ |
| Water viscosity | 1.00 | cp |
| Gas density | 0.0016 | $g/cm^3$ |
| Gas viscosity | 0.02 | cp |
| Mud-filtrate density | 1.00 | $g/cm^3$ |
| Mud-filtrate viscosity | 1.00 | cp |
| Formation temperature | 230 | °F |
| Initial formation pressure | 3650 | psi |
| Mud hydrostatic pressure | 3800 | psi |
| Mudcake reference permeability | 0.03 | md |
| Mudcake reference porosity | 0.30 | [ ] |
| Mud solid fraction | 0.06 | [ ] |
| Mudcake maximum thickness | 1.02 | cm |
| Mudcake compressibility exponent | 0.40 | [ ] |
| Mudcake exponent multiplier | 0.10 | [ ] |
| Absolute permeability | 100 | md |
| Non-shale porosity | 0.15 | [ ] |
| Shale porosity | 0.12 | [ ] |
| Volumetric concentration of quartz | 0.30 | [ ] |
| Volumetric concentration of limestone | 0.15 | [ ] |
| Volumetric concentration of dolomite | 0.25 | [ ] |
| Volumetric concentration of shale | 0.15 | [ ] |
| Volumetric concentration of clay | 0.60 | [ ] |
| Initial water saturation | 0.15 | [ ] |
| Wet shale density | 2.64 | $g/cm^3$ |
| Wellbore radius | 14.54 | cm |
| Formation maximum invasion time | 3.00 | days |

**Table 4.3:** Synthetic Case No. 2: Summary of assumed rock-fluid properties (Brooks-Corey's parameters).

| $P_c^{\,0}$ [psi.darcy$^{1/2}$] | $e_p$ | $k^0_{rh}$ | $e_h$ | $k^0_{rw}$ | $e_w$ | $S_{wr}$ | $S_{hr}$ |
|---|---|---|---|---|---|---|---|
| 4.00 | 15.0 | 0.30 | 3.00 | 0.90 | 3.00 | 0.08 | 0.15 |

**Table 4.4:** Synthetic Case No. 2: Model (actual) properties, nonlinear inversion (NL, Method No. 1), and conventional linear inversion (L) results for non-shale porosity ($\phi_s$), non-shale water saturation ($S_{ws}$), and volumetric concentrations of shale ($C_{sh}$), quartz ($C_Q$), limestone ($C_L$), and dolomite ($C_D$) for each layer.

| **Layer thickness [ft]** | | $\phi_s$ | $S_{ws}$ | $C_{sh}$ | $C_Q$ | $C_L$ | $C_D$ |
|---|---|---|---|---|---|---|---|
| | **Actual** | 0.15 | 0.15 | 0.15 | 0.30 | 0.15 | 0.25 |
| **10** | **NL** | 0.150 | 0.150 | 0.150 | 0.301 | 0.152 | 0.247 |
| | **L** | 0.152 | 0.246 | 0.134 | 0.268 | 0.143 | 0.300 |
| | **Actual** | 0.15 | 0.15 | 0.15 | 0.30 | 0.15 | 0.25 |
| **2** | **NL** | 0.150 | 0.150 | 0.150 | 0.301 | 0.151 | 0.249 |
| | **L** | 0.198 | 0.313 | 0.136 | 0.000 | 0.000 | 0.669 |
| | **Actual** | 0.15 | 0.15 | 0.15 | 0.30 | 0.15 | 0.25 |
| **1** | **NL** | 0.150 | 0.151 | 0.150 | 0.303 | 0.154 | 0.243 |
| | **L** | 0.183 | 0.447 | 0.260 | 0.000 | 0.000 | 0.556 |
| | **Actual** | 0.15 | 0.15 | 0.15 | 0.30 | 0.15 | 0.25 |
| **0.5** | **NL** | 0.150 | 0.151 | 0.150 | 0.302 | 0.153 | 0.245 |
| | **L** | 0.110 | 1.000 | 0.600 | 0.141 | 0.147 | 0.000 |

**Table 4.5:** Synthetic Case No. 2: Relative errors (%) for estimations obtained with conventional linear (L) and nonlinear inversion (NL, Method No. 1) algorithms for non-shale porosity ($\phi_s$), non-shale water saturation ($S_{ws}$), and volumetric concentrations of shale ($C_{sh}$), quartz ($C_Q$), limestone ($C_L$), and dolomite ($C_D$) for each layer.

| **Layer thickness [ft]** | | $\phi_s$ | $S_{ws}$ | $C_{sh}$ | $C_Q$ | $C_L$ | $C_D$ |
|---|---|---|---|---|---|---|---|
| **10** | **NL** | 0.0 | 0.0 | 0.0 | 0.3 | 1.3 | 1.2 |
| | **L** | 1.3 | 64.0 | 10.7 | 10.7 | 4.7 | 20.0 |
| **2** | **NL** | 0.0 | 0.0 | 0.0 | 0.3 | 0.7 | 0.4 |
| | **L** | 32.0 | 108.7 | 9.3 | 100.0 | 100.0 | 167.6 |
| **1** | **NL** | 0.0 | 0.7 | 0.0 | 1.0 | 2.6 | 2.8 |
| | **L** | 22.0 | 198.0 | 73.3 | 100.0 | 100.0 | 122.4 |
| **0.5** | **NL** | 0.0 | 0.7 | 0.0 | 0.7 | 2.0 | 2.0 |
| | **L** | 26.7 | 566.7 | 300.0 | 53.0 | 2.0 | 100.0 |

**Table 4.6:** Synthetic Case No. 3: Summary of assumed Archie's parameters and matrix, mud, fluid, and formation properties.

| Variable | Value | Units |
|---|---|---|
| Archie's tortuosity factor, *a* | 1.00 | [ ] |
| Archie's cementation exponent, *m* | 2.00 | [ ] |
| Archie's saturation exponent, *n* | 2.00 | [ ] |
| Connate water salt concentration | 80 | kppm NaCl |
| Bound water resistivity at 230°F | 0.018 | ohm.m |
| Mud-filtrate salt concentration | 3.5 | kppm NaCl |
| Water density | 1.00 | $g/cm^3$ |
| Water viscosity | 1.00 | cp |
| Gas density | 0.0016 | $g/cm^3$ |
| Gas viscosity | 0.02 | cp |
| Mud-filtrate density | 1.00 | $g/cm^3$ |
| Mud-filtrate viscosity | 1.00 | cp |
| Formation temperature | 230 | °F |
| Initial formation pressure | 3650 | psi |
| Mud hydrostatic pressure | 3800 | psi |
| Mudcake reference permeability | 0.03 | md |
| Mudcake reference porosity | 0.30 | [ ] |
| Mud solid fraction | 0.06 | [ ] |
| Mudcake maximum thickness | 1.02 | cm |
| Mudcake compressibility exponent | 0.40 | [ ] |
| Mudcake exponent multiplier | 0.10 | [ ] |
| Absolute permeability | 50 | md |
| Shale porosity | 0.10 | [ ] |
| Volumetric concentration of clay | 0.50 | [ ] |
| Wet shale density | 2.64 | $g/cm^3$ |
| Wellbore radius | 14.54 | cm |
| Formation maximum invasion time | 3.00 | days |

**Table 4.7:** Synthetic Case No. 3: Values assumed for non-shale porosity ($\phi_s$), non-shale water saturation ($S_{ws}$), and volumetric concentrations of shale ($C_{sh}$), quartz ($C_Q$), limestone ($C_L$), and dolomite ($C_D$) for each layer.

| **Layer thickness [ft]** | $\phi_s$ | $S_{ws}$ | $C_{sh}$ | $C_Q$ | $C_L$ | $C_D$ |
|---|---|---|---|---|---|---|
| 3 | 0.00 | 1.00 | 1.00 | 0.00 | 0.00 | 0.00 |
| 3 | 0.15 | 0.20 | 0.19 | 0.25 | 0.30 | 0.11 |
| 2 | 0.12 | 0.25 | 0.03 | 0.35 | 0.23 | 0.27 |
| 1 | 0.14 | 0.22 | 0.19 | 0.12 | 0.32 | 0.23 |
| 1 | 0.10 | 0.26 | 0.18 | 0.23 | 0.15 | 0.34 |
| 3 | 0.08 | 0.28 | 0.18 | 0.31 | 0.25 | 0.18 |
| 2 | 0.04 | 0.32 | 0.17 | 0.28 | 0.16 | 0.35 |
| 3 | 0.06 | 0.30 | 0.20 | 0.21 | 0.24 | 0.29 |
| 3 | 0.00 | 1.00 | 1.00 | 0.00 | 0.00 | 0.00 |
| 3 | 0.15 | 0.75 | 0.19 | 0.25 | 0.30 | 0.11 |
| 2 | 0.12 | 0.85 | 0.03 | 0.35 | 0.23 | 0.27 |
| 1 | 0.14 | 0.80 | 0.19 | 0.12 | 0.32 | 0.23 |
| 1 | 0.10 | 0.87 | 0.18 | 0.23 | 0.15 | 0.34 |
| 3 | 0.08 | 0.90 | 0.18 | 0.31 | 0.25 | 0.18 |
| 2 | 0.04 | 0.95 | 0.17 | 0.28 | 0.16 | 0.35 |
| 3 | 0.06 | 0.92 | 0.20 | 0.21 | 0.24 | 0.29 |
| 3 | 0.00 | 1.00 | 1.00 | 0.00 | 0.00 | 0.00 |

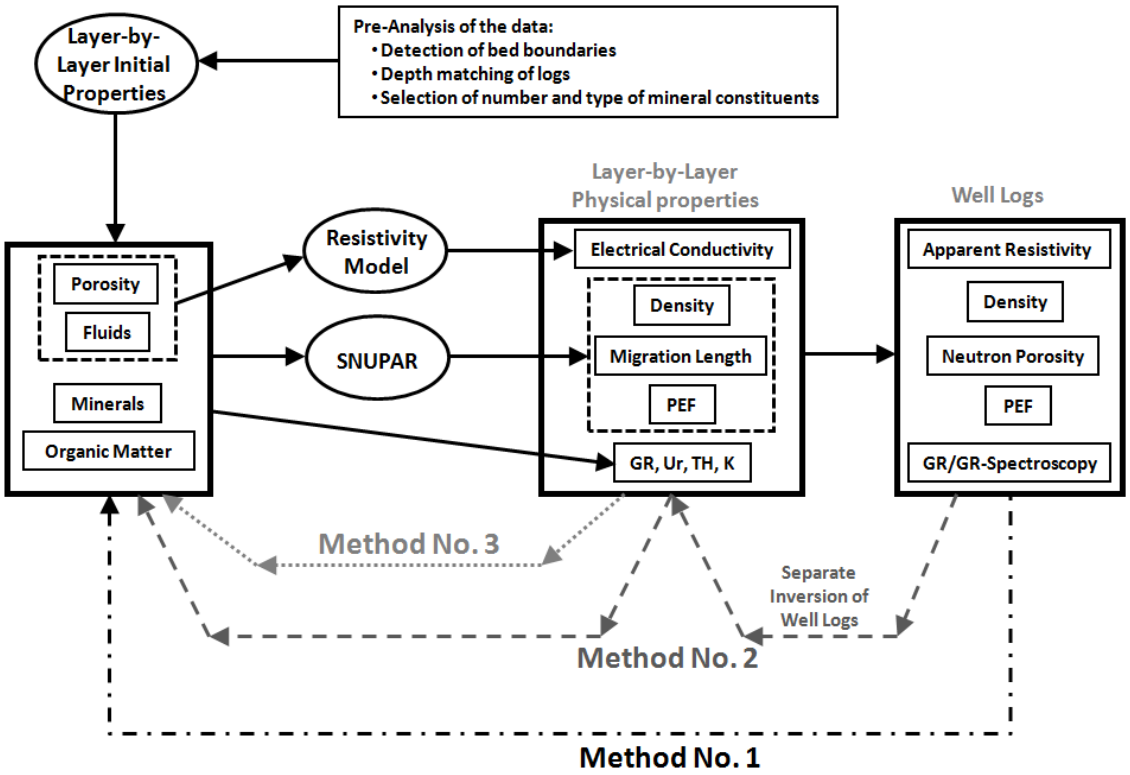


**Figure 4.1:** Workflows for the three nonlinear joint inversion methods introduced in this chapter. Inversion methods estimate unknown petrophysical properties and volumetric/weight concentrations of rock mineral constituents in the presence of mud-filtrate invasion, thin beds, and complex lithology. Nonlinear inversion progressively improves the agreement between well logs and their numerical simulations.

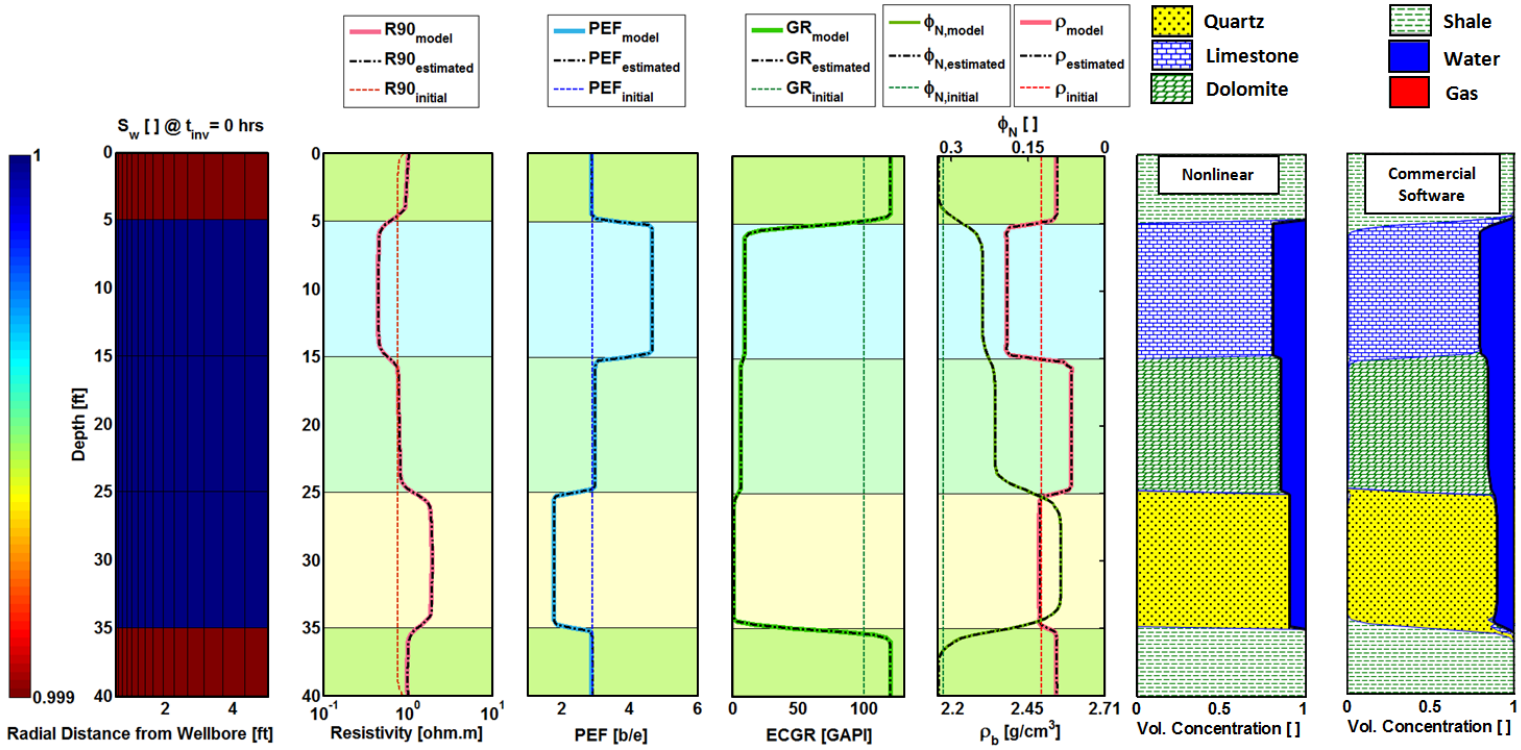


**Figure 4.2:** Synthetic Case No. 1, consisting of three thick layers of pure limestone, pure dolomite, and pure quartz. Comparison of final simulated well logs (dash-dotted black line), input well logs (solid line), and simulated well logs for the initial guess (dashed line). The left-hand panel shows the spatial distribution (radial and vertical directions) of water saturation for a fully water-saturated formation. Results are shown for array-induction resistivity (second left-hand panel), PEF (third left-hand panel), GR (fourth left-hand panel), density and neutron porosity (water-filled limestone porosity units, fifth left-hand panel) logs. The two right-hand panels compare final volumetric concentrations of mineral constituents, porosity, and water saturation obtained from conventional linear and nonlinear joint inversion (Method No. 3) of resistivity, density, neutron porosity, GR, and PEF logs.

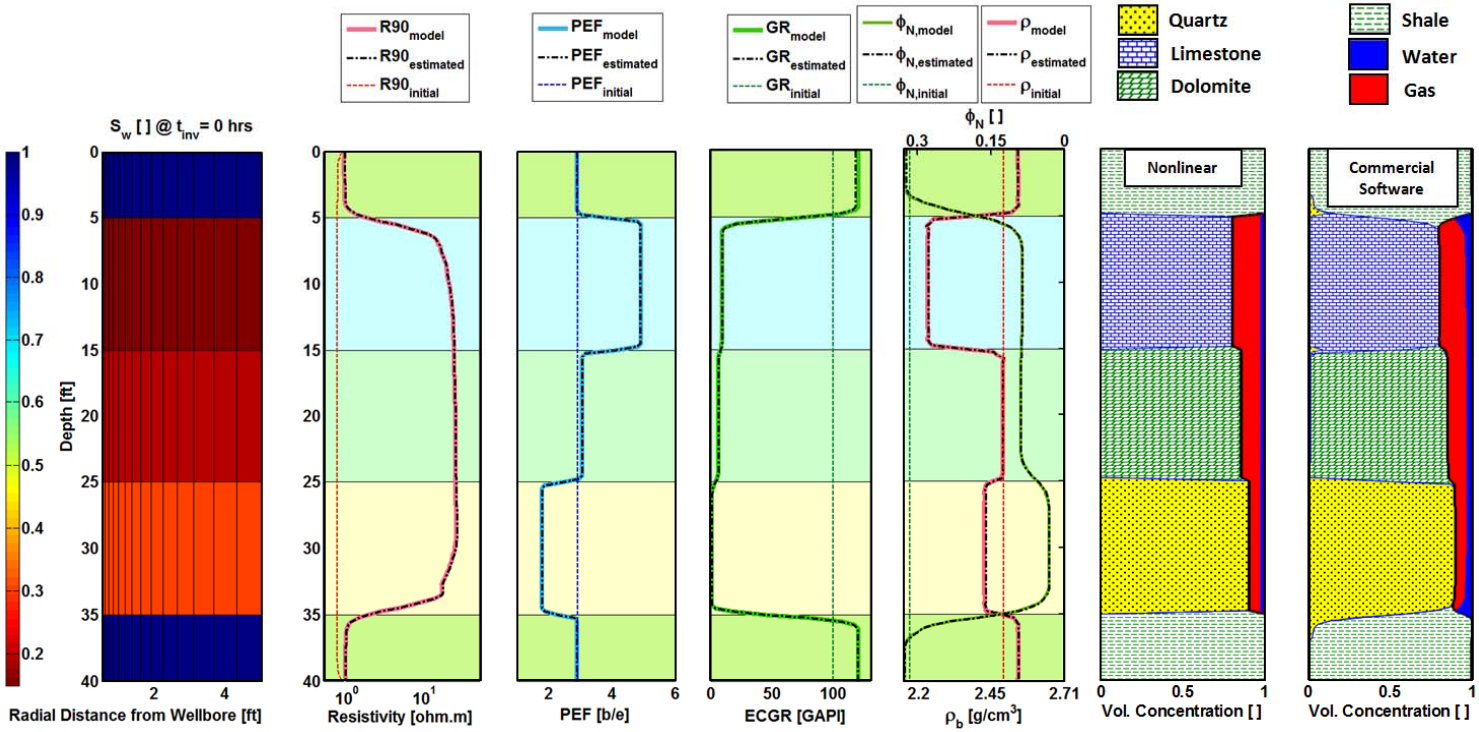


**Figure 4.3:** Synthetic Case No. 1, consisting of three thick layers of pure limestone, pure dolomite, and pure quartz. Comparison of final simulated well logs (dash-dotted black line), assumed input well logs (solid line), and simulated well logs for the initial guess (dashed line). The left-hand panel shows the spatial distribution (radial and vertical directions) of water saturation for a formation saturated with gas and irreducible water. Results are shown for array-induction resistivity (second left-hand panel), PEF (third left-hand panel), GR (fourth left-hand panel), density and neutron porosity (water-filled limestone porosity units, fifth left-hand panel) logs. The two right-hand panels compare final volumetric concentrations of mineral constituents, porosity, and water saturation obtained from conventional linear and nonlinear joint inversion (Method No. 3) of resistivity, density, neutron porosity, GR, and PEF logs.

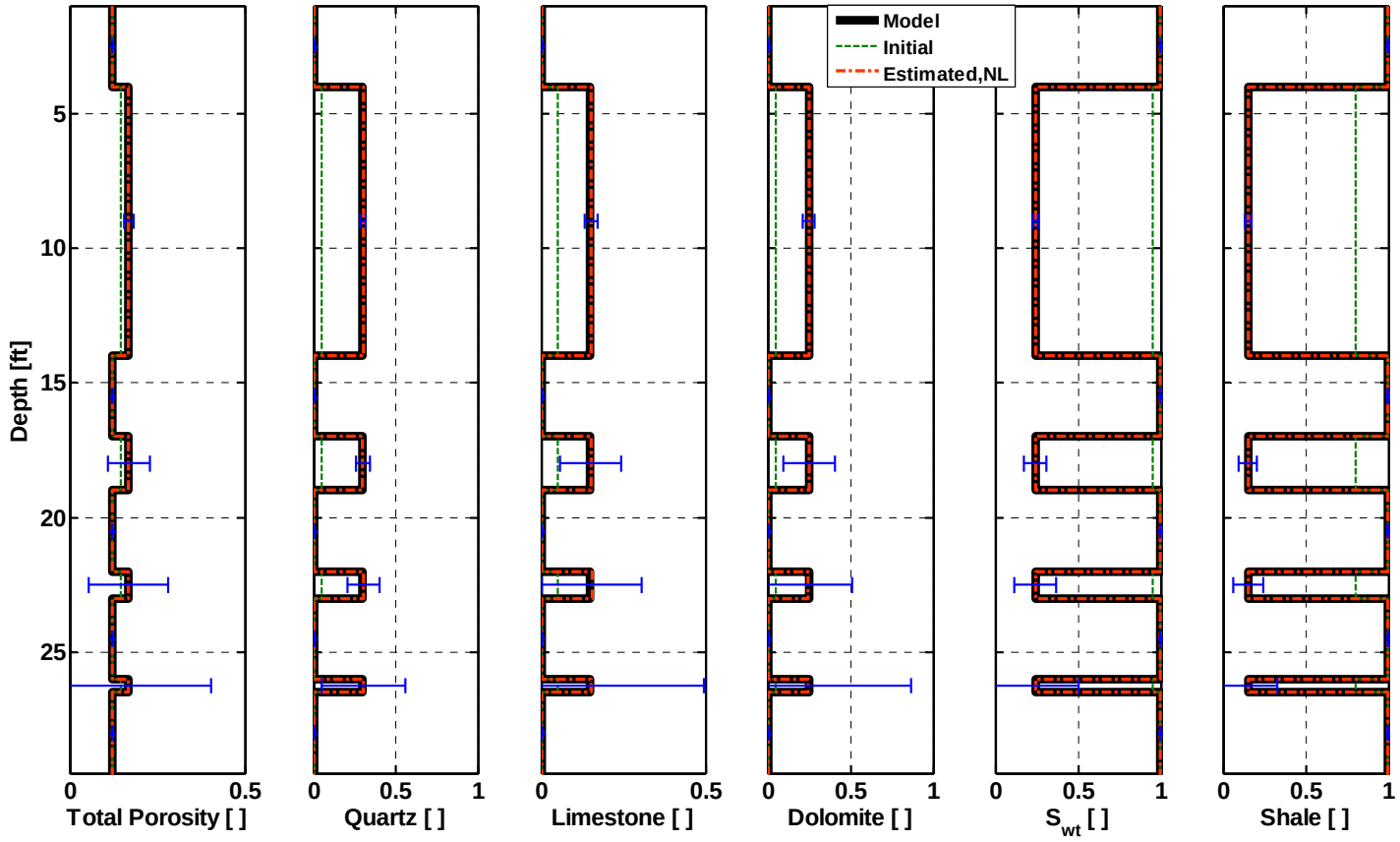


**Figure 4.4:** Synthetic Case No. 2: Comparison of model (actual) values (black solid line), initial guess (green dashed line), and final estimates (red dash-dotted line) of volumetric concentrations of mineral constituents, porosity, and water saturation with corresponding uncertainty bars (calculated with 5% additive zero-mean Gaussian random perturbations of input logs, including resistivity, density, neutron porosity, GR, and PEF). Panels from left to right show total porosity, volumetric concentration of quartz, volumetric concentration of limestone, volumetric concentration of dolomite, total water saturation, and volumetric concentration of shale.

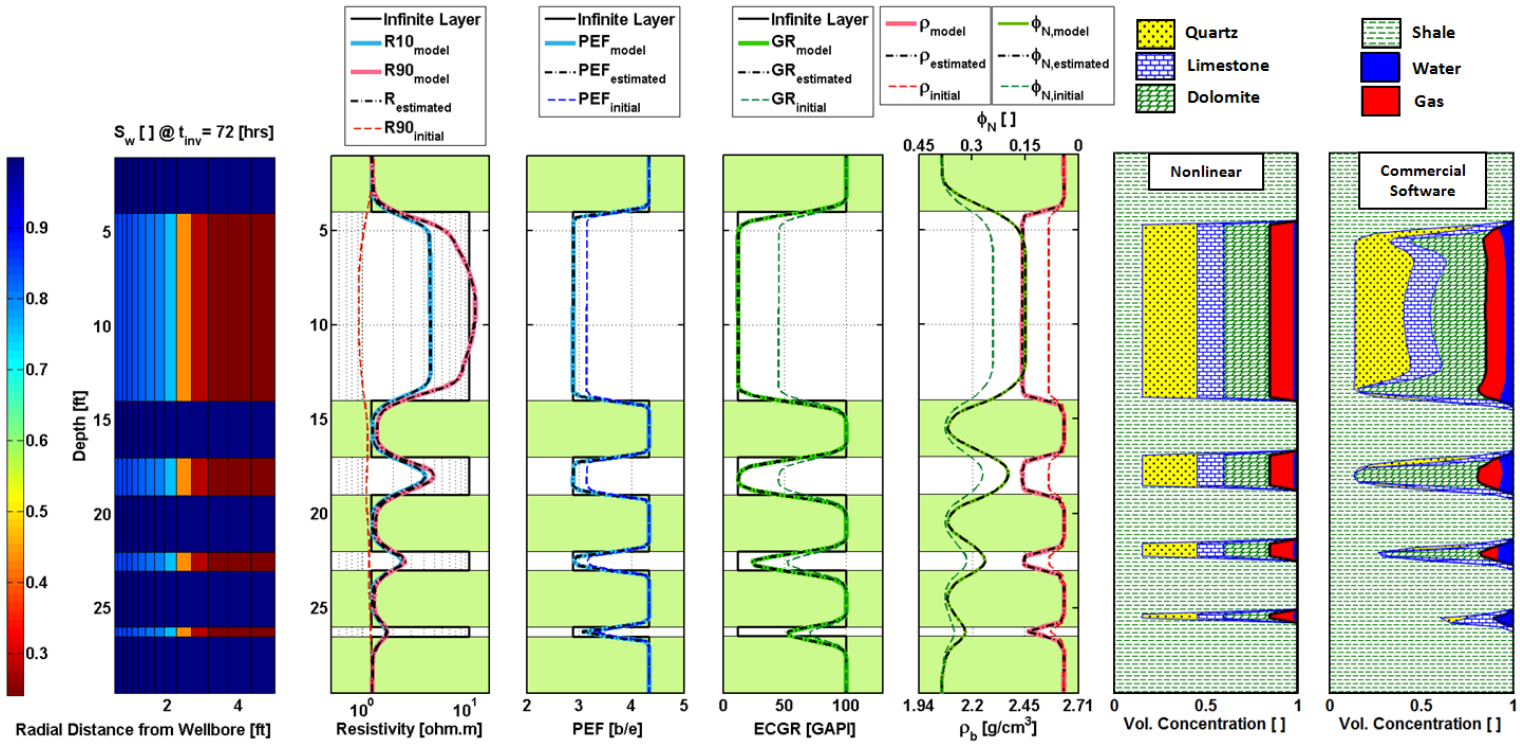


**Figure 4.5:** Synthetic Case No. 2 consisting of four non-shale layers with varying thickness ranging from 0.5 ft to 10 ft with similar mineral composition and petrophysical properties in all layers. Comparison of final simulated well logs (dash-dotted black line), input well logs (solid line), and simulated well logs for the initial guess (dashed line). The left-hand panel shows the spatial distribution (radial and vertical directions) of water saturation after 3 days of WBM-filtrate invasion. Results are shown for array-induction resistivity (second left-hand panel), PEF (third left-hand panel), GR (fourth left-hand panel), density and neutron porosity (water-filled limestone porosity units, fifth left-hand panel) logs. The two right-hand panels compare final volumetric concentrations of mineral constituents, porosity, and water saturation obtained from conventional linear and nonlinear joint inversion (Method No. 1) of resistivity, density, neutron porosity, GR, and PEF logs.

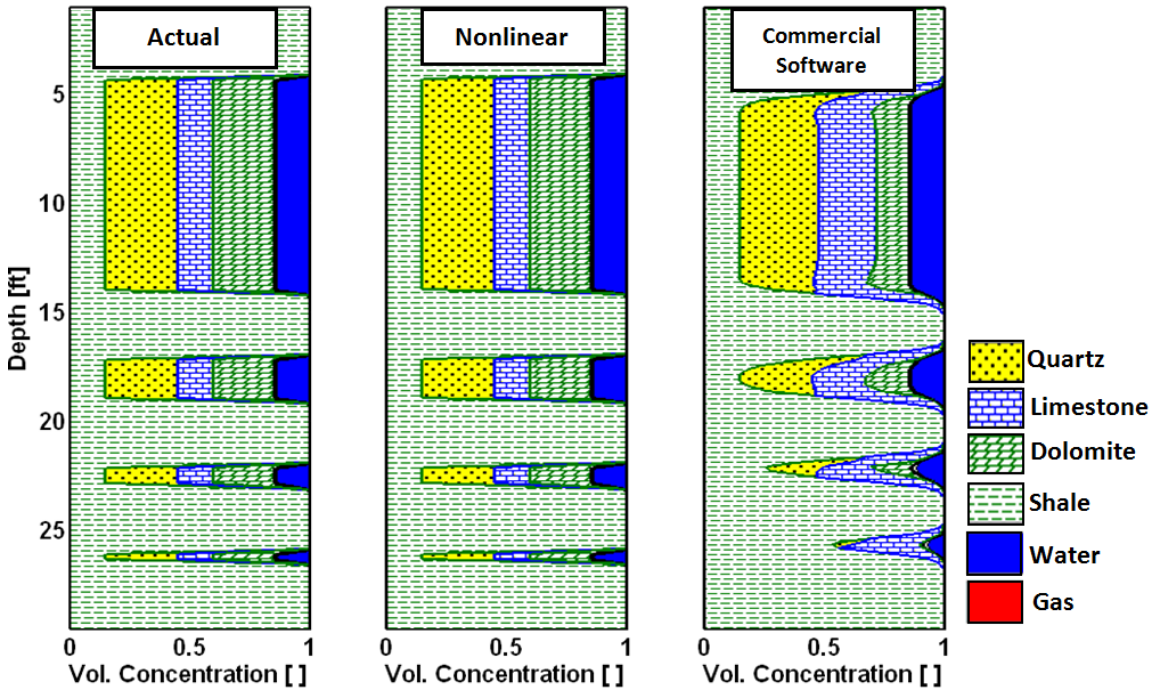


**Figure 4.6:** Synthetic Case No. 2: Comparison of final porosity, water saturation, and volumetric concentrations of shale and mineral constituents obtained from conventional linear (right-hand panel) and nonlinear (center panel) joint inversion (Method No. 1) of resistivity, density, neutron, GR, and PEF logs against actual values (left-hand panel). The formation is fully saturated with water. Mineral composition and petrophysical properties are equal in all the four permeable layers. None of the permeable zones is invaded with mud filtrate.

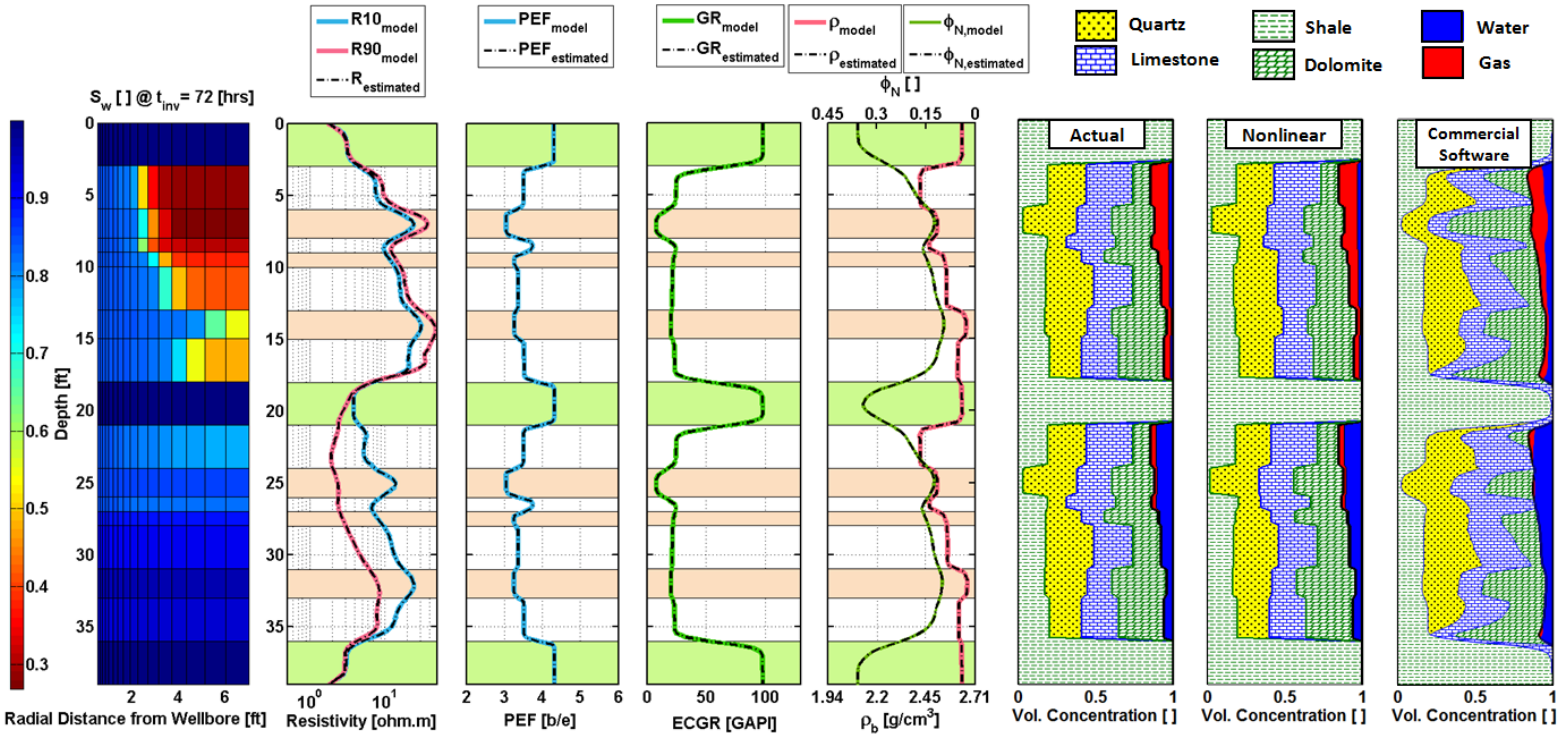


**Figure 4.7:** Synthetic Case No. 3, consisting of multi-layer, successive thin beds in two hydraulically separated gas-bearing and water-bearing zones. Comparison of final simulated well logs (dash-dotted black line) and input well logs (solid line). The left-hand panel shows the spatial distribution (radial and vertical directions) of water saturation after 3 days of WBM-filtrate invasion. Results are shown for array-induction resistivity (second left-hand panel), PEF (third left-hand panel), GR (fourth left-hand panel), density and neutron porosity (water-filled limestone porosity units, fifth left-hand panel) logs. The three right-hand panels compare volumetric concentrations of shale and mineral constituents, porosity, and water saturation obtained from conventional linear and nonlinear joint inversion (Method No. 1) of resistivity, density, neutron porosity, GR, and PEF logs against actual values.

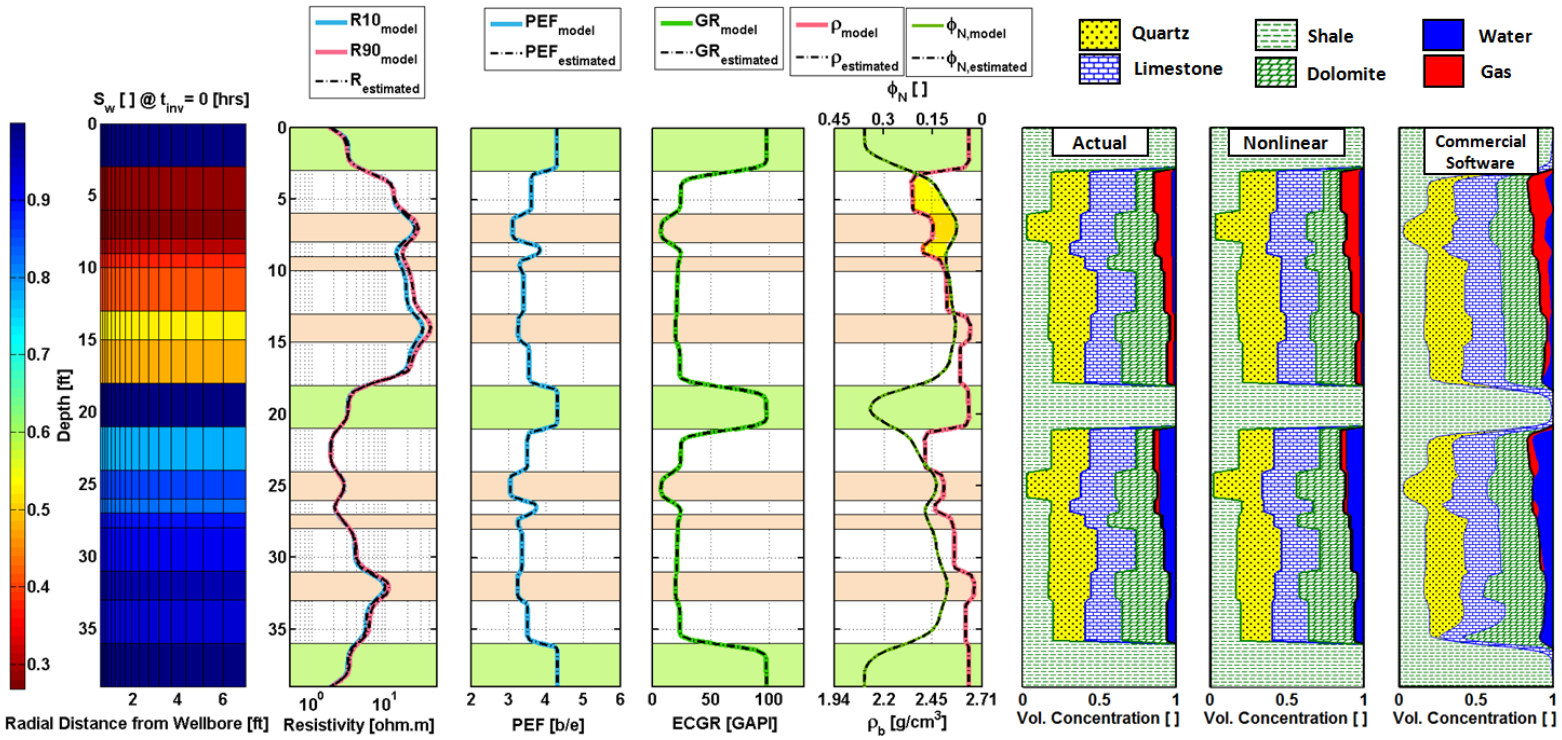


**Figure 4.8:** Synthetic Case No. 3, consisting of multi-layer, successive thin beds in two hydraulically separated gas-bearing and water-bearing zones. Comparison of final simulated well logs (dash-dotted black line) and input well logs (solid line). The left-hand panel shows the spatial distribution (radial and vertical directions) of water saturation before WBM-filtrate invasion. Results are shown for array-induction resistivity (second left-hand panel), PEF (third left-hand panel), GR (fourth left-hand panel), density and neutron porosity (water-filled limestone porosity units, fifth left-hand panel) logs. The three right-hand panels compare volumetric concentrations of shale and mineral constituents, porosity, and water saturation obtained from conventional linear and nonlinear joint inversion (Method No. 2) of resistivity, density, neutron porosity, GR, and PEF logs against actual values.

# Chapter 5: Petrophysical and Compositional Evaluation of Carbonate Formations Based on Nonlinear Joint Inversion of Conventional Well Logs

Chapter 4 introduced new petrophysical/compositional interpretation techniques based on conventional well logs for formations with complex lithology, including thin beds, and influenced by mud-filtrate invasion. Such techniques adopt different strategies for nonlinear joint inversion of nuclear and resistivity logs to assess porosity and volumetric/weight concentrations of mineral/fluid constituents. One particular application of the methods introduced is petrophysical and compositional evaluation of carbonate formations, where complex lithology and thin beds are commonplace.

This chapter documents the successful application of the newly introduced methods (Chapter 4) on two carbonate formations. We compare results obtained from (a) the nonlinear joint inversion method, (b) commercial software, and (c) core/X-Ray Diffraction (XRD) data (whenever available). For one of the carbonate field examples, where XRD data are available, the comparison shows that nonlinear joint inversion improves the assessment of porosity by more than 30%.

## 5.1 INTRODUCTION

Chapter 4 introduced three methods to estimate porosity and volumetric/weight concentrations of mineral/fluid constituents in thinly-bedded formations with complex lithology and invaded with mud-filtrate invasion. The focus of the present chapter is on the application of the previously introduced methods to carbonate formations. Conventional compositional evaluation of carbonate formations includes commercial multi-mineral linear/semi-linear methods based on well logs, neutron-capture spectroscopy, gamma-ray (GR) spectroscopy, and core (i.e., XRD, Fourier Transform

Infrared Transmission (FTIR) spectroscopy, and X-Ray Fluorescence (XRF)) measurements. In Chapter 4, we showed that commercial multi-mineral linear/semi-linear software is not always reliable in the presence of complex lithology, thin beds, and mud-filtrate invasion. Neutron-capture spectroscopy and gamma-ray spectroscopy measurements are also affected by shoulder beds, which significantly influence mineralogy assessment in thin beds. Core measurements are known to be the most accurate reference for petrophysical/compositional assessment. However, they are limited to small sparse samples along the wellbore. Additionally, XRD and FTIR spectroscopy measurements are not reliable in the evaluation of some minerals such as clay and quartz (Sondergeld et al., 2010). The previously introduced methods and the numerical synthetic examples of Chapter 4 are promising for the assessment of challenging formations such as carbonates.

Among the three methods introduced in Chapter 4, the first method takes into account the radial distribution of fluid saturation on well logs and numerically corrects inversion results for the effect of mud-filtrate invasion as well as shoulder-bed effects. The second method consists of two steps, separate inversion of well logs to assess bed physical properties and joint inversion of bed properties to estimate formation properties. This method is efficient for thinly-bedded formations where mud-filtrate invasion is negligible. The third method is a depth-by-depth/layer-by-layer inversion technique, which is recommended for formations with thick beds and complex lithology.

Carbonate formations studied in this chapter consist of thin beds and have complex lithology, including quartz, calcite, dolomite, clay minerals, and heavy minerals such as siderite. We observe no separation between apparent resistivity logs, which is an indication either of negligible or of very deep mud-filtrate invasion. Thus, it is not necessary to correct for the effect of invasion in these two cases.

In the field examples considered in this chapter, where mud-filtrate invasion is very deep or negligible, one can use either the first or the second method. However, the second method is preferable to reduce CPU time. The second method, referred to as fast nonlinear joint inversion of bed physical properties, estimates bed properties corrected for shoulder-bed effects by inverting well logs individually. Next, it uses Schlumberger's commercial software, SNUPAR, to assess porosity and volumetric/weight concentrations of mineral constituents.

Finally, we compare results obtained from nonlinear joint inversion methods against (a) results obtained from commercial software and (b) XRD/core data, wherever available. Commercial multi-mineral software requires XRD data for calibration when assessing volumetric/weight concentrations of mineral constituents in field examples. XRD data in water-saturated zones are preferable for model calibration when using commercial software. However, there are no XRD data available for Field Example No. 2 and no XRD data are available in the water-saturated zones of the Field Example No. 1. Thus, we have not calibrated the model used in commercial software with XRD/core data in the second field example.

The following sections provide a brief explanation of the formation properties and the results of petrophysical/compositional evaluation in the two field examples.

## 5.2 FIELD EXAMPLE NO. 1: HYDROCARBON-BEARING CARBONATE FORMATION

Field Example No. 1 considers a hydrocarbon-bearing carbonate formation. Based on sedimentological studies, reservoir facies consist of sandstone, mixed sandstone, dolostone, pelecypod limestone, foraminiferal limestone-siltstone, and shale, deposited in a shallow-marine carbonate platform. The presence of a variety of minerals in the formation makes it difficult to estimate porosity using conventional methods. Possible

inaccuracies in the estimation of volumetric concentrations of mineral constituents may lead to measurable errors in the assessment of porosity and water saturation. Drilling mud is water-base mud (WBM) and well logs were sampled at a rate of 0.5 ft. **Table 5.1** summarizes the average petrophysical properties assumed for the oil-bearing bed in this field example. Average values of porosity, water saturation, and volumetric concentration of shale are used as a uniform, parsimonious guess to initialize the nonlinear inversion. The rock is also assumed to be composed of pure dolomite as part of the initialization of nonlinear inversion.

Core measurements indicate that the formation exhibits very low permeability and porosity. On the other hand, the separation between shallow and deep dual laterolog resistivity logs is negligible and there is no cross-over between neutron porosity and density logs. Thus, we may safely assume that mud-filtrate invasion is very deep and that its corresponding differential effect on well logs is not significant. The saturating fluid in the invaded formation is therefore mud filtrate, residual hydrocarbon, and free hydrocarbon, which is not displaced by mud filtrate. **Table 5.2** summarizes the assumed Archie's parameters and matrix, fluid, and formation properties. Well logs available for nonlinear inversion are GR, dual laterolog resistivity, density, and neutron porosity. Due to the presence of barite in the mud, the photoelectric factor (PEF) log is not available in this case.

The mineralogical composition reported from laboratory measurements indicates that the rock matrix includes dolomite, quartz, limestone, siderite, pyrite, and K-feldspar, with illite as the predominant clay type. This analysis is available at a few points in the depth zone of interest with an implicit measurement error of ±0.15 for volumetric mineral concentrations. Because the average volumetric concentrations of pyrite and K-feldspar

are lower than 0.04 in the depth zone of interest, we neglect them in the nonlinear inversion. This choice helps to reduce significant non-uniqueness in the estimation.

We observe that resistivity values in layers No. 2 and No. 6 suddenly increase to 500 ohm.m, but this sharp change is not detected in other well logs. Presence of non-connected porosity could be the reason of such a behavior. The physics of resistivity measurements is conducive to the detection of inter-connected porosity, while that of density and neutron porosity logs is conducive to the detection of total porosity. Therefore, it is possible that the inversion underestimates resistivity values across those layers.

**Figure 5.1** compares the measured well logs to those obtained from final inversion products. The same figure compares volumetric concentrations of mineral constituents and petrophysical properties obtained from nonlinear inversion against mineralogical and porosity measurements performed on core samples and estimations performed with commercial linear inversion software. **Table 5.3** describes the final estimates of non-shale porosity and water saturation in permeable layers.

Even though the PEF log is not available as an input for inversion, estimates of porosity and volumetric concentrations of mineral constituents obtained with nonlinear inversion agree with those of core measurements. On the other hand, the commercial linear method over-estimates porosity by a factor of three. It is likely that the biased estimations of petrophysical properties and volumetric mineral concentrations obtained with commercial linear estimation software are due to unaccounted shoulder-bed effects or unaccounted nonlinear relationship between formation petrophysical/compositional properties and well logs. Even though the depth zone of interest is a hydrocarbon-bearing interval with no water production, the two commercial inversion methods estimate average water saturation higher than 0.50, which is due to deep WBM invasion.

Nonlinear inversion is also unable to estimate initial water saturation in this case due to very deep mud-filtrate invasion, which makes resistivity logs insensitive to dynamic petrophysical properties.

## 5.3 FIELD EXAMPLE NO. 2: THINLY-BEDDED HYDROCARBON-BEARING CARBONATE FORMATION

Field Example No. 2 is another hydrocarbon-bearing carbonate formation. Core measurements indicate that porosity and permeability vary in the range of 0.15-0.20 and 3-23 md, respectively, in the zone of interest. Available conventional well logs input to the inversion include PEF, GR, density, neutron porosity, and laterolog electrical resistivity with a sampling rate of 0.5 ft. Drilling mud is WBM. Inversion starts with an initial guess obtained from average porosity, water saturation, and volumetric concentration of shale calculated from conventional petrophysical interpretation techniques (**Table 5.4**). Mineral types are usually identified based on available XRD data. However, in this field example, XRD data are not available. Thus, we assume that the formation contains common rock minerals found in carbonate formations including quartz, dolomite, and calcite. Clay type is also assumed to be illite. Initial guess for volumetric concentrations of mineral constituents is arbitrarily chosen to be equal to concentration of each. In Field Example No. 2, the choice of initial guess is not crucial because the inverse problem is even-determined (PEF is reliable and, consequently, the number of well logs and unknown parameters are equal).

The separation between shallow and deep dual laterolog resistivity logs is negligible. Consequently, we assume that mud-filtrate invasion is either very deep or very shallow and that its corresponding differential effect on well logs is not significant. The assumed Archie's parameters and matrix, fluid, and formation properties are listed in **Table 5.5**.

**Figure 5.2** compares the measured well logs and their numerical simulations. Additionally, the same figure includes the final petrophysical and compositional estimates obtained with commercial software and those obtained from nonlinear inversion. **Table 5.6** compares the final estimates of non-shale porosity obtained with nonlinear inversion to core measurements in permeable layers, where they are available. Due to presence of non-connected porosity in this formation, estimated porosity values are lower than those of core measurements.

The estimates of volumetric concentrations of mineral constituents obtained with nonlinear joint inversion and commercial software are different. However, there are no XRD data available to validate either set of estimates in this case.

## 5.4 CONCLUSIONS

Chapter 5 documents successful applications of the nonlinear joint inversion methods introduced in Chapter 4 on two carbonate formations with complex lithology. Results obtained for both examples were compared against results obtained with commercial software. Inputs to inversion include any combination of conventional well logs such as density, neutron porosity, electrical resistivity, GR, and PEF, as well as formation properties such as Archie's parameters, in-situ fluid properties, and type and chemical formula of available minerals. In Field Example No. 1, a PEF log was not available and the inversion is under-determined. However, in the absence of PEF, comparison of the estimates for porosity, water saturation, and volumetric concentrations of mineral constituents against core/XRD data indicated improvements of more than 30% in the assessment of porosity. Estimates of water saturation, however, are not reliable, due to the presence of very deep WBM-filtrate invasion.

In Field Example No. 1, volumetric concentration of clay estimated by the nonlinear joint inversion method was greater than the values reported by XRD measurements. Such a difference is expected because XRD measurements usually underestimate clay concentration (Sondergeld et al., 2010). Comparison of results obtained with nonlinear joint inversion against commercial software results, however, shows a significant difference. This behavior can be explained by the complex lithology in both field examples and also the thin beds and shoulder-bed effects in the second field example.

The inverse problem in this study was under-determined in Field Example No. 1 and even-determined in Field Example No. 2. By adding another unknown (e.g., non-connected porosity) to the problem, both cases become under-determined and non-uniqueness of results becomes inevitable. Consequently, one cannot reliably distinguish between interconnected and non-connected porosity. However, the interpretation method enables including both inter-connected and non-connected porosity in the petrophysical model to quantify their corresponding influence on well logs.

**Table 5.1:** Carbonate Field Example No. 1: Summary of calculated averaged petrophysical properties.

| Variable | Value | Units |
|---|---|---|
| Thickness | 28 | ft |
| Absolute permeability, $k$ | 0.46 | md |
| Non-shale porosity, $\phi_s$ | 0.057 | [ ] |
| Volumetric concentration of shale, $C_{sh}$ | 0.25 | [ ] |

**Table 5.2:** Carbonate Field Example No. 1: Summary of assumed Archie's parameters and matrix, fluid, and formation properties.

| Variable | Value | Units |
|---|---|---|
| Archie's tortuosity factor, $a$ | 1.00 | [ ] |
| Archie's cementation exponent, $m$ | 2.00 | [ ] |
| Archie's saturation exponent, $n$ | 2.00 | [ ] |
| Connate water salt concentration | 125 | kppm NaCl |
| Mud filtrate resistivity at 194°F | 0.09 | ohm.m |
| Water density | 1.00 | $g/cm^3$ |
| Water viscosity | 1.00 | cp |
| In-situ oil density | 0.70 | $g/cm^3$ |
| Formation temperature | 194 | °F |
| Wet clay density | 2.54 | $g/cm^3$ |
| Volumetric concentration of clay | 0.60 | [ ] |
| Shale porosity | 0.03 | [ ] |
| Wellbore radius | 10.63 | cm |

**Table 5.3:** Carbonate Field Example No. 1: Nonlinear inversion results obtained for porosity and water saturation for each layer.

| Layer No. | Layer thickness [ft] | $\phi_s$ | $S_w$ |
|---|---|---|---|
| 1 | 3.5 | 0.001 | 0.45 |
| 2 | 2.5 | 0.08 | 0.17 |
| 3 | 3.0 | 0.02 | 0.64 |
| 4 | 2.0 | 0.05 | 0.34 |
| 5 | 3.5 | 0.09 | 0.21 |
| 6 | 4.0 | 0.07 | 0.15 |
| 7 | 2.5 | 0.04 | 0.57 |

**Table 5.4:** Carbonate Field Example No. 2: Summary of calculated averaged petrophysical properties.

| Variable | Value | Units |
|---|---|---|
| Thickness | 71 | ft |
| Absolute permeability, $k$ | 20 | md |
| Non-shale porosity, $\phi_s$ | 0.19 | [ ] |
| Volumetric concentration of shale, $C_{sh}$ | 0.15 | [ ] |

**Table 5.5:** Carbonate Field Example No. 2: Summary of assumed Archie's parameters and matrix, fluid, and formation properties.

| Variable | Value | Units |
|---|---|---|
| Archie's tortuosity factor, *a* | 1 | [ ] |
| Archie's cementation exponent, *m* | 1.5 | [ ] |
| Archie's saturation exponent, *n* | 2 | [ ] |
| Connate water salt concentration | 200 | kppm NaCl |
| Water density | 1.0 | $g/cm^3$ |
| Water viscosity | 1.0 | cp |
| In-situ oil density | 0.8 | $g/cm^3$ |
| Formation temperature | 210 | °F |
| Wet clay density | 2.54 | $g/cm^3$ |
| Volumetric concentration of clay | 0.90 | [ ] |
| Shale porosity | 0.02 | [ ] |
| Wellbore radius | | cm |

**Table 5.6:** Carbonate Field Example No. 2: Nonlinear inversion results obtained for porosity and water saturation for each layer.

| Depth [ft] | Estimated porosity | Core porosity |
|---|---|---|
| X526 | 0.12 | 0.153 |
| X545 | 0.19 | 0.203 |
| X553 | 0.19 | 0.202 |

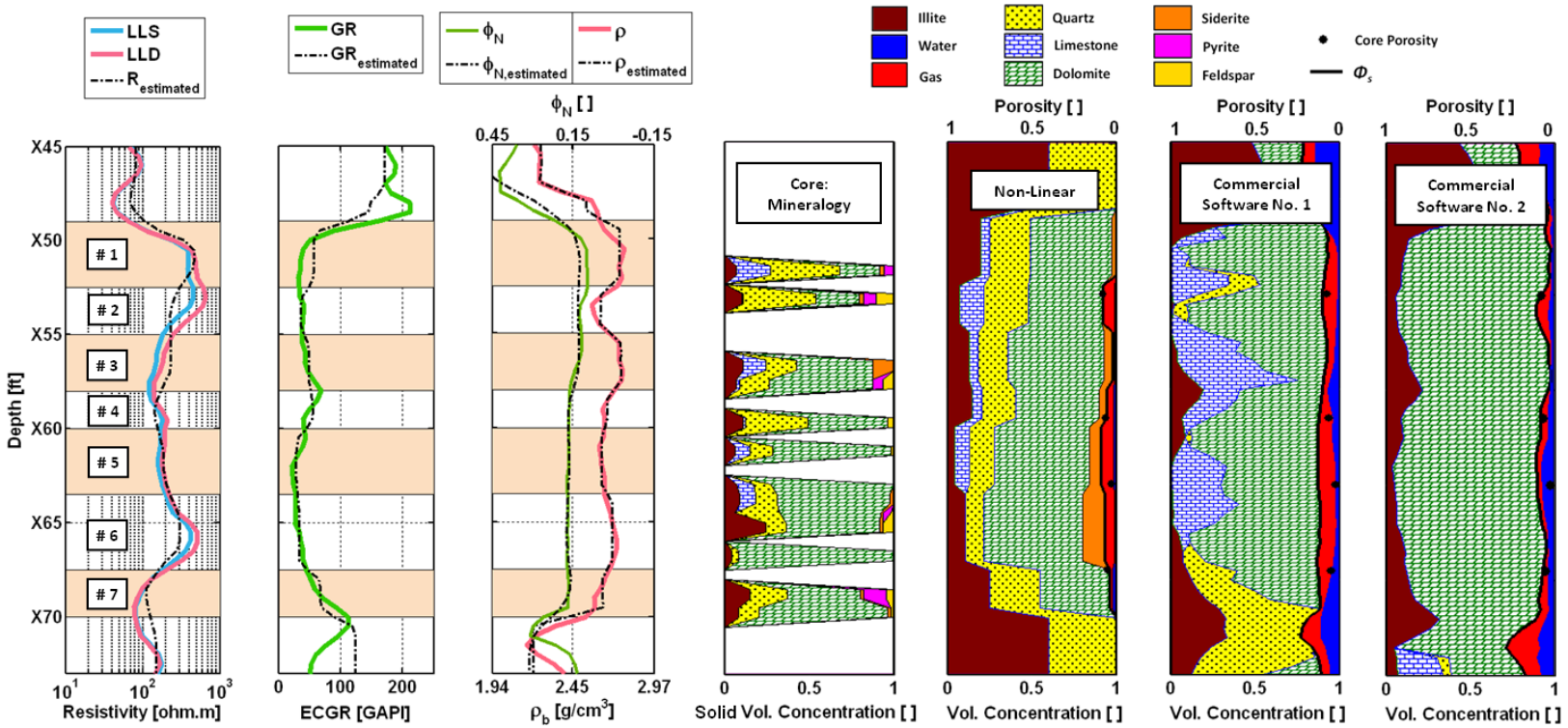


**Figure 5.1**: Carbonate Field Example No. 1: Comparison of final simulated well logs (black dash-dotted line) and measured logs (solid line). Results are shown for dual laterolog resistivity (left-hand panel), GR (second left-hand panel), density and neutron porosity (water-filled limestone porosity units, third left-hand panel) well logs. The center panel shows the map of solid volumetric concentrations of mineral components obtained from mineralogical analysis. The first two right-hand panels describe volumetric concentrations of mineral constituents, porosity, and water saturation obtained from two commercial software. The third right-hand panel includes the same properties obtained from nonlinear joint inversion of resistivity, density, neutron porosity, and GR logs.

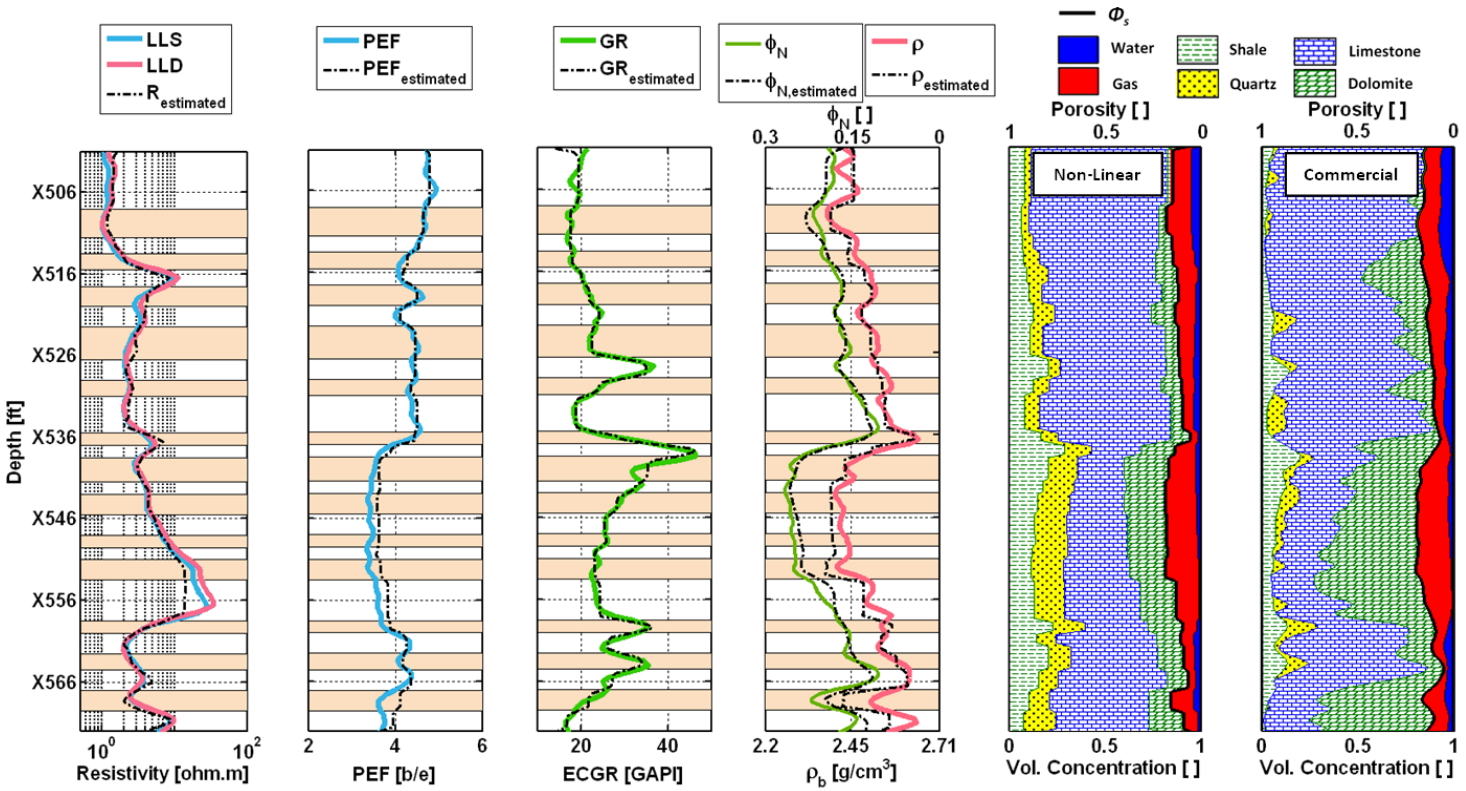


**Figure 5.2**: Carbonate Field Example No. 2: Comparison of final simulated well logs (black dash-dotted line) and measured logs (solid line). Results are shown for dual laterolog resistivity (left-hand panel), PEF (second left-hand panel), GR (third left-hand panel), density and neutron porosity (water-filled limestone porosity units, fourth left-hand panel) well logs. The first right-hand panel describes volumetric concentrations of mineral constituents, porosity, and water saturation obtained from commercial software. The second right-hand panel describes the same properties obtained from nonlinear joint inversion of resistivity, density, neutron porosity, and GR logs.

# Chapter 6: Quantitative Method for Estimating Total Organic Carbon and Porosity, and for Diagnosing Mineral Constituents from Well Logs in Shale-Gas Formations

Reliable estimates of shale properties are critical for detecting perforation zones or candidates for hydro-fracturing jobs. Current methods for in-situ compositional and petrophysical assessment of organic-shale formations are largely based on qualitative responses and empirical formulae. Even core-based measurements can be inconsistent and inaccurate when evaluating clay minerals and other grain constituents.

In this chapter, we test the application of one of the interpretation methods introduced in Chapter 4 for organic-shale evaluation from well logs. The objective is to estimate total porosity, total organic carbon (TOC), and volumetric/weight concentrations of mineral/fluid constituents. After detecting bed boundaries, the first step of the method is to perform separate inversion of individual well logs to estimate bed properties such as density, neutron migration length, electrical conductivity, photoelectric factor (PEF), and thorium (Th), uranium (Ur), and potassium (K) volumetric concentrations. Next, we construct a multi-layer petrophysical model specific to organic shale using an initial guess obtained from conventional petrophysical interpretation or from X-Ray Diffraction (XRD) data; we calculate bed properties using the initial layer-by-layer values. Final estimates of organic shale properties are obtained by progressively minimizing the difference between calculated and measured bed properties. A unique advantage of this method is the possibility of implicitly correcting for shoulder-bed effects on well logs, which are prevalent in shale-gas plays. Another advantage is the possibility of calculating accurate well-log responses for specific petrophysical, mineral, fluid, and kerogen properties.

Examples are described of the successful application of the new organic-shale evaluation method in the Haynesville shale-gas formation. This formation includes complex solid compositions and thin beds where rapid depth variations of both mineral/fluid constituents are commonplace. Comparison of estimates for total porosity, total water saturation, and TOC obtained from (a) conventional commercial software, (b) our organic-shale evaluation method, and (c) core/XRD measurements indicates an improvement of more than 50% in estimates of total porosity and water saturation when calculated with the newly developed method. The estimated TOC is also in agreement with core laboratory measurements.

## 6.1 INTRODUCTION

Evaluation of shale properties such as TOC, total porosity, gas-filled porosity, fluid saturation, and grain composition remains a technical challenge to the petroleum industry. Conventional log interpretation methods are not reliable for these unconventional reservoirs, and no general guidelines exist for the petrophysical interpretation of organic-shale formations.

Accurate mineralogy evaluation, in addition to geological knowledge, can improve the evaluation of in-situ mechanical properties and, consequently, aid in determining perforation intervals in hydrocarbon-bearing shale. Improving estimates of volumetric concentrations of mineral constituents also improves the estimation of porosity, TOC, and water saturation. Several methods have been developed to estimate or measure volumetric/weight concentrations of mineral constituents, including commercial multi-mineral linear solvers, neutron-capture spectroscopy, gamma-ray spectroscopy, and core measurements (i.e., XRD, Fourier Transform Infrared Transmission (FTIR) spectroscopy, and X-Ray Fluorescence (XRF) measurements). Even though some of

these methods are reliable in conventional reservoirs, they are not in the presence of thin beds and complex mineral compositions. Among such methods, core measurements are thought to provide the most reliable estimates of mineral concentrations. Even XRD and FTIR spectroscopy measurements can be inconsistent and inaccurate when evaluating clay minerals and, sometimes, grain constituents (Sondergeld et al., 2010).

Assessment of TOC in organic-shale formations is another salient technical challenge. Uranium concentration is usually considered for the estimation of TOC. However, there is not always a statistical correlation between uranium concentration, gamma-ray (GR) response, and TOC (Passey et al., 2010). Passey et al. (1990) introduced and later revised (Passey et al., 2010) the $\Delta$logR technique to estimate TOC, which has become popular among shale-gas petrophysicists.

Evaluating total porosity and fluid saturations requires accurate density estimates of pure minerals and their volumetric concentrations, as well as a reliable fluid saturation model. Uncertainty always exists, however, in density estimation for kerogen and clay minerals. Most of the available saturation models also depend on electrical resistivity logs, which are themselves affected both by pyrite and by the semi-conductor kerogen often present in hydrocarbon-bearing shale. Fundamental research is still needed to advance reliable saturation-resistivity models for shale-gas formations.

In addition to complications in estimating TOC, gas-filled porosity, and volumetric concentrations of mineral/fluid constituents in shale-gas formations, significant spatial heterogeneity and prevalent thin beds make well-log interpretation significantly more challenging than in conventional plays. Some publications describe algorithms and techniques for optimized well-log interpretation in organic-shale formations (Quirein et al., 2010). However, none of the conventional depth-by-depth well-log interpretation methods addresses the problem of shoulder-bed effects due to

inter-bedding in shale-gas formations. Shoulder-bed effects are not only observed in well logs such as neutron-capture spectroscopy, but can also bias conventional interpretation methods when implemented directly on well logs.

Recent publications have introduced new methods to reduce shoulder-bed effects, to improve the petrophysical interpretation of thinly-bedded siliciclastic formations (Sanchez-Ramirez et al., 2009), and to improve lithology evaluation in thinly-bedded invaded carbonates and siliciclastic formations (Heidari et al., 2010). In this chapter, we adapt a method previously introduced in Chapter 4 to reduce shoulder-bed effects in the evaluation of mineral/fluid compositions on the interpretation of organic shale formations.

The adaptation of one of the methods introduced in Chapter 4 includes a new automatic nonlinear joint inversion method to estimate volumetric/weight concentrations of mineral constituents, fluid, and kerogen from well logs in the presence of complex matrix composition in organic-shale formations. We first detect bed boundaries using all the available well logs or borehole images. Next, we apply separate inversion of density, neutron porosity, electrical resistivity, GR-spectroscopy, and PEF measurements to estimate density, electrical conductivity, Th, Ur, K, and PEF in each bed of the multi-layer formation. A multi-layer petrophysical model is then constructed with an initial guess for petrophysical properties and volumetric/weight concentrations of mineral constituents and kerogen. Based on the volumetric concentrations of minerals/fluids and their chemical formulae, we calculate neutron migration length and PEF using Schlumberger's SNUPAR commercial software (McKeon and Scott, 1989). Likewise, we calculate electrical conductivity, density, and Th, Ur, and K concentrations in each bed. The difference between estimated and calculated bed properties is then progressively

decreased by updating volumetric/weight concentrations of mineral/fluid constituents in the multi-layer model.

The following sections briefly describe the adapted nonlinear joint inversion method for assessment of volumetric concentrations of mineral/fluid constituents in hydrocarbon-bearing shale. We document an example of application for one challenging synthetic organic-shale formation constructed to replicate an actual field example and for field data acquired in the Haynesville shale-gas formation.

## 6.2 METHOD

In Chapter 4, we introduced a nonlinear joint inversion method referred to "fast nonlinear joint inversion of bed physical properties", to estimate volumetric concentrations of mineral constituents, porosity, and fluid saturations in thinly-bedded shaly-sand and carbonate formations from conventional well logs. This method was found to perform best on reservoirs where mud-filtrate invasion is negligible or could be assumed to be piston-like. In the case of organic-shale formations, we assume that mud-filtrate invasion effects are negligible. Following this assumption, the fast nonlinear joint inversion of bed properties becomes an effective method for petrophysical/compositional evaluation of organic-shale formations with complex lithology and thin beds. In the present chapter, we modify the method referred to "fast nonlinear joint inversion of bed physical properties" for organic-shale formations by adopting a petrophysical model for organic shale to accurately correlate volumetric/weight concentrations of mineral/fluid constituents with well logs. The following sections describe the assumed petrophysical model for organic shale and briefly explain the adapted inversion technique.

### 6.2.1 Assumed Model for Organic Shale

Several recent publications assume a petrophysical model for organic shale which includes organic matter, non-organic minerals (e.g., clay minerals and non-clay minerals), and total pore space (Quirein et al., 2010; Passey et al., 2010; Ambrose et al., 2010; LeCompte et al., 2009). The total pore space consists of bound water saturation, free water saturation, hydrocarbon saturation (e.g., sorbed gas and free gas saturation), and isolated pore volume. **Figure 6.1** describes the petrophysical model assumed by our inverse/forward numerical simulations of petrophysical properties and well logs in organic-shale formations.

Although the adopted petrophysical model for organic shale contains bound water saturation, free water saturation, and isolated pore volume, the inversion method introduced in this chapter only estimates total porosity and total water/hydrocarbon saturation in organic-shale formations.

### 6.2.2 Joint Inversion of Well Logs to Assess Shale Properties

Among the three methods introduced in Chapter 4 for joint inversion of well logs, we choose the second method, referred to "fast nonlinear joint inversion of bed physical properties". The main reasons for this choice are (a) the method's efficiency in the presence of thin beds, and (b) the fact that we can assume negligible mud-filtrate invasion in organic shale.

The adapted organic-shale interpretation method starts with pre-analysis of well logs such as density, neutron porosity, electrical resistivity, PEF, and GR/GR-spectroscopy. Pre-analysis includes data quality control, depth shifting, and the assessment of formation mineral/fluid types and properties. Then, we detect bed boundary locations based on any desired combination of well logs or image logs. In this chapter, bed boundary locations are chosen based on inflection points of density, PEF,

and array-induction apparent resistivity logs. The next step is the separate inversion of well logs, which yields bed physical properties such as layer-by-layer density, neutron migration length, electrical conductivity, PEF, and Ur, Th, and K concentrations. We implement a linear algorithm for density, PEF, and GR-spectroscopy inversion, and a nonlinear gradient-based algorithm for neutron porosity and resistivity inversion. This step makes it possible to obtain accurate results in the presence of shoulder-bed effects in thinly-bedded formations. Finally, we apply a nonlinear joint inversion algorithm on the estimated bed properties using Schlumberger's SNUPAR commercial software (McKeon and Scott, 1989) to estimate layer-by-layer shale properties, including total porosity, TOC, total water saturation, and volumetric/weight concentrations of mineral constituents. The assumed shale petrophysical model, together with the resistivity model assumed in organic-shale formations, are the link between bed properties (density, neutron migration length, electrical conductivity, PEF, and Ur, Th, and K concentrations) and shale properties (total porosity, total water saturation, TOC, and volumetric/weight concentrations of mineral constituents).

In organic-shale formations, the number of unknown shale properties is usually greater than the number of available well logs, which causes non-uniqueness of results. To mitigate non-uniqueness of results, the choice of initial guess for the joint inversion becomes important. Additionally, a realistic initial guess expedites the convergence rate, and, consequently, reduces CPU time. We recommend three choices for initial guess: (a) an initial guess based on XRD/core data, (b) an initial guess based on point-by-point nonlinear joint inversion (Chapter 4), and (c) an initial guess based on conventional petrophysical interpretation and linear multi-mineral solvers. For the synthetic case, however, a parsimonious initial guess is chosen to test the robustness of the method.

## 6.3 SYNTHETIC CASE

We construct the synthetic case based on specific petrophysical properties of a Haynesville shale-gas field example. The objective is to investigate the efficiency of our estimation method in the presence of shoulder-bed effects, as well as in the presence of complex lithology and kerogen in organic-shale formations. The synthetic case consists of a combination of layers from 1 to 10 ft thickness and thin beds. Assumed mineral constituents and fluids include quartz, calcite, pyrite, illite, chlorite, plagioclase, kerogen, bound water, and gas. Mud-filtrate invasion effects on well logs are assumed to be negligible. Well logs input to the inversion are array-induction apparent resistivity, neutron porosity, density, PEF, and GR-spectroscopy (Th, Ur, and K logs). **Table 6.1** summarizes the assumed formation properties for this synthetic case.

**Figure 6.2** compares numerically simulated well logs, separate inversion results for each log, and actual bed properties assumed in the multi-layer synthetic case. Although shoulder-bed effects are significant in thin beds, the difference between model and estimated bed properties is lower than 1%. There is a significant difference, however, between estimated and measured center-bed values of neutron migration length. In the next step, we use the estimated bed properties as inputs to the joint inversion algorithm to estimate static petrophysical properties and volumetric concentrations of mineral constituents and kerogen.

**Figure 6.3** compares initial guess, estimated values, and actual total porosity, water saturation, and volumetric concentrations of mineral constituents and kerogen. Error (uncertainty) bars for estimated properties in each layer were calculated by adding 5% zero-mean Gaussian random perturbations to all the well logs input to the inversion. The uncertainty of inversion products due to noisy data increases with decreasing layer thickness.

Next, we select center-bed values of each log as input to the joint inversion algorithm instead of results obtained from separate inversion of well logs. The difference between center-bed well-log values and actual bed properties is more significant for both neutron porosity and electrical resistivity, where less vertical resolution causes more severe shoulder-bed effects. **Figure 6.4** compares the actual volumetric concentrations of minerals, fluids, and kerogen and their estimated values obtained when choosing center-bed well-log values as inputs to the joint inversion. Neglecting shoulder-bed effects causes significant errors in estimates of volumetric concentrations of mineral constituents and kerogen (more than 20% in estimates of kerogen) across beds thinner than 3 ft.

## 6.4 FIELD EXAMPLE NO. 1: THE HAYNESVILLE SHALE-GAS FORMATION

Field Example No. 1 is a well located in the Haynesville shale-gas formation. It is selected to examine the accuracy and reliability of the introduced method for evaluation of organic-shale formations. The late-Jurassic Haynesville formation is located in east Texas and northwestern Louisiana. It was deposited in a restricted intra-shelf basin on the evolving Gulf Coast passive margin (Quirein et al., 2010; Spain et al., 2010). Mature TOC is between 2% and 5%, while clay content is usually lower than 50% (Quirein et al., 2010). Completion planning is critical in the Haynesville formation due to significant variations in mineral and petrophysical properties. Erroneous decisions about completion intervals can turn a potentially productive well into a poorly completed one (LeCompte et al., 2009).

For shale evaluation in this example, we use neutron porosity, density, array-induction resistivity, and PEF logs as inputs to the estimation methods. **Figure 6.5** shows the well logs in the selected depth interval in the Haynesville formation. The top zone is an organic-shale formation and the bottom zone is a carbonate formation. The focus of

the study is on the top zone; however, we also apply the method to the bottom zone to verify its accuracy and reliability in different formations.

The choice of initial guess is important in complex formations such as organic shale due to the pervasive non-uniqueness of inversion results in the presence of a large number of mineral constituents. In this field example, we choose an initial guess based on XRD data. In zones where XRD data are not available, the initial guess can be selected from results obtained with commercial/linear multi-mineral solvers.

Based on XRD reports and laboratory measurements we assume that the Haynesville shale consists of non-clay minerals such as quartz, calcite, plagioclase, pyrite, and negligible amount of dolomite, clay minerals such as illite and chlorite, and kerogen type II. The XRD analysis shows some minerals with less than 2% weight concentration. We eliminate those minerals in the estimation or lump them together with similar minerals to decrease non-uniqueness of inversion results.

Another way to reduce non-uniqueness of inversion results is to impose constraints on them. We investigate XRD data to explore possible correlations among volumetric/weight concentrations of minerals. **Figures 6.6a** and **6.6b** show linear relationships between weight concentrations of quartz and plagioclase, and weight concentrations of illite and chlorite, respectively. We enforce these linear relationships as constraints in the joint inversion to reduce non-uniqueness and increase accuracy of results.

Different rock types exhibit specific sets of formation properties, and consequently, specific sets of petrophysical properties, TOC, and mineral concentrations. Thus, rock classification is desirable in the compositional and petrophysical interpretation of organic shale. We classify rock types based on the estimated weight concentration of calcite, weight concentration of quartz, GR response, and porosity. Calcite and quartz are

chosen because they are the most dominant minerals in the formation. It is also possible to use clay concentration instead of GR. Estimates of the required parameters in rock classification can be obtained from either (a) XRD/core measurements or (b) values estimated with joint inversion. We choose the second approach for Field Example No. 1 because XRD data are not continuous and are not available at all desired depths.

To classify rock types based on inversion results, we first assume one rock type in the formation, estimate petrophysical properties, TOC, and volumetric/weight concentrations of mineral constituents via joint inversion, and perform rock-typing. After classifying rock types, we repeat the analysis and improve both shale petrophysical evaluation and rock classification. **Figure 6.7a** shows a cross-plot of final estimates for weight concentrations of quartz and calcite and the two classified rock types. The color bar identifies GR magnitude, which is roughly correlated with the amount of clay-minerals. In rock type B, weight concentration of calcite increases with a decrease in the weight concentration of quartz. GR magnitude and clay concentration also decrease in rock type B. **Figure 6.7b** describes the variation of porosity in addition to weight concentrations of calcite and quartz for the two rock types. Total porosity is smaller in rock type B than in rock type A. **Figure 6.8** shows the location of the two rock types in the well. Based on rock classification, we assign different Archie's parameters to rock types A and B in the estimation of properties via joint inversion.

**Table 6.2** summarizes the assumed Archie's parameters and matrix, fluid, and formation properties in Field Example No. 1. The well was drilled with water-base mud (WBM); however, we assume the effect of mud-filtrate invasion on well logs to be negligible.

**Figure 6.8** compares the final estimates of total porosity, total water saturation, TOC, and weight concentrations of mineral constituents against estimates obtained with

commercial software, XRD data, and core measurements. There is a good agreement between estimates of total porosity and total water saturation obtained with the two methods and core measurements. However, the commercial software yields errors higher than 80% and 50% in the assessment of total porosity and total water saturation, respectively. Estimates of weight concentrations of mineral constituents are also in agreement with XRD data, while the commercial software overestimates weight concentration of quartz and underestimates weight concentration of calcite. Estimates of TOC obtained with joint nonlinear inversion and commercial software are in agreement with laboratory measurements. In this example, we assumed a typical chemical formula for kerogen type II in the inversion. Estimates of volumetric/weight concentration of kerogen, and consequently, TOC, could be readily improved by adopting a more accurate chemical formula for kerogen.

Comparison of the results obtained with different methods for Field Example No. 1 confirms the accuracy and reliability of the nonlinear inversion methods introduced in this chapter for the petrophysical and compositional evaluation of organic shale. However, as in the case of most well-log interpretation methods, estimates obtained with joint nonlinear inversion are not reliable in the presence of washouts or other detrimental borehole conditions.

## 6.5 CONCLUSIONS

We successfully tested a new method for petrophysical evaluation of organic shale based on nonlinear joint inversion of conventional well logs. The method estimates total porosity, volumetric/weight concentration of kerogen, and volumetric/weight concentrations of mineral/fluid constituents, and was tested on both synthetic data and field data acquired in the Haynesville shale-gas formation. Accurate petrophysical and

compositional evaluation makes rock classification possible in organic shale. We observed an improvement of more than 50% in estimates of total porosity and water saturation obtained with nonlinear inversion compared to results obtained with commercial software. The estimated porosity, water saturation, and TOC were also in agreement with laboratory measurements in both field examples.

Most commercial software available requires either XRD/core data for calibration in the evaluation of lithology, or empirical relationships for assessment of TOC. The interpretation method introduced in this chapter does not require empirical relationships to estimate volumetric/weight concentration of kerogen or arbitrary calibration factors. Only reliable chemical formulae for kerogen and mineral constituents are necessary to secure reliable results. Another advantage of the new organic-shale evaluation method over conventional methods (e.g., commercial/linear multi-mineral software and neutron-capture spectroscopy) is that it implicitly reduces shoulder-bed effects in the presence of thin beds, which is a significant concern in the petrophysical evaluation of organic shale. The interpretation method introduced in this chapter evaluates properties across depth intervals where well logs are available with minor pre-processing and/or calibration efforts. This feature becomes important in cases where XRD measurements and/or core date are sparse.

Inputs to the joint inversion method are conventional well logs, such as density, neutron porosity, electrical resistivity, GR/GR-spectroscopy, and PEF. The method remains stable in the absence of any of these logs. Non-uniqueness of results increases, however, with a decrease in the number of input logs and an increase in the number of unknown formation properties. In such cases, both an accurate initial guess and the enforcement of model or data constraints can improve the results.

Even though in most of the test examples the method introduced was reliable and accurate to evaluate shale properties, the presence of layers thinner than 3 ft and more than 5% Gaussian random noise in well logs affected the estimates of total porosity and water saturation by more than 30% and the estimates of weight concentration of kerogen by more than 10%. Consequently, results will not be reliable in the presence of washouts or detrimental borehole conditions. We found that separate inversion of well logs can be used to diagnose dubious quality data. Well-log inversion is also helpful in detecting depth shifts in well logs. Inaccuracies in bed-boundary locations, as well as depth-shifts in well logs, can significantly affect inversion results. Moreover, the effect of bed-boundary location on inversion results is more significant in the presence of thin beds.

**Table 6.1:** Synthetic Case: summary of assumed Archie's parameters and fluid and formation properties.

| Variable | Value | Units |
|---|---|---|
| Archie's tortuosity factor, *a* | 1.00 | [ ] |
| Archie's cementation exponent, *m* | 2.00 | [ ] |
| Archie's saturation exponent, *n* | 2.00 | [ ] |
| Connate water salt concentration | 200 | kppm NaCl |
| Bound water salt concentration | 200 | kppm NaCl |
| Water density | 1.00 | g/cm3 |
| Gas density | 0.0016 | g/cm3 |
| Formation temperature | 265 | °F |
| Wellbore radius | 21.59 | cm |

**Table 6.2:** Field Example No. 1: summary of assumed Archie's parameters and matrix, fluid, and formation properties.

| Variable | Value | Units |
|---|---|---|
| Archie's tortuosity factor, *a* | 1.00 | [ ] |
| Archie's cementation exponent, *m*, for Rock Type A | 1.60 | [ ] |
| Archie's cementation exponent, *m*, for Rock Type B | 2.00 | [ ] |
| Archie's saturation exponent, *n* | 2.00 | [ ] |
| Connate water salt concentration | 200 | kppm NaCl |
| Bound water salt concentration | 200 | kppm NaCl |
| Water density | 1.00 | g/cm3 |
| Gas density | 0.0016 | g/cm3 |
| Kerogen density | 1.2 | g/cm3 |
| Dry clay density | 2.84 | g/cm3 |
| Formation temperature | 265 | °F |
| Wellbore radius | 11.11 | cm |

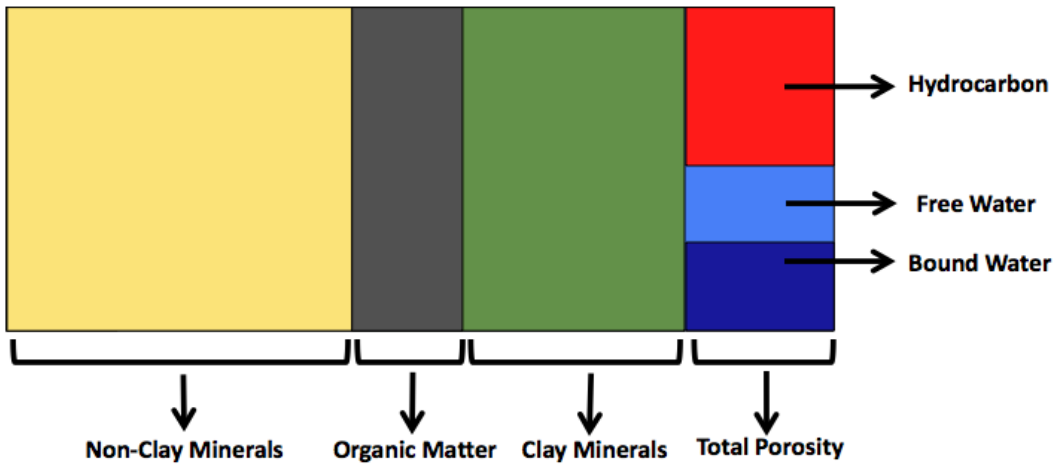


**Figure 6.1:** Petrophysical model for organic shale assumed in forward/inverse numerical simulations described in this chapter.

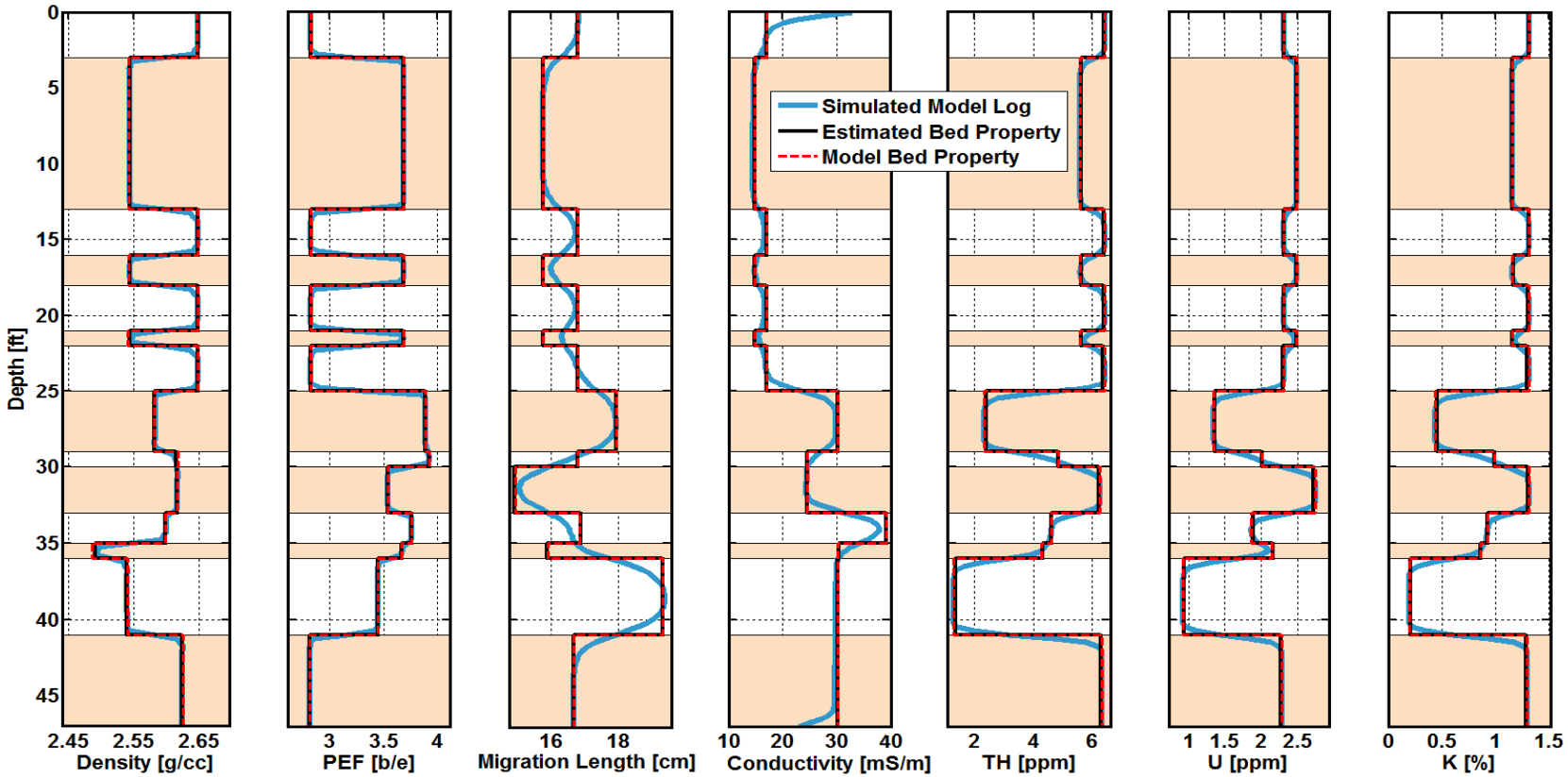


**Figure 6.2:** Synthetic Case: Comparison of simulated model (actual) logs (blue solid line), model bed properties (black solid line), and bed properties estimated from separate inversion of well logs (red dashed line). Panels from left to right show density, PEF, neutron migration length, electrical conductivity, and volumetric concentrations of Th, Ur, and K.

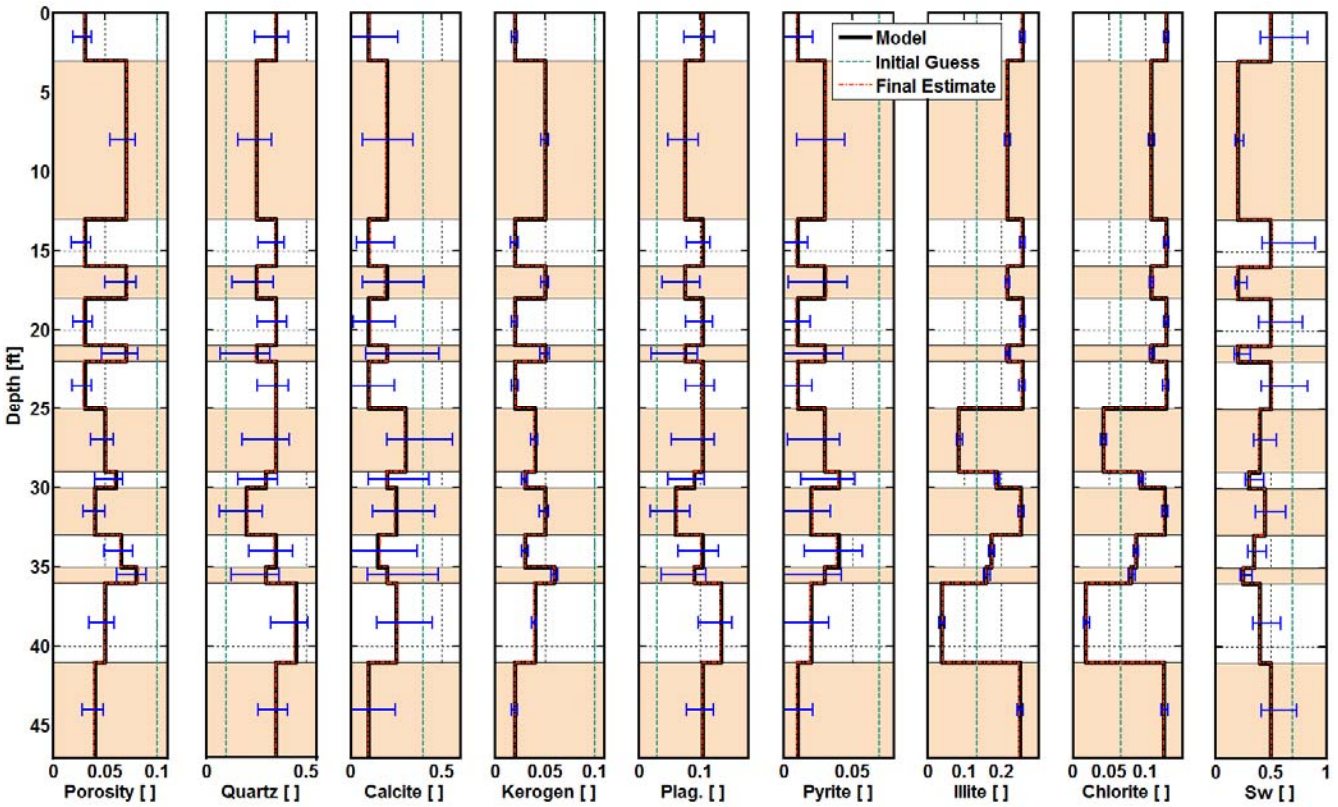


**Figure 6.3:** Synthetic Case: Comparison of model (actual) values (black solid line), initial guess (green dashed line), and final estimates (red dash-dotted line) of volumetric concentrations of mineral constituents, total porosity, volumetric concentration of kerogen, and total water saturation along with corresponding uncertainty bars (calculated with 5% zero-mean Gaussian random perturbations on the original synthetic well logs, including array-induction resistivity, density, neutron porosity, GR-spectroscopy, and PEF). Panels from left to right show total porosity, volumetric concentrations of quartz, calcite, kerogen, plagioclase, pyrite, illite, chlorite, and total water saturation.

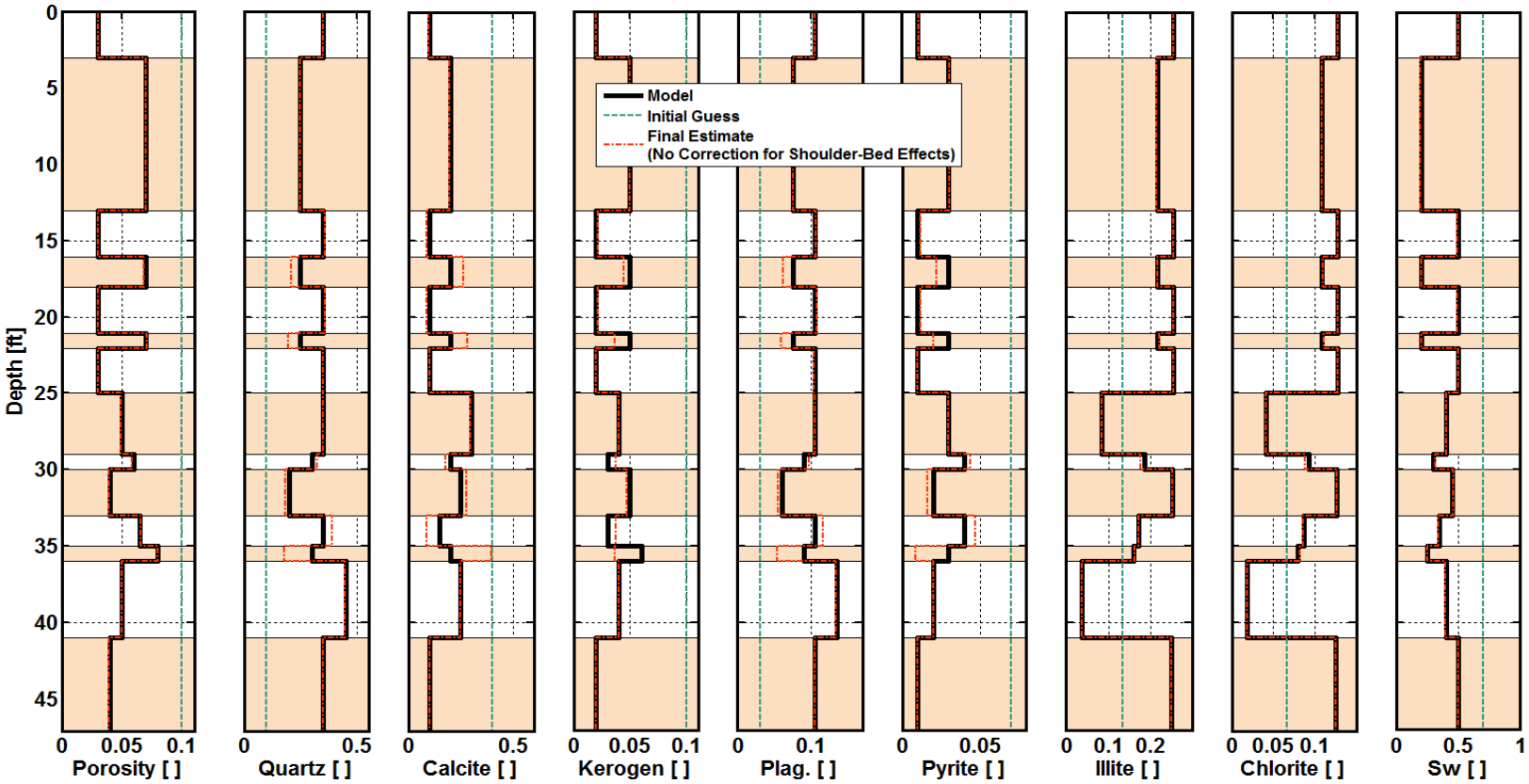


**Figure 6.4:** Synthetic Case: Comparison of model (actual) values (black solid line), initial guess (green dashed line), and final estimates (red dash-dotted line) of volumetric concentrations of mineral constituents, total porosity, volumetric concentration of kerogen, and total water saturation. Shoulder-bed effects are not corrected when applying separate inversion of well logs. Bed properties are selected from center-bed values. Panels from left to right show total porosity, volumetric concentrations of quartz, calcite, kerogen, plagioclase, pyrite, illite, chlorite, and total water saturation.

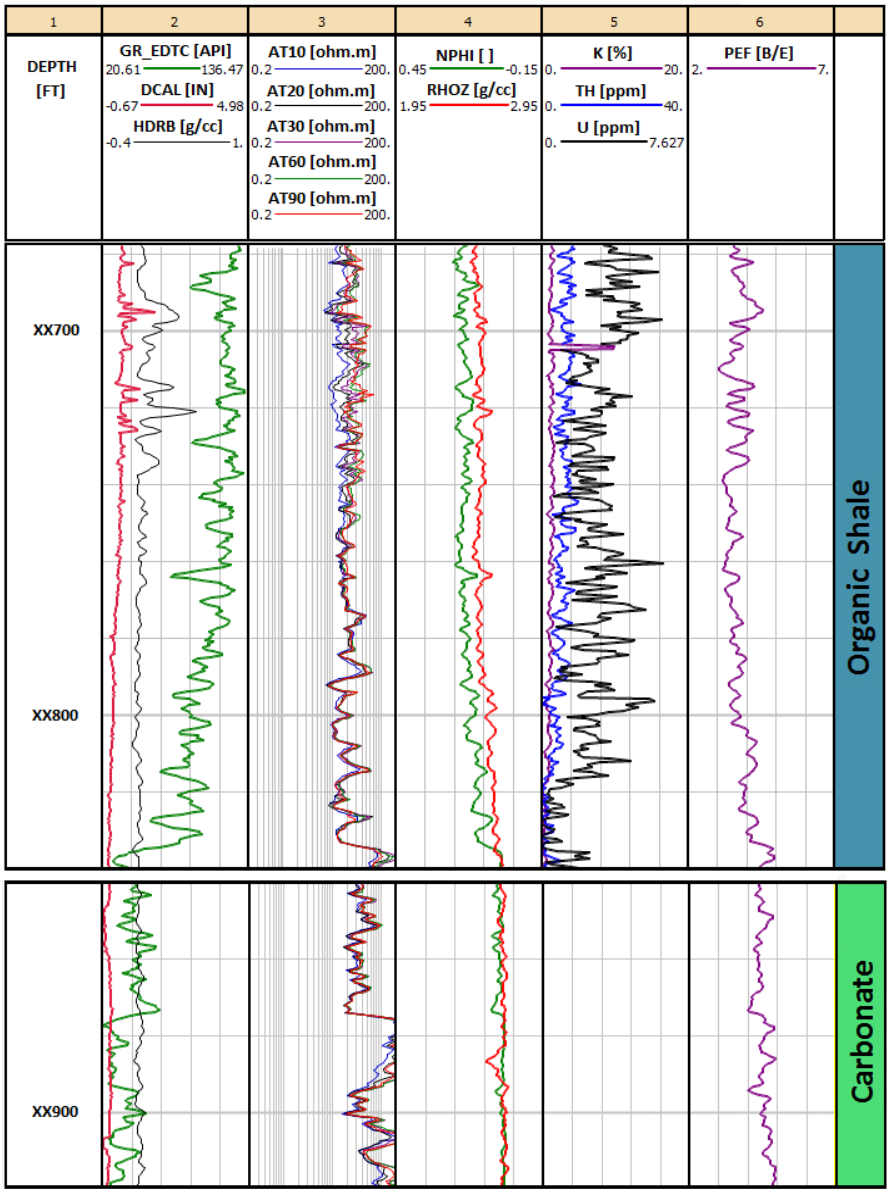


**Figure 6.5:** Field Example No. 1: Well logs across the selected depth interval in the Haynesville shale-gas formation. The top zone is an organic-shale and the bottom zone is a carbonate formation. Panels from left to right show depth, GR, caliper, and density correction, array-induction apparent resistivity, neutron porosity and density, GR-spectroscopy, and PEF logs.

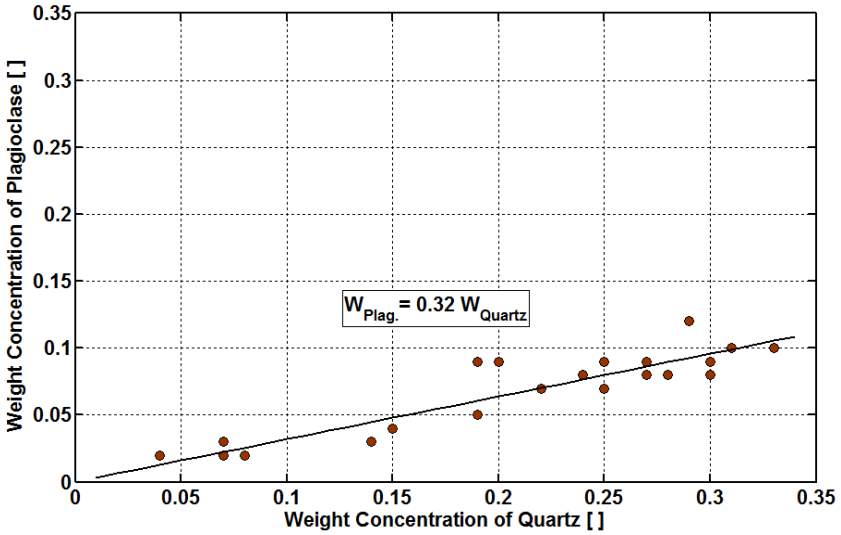


**(a)**

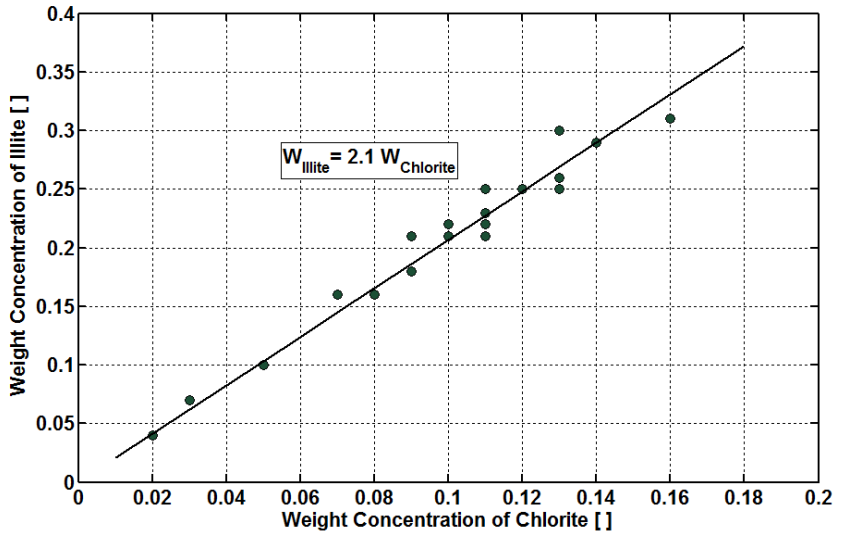


**(b)**

**Figure 6.6:** Field Example No. 1: Relationship between weight concentrations obtained from XRD measurements for (a) plagioclase and quartz, and (b) illite and chlorite. These linear relationships are input to the joint inversion to decrease non-uniqueness of estimated properties.

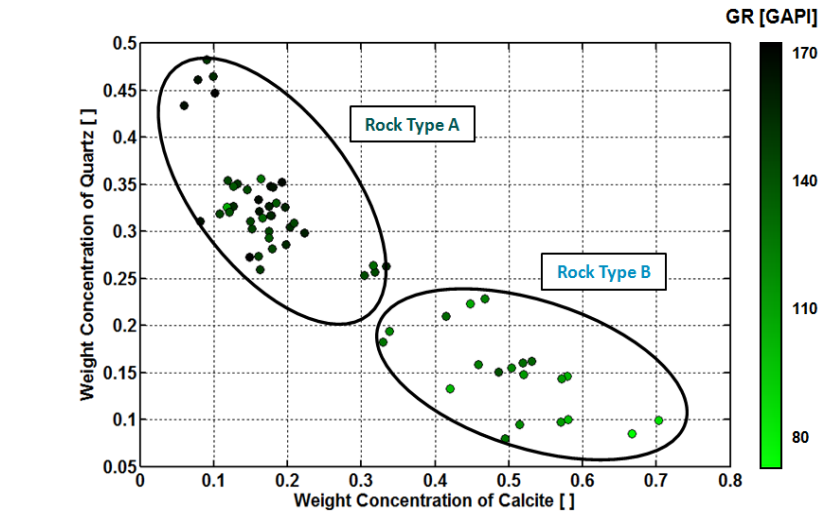


**(a)**

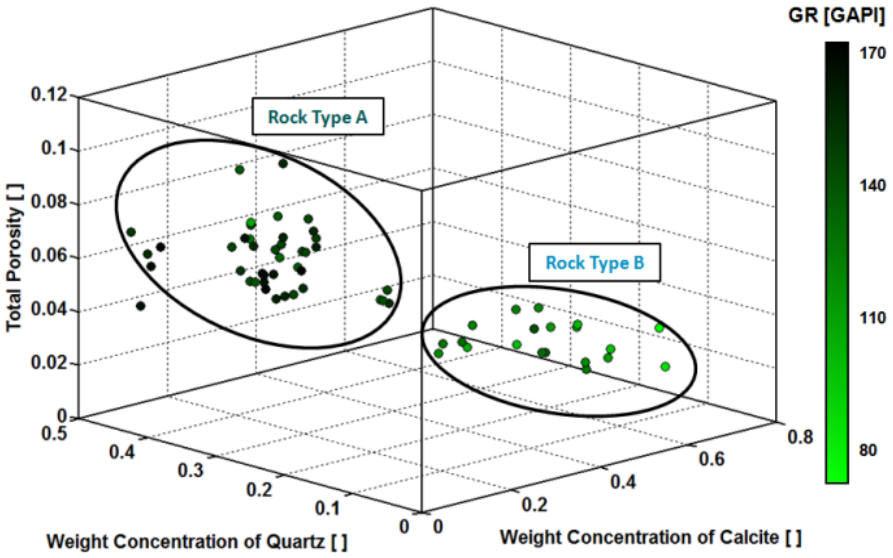


**(b)**

**Figure 6.7:** Field Example No. 1: Rock classification based on (a) estimated weight concentrations of quartz and calcite, and (b) estimated total porosity and weight concentrations of quartz and calcite for the depth interval XX690-XX830 ft. The color bar describes GR magnitude, which is roughly correlated with the volumetric concentration of clay-minerals. Two major rock types, described as A and B, are identified in this formation.

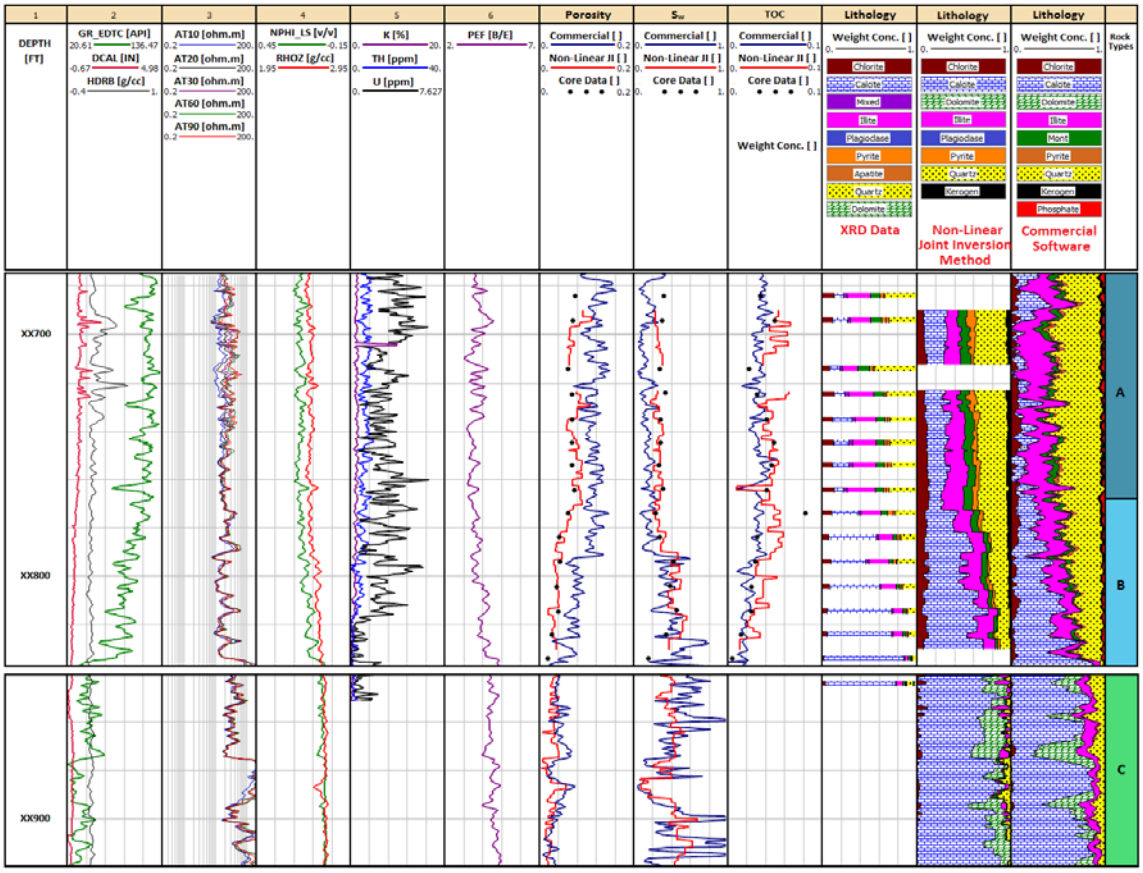


**Figure 6.8:** Field Example No. 1: Comparison of results for total porosity (seventh left-hand panel), total water saturation (eighth left-hand panel), TOC (ninth left-hand panel), weight concentrations of mineral constituents from XRD data (tenth left-hand panel), weight concentrations of mineral constituents from the nonlinear joint inversion method introduced in this chapter (eleventh left-hand panel), and weight concentrations of mineral constituents from commercial software (twelfth left-hand panel). Panels from left to right show depth, GR, caliper, and density correction, array-induction apparent resistivity, neutron porosity and density, GR-spectroscopy, and PEF logs. The right-hand panel describes the three rock types inferred in this formation.

# Chapter 7: Summary, Conclusions, and Recommendations

This chapter summarizes the main contributions of the research described in this dissertation, provides the main conclusions drawn from the results, and offers recommendations for future research.

## 7.1 SUMMARY

The objective of this dissertation was to introduce and test new methods to estimate static and dynamic petrophysical properties, as well as to quantify mineralogy in formations with complex lithology. The general strategy adopted in all the approaches introduced is the joint inversion of conventional well logs. Advantages of the methods introduced in this dissertation compared to conventional petrophysical/ compositional evaluation can be summarized as follows:

- Explicit assimilation of shoulder-bed effects.
- Assessment of dynamic petrophysical properties (i.e., absolute permeability, movable hydrocarbon saturation, and saturation-dependent capillary pressure and relative permeability) in addition to static petrophysical properties (i.e., porosity and water saturation).
- Accurate petrophysical/compositional evaluation in thinly-bedded formations.
- Incorporation of the effect of water-base mud-filtrate (WBM) or oil-base mud-filtrate (OBM) invasion on well logs to improve the accuracy of petrophysical/compositional evaluation.
- Explicit consideration of the different volumes of investigation of measurements involved in the interpretation.

In the first part of this dissertation, I described a method for the assessment of residual hydrocarbon saturation based on the combined numerical simulation of nuclear and electrical resistivity logs. This method can be implemented in two ways: (1) quantification of the influence of residual hydrocarbon saturation on the radial distribution of fluid saturation due to invasion, and (2) appraisal of invasion effects on the vertical distribution of fluid saturation within a flow unit that exhibits both hydrocarbon and water saturation in capillary equilibrium. I applied the first approach to a tight-gas sand formation invaded with WBM to estimate residual gas saturation. The second approach was applied to a hydrocarbon-bearing siliciclastic reservoir invaded with OBM to quantify the vertical variation of residual oil saturation and its influence on well logs.

In the second part of this dissertation, I introduced a method to assess dynamic petrophysical properties such as saturation-dependent capillary pressure and relative permeability in water-bearing sands invaded with OBM. This method requires the input of electrical resistivity measurements with different depths of investigation. Although the method introduced is appropriate for both hydrocarbon- and water-bearing zones, the focus of the research described is on water-bearing sands. The reasons for this choice are (a) immiscibility between OBM and in-situ fluids and (b) maximum sensitivity of array-induction electrical resistivity measurements to dynamic petrophysical properties in water-bearing zones. I applied this method to three siliciclastic field examples covering a wide range of porosity and permeability values. All the field examples included hydrocarbon-bearing zones underlain by active aquifers. I cross-validated the estimated saturation-dependent capillary pressure with the vertical variation of water saturation in the hydraulically connected reservoir. In addition to the field examples, I conducted sensitivity analysis to identify the reliability margins for assessing static/dynamic petrophysical properties of water-bearing sands. Properties such as saturation-dependent

capillary pressure and relative permeability obtained in water-bearing zones could be used in hydrocarbon-bearing zones to improve petrophysical interpretation and estimates of movable hydrocarbon reserves.

Finally, I developed three fully-automatic nonlinear joint inversion methods to estimate porosity and volumetric/weight concentrations of mineral/fluid constituents in challenging formations. Inputs to the joint inversion process are conventional well logs including density, neutron porosity, GR/GR-spectroscopy, electrical resistivity, and PEF. Inversion is still possible in the absence of any of these measurements. The first method is the most general method, and corrects for the effects of mud-filtrate invasion and shoulder beds in formations with complex lithology. Although this method is not time-efficient, I recommend it for thinly-bedded and invaded formations with complex lithology. The second method is faster than the first method because it neglects the effect of invasion on well logs. I recommend the second method for thinly-bedded formations with complex lithology also, but to achieve the most accurate results, the effect of mud-filtrate invasion should be negligible. The third method is a fast depth-by-depth approach recommended for formations with thick beds and complex lithology. This method does not correct for either shoulder-bed or mud-filtrate invasion effects.

Field examples of carbonate formations were the first candidates of complex lithology I used to verify the accuracy of results obtained with the proposed nonlinear joint inversion methods. I also adopted and modified one of the nonlinear joint inversion methods introduced for petrophysical/compositional evaluation of organic-shale formations, assuming that the effect of mud-filtrate invasion was negligible in these formations. I applied this method to an organic-shale field example located in the Haynesville formation to estimate total organic carbon (TOC), total porosity, total water saturation, and the volumetric/weight concentrations of mineral constituents, and to

perform rock typing. I compared results obtained from the nonlinear joint inversion method against (a) core/X-Ray Diffraction (XRD) data and (b) the results obtained from conventional petrophysical interpretation and linear/semi-linear mineralogy solvers, thereby confirming the reliability and accuracy of the new method against conventional methods.

## 7.2 CONCLUSIONS

This section lists the conclusions drawn from the results reported in different chapters of the dissertation.

### 7.2.1 Assessment of Residual Hydrocarbon Saturation with the Combined Quantitative Interpretation of Electrical Resistivity and Nuclear Logs

i. Combined quantitative interpretation of electrical resistivity and nuclear logs is successful in assessing residual hydrocarbon saturation. This method estimates residual hydrocarbon saturation by quantifying the effect of radial and vertical variations of fluid saturations, due to mud-filtrate invasion and layering on well logs.

ii. In formations invaded by WBM, the sensitivity of the method to residual hydrocarbon saturation is significant. Because WBM-filtrate and in-situ hydrocarbon are immiscible, the method can diagnose residual hydrocarbon saturation efficiently.

iii. In formations invaded by OBM, invading fluid and in-situ hydrocarbon are miscible. Miscibility of OBM-filtrate and in-situ hydrocarbon reduces the sensitivity of electrical resistivity and nuclear logs to residual hydrocarbon saturation. However, nuclear logs are still marginally

affected by the presence of residual hydrocarbon saturation, which may cause cross-over between neutron porosity and density measurements.

iv. The sensitivity of the method to residual hydrocarbon decreases in formations where (a) mud-filtrate invasion is radially shallow, (b) porosity is low, or (c) the density of in-situ hydrocarbon is high.

v. Uncertainty and inaccuracy in inputs for the simulation of mud-filtrate invasion cause inaccuracy in the assessment of residual hydrocarbon saturation. Inputs to the simulation of mud-filtrate invasion include petrophysical properties of the formation, mud properties, and invasion parameters such as invasion rate, overbalance pressure, and time of mud-filtrate invasion.

### 7.2.2 Estimation of Dynamic Petrophysical Properties of Water-Bearing Sands Invaded with Oil-Base Mud from Multi-Physics Borehole Geophysical Measurements

i. The method requires electrical resistivity measurements with different depths of investigation to estimate dynamic petrophysical properties (i.e., absolute permeability, movable hydrocarbon saturation, and saturation-dependent capillary pressure and relative permeability). However, the inverse problem is under-determined and, consequently, non-unique due to the large number of unknown properties (including Brooks-Corey's parameters) compared to the number of well logs which are sensitive to the unknown properties. In this non-unique problem, the choice of initial guess is critical; hence, I applied an iterative serial inversion technique instead of simultaneous inversion.

ii. Although the common assumption is that the mud-filtrate front is piston-like in the presence of OBM, sensitivity analysis in this dissertation showed that an invasion front can be smooth in the presence of OBM. A smooth radial invasion front makes conventional petrophysical interpretation challenging. However, the method introduced uses the effect of a radially smooth invasion front on well logs with different depths of investigation to assess dynamic petrophysical properties, which is difficult with conventional methods.

iii. Presence of OBM in water-bearing zones provides the maximum sensitivity of electrical resistivity logs to dynamic petrophysical properties of the formation due to (a) immiscibility between mud-filtrate and in-situ hydrocarbon, (b) negligible effect of salt mixing, and (c) significant electrical resistivity difference between the invaded and non-invaded zones.

iv. Cross-validation of the estimated saturation-dependent capillary pressure with vertical variations of water saturation in two field examples confirmed the reliability of the method in assessing saturation-dependent capillary pressure.

v. The sensitivity of the method is marginal to dynamic petrophysical properties if (a) there is no separation between electrical resistivity logs, (b) the radial length of mud-filtrate invasion is extremely large (larger than 8 ft) or negligible (smaller than 0.5 ft), (c) the porosity and permeability of the formation are large (more than 25 porosity units and more than 500 md, respectively), or (d) the connate water salinity is small in formations invaded by OBM.

### 7.2.3 Improved Estimation of Mineral and Fluid Volumetric/Weight Concentrations in Thinly-Bedded and Invaded Formations

i. In Chapter 4, I introduced and successfully tested three fully-automatic estimation methods on synthetic examples, and showed the higher reliability of these methods compared to conventional methods in the presence of (a) complex lithology, (b) light hydrocarbon, (c) thin beds and shoulder-bed effects on well logs, and (d) mud-filtrate invasion.

ii. As mentioned above, I recommend the first method for thinly-bedded invaded formations with complex lithology. In deeply invaded formations, however, the assessment of hydrocarbon pore volume is not reliable due to lack of sensitivity of well logs to the non-invaded part of the formation. I recommend the second method for thinly-bedded formations with complex lithology in which the effect of mud-filtrate invasion is negligible or invasion is radially deep (deeper than 8 ft). The third method works well for thick formations with complex lithology, where the effects of invasion and shoulder beds are negligible.

iii. The accuracy of results obtained with all the methods decreases if (a) knowledge about the type of available minerals is not accurate, (b) the input chemical formula for mineral constituents is not accurate, (c) bed-boundary locations are not chosen accurately, or (d) input well logs are affected by noise.

iv. Perturbations of one log-sampling interval on bed-boundary locations affect the final inversion products by more than 30% in beds thinner than 2 ft.

v. Presence of 5% noise on neutron porosity, density, electrical resistivity, GR, and PEF may affect final estimates for petrophysical/compositional properties by 50% in gas-bearing and by 30% in heavy oil-bearing formations.

### 7.2.4 Petrophysical/Compositional Evaluation of Carbonate Formations Based on Nonlinear Joint Inversion of Conventional Well Logs

i. I verified the application of the methods introduced in Chapter 4 on carbonate formations for assessment of porosity, water saturation, and volumetric/weight concentrations of mineral constituents. The methods were reliable in cases of complex lithology and thin beds.

ii. Results obtained for porosity, water saturation, and volumetric concentrations of mineral constituents were in agreement with core/XRD data in one of the field examples where XRD/core data were available. Conventional methods, however, did not provide accurate results. The new method estimates a higher concentration of clay than found with XRD measurements. This result can be explained by the fact that XRD measurements underestimate clay (Sondergeld et al., 2010).

iii. Although we can quantify the effects of both non-connected and inter-connected porosity on well logs, the assessment of non-connected porosity is not accurate in under-determined inversion. Thus, in the present study there is uncertainty in the assessment of petrophysical/compositional properties in the presence of non-connected porosity.

### 7.2.5 A Quantitative Method for Estimating Total Organic Carbon and Porosity and for Diagnosing Mineral Constituents from Well Logs in Shale-Gas Formations

i. The new shale evaluation method based on conventional logs is reliable in the assessment of total porosity, total water saturation, TOC, and the volumetric/weight concentrations of mineral constituents. I documented improvements of more than 50% in porosity and water saturation compared to conventional petrophysical interpretation.

ii. Unlike conventional shale interpretation methods, the method introduced does not require empirical formulae or calibration factors for the assessment of kerogen or any other mineral constituents. It only requires the chemical formula of the mineral constituents and kerogen as inputs.

iii. The new method takes into account corrections for shoulder-bed effects in the presence of thin beds. This capability is a major advantage of the new method over conventional strategies in the evaluation of organic-shale formations, where rapid vertical variations of mineral/fluid concentrations are commonplace.

iv. The new method for organic-shale evaluation provides accurate results at depths where good-quality well logs are available. However, XRD/core measurements are sparse and may not reflect all the vertical variations in formation properties.

v. XRD/core measurements are conventionally used in rock classification. However, XRD/core data are not available for all petrophysical beds. The proposed method provides estimates of porosity, volumetric/weight concentrations of mineral/fluid constituents, and kerogen for any desired petrophysical bed. These estimates can be used for rock classification.

vi. The accuracy of results decreases if (a) some well logs are depth shifted compared to other logs, (b) the location of bed boundaries is not accurate, (c) the assumed mineral types in the formation are not correct, or (d) the chemical formulae assumed for mineral constituents and kerogen are not accurate.

vii. In organic-shale formations, the number of unknown formation properties is usually greater than the number of reliable input well logs due to the presence of complex lithology. This leads to an under-determined inverse problem. Consequently, the choice of initial guess for formation properties such as porosity, TOC, and volumetric/weight concentrations of mineral/fluid constituents is crucial.

## 7.3 RECOMMENDATIONS

The following is a list of recommendations for future research that could expand the technical work presented in this dissertation:

i. Unlike raw electrical resistivity measurements, apparent resistivity logs sometimes experience sharp unrealistic variations close to bed boundaries, depending on adjacent bed properties. These unrealistic electrical resistivity values could cause divergence in the nonlinear joint inversion of electrical resistivity logs for assessment of dynamic petrophysical properties. The choice of raw electrical resistivity over apparent electrical resistivity measurements would improve the accuracy of results in multi-layer formations.

ii. Mud-filtrate invasion could be assumed to be piston-like for certain formations (e.g., high-porosity, high-permeability formations). Following

this assumption, the depth of mud-filtrate invasion could be estimated based on the joint inversion of electrical resistivity measurements. CPU time could then be decreased by eliminating the numerical simulation of fluid flow in porous media. This advantage would be significant in the case of high-angle/horizontal wells, where three-dimensional (3D) numerical simulation of mud-filtrate invasion is not time-efficient.

iii. Gradient-based inversion methods adopted in this dissertation can easily become trapped in local minima. Additionally, in the case of multiple answers to an under-determined problem, gradient-based methods are highly dependent on the initial guess. Non-gradient based methods, such as Bayesian methods, could be a good substitute for gradient-based methods for joint inversion of well logs.

iv. Including neutron-capture spectroscopy measurements in the joint inversion would reduce non-uniqueness of results in formations with complex lithology, where inversion is under-determined. This requires a fast forward method for the numerical simulation of neutron-capture spectroscopy measurements. Assimilating neutron-capture spectroscopy measurements will improve the accuracy of interpretations and reduce the dependency on initial guesses of formation properties.

v. Results obtained from the shale evaluation method introduced in this dissertation are highly affected by the assumed resistivity-saturation-porosity model. However, none of the available shaly-sand models is reliable in the presence of kerogen and pyrite. Introducing new resistivity models that are physically consistent with organic-shale formations will

improve the accuracy of petrophysical/compositional evaluation of these formations.

vi. Sonic simulation using mixing laws is sensitive to different fluid phases, as well as to different elastic rock properties and pore shapes. Combining the numerical simulation of sonic measurements and dispersion curves with nuclear and electrical resistivity logs will (a) reduce the non-uniqueness of the results and (b) enable reliable assessments of elastic rock properties in formations with complex lithology.

vii. This dissertation studied the effects of mud-filtrate invasion on well logs in vertical wells. The research could be extended to high-angle/horizontal wells by (a) modeling 3D water- and oil-base mud-filtrate invasion in different formations with different inclusion phases, matrices, water salinity, and rock-fluid properties, and (b) modeling both wireline and logging-while-drilling (LWD) electrical resistivity and nuclear logs numerically in high-angle/horizontal wells. It would then be possible to quantify the effects of well deviation angle, bed thickness, and mud-filtrate invasion on well logs.

viii. Comparison of LWD and wireline measurements would enable one to quantify the effect of mud-filtrate invasion on well logs without numerical simulation of fluid flow in porous media. This could be used to quantify dynamic petrophysical properties of formations.

# Appendix A: Separate Linear Inversion of Density, PEF, and GR-Spectroscopy Logs to Estimate Physical Properties of Individual Layers

Separate inversions are performed for density, PEF, and GR-spectroscopy logs to estimate layer-by-layer values of density, PEF, and Ur, Th, and K concentrations, respectively. Input data consist of sampled well logs. The objective of the separate inversion is to "sharpen" each of the logs by reducing shoulder-bed effects. It is assumed that bed boundaries have been detected prior to performing the inversion.

The objective of separate linear inversion of density, PEF, and GR-spectroscopy logs is to estimate layer-by-layer values of density, PEF, and Ur, Th, and K concentrations. Bed physical properties are estimated by minimizing the quadratic cost function given by

$$\mathbf{C}(\mathbf{p}) = \left\| \mathbf{d}(\mathbf{p}) - \mathbf{d}_m \right\|_2^2 + \alpha^2 \left\| \mathbf{p} - \mathbf{p}_0 \right\|_2^2, \tag{A.1}$$

where $\mathbf{d}$ is the vector of numerically simulated density, PEF, GR-spectroscopy, electrical resistivity, or neutron porosity logs, $\mathbf{d}_m$ is the vector of well logs, $\alpha$ is a regularization (stabilization) parameter, $\mathbf{p}$ designates the vector of corresponding layer-by-layer properties (e.g., density, PEF, Ur, Th, and K concentrations, neutron migration length, and electrical resistivity), and $\mathbf{p}_0$ is the vector of a reference model which can be selected based on (a) center-bed values, (b) the average of well logs in each bed, or (c) the average of well logs in the entire depth interval considered for inversion. Vectors $\mathbf{d}$ and $\mathbf{p}$ are respectively given by

$$\mathbf{d} = \left[ d_1, ..., d_{n_{sp}} \right]^T, \tag{A.2}$$

and

$$\mathbf{p} = \left[ p_1, ..., p_{n_b} \right]^T, \tag{A.3}$$

where the superscript "*T*" indicates transpose, $n_{sp}$ is the number of sampling points in each well log, and $n_b$ is the number of beds.

The stabilization parameter in Equation (A.1) provides a way to adjust the relative importance of fitting the data and estimating a relatively smooth vertical distribution of properties. The regularization parameter is obtained using Hansen's (1994) L-curve strategy. A data weighting matrix is not needed here because inversion is applied separately on each of the well logs. For density, PEF, and GR-spectroscopy measurements, we assume a deterministic linear dependence between bed physical properties (i.e., density, PEF, and Ur, Th, and K concentrations) and measured logs. This linear dependence is given by

$$\mathbf{d}(\mathbf{p}) = \mathbf{K} \bullet \mathbf{p}, \tag{A.4}$$

where **K** designates a matrix of pre-calculated FSFs for density, PEF, or GR-spectroscopy measurements. For more accurate density inversion results, one can opt to treat short-spaced (SS) and long-spaced (LS) density measurements as separate input measurements. Mendoza et al. (2009) implemented the same linear inversion method for multi-sector LWD density measurements.

In the case of a linear relationship between bed physical properties and measured logs Equation (A.1) is solved via

$$\left[ \mathbf{K}^T \bullet \mathbf{K} + \alpha^2 \mathbf{I} \right] \bullet \mathbf{p} - \alpha^2 \mathbf{I} \bullet \mathbf{p}_0 = \mathbf{K}^T \bullet \mathbf{d}_m, \tag{A.5}$$

where **I** is unity matrix and the superscript "*T*" indicates transposition.

# Appendix B: Separate Nonlinear Inversion of Neutron Porosity and Apparent Resistivity Measurements

The functional relationships between (a) neutron porosity measurements and layer-by-layer neutron migration length, and (b) electrical resistivity measurements and layer-by-layer resistivity are not linear. Thus, Equation (A.4) is not valid for electrical resistivity and neutron porosity measurements. To circumvent that problem, we minimize the quadratic cost function (Equation (A.1)) using a nonlinear approach. This is accomplished by calculating numerically (finite difference) the entries of the Jacobian matrix at every linear iteration and by implementing the Levenberg-Marquardt minimization method (Marquardt, 1963). In doing so, linear iterative refinement (Mendoza et al., 2010) is used for the rapid numerical simulation of neutron porosity logs. For the case of inversion of array-induction (AIT[6]) resistivity logs, the corresponding entries of the Jacobian matrix are obtained via finite-difference calculations of apparent resistivity logs. A similar approach could be implemented with raw borehole-corrected electrical conductivity measurements.

To improve the convergence rate of the minimization method, we transform neutron porosity logs into migration-length logs, and perform the inversion to yield layer-by-layer values of migration length. Likewise, the inversion of apparent resistivity logs is implemented with apparent conductivity logs (Inverse of apparent resistivity logs) to yield layer-by-layer values of electrical conductivity.

6 Mark of Schlumberger

## Appendix C: Nonlinear Joint Inversion of Individual Layer Properties

The objective of joint inversion of layer-by-layer density, migration length, electrical conductivity, PEF, and GR-spectroscopy values is to estimate porosity, water saturation, and volumetric/weight concentrations of mineral constituents. The inversion is performed from layer-by-layer properties obtained from the separate inversion of well logs described in Appendices A and B.

Physical properties for each layer are estimated by minimizing the layer-by-layer quadratic cost function given by

$$\mathbf{C}(\mathbf{x}) = \left\| \mathbf{W_d} \bullet \left[ \mathbf{p}(\mathbf{x}) - \mathbf{p}_{\boldsymbol{m}} \right] \right\|_2^2 + \alpha^2 \left\| \mathbf{x} \right\|_2^2, \tag{C.1}$$

subject to

$$0 \le x_i \le 1, \tag{C.2}$$

and

$$\sum_{i=1}^{n_c} C_i + C_{sh} + \phi_s = 1, \tag{C.3}$$

where $\mathbf{W_d}$ is a data weighting matrix, $\mathbf{p}$ is the vector of physical properties in each bed (e.g., density, PEF, Ur, Th, and K concentrations, neutron migration length, and electrical conductivity), $\mathbf{p}_{\boldsymbol{m}}$ is the vector of model physical properties estimated from well logs in each bed, $\alpha$ is a regularization (stabilization) parameter, $n_c$ is the predefined number of mineral constituents, $C_i$ is volumetric concentration of the assumed mineral constituents,

$C_{sh}$ is volumetric concentration of shale, $\phi_s$ is non-shale porosity, and $\mathbf{x}$ is the vector of formation properties, given by

$$\mathbf{x} = \left[ C_1, C_2, ..., C_{n_c}, C_{sh}, \phi_s, S_w \right]^T, \tag{C.4}$$

where $S_w$ is total water saturation. The vector of numerically simulated layer-by-layer properties is given by

$$\mathbf{p} = \left[ L_m, \rho_b, PEF, \boldsymbol{\sigma}, Ur, Th, K \right]^T, \tag{C.5}$$

where $L_m$ is neutron migration length, $\rho_b$ is bulk density, and $\boldsymbol{\sigma}$ designates apparent electrical conductivity logs with variable radial lengths of investigation (multiple logs depending on the type of logging tool used to acquire resistivity measurements).

The data weighting matrix in Equation (C.1) controls the importance of each physical property included in the inversion. $\mathbf{W_d}$ is given by

$$\mathbf{W_d} = \begin{bmatrix} \frac{1}{p_{m,1}} & . & . & . & 0 \\ . & . & & & . \\ . & & . & & . \\ . & & & . & . \\ 0 & . & . & . & \frac{1}{p_{m,n_l}} \end{bmatrix}, \tag{C.6}$$

where $n_l$ is the number of well logs.

We minimize the cost function defined in Equation (C.1) with the Levenberg-Marquardt method (Marquardt, 1963) and use Schlumberger's SNUPAR commercial

software (McKeon and Scott, 1989) to estimate neutron migration length and PEF and for the numerical calculation (finite difference) of the corresponding entries of the Jacobian matrix (partial derivatives of entries of vector **p** with respect to entries of vector **x**). The stabilization parameter, $\alpha$, included in Equation (C.1) is selected via Hansen's (1994) L-curve method.

# List of Symbols

| | |
|---|---|
| $\Delta t$ | Sonic interval transient time, [ms] |
| $a$ | Archie's tortuosity factor, [ ] |
| **C(x)** | Cost function, [ ] |
| $C_{cl}$ | Volumetric concentration of clay, [ ] |
| $C_D$ | Volumetric concentration of dolomite, [ ] |
| $C_L$ | Volumetric concentration of limestone, [ ] |
| $C_m$ | Volumetric concentration of minerals, [ ] |
| $C_Q$ | Volumetric concentration of quartz, [ ] |
| $C_{sh}$ | Volumetric concentration of shale, [ ] |
| **d** | Vector of simulated logs |
| $\mathbf{d_m}$ | Vector of measured or model logs |
| $e_h$ | Hydrocarbon phase experimental exponent for Brooks-Corey's equation, [ ] |
| $e_p$ | Pore-size distribution exponent, [ ] |
| $e_w$ | Water phase experimental exponent for Brooks-Corey's equation, [ ] |
| $g$ | Gravity constant, [m/s$^2$] |
| $h$ | Depth, [ft] |
| **I** | Unity matrix, [ ] |
| **J** | Jacobian matrix |
| **K** | Matrix of FSFs for density, PEF, or GR-spectroscopy tools |
| $k$ | Absolute permeability, [md] |
| $k^0_{rh}$ | $k_{rh}$ end point, [ ] |
| $k^0_{rw}$ | $k_{rw}$ end point, [ ] |
| $k_r$ | Absolute permeability in radial direction, [md] |
| $k_{rh}$ | Hydrocarbon phase relative permeability, [ ] |
| $k_{rw}$ | Water relative permeability, [ ] |
| $k_z$ | Absolute permeability in vertical direction, [md] |
| $L_m$ | Neutron migration length, [cm] |
| $m$ | Archie's cementation exponent, [ ] |
| $n$ | Archie's saturation exponent, [ ] |
| $n_b$ | Number of beds, [ ] |
| $n_c$ | Number of mineral constituents, [ ] |
| $n_l$ | number of well logs, [ ] |
| $n_{sp}$ | number of sampling points in each well log, [ ] |

| | |
|---|---|
| $n_u$ | number of unknowns, [ ] |
| $\mathbf{p}$ | Vector of simulated layer-by-layer properties |
| $\mathbf{p_0}$ | Vector of reference layer-by-layer model properties |
| $P_c$ | Capillary pressure, [psi] |
| $P_c^{\,0}$ | Coefficient for $P_c$ equation, [psi.darcy$^{1/2}$] |
| $\mathbf{p_m}$ | Vector of model layer-by-layer properties |
| $R$ | Apparent resistivity measurements, [ohm.m] |
| $R_t$ | True formation resistivity, [ohm.m] |
| $R_w$ | Connate water resistivity, [ohm.m] |
| $R_{wb}$ | Bounded water resistivity, [ohm.m] |
| $S^*$ | Effective saturation, [ ] |
| $S_{gi}$ | Initial gas saturation, [ ] |
| $S_{gr}$ | Residual gas saturation, [ ] |
| $S_h$ | Total hydrocarbon saturation, [ ] |
| $S_{hr}$ | Residual hydrocarbon saturation, [ ] |
| $S_N$ | Normalized water-phase saturation, [ ] |
| $S_{or}$ | Residual oil saturation, [ ] |
| $S_w$ | Total water saturation, [ ] |
| $S_{wb}$ | Bounded water saturation, [ ] |
| $S_{wr}$ | Irreducible water saturation, [ ] |
| $S_{ws}$ | Non-shale water saturation, [ ] |
| $t_{inv}$ | Time of mud-filtrate invasion, [hours], [days] |
| $TOC_{wt}$ | Weight percentage of TOC [ ] |
| $U$ | Volumetric photoelectric factor, [ ] |
| $V_{cl}$ | Volume of clay, [cm$^3$] |
| $V_m$ | Matrix volume, [cm$^3$] |
| $V_p$ | Sonic compression-wave velocity, [m/s] |
| $V_{ps}$ | Pore-space volume, [cm$^3$] |
| $V_r$ | Volume of rock including fluids, [cm$^3$] |
| $V_s$ | Sonic shear-wave velocity, [m/s] |
| $V_{sh}$ | Volume of wet shale, [cm$^3$] |
| $W_{chlorite}$ | Weight concentration of chlorite, [ ] |
| $\mathbf{W_d}$ | Data weighting matrix, [ ] |
| $W_{illite}$ | Weight concentration of illite, [ ] |
| $W_{plag.}$ | Weight concentration of plagioclase, [ ] |
| $W_{quartz}$ | Weight concentration of quartz, [ ] |

# List of Greek Symbols

| | |
|---|---|
| $\alpha$ | Regularization parameter, [ ] |
| $\phi_D$ | Density porosity, [ ] |
| $\phi_{D,sh}$ | Density porosity in a "pure" shale zone, [ ] |
| $\phi_D^{sh}$ | Density porosity corrected for shale, [ ] |
| $\phi_N$ | Neutron porosity, [ ] |
| $\phi_{N,sh}$ | Neutron porosity in a "pure" shale zone, [ ] |
| $\phi_N^{sh}$ | Neutron porosity corrected for shale, [ ] |
| $\phi_s$ | Non-shale porosity, [ ] |
| $\phi_{sh}$ | Shale porosity, [ ] |
| $\phi_t$ | Total porosity, [ ] |
| $\gamma$ | Interfacial tension between water and hydrocarbon phases, [dynes/cm] |
| $\rho_b$ | Bulk density, [g/cm$^3$] |
| $\rho_{cl}$ | Clay density, [g/cm$^3$] |
| $\rho_f$ | Fluid density, [g/cm$^3$] |
| $\rho_h$ | Hydrocarbon density, [g/cm$^3$] |
| $\rho_m$ | Matrix density, [g/cm$^3$] |
| $\rho_{sh}$ | Shale density, [g/cm$^3$] |
| $\rho_{silt}$ | Silt density, [g/cm$^3$] |
| $\rho_w$ | Water density, [g/cm$^3$] |
| $\sigma$ | Electrical conductivity, [S/m] |
| $\theta$ | Contact angle between water and hydrocarbon phases, [degree] |

# Acronyms

| | |
|---|---|
| 1D | One Dimensional |
| 2D | Two Dimensional |
| 3D | Three Dimensional |
| AI | After Mud-Filtrate Invasion |
| AIT® | Array-Induction Tool |
| BI | Before Mud-Filtrate Invasion |
| CMG | Computer Modeling Group, Ltd. |
| CPU | Computer Processing Unit |
| DLT® | Dual Laterolog Tool |
| DTCO | Delta-T Compressional |
| DTSM | Delta-T Shear |
| ECGR | Environmentally Corrected Gamma-Ray |
| FSF | Flux Sensitivity Function |
| FTIR | Fourier Transform Infrared Transmission |
| GEM® | Compositional Simulator from CMG |
| GR | Gamma-Ray |
| K | Potassium |
| kppm | Kilo Parts Per Million |
| L | Linear |
| LS | Long-Spaced |
| LWD | Logging-While-Drilling |
| MID | Matrix Identification |
| NL | Nonlinear |
| NMR | Nuclear Magnetic Resonance |
| OBM | Oil-Base Mud |
| PEF | Photoelectric Factor |
| PVT | Pressure-Volume-Temperature |
| SNUPAR | Schlumberger Nuclear Parameter code |
| SS | Short-Spaced |
| STARS® | Multi-Component Thermal Reservoir Simulator from CMG |
| $T$ | Transpose of a matrix |
| TCMR | Total CMR porosity |
| Th | Thorium |
| TOC | Total Organic Carbon |

| | |
|---|---|
| Ur | Uranium |
| UTAPWeLS | University of Texas at Austin Petrophysical and Well-Log Simulator |
| WBM | Water-Base Mud |
| XRD | X-Ray Diffraction |
| XRF | X-Ray Fluorescence |

# References


Abdollah Pour, R., 2008, Equation-of-State, Compositional, One-Dimensional Radial Flow Method to Simulate Invasion and Fluid Withdrawal in the Presence of Oil- or Water-Base Muds: *Master's Thesis*, The University of Texas at Austin.

Aissaoui, A., 1983, Étude Théorique et Expérimentale de l'Hystérésis des Pressions Capillaires et des Perméabilités Relatives en Vue du Stockage Souterrain de Gaz: *Ph.D. Dissertation*, École des Mines de Paris.

Alpak, F. O., Torres-Verdín, C., Habashy, T. M., and Sepehrnoori, K., 2008, Estimation of in-situ petrophysical properties from wireline formation tester and induction logging measurements: A joint inversion approach: *Journal of Petroleum Science and Engineering*, vol. 63, pp. 1–17.

Ambrose, R. J., Hartman, R. C., Diaz-Campos, M., Akkutlu, Y., and Sondergeld, C. H., 2010, New considerations for shale gas in place calculations: SPE 131772, *Proceedings of the SPE Unconventional Gas Conference*: Society of Petroleum Engineers, Pittsburgh, Pennsylvania, February 23–25.

Angeles Boza, R. M., 2009, Simulation and Interpretation of Formation-Tester Measurements Acquired in the Presence of Mud-Filtrate Invasion, Multi-Phase Flow, and Deviated Wellbores: *Ph.D. Dissertation*, The University of Texas at Austin.

Angeles, R., Torres-Verdín, C., Sepehrnoori, K., and Elshahawi, H., 2011, History matching of multi-phase flow formation-tester measurements acquired with focused sampling probes in deviated wells: *Petrophysics*, vol. 52, no. 1, pp. 14–31.

Biot, M. A, 1956, Theory of propagation of elastic waves in a fluid saturated porous solid. I. Low frequency range and II. Higher-frequency range: *Journal of the Acoustical Society of America*, vol. 28, pp. 168–191.

BP, 2003, The UK upstream asset portfolio, BP Exploration, Farburn Industrial Estate, Dyce, Aberdeen, U.K.

Brooks, R. H. and Corey, A. J., 1964, Hydraulic Properties of Porous Media: Hydrology Papers 3, Colorado State University, Fort Collins, Colorado.

Busch, J. M., Fortney, W. G., and Berry, L. N., 1987, Determination of lithology from well logs by statistical analysis: *SPE Formation Evaluation*, vol. 2, no. 4, pp. 412–418.

Chierici, G. L., Ciucci, G. M., and Long, G., 1963, Experimental research on gas saturation behind the water front in gas reservoirs subjected to water drive:

*Proceedings of the World Petroleum Conference*, Frankfurt, June 1963, pp. 483–498.

Clavier, C., Coates, G., and Dumanoir, J., 1977, The theoretical and experimental bases for the dual water model for the interpretation of shaly sands: SPE 6859, *Proceedings of the AIME Annual Technical Conference and Exhibition*: Society of Petroleum Engineers, Denver, Colorado, October 9-12.

Clavier, C. and Rust, D. H., 1976, MID-plot: a new lithology technique: *The Log Analyst*, vol. 17, no. 6, pp. 16–24.

Computer Modeling Group Ltd., 2008, User's guide: STARS: Computer Modeling Group Ltd., Calgary, Alberta, Canada.

Corey, A. T., 1994, Mechanics of Immiscible Fluids in Porous Media: Water Resources Publications, Highland Ranch, Colorado.

Cuddy, S. J., 2000, Litho-facies and permeability prediction from electrical logs using fuzzy logic: *SPE Reservoir Evaluation & Engineering*, vol. 3, no. 4, pp. 319–324.

Doveton, J. H., 1994, Geologic Log Analysis using Computing Methods: AAPG Computer Applications in Geology, no. 2, Tulsa, Oklahoma.

Gassmann, F., 1951, Über die Elastizität Poröser Medien: *Vierteljahrsschrift der Naturforschenden Gesellschaft in Zürich*, vol. 96, pp. 1–23.

Gaymard, R. and Poupon, A., 1968, Response of neutron and formation density logs in hydrocarbon bearing formations: *The Log Analyst*, vol. 9, no. 5, pp. 3–11.

Gonçalves, C. A., Harvey, P. K., and Lovell, M. A., 1995, Application of a multilayer neural network and statistical techniques in formation characterization: Paper FF, *Transactions of the SPWLA 36th Annual Logging Symposium*, Paris, France, June 26–29.

Hansen, P. C., 1994, Regularization Tools: A Matlab package for analysis and solution of discrete ill-posed problems: *Numerical Algorithms*, vol. 6, no. 1, pp. 1–35.

Heidari, Z., Torres-Verdín, C., and Preeg, W. E., 2010, Improved estimation of mineral and fluid volumetric concentrations in thinly-bedded and invaded formations: Paper QQ, *Transactions of the SPWLA 51st Annual Logging Symposium*, Perth, Australia, June 19–23.

Heidari, Z., Torres-Verdín, C., Mendoza, A., and Wang, G. L., 2011, Assessment of residual hydrocarbon saturation with the combined quantitative interpretation of resistivity and nuclear logs: *Petrophysics*, vol. 52, no. 3, pp. 217–237.

Herron, S. L. and Herron, M. M., 1996, Quantitative lithology: An application for open and cased hole spectroscopy: Paper E, *Transactions of the SPWLA 37th Annual Logging Symposium*, New Orleans, Louisiana, June 16–19.

Herron, M. M., Herron, S. L., Grau, J. A., Seleznev, N. V., Philips, J., Sherif, A. E., Farag, S., Horkowtiz, J. P., Neville, T. J., and Hsu, K., 2002, Real-time petrophysical analysis in siliciclastics from the integration of spectroscopy and triple-combo logging: SPE 77631, *Proceedings of the SPE Annual Technical Conference and Exhibition*: Society of Petroleum Engineers, San Antonio, Texas, September 29–October 2.

Honarpour, M., Leonard, K., and Herbert, H. A., 1986, Relative Permeability of Petroleum Reservoirs: C.R.C. Press, Boca Raton, Florida, pp. 15–43.

Honarpour, M., Leonard, K., and Herbert, H. A., 1982, Empirical equations for estimating two-phase relative permeability in consolidated rock: *Journal of Petroleum Technology*, vol. 34, no. 12, pp. 2905–2908.

Jacobsen, S., May, D., Grant, J., and Little, J., 2006, Producibility prediction in gas sands through effective integration of NMR, resistivity, and porosity log data: Paper I, *Transactions of the SPWLA 46th Annual Logging Symposium*, Veracruz, Mexico, June 4–7.

Jerauld, G. R., 1997, Prudhoe bay gas/oil relative permeability: *SPE Reservoir Engineering*, vol. 12, no. 1, pp. 66–73.

Kleppe, J., Delaplace, P., Leormand, R., Hamon, G., and Chaput, E., 1997, Representation of capillary pressure hysteresis in reservoir simulation: SPE 38899, *Proceedings of the SPE Annual Technical Conference and Exhibition*: Society of Petroleum Engineers, San Antonio, Texas, October 5–8.

Kralik, J. G., Manak, L. J., Jerauld, G. R., and Spence, A. P., 2000, Effect of trapped gas on relative permeability and residual oil saturation in an oil-wet sandstone: SPE 62997, *Proceedings of the SPE Annual Technical Conference and Exhibition*: Society of Petroleum Engineers, Dallas, Texas, October 1–4.

Land, C. S., 1971, Comparison of calculated with experimental imbibition relative permeability: SPE 3360, *Proceedings of the SPE Rocky Mountain Regional Meeting*: Society of Petroleum Engineers, Billings, Montana, June 2–4.

Land, C. S., 1968, Calculation of imbibition relative permeability for two- and three-phase flow from rock properties: *AIME Transactions*, vol. 243, pp. 149–156.

LeCompte, B., Franquet, J. A., and Jacobi, D., 2009, Evaluation of Haynesville shale vertical well completions with a mineralogy based approach to reservoir geomechanics: SPE 124227, *Proceedings of the SPE Annual Technical Conference and Exhibition*: Society of Petroleum Engineers, New Orleans, Louisiana, October 4–7.

Liu, Z., Torres-Verdín, C., Wang, G. L., Mendoza, A., Zhu, P., and Terry, R., 2007, Joint inversion of density and resistivity logs for the improved petrophysical assessment of thinly-bedded clastic rock formations: Paper VV, *Transactions of the SPWLA 48th Annual Logging Symposium*, Austin, Texas, June 3–6.

Liu, Z., 2007, Joint Inversion of Density and Resistivity Logs for the Improved Petrophysical Assessment of Thinly-Bedded Clastic Rock Formations: *Master's Thesis*, The University of Texas at Austin, Austin, Texas.

Ma, T. D. and Youngren, G. K., 1994, Performance of immiscible water-alternating-gas (IWAG) injection at Kuparuk river unit, north slope Alaska: SPE 2860, *Proceedings of the SPE Annual Meeting*: Society of Petroleum Engineers, New Orleans, Louisiana, September 25–28.

Malik, M., Salazar, J. M., Torres-Verdín, C., Wang, G. L., Lee, H. J., and Sepehrnoori, K., 2008, Effects of petrophysical properties on array-induction measurements acquired in the presence of oil-base mud-filtrate invasion: *Petrophysics*, vol. 49, no. 1, pp. 74–92.

Marquardt, D. W., 1963, An algorithm for least-squares estimation of nonlinear parameters: *SIAM Journal of Applied Mathematics*, vol. 11, pp. 431–441.

Martin, A. J., Robertson, D., Wreford, J., and Lindsay, A., 2005, High-accuracy oriented perforating extends the sand-free production life of Andrew field: SPE 93639, *Proceedings of the SPE at Offshore Europe*: Society of Petroleum Engineers, Aberdeen, Scotland, U.K., September 6-9.

Mavko, G., Mukerji, T., and Dvorkin, J., 2009, The Rock Physics Handbook: Tools for Seismic Analysis of Porous Media: Second Edition, Cambridge University Press, New York, New York.

Mayer, C. and Sibbit, A., 1980, Global, a new approach to computer-processed log interpretation: SPE 9341, *Proceedings of the SPE Annual Technical Conference and Exhibition*: Society of Petroleum Engineers of AIME, Dallas, Texas, September 21–24.

McKeon, D. C. and Scott, H. D., 1989, SNUPAR-a nuclear parameter code for nuclear geophysics applications: *IEEE Transactions on Nuclear Science*, vol. 36, no. 1, pp. 1215–1219.

Mendoza, A., Preeg, W., Torres-Verdín, C., and Alpak, F. O., 2007, Monte Carlo modeling of nuclear measurements in vertical and horizontal wells in the presence of mud-filtrate invasion and salt mixing: *Petrophysics*, vol. 48, no. 1, pp. 28–44.

Mendoza, A., Torres-Verdín, C., Preeg, W. E., Rasmus, J., Radtke, R. J., and Stockhausen, E., 2009, Inversion of sector-based LWD density measurements acquired in laminated sequences penetrated by high-angle and horizontal wells: Paper N, *Transactions of the SPWLA 50th Annual Logging Symposium*, The Woodlands, Texas, June 21–24.

Mendoza, A., Torres-Verdín, C., and Preeg, W. E., 2010, Linear iterative refinement method for the rapid simulation of borehole nuclear measurements, Part I: Vertical wells: *Geophysics*, vol. 75, no. 1, pp. E9–E29.

Mezzatesta, A. G., Mendez, F. E., Rodriguez, E. F., and Georgi, D., 2006, A novel approach to numerical simulation of conventional, multicomponent induction, and magnetic resonance data in shaly-sand and carbonate systems: Paper GGG, *Transactions of the SPWLA 47th Annual Logging Symposium*, Veracruz, Mexico, June 4–7.

Mohanty, K. K., Davis, H. T., and Scriven, L. E., 1987, Physics of oil entrapment in water-wet rock: *SPE Reservoir Engineering*, vol. 2, no. 1, pp. 113–128.

Mulyadi, H., Curtin, U., Amin, R., and Kennaird, T., 2000, Measurement of residual gas saturation, in water-driven gas reservoirs: comparison of various core analysis techniques: SPE 64710, *Proceedings of the SPE International Oil and Gas Conference and Exhibition*: Society of Petroleum Engineers, Beijing, China, November 7–10.

Passey, Q. R., Creaney, S., Kulla, J. B., Moretti, F. J., and Stroud, J. D., 1990, A practical model for organic richness from porosity and resistivity logs: *The American Association of Petroleum Geologists*, vol. 74, no. 12, pp. 1777–1794.

Passey, Q. R., Bohacs, K. M., Esch, W. L., Klimentidis, R., and Sinha, S., 2010, From oil-prone source rock to gas-producing shale reservoir – Geologic and petrophysical characterization of unconventional shale-gas reservoirs: SPE 131350, *Proceedings of the CPS/SPE International Oil and Gas Conference and Exhibition in China*: Society of Petroleum Engineers, Beijing, China, June 8–10.

Pentland, C. H., Al-Mansoori, S., Iglauer, S., Bijeljic, B., and Blunt, M. J., 2008, Measurement of non-wetting phase trapping in sand packs: SPE 115697, *Proceedings of the SPE Annual Technical Conference and Exhibition*: Society of Petroleum Engineers, Denver, Colorado, September 21–24.

Pickett, G. R., 1966, A review of current techniques for determination of water saturation from logs: *Journal of Petroleum Technology*, vol. 18, no. 11, pp. 1425–1433.

Poupon, A., Clavier, C., Dumanoir, J., Gaymard, R., and Misk, A., 1970, Log analysis of sand-shale sequences: A systematic approach: *Journal of Petroleum Technology*, vol. 22, no. 7, pp. 867–881.

Quirein, J., Kimminau, S., La Vigne, J., Singer, J., and Wendel, F., 1986, A coherent framework for developing and applying multiple formation evaluation models: Paper DD, *Transactions of the SPWLA 27th Annual Logging Symposium*, Houston, Texas, June 9–13.

Quirein, J., Witkowsky, J., Truax, J., Galford, J., Spain, D., and Odumosu, T., 2010, Integrating core data and wireline geochemical data for formation evaluation and characterization of shale gas reservoirs: SPE 134559, *Proceedings of the SPE Annual Technical Conference and Exhibition*: Society of Petroleum Engineers, Florence, Italy, September 19–22.

Salazar, J. M., Torres-Verdín, C., Alpak, F. O., Habashy, T. M., and Klein, J. D., 2006, Estimation of permeability from array induction measurements: applications to the petrophysical assessment of tight-gas sands: *Petrophysics*, vol. 47, no. 6, pp. 527–544.

Salazar, J. M., Malik, M., Torres-Verdín, C., Wang, G. L., and Duan, H., 2007, Fluid density and viscosity effects on borehole resistivity measurements acquired in the presence of oil-based mud and emulsified surfactants: SPE 109946, *Proceedings of the SPE Annual Technical Conference and Exhibition*: Society of Petroleum Engineers, Anaheim, California, November 11–14.

Salazar, J. M. and Torres-Verdín, C., 2009, Quantitative comparison of processes of oil- and water-base mud-filtrate invasion and corresponding effects on borehole resistivity measurements: *Geophysics*, vol. 74, no. 1, pp. E57–E73.

Sanchez-Ramirez, J. A., Torres-Verdín, C., Wang, G. L., Mendoza, A., Wolf, D., Liu, Z., and Schell, G., 2009, Field examples of the combined petrophysical inversion of gamma-ray, density, and resistivity logs acquired in thinly-bedded clastic rock formations: *Petrophysics*, vol. 51, no. 4, pp. 247–263.

Sanchez-Ramirez, J. A., Torres-Verdín, C., Wang, G. L., Mendoza, A., Wolf, D., Liu, Z., and Schell, G., 2009, Field examples of the combined petrophysical inversion of gamma-ray, density, and resistivity logs acquired in thinly-bedded clastic rock formations: Paper DDD, *Transactions of the SPWLA 50th Annual Logging Symposium*, The Woodlands, Texas, June 21–24.

Sanchez -Ramirez, J. A., 2009, Field Examples of the Combined Petrophysical Inversion of Gamma-Ray, Density, and Resistivity Logs Acquired in Thinly-Bedded Clastic Rock Formations: *Master's Thesis*, The University of Texas at Austin.

Schlumberger log interpretation charts, 2005: Schlumberger, Houston, Texas.

Sondergeld, C. H., Newsham, K. E., Comisky, J. T., Rice, M. C., and Rai, C. S., 2010, Petrophysical considerations in evaluating and producing shale gas resources: SPE 131768, *Proceedings of the SPE Unconventional Gas Conference*: Society of Petroleum Engineers, Pittsburgh, Pennsylvania, February 23–25.

Spain, D. R. and Anderson, G. A., 2010, Controls on reservoir quality and productivity in the Haynesville Shale, northwestern Gulf of Mexico Basin: *Gulf Coast Association of Geological Societies Transactions*, vol. 60, pp. 657–668.

Spears, R. W., Shray, F., Jacobsen, S., Bowers, M. C., and Nicosia, F., 2008, Where quicklook petrophysics goes wrong: A case study in a mature south Texas gas field: Paper PPP, *Transactions of the SPWLA 48th Annual Logging Symposium*, Edinburgh, Scotland, May 25–28.

Suicmez, V. S., Piri, M., and Blunt, M. J., 2007, Surprising trends on trapped hydrocarbon saturation with wettability: *Proceedings of SCA*: Society of Core Analysts, Calgary, Canada, September 10–12.

Suzanne, K., Hamon, G., Billiotte, J., and Trocme, V., 2001, Distribution of trapped gas saturation in heterogeneous sandstone reservoirs: *Proceedings of the International Symposium of the Society of Core Analysts*, Edinburgh, Scotland, September 17–19.

Suzanne, K., Hamon, G., and Billiotte, J., 2003, Experimental relationships between residual gas saturation and initial gas saturation in heterogeneous sandstone reservoirs: SPE 84038, *Proceedings of the SPE Annual Technical Conference and Exhibition*: Society of Petroleum Engineers, Denver, Colorado, October 5–8.

Thomas, E. C. and Stieber, S. J., 1975, The distribution of shale in sandstones and its effect upon porosity: Paper T, *Transactions of the SPWLA 16th Annual Logging Symposium*, New Orleans, Louisiana, June 4–7.

Timur, A., 1968, An investigation of permeability, porosity, and residual water saturation relationship for sandstone reservoirs: *The Log Analyst*, vol. 9, no. 4, pp. 8–17.

Torres-Verdín, C., Alpak, F. O., and Habashy, T. M., 2006, Petrophysical inversion of borehole array-induction logs: Part II-field data examples: *Geophysics*, vol. 71, no. 5, pp. G261–G268.

Trewin, B. and Morrison, S., 1990, Reconciliation of core and log residual oil saturation through application of in-situ saturation monitoring: in Advances in Core Evaluation, Worthington, P. F., and Chardaire-Rivière, C., Editors, Gordon and Breach Science Publishers, London, England.

Wang, G. L., Torres-Verdín, C., Salazar, J. M., and Voss, B., 2009, Fast 2D inversion of large borehole EM induction data sets with an efficient Fréchet-derivative approximation: *Geophysics*, vol. 74, no. 1, pp. E75–E91.

Wyllie, M. R. J., Gregory, A. R., and Gardner, L. W., 1956, Elastic wave velocities in heterogeneous and porous media: *Geophysics*, vol. 21, no. 1, pp. 41–70.

Zeybek, M., Ramakrishnan, T. S., Al-Otaibi, S. S., Salamy, S. P., and Kuchuk, F. J., 2004, Estimating multiphase-flow properties from dual-packer formation-tester interval tests and openhole array resistivity measurements: *SPE Reservoir Evaluation & Engineering*, vol. 7, no. 1, pp. 40–46.

Zinszner, B. and Pellerin, F. M., 2007, A Geoscientist's Guide to Petrophysics: Editions Technip, Paris, France.